



eman ta zabal zazu



Universidad  
del País Vasco

Euskal Herriko  
Unibertsitatea

---

# Meteorological phenomena on Mars studied with Mars Express VMC images

---

*A thesis submitted in fulfillment of the requirements  
for degree of Doctor of Philosophy by*

**Jorge Hernández Bernal**

Supervised by:

Prof. Agustín Sánchez Lavega

Dr. Teresa del Río Gaztelurrutia

Bilbao, October 2022



*"Todo el mundo va a estar en la pelea por esos recursos  
[los minerales críticos para la transición energética]"*

Arantxa Tapia, Consejera de Desarrollo Económico del Gobierno Vasco  
28 de abril de 2022 en el Bizkaia Aretoa

*"Vamos a llegar a 2100 con un aumento de temperatura de 1.5°C.  
No tengo ninguna duda. La tecnología nos ayudará"*

Antonio Brufau, Presidente de Repsol.  
28 de abril de 2022 en el Bizkaia Aretoa

*"No credible pathway to 1.5°C [is] in place"*

UN Environment Program, Emission Gap Report 2022

*"For decades, many in the fossil fuel industry have invested heavily in pseudo-science and public relations with a false narrative to minimize their responsibility for climate change and undermine ambitious climate policies. They exploited precisely the same scandalous tactics as Big Tobacco decades before."*

António Guterres, UN Secretary General

*"If we teach only the findings and products of science – no matter how useful and even inspiring they may be – without communicating its critical method, how can the average person possibly distinguish science from pseudoscience?"*

Carl Sagan, The Demon-Haunted World: Science as a Candle in the Dark



# Agradecimientos

Quiero agradecer muy especialmente a mis directores de tesis, Agustín y Teresa, por todas las oportunidades que me han dado, el tiempo y la energía que me han dedicado, la paciencia que han tenido conmigo, la disponibilidad, el apoyo diario, y todos los aprendizajes. Es un privilegio hacer un doctorado en un entorno con un trato humano tan cercano y un nivel científico tan alto como el del Grupo de Ciencias Planetarias. Agradezco también a Ricardo Hueso su cercanía y todas sus enseñanzas.

This thesis was developed in the frame of the Mars Express VMC project, supported by the European Space Agency. This has involved a close collaboration with many colleagues. I want to acknowledge Alejandro Cardesín, who has taught me so much about how to operate spacecrafts and has provided so much technical support; Eleni Ravanis, who was a great colleague and now a great friend and collaborator; Abel de Burgos Sierra, who developed the VMC flat that has enabled so many amazing developments; Simon Wood for so much technical support; Marc Costa, for his support regarding SPICE; and also Julia Marín, Donald Merritt, and all the Mars Express Science Ground Segment, colleagues working at ESAC, ESOC, and ESTEC, and planners from the other instruments with whom I have interacted and learnt, with a special mention to Daniela Tirsch and Ernst Hauber, who are always kindly open to listen my ideas to do new things with HRSC; and with a memory to Brigitte Gondet, who operated OMEGA for so many years and provided some images used in this thesis.

J'ai été trois mois au LMD, où j'ai appris beaucoup de choses sur la modélisation des atmosphères planétaires. Je remercie Aymeric Spiga pour son temps et dévouement. Et aussi les autres collègues du LMD: Ehouarn, Maëlle, Antoine, Anthony, et beaucoup d'autres personnes à Jussieu.

Volviendo a Bilbao y más allá de la tesis, ha sido un placer interactuar con los demás miembros del Grupo de Ciencias Planetarias, hablar con José Félix Rojas, y con Santiago Pérez Hoyos, a quien tanto admiro y agradezco el apoyo y la esperanza que me inspira y con quien tanto he colaborado para empezar a hablar de Ética Espacial. He compartido muchas comidas y otras actividades con miembros del Grupo de Ciencias Planetarias y del departamento de Física Aplicada, que han sido una compañía en el día a día y han hecho estos años mucho más amenos: Aritz, Arrate, Asier Anguiano, Asier Munguira, Hao, Iñaki, Itziar, Joan, Mateu, Naiara, Peio. Eskerrik asko!

He tenido la suerte de conocer a buenos amigos y amigas en Bilbao con quienes he compartido largas conversaciones muy enriquecedoras y que me han prestado un gran apoyo durante el desarrollo de esta tesis: Teresa, Eder y Aless, Carmen y Daniel, Pablo, Aitor, Vero, Idoia y Jon, Loa...

Otros amigos en Salamanca y en otras partes del mundo son un gran apoyo e inspiración en el día a día y siempre ponen mucho interés en el desarrollo de mis investigaciones, pensamientos, ideas, y proyectos: Adriana, Sónia, Elvira Hernández, María Losada, Inma Cid, Sergio Sanjurjo, Marco Hernández, Laura, Nair... Otros amigos de generaciones anteriores me conocieron casi de niño y me han visto crecer, prestándome todo su apoyo y mentoría: Alejandra Casas, Pedro y Ana, y Carlos Tejero.

Algo está pasando en el mundo. Algo muchísimo más importante que la exploración de otros planetas y que amenaza a nuestra civilización a corto plazo mientras cientos de miles de personas mueren ya al año. Hablemos claro, digamos la verdad, actuemos ahora, y organicemos asambleas climáticas para resolver el mayor problema de nuestra historia con justicia climática. Tengo que agradecer a todas mis compañeras y compañeros de Scientist Rebellion, Extinction Rebellion, y Futuro Vegetal todo lo que hacen y las interesantes conversaciones y reflexiones que me aportan. A Vero, que tanto me ha aportado con su carácter tan humano, y que siempre pone a prueba mis ideas. A Romain y Agnès. A Antonio y Adrián, con quienes he compartido tantas reflexiones enriquecedoras. A todas las personas que asumen las consecuencias de recurrir a la desobediencia civil por la causa más trascendente de la historia de la humanidad, y a todo el equipo de cientos de personas que desde posiciones más discretas dan el apoyo técnico necesario. No es ya ecologismo, es coherencia con la gravedad de vivir en una fantasía que empieza a desmoronarse. Otro mundo es posible, en el mismo planeta.

Muchos de los recursos bibliográficos que he usado durante esta tesis han sido accesibles gracias a sci-hub, una plataforma que pone a disposición de todo el mundo una literatura científica que de otro modo sería difícilmente accesible. Es de agradecer que Alexandra Elbakyan pusiera en marcha este proyecto que tanto está aportando al mundo.

Por último, agradezco a mis padres su apoyo, a mi hermana Noelia, que siempre ha sido mi mayor mentora y mi mejor profesora, a Carlos, y al resto de mi familia.







# Ecological footprint of this thesis

Every activity involves an ecological footprint. In the current industrial agricultural system, food is one of the main sources of ecological impact and one of the most unsustainable sectors. There are several ways in which academia produces an ecological footprint, including: construction and heating of buildings where we work; computers, machines, and any other objects; electricity consumption; and traveling. These items involve not just a carbon footprint associated with their energy consumption, but also other greenhouse gases and an impact associated with the raw materials that are mostly not part of a circular economy, and the industrial processes associated with the manufacturing.

The ecological footprint is NOT a personal issue. We cannot fix this problem by individual actions while we are part of this unsustainable society, in which even food production (meat but also vegetables) involves a wide variety of unsustainable processes. However, assessing the footprint of our lives and the things we do in our day a day provides useful knowledge to understand the problem and try to search for solutions in common. This page comprises a simple assessment of the carbon footprint associated with this thesis, including only travels and electricity consumption.

As part of this thesis, I have traveled roughly 32000 km, using planes, cars, buses, and trains, and without considering public transport in cities. The carbon footprint associated with these displacements sums a total of 6.3 Tons of CO<sub>2</sub>. By doing some of my trips staying on the ground instead of taking planes and by not doing some trips, this carbon footprint has been reduced by 2.4 Tons. Online conferences and meetings due to the pandemic situation are not considered in this assessment.

In addition to trips, this thesis has involved computational resources. I did not monitor actively the CPU consumption, but a rough estimation including working stations and servers results in a carbon footprint of around 500 kg. We have to consider that all these machines include electronics that cannot be recycled. This is an important source of unsustainability. Both Spain and France use nuclear energy as part of their mixes, therefore a quantity of nuclear waste is also associated with this thesis. Given the coming reduction of fossil fuel availability, and the limitations of other sources of energy, this is not just about reducing the carbon footprint, but about reducing the energy consumption in general.

Finally, we cannot forget that the space sector relies on rocket launches. These launches have different kinds of impacts and they contribute to the greenhouse effect in different ways. It is estimated that the Soyuz Fregat rocket that launched Mars Express emits a total amount of 243 Tons of CO<sub>2</sub> ( <https://everydayastronaut.com/rocket-pollution/> ). I admit that this point is a topic in my task list and for now I cannot give a careful assessment of this point.



# Table of contents

Resumen (summary in Spanish) .....	1
Glossary .....	7
Synthesis.....	11
1. Introduction .....	12
2. Theoretical framework and Methodology .....	14
2.1. The atmosphere and climate of Mars.....	14
2.1.1. The Martian orbit and rotation.....	14
2.1.2. Timekeeping on Mars .....	14
2.1.3. Topography of Mars.....	18
2.1.4. Atmospheric characteristics and thermal structure .....	19
2.1.5. The global circulation.....	22
2.1.6. Aerosols and their climatology .....	24
Dust and dust storms .....	24
Condensate clouds .....	27
Low altitude water ice clouds.....	28
Mesospheric clouds and dust .....	29
2.1.7. A meteorological calendar of Mars.....	32
2.1.8. Summary of missions and instruments .....	34
2.2. MEX/VMC. Calibration, Data Processing and Operations .....	40
2.2.1. The capabilities of VMC.....	42
2.2.2. Photometric calibration and low level data processing.....	44
2.2.3. Geometric calibration .....	44
Determination of VMC orientation and iFOV.....	46
Time: Using Phobos as a clock .....	48
2.2.4. Operations.....	49
Medium Term Planning (MTP) .....	50
Short Term Planning (STP).....	51

2.2.5.	Level 4 data processing for HDR products .....	52
2.2.6.	Internal infrastructure and web apps .....	56
2.3.	Instruments and tools .....	60
2.3.1.	Data from other Instruments used in this Thesis.....	60
2.3.2.	Software .....	60
Elkano:	broad use for planetary images.....	61
Mars Studio	.....	62
Marstime	.....	63
2.3.3.	LMD models .....	64
GCM	.....	64
Mesoscale model	.....	64
Mars Climate Database (MCD)	.....	65
3.	Objectives and publications .....	66
4.	Summary and discussion.....	69
4.1.	Dust Storms and the Global Dust Storm in Martian Year 34.....	69
4.2.	Orographic clouds. The Arsia Mons Elongated Cloud (AMEC).....	70
4.2.1.	The orographic cloud mechanisms on Mars.....	71
4.2.2.	The Arsia Mons Elongated Cloud (AMEC).....	71
4.2.3.	Near CO <sub>2</sub> condensation temperatures in the AMEC .....	74
4.2.4.	Is the AMEC one of a kind? .....	74
4.3.	Mesospheric clouds, observing the twilight.....	76
4.3.1.	A systematic study of clouds in twilight .....	78
4.3.2.	Mesospheric cloud tracking in twilight.....	80
5.	References .....	81
	Published works .....	91
	Conclusions .....	99
	Annex .....	105





## Resumen (summary in Spanish)

La atmósfera de Marte está en su mayor parte compuesta por Dióxido de Carbono y se caracteriza por tener una presión atmosférica muy baja, de sólo 650 Pa de media a nivel de superficie. La baja densidad de esta atmósfera supone una baja inercia térmica, y en Marte no hay océanos como los de la Tierra que puedan elevar esta inercia térmica. Como resultado, la atmósfera de Marte responde muy rápidamente a los cambios de insolación y presenta una dinámica extraordinariamente rápida.

De forma análoga a la Tierra, Marte presenta una inclinación de su eje de rotación respecto a su plano orbital de unos 23°, y como consecuencia, un ciclo estacional análogo al de la Tierra. Sin embargo, es la alta excentricidad de su órbita lo que más diferencias produce entre unas épocas del año y otras. Así, la época del afelio es una época más fría, que coincide con la primavera y verano del hemisferio Norte (primera mitad del año); y la época del perihelio es una época más calurosa, que coincide con la primavera y verano del hemisferio Sur (segunda mitad del año).

Otra característica esencial de la atmósfera de Marte es la constante presencia de polvo. La superficie de Marte está en su mayor parte cubierta de polvo, que puede elevarse en la atmósfera y quedar en suspensión. Así, cierta cantidad de polvo está siempre presente en la atmósfera. El polvo puede elevarse al soplar el viento cerca del suelo, y también con fenómenos tales como los dust devils, frecuentemente observados por las misiones en superficie.

Además del polvo constantemente en suspensión, se dan ocasionalmente tormentas de polvo, que son especialmente frecuentes durante la segunda mitad del año debido a la mayor insolación incidente. En la primera mitad del año las tormentas de polvo sólo son comunes en el borde de los casquetes polares, donde el alto gradiente térmico produce vientos rápidos que pueden elevar polvo desde el suelo. el máximo exponente de las tormentas de polvo son las tormentas globales de polvo, que se dan sólo algunos años durante la segunda mitad del año.

El efecto radiativo del polvo, sea en suspensión o en forma de tormentas tiene fuertes efectos en la circulación global a través de sus efectos radiativos, de forma equivalente a las nubes de agua en la Tierra.

En Marte también existen nubes. Una pequeña cantidad de vapor de agua suele existir en suspensión en la atmósfera, y cuando se dan las condiciones adecuadas de presión parcial y temperatura, esta puede congelarse en forma de cristales de hielo que forman nubes. Llamativamente, el principal componente de la atmósfera, el Dióxido de Carbono, puede



## Meteorological phenomena on Mars studied with Mars Express VMC images.

también formar nubes cuando en situaciones muy particulares se forman bolsas de aire extremadamente frío en la mesosfera, o a alturas menores en la noche polar.

Esta tesis consiste en el estudio de fenómenos meteorológicos en la atmósfera de Marte usando principalmente imágenes obtenidas con la cámara VMC del orbitador europeo Mars Express. VMC es una cámara sencilla, con características similares a las de una webcam de los años 2000, y fue enviada a Marte como una simple cámara de ingeniería cuyo único propósito era confirmar la separación del aterrizador Beagle 2. VMC cumplió con su misión original en 2003, y no funcionó otra vez hasta 2007, cuando fue encendida nuevamente para tomar imágenes de Marte con fines de divulgación científica.

Tras varios años, el interés científico de estas imágenes fue reconocido y en 2016 a través de un convenio entre la Agencia Espacial Europea (ESA) y la Universidad del País Vasco (UPV/EHU), comenzó un proyecto para convertir VMC en un nuevo instrumento científico de Mars Express.

Esta tesis se ha desarrollado en el marco de ese proyecto, por lo que los desarrollos metodológicos expuestos en la tesis han contribuido también a la conversión de esta simple webcam que es VMC en un instrumento científico completamente operativo. Estos desarrollos metodológicos incluyen la calibración fotométrica, geométrica, y temporal de VMC; el desarrollo de la pipeline de procesado y archivado de datos que funciona operacionalmente en el servidor de VMC dentro de la red informática de la ESA; la participación en las operaciones de Mars Express; y el desarrollo de multitud de sistemas, bases de datos, paquetes de software, y aplicaciones para la visualización, procesado, y análisis de los datos.

Esta base metodológica ha posibilitado el desarrollo de una investigación científica centrada en diferentes fenómenos meteorológicos que resultaban especialmente bien accesibles para VMC, y que en cambio eran más difíciles de observar para otros instrumentos y misiones que orbitan Marte. Esto se debe a que VMC, a pesar de sus evidentes limitaciones técnicas, tiene una serie de características particulares que sobresalen sobre las de otras cámaras que ha habido orbitando Marte hasta muy recientemente. En particular: 1. La capacidad de obtener imágenes de disco completo desde los apocentros de Mars Express. 2. La órbita no heliosíncrona de Mars Express, que permite observar una multitud de horas locales variadas. 3. La capacidad de VMC de tomar largas series de imágenes con las que es posible componer vídeos que muestran la dinámica de los fenómenos meteorológicos.

Así, son 3 los fenómenos meteorológicos estudiados en el marco de esta tesis:

- La incidencia de la gran tormenta de polvo de 2018 sobre la región polar sur.
- Las nubes noctilucentes. Incluyendo el primer estudio sistemático de este tipo de nubes en Marte, donde son más frecuentes que en la Tierra.

Meteorological phenomena on Mars studied with Mars Express VMC images.

- La nube elongada de Arsia Mons (AMEC). Un fenómeno extraordinario que se ha descrito en una publicación científica por primera vez.

La tormenta global de polvo de 2018 comenzó en el hemisferio Norte, lo que, de acuerdo con el limitado número de casos estudiados, parece ser inusual. En pocos días la tormenta creció hasta alcanzar la escala global y penetrar la región polar sur. Gracias a la órbita polar de Mars Express y a la capacidad de VMC de obtener imágenes de disco completo, fue posible monitorear la tormenta sobre el conjunto de la región polar sur durante varias semanas.

Las observaciones de VMC revelan que el polvo penetró de forma inhomogénea en la región cubierta por el casquete polar, y la cobertura de polvo variaba notablemente de unos días a otros. Las observaciones de VMC separadas por típicamente una media hora permitieron observar masas de polvo desplazándose sobre el casquete, lo que permitió medir los vientos dominantes. Este tipo de medidas directas de viento no son comunes en Marte, y son especialmente interesantes en las proximidades de los polos, donde la circulación de los vientos suele estar caracterizada por los vórtices polares.

Las observaciones de VMC analizadas en el marco de esta tesis muestran también la presencia de enormes bandas de aerosoles rodeando el polo. Estas bandas penetraban la noche, lo que permitió estimar su altura en unos 10-30km. El hecho de que eran claramente más visibles en las proximidades del crepúsculo indica que muy probablemente estaban compuestas de condensados, a todas luces de cristales de hielo de agua.

El segundo fenómeno meteorológico estudiado en el marco de esta tesis son las nubes noctilucentes. Las nubes en general tienen en Marte mayor facilidad para formarse en altura que en la Tierra. Como resultado, las nubes noctilucentes son muy comunes en Marte, y muy probablemente fueron observadas por primera vez en observaciones telescópicas en la década de 1890. Dado que la mayor parte de las imágenes de Marte obtenidas por los orbitadores en las últimas décadas muestran únicamente la hora local del mediodía, el crepúsculo es una hora del día poco estudiada a través de imágenes.

VMC ha pasado unos 15 años obteniendo miles de imágenes de Marte, y una fracción muy alta de ellas muestra el amanecer. Esto hace de VMC el mejor instrumento disponible hasta muy recientemente para este tipo de estudio. Con el fin de explotar esta capacidad, se desarrolló un software capaz de analizar automáticamente las imágenes de VMC en busca de nubes noctilucentes en la parte nocturna del planeta. También se desarrollaron métodos avanzados para medir la altura de estas nubes utilizando las particulares condiciones geométricas que las hacen visibles en la noche.

Como resultado de este trabajo se ha obtenido una base de datos que contiene más de 400 nubes noctilucentes, lo que constituye el primer estudio sistemático de este tipo de

## Meteorological phenomena on Mars studied with Mars Express VMC images.

nubes en Marte. Se ha estudiado la distribución espacial y temporal de estas nubes y se ha comparado con observaciones previas de nubes mesosféricas en Marte. Una concentración inesperadamente alta de estas nubes se da durante el otoño e invierno local en las latitudes medias. Curiosamente, las escasas nubes mesosféricas reportadas por estudios previos en las proximidades del crepúsculo parecen mostrar una tendencia similar, pero es este estudio sistemático el que la hace claramente visible.

No es posible determinar la composición de estas nubes utilizando únicamente VMC. Pero las observaciones previas de nubes mesosféricas en latitudes medias en las proximidades del crepúsculo parecen indicar que puede haber presentes nubes de hielo de agua, y también de dióxido de carbono.

El tercer fenómeno meteorológico estudiado en el marco de esta tesis es la nube elongada de Arsia Mons (AMEC). Se trata de la nube orográfica más grande jamás observada en el sistema solar, al alcanzar una extensión de hasta 1800 km. Esta nube expresa una dinámica inusualmente rápida, al formarse en sólo 3 horas justo después del amanecer y disolverse muy rápidamente. En una primera parte del estudio se emplearon imágenes de todos los instrumentos de imagen que por sus características podían observar la nube, y se hizo una amplia descripción observacional del fenómeno. Posteriormente y en colaboración con el Laboratorio de Meteorología Dinámica (LMD) se ejecutaron simulaciones de mesoescala para intentar comprender la formación de esta inusual nube.

El estudio de la AMEC ha desvelado mecanismo de formación de nubes orográficas que previamente no se había detectado en Marte. Estudios previos revelaron que las nubes orográficas en la primera mitad del año se forman con el ascenso de masas de aire húmedo por las laderas de las montañas. El nuevo estudio elaborado en el marco de esta tesis revela que en la segunda mitad del año, debido a las temperaturas más altas, este mecanismo es esencialmente incapaz de elevar el aire húmedo a una altura suficiente para condensar, y en cambio las nubes orográficas se forman cuando ondas de gravedad originadas por la interacción del viento con las montañas se propagan verticalmente y perturban la hygropausa.

En efecto, las simulaciones de mesoescala para el caso de la AMEC predicen una fuerte onda de gravedad que se propaga verticalmente desde Arsia Mons y produce una bolsa de aire frío de hasta 30K bajo la temperatura ambiente a una altura de unos 40-50 km. Esta bolsa de aire frío observada en las simulaciones coincide extraordinariamente bien en términos espaciales y temporales con la zona donde la AMEC se forma de acuerdo con las observaciones.

Sin embargo, las simulaciones numéricas son incapaces de dar una explicación convincente para la formación de la cola extremadamente larga de la AMEC. Existen fuertes indicios que indican que esta cola se forma cuando la nube formada en la bolsa de aire frío es transportada por el fuerte viento del Este, pero suponiendo que esta advección

## Meteorological phenomena on Mars studied with Mars Express VMC images.

se dé en condiciones de equilibrio termodinámico, la nube debería evaporarse al abandonar la bolsa de aire frío donde se forma. Parece entonces que debe de haber algún mecanismo que no ha sido posible comprender detrás de la extremada elongación de esta peculiar nube. Este mecanismo podría consistir en un campo de temperaturas diferente al que predicen las simulaciones, en algún tipo de mecanismo microfísico desconocido que retrase la evaporación de los cristales de hielo de agua, en alguna combinación de estos factores, o algún otro tipo de mecanismo por el momento indeterminado.

El estudio de estos fenómenos meteorológicos muestra que VMC es una pequeña cámara con un enorme potencial científico. Y además revela la riqueza de los fenómenos meteorológicos que se dan en Marte al amanecer, un momento del día escasamente estudiado y que probablemente aún guarda muchos secretos.

Meteorological phenomena on Mars studied with Mars Express VMC images.

# Glossary

## **General terms**

- DDS: Data Distribution Service
- EAICD: Experiment Archive Interface Control Document
- ESA: European Space Agency
- ESAC: European Space Astronomy Center
- ESOC: European Space Operations Center
- FOV: Field of Fiew
- FUM: VMC Flight User Manual
- GCM: General Circulation Model
- GCP: Grupo de Ciencias Planetarias
- HDR: High Dynamic Range
- iFOV: instantaneous Field of View
- LMD: Laboratoire de Météorologie Dynamique
- Ls: Solar Longitude
- LTP: Long Term Planning
- LTST: Local True Solar Time
- MCD: Mars Climate Database
- MM: Mesoscale Model
- MMM: Mars Mesoscale Model
- MTP: Medium term Planning
- MY: Martian Year
- PDS: Planetary Data System
- PSA: ESA Planetary Science Archive
- SPICE: Spacecraft Planet Instrument C-matrix Events
- SGS: Science Ground Segment
- STP: Short Term Planning
- UMSF: Unmanned Spaceflight Forums
- UPV/EHU: University of the Basque Country, Universidad del País Vasco/Euskal Herriko Uniberstsitea
- WRF: Weather Research and Forecast
- TOA: Top of Atmosphere

## **Meteorological phenomena**

- ACB: Aphelion Cloud Belt
- AMEC: Arsia Mons Elongated Cloud
- DDL: Detached Dust Layer
- GDS: Global Dust Storm
- NPH: North Polar Hood
- PCT: Perihelion Cloud Trails
- SPH: South Polar Hood

Meteorological phenomena on Mars studied with Mars Express VMC images.

### **Missions and instruments**

- ACS: Atmospheric Chemistry Suite
- ASPERA: Analyser of Space Plasmas & Energetic Atoms
- CaSSIS: Colour and Stereo Surface Imaging System
- CRISM: Compact Reconnaissance Imaging Spectrometer
- CTX: Context Camera
- EMIRS: Emirates Mars Infrared Spectrometer
- EXI: Emirates eXploration Imager
- HiRISE: High Resolution Imaging Science Experiment
- HRSC: High Resolution Stereo Camera
- HiRIC: High Resolution Imaging Camera
- IRTM: Infrared Thermal Mapper
- IUVS: Imaging Ultraviolet Spectrometer
- MAVEN: Mars Atmosphere and Volatile Evolution
- M2020: Mars 2020 / Perseverance
- MARCI: Mars Color Imager
- MaRS: Mars Radio Science
- MAWD: Mars Atmospheric Water Detector
- MCC: Mars Color Camera
- MCS: Mars Climate Sounder
- MER: Mars Explorations Rover
- MEX: Mars Express
- MGS: Mars Global Surveyor
- MMS: Mars Mineralogical Spectrometer
- MOC: Mars Orbiter Camera
- MOLA: Mars Orbiter Laser Altimeter
- MOM: Mars Orbiter Missions
- MoRIC: Moderate Resolution Imaging Camera
- MRO: Mars Reconnaissance Orbiter
- MSL: Mars Science Laboratory
- MSM: Methane Sensor for Mars
- NOMAD: Nadir and Occultation for Mars Discovery
- ODY: Mars Oddysey
- OMEGA: Observatoire pour la Minéralogie, l'Eau, les Glaces et l'Activité
- PFS: Planetary Fourier Spectrometer
- REMS: Rover Environmental Monitoring Station

Meteorological phenomena on Mars studied with Mars Express VMC images.

- SPICAM: SPectroscopy for the Investigation of the Characteristics of the Atmosphere of Mars
- TES: Thermal Emission Spectrometer
- TGO: Trace Gas Orbiter
- THEMIS: Thermal Emission Imaging System
- VIS: Visible camera aboard Viking orbiters
- VMC: Visual Monitoring Camera



Meteorological phenomena on Mars studied with Mars Express VMC images.

Meteorological phenomena on Mars studied with Mars Express VMC images.

# Synthesis

## 1. Introduction

This thesis pursues the study of different meteorological phenomena in the atmosphere of Mars, based on images obtained with the VMC camera onboard the European Mars Express orbiter. VMC was included in Mars Express as an engineering instrument, only intended to monitor the separation of the Beagle 2 lander, in 2003. From 2007 to 2016, VMC was employed as an outreach camera and in 2016 a new project to use VMC as a new science instrument devoted to the investigation of the Martian atmosphere was started in collaboration with the Grupo de Ciencias Planetarias (GCP) in the University of the Basque Country (UPV/EHU). Professor Agustín Sánchez Lavega was named science lead for VMC acting since 2016 as PI of the camera.

This thesis has been developed in the Grupo de Ciencias Planetarias as part of the VMC science team, with a stay of three months at the LMD (Laboratoire de Météorologie Dynamique; Paris, France) that qualifies the thesis for an international mention under regulations of the UPV/EHU.

The methodological developments of this thesis have contributed to the scientific recommissioning of VMC, and they include contributions to operations, data processing, and different software packages for the scientific exploitation of VMC data. Apart from VMC, data from additional six instruments have been exploited during the development of this thesis. Moreover, numerical atmospheric models of the Martian atmosphere both general circulations models and mesoscale models, have been used to provide physical insight into the origin of the observed phenomena.

The general scientific objective of this thesis is the study of meteorological phenomena on Mars, profiting from the particular capabilities of VMC and thus we have focused on meteorological phenomena that were exceptionally well covered by VMC. Indeed, the polar orbit of Mars Express, the high altitude of its non-sun-synchronous orbit, the wide field of view of VMC, and its capability to acquire long series of images, make from VMC a privileged observer of phenomena usually not reachable for many other instruments orbiting Mars.

The phenomena studied in this thesis are: the impact of the Global Dust Storm 2018 (GDS 2018) on the South Polar Cap of Mars; the Arsia Mons Elongated Cloud (AMEC); and the mesospheric clouds in twilight. The AMEC was first reported in a peer-reviewed paper in the context of this thesis, and mesospheric models have been run at the LMD to describe

Meteorological phenomena on Mars studied with Mars Express VMC images.

the physics underlying the formation of this cloud. The thesis also includes the first systematic study of mesospheric clouds in twilight.

The outline of this Synthesis is as follows. Section 2 provides a state of the art on the knowledge of the Martian atmosphere, meteorological phenomena, and missions exploring Mars; followed by an explanation of the methodologies developed within this thesis. Section 3 presents the objectives of this thesis and the publications where they are covered. Section 4 provides some results and discussion about the different meteorological phenomena studied.

Conclusions are presented in a separate section. And the papers that support this thesis are available in the Annex.

## 2. Theoretical framework and Methodology

### 2.1. The atmosphere and climate of Mars

#### 2.1.1. The Martian orbit and rotation

The orbit and rotation of a planet determine distribution and cycles of insolation, which is the main source of energy in the case of planets like Earth and Mars (Sánchez-Lavega, 2010), and thus is a key factor in their climatology. The main orbital parameters of Mars are given in Table 1, with the equivalent values for Earth also given for reference.

Mars is further from the Sun than Earth, and this translates into lower insolation and a longer year. Both planets exhibit a similar axial tilt, which results in the existence of seasons; however, the orbital eccentricity is much higher in the case of Mars and this has a strong impact on its seasons. This impact depends on the relative position of the aphelion/perihelion and the solstices/equinoxes, which evolves over timescales of ~10 000 years; the current Martian climate is characterized by a strong dichotomy between the first and the second halves of the year due to the current proximity of the extreme orbital positions to the solstices (Clancy et al. 1996; Barnes et al., 2017).

The mean synodic rotation period (the duration of the mean solar day) is very similar in both planets. A Martian day is commonly called a sol.

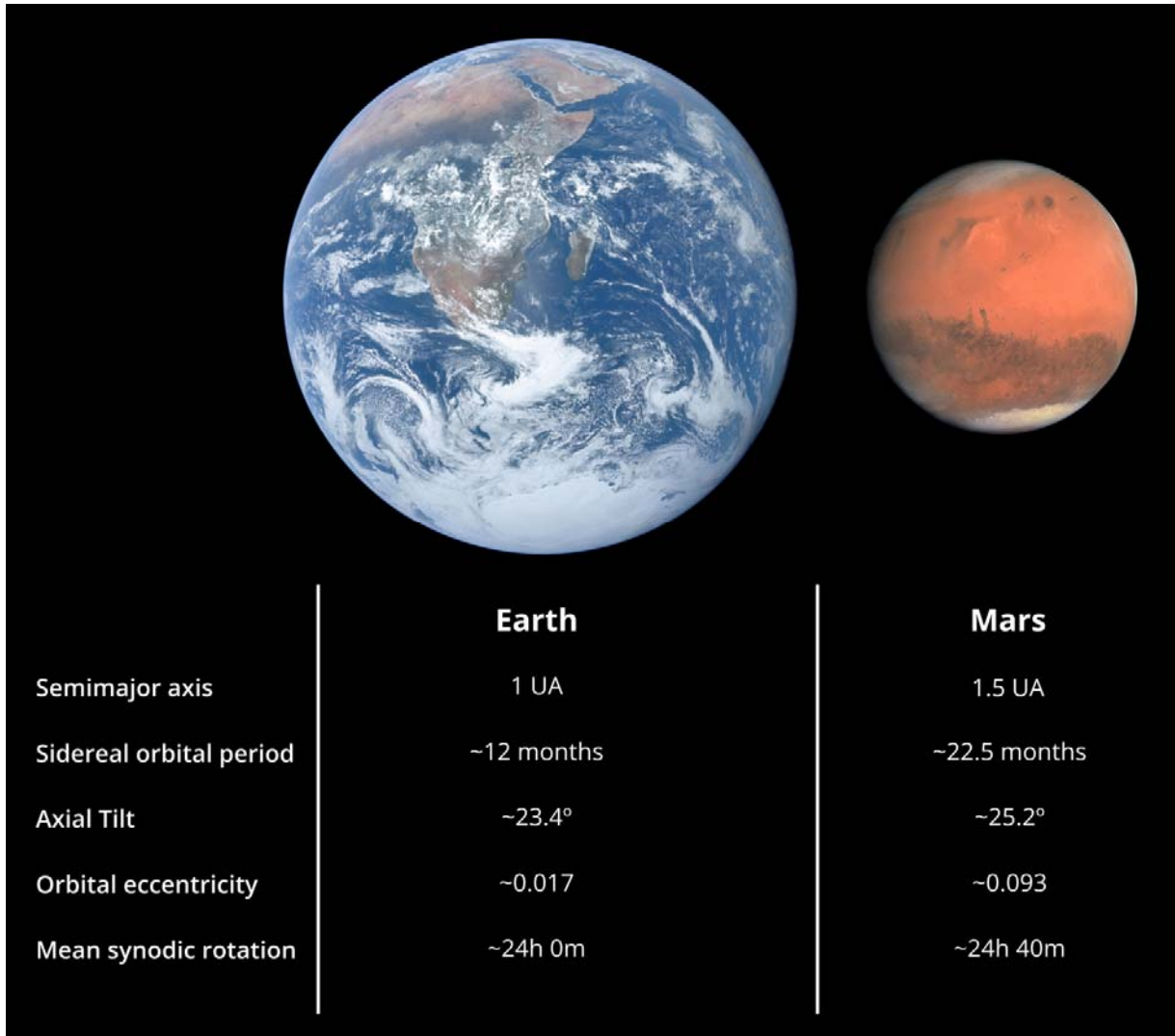
#### 2.1.2. Timekeeping on Mars

The study of the meteorology and climate of a planet requires establishing a timekeeping that relates to its orbit and rotation. Earth timekeeping is complex, it includes time zones and leap years are required to solve the incommensurability problem, because the Earth calendar needs to be an accurate tool to organize societies. Timekeeping on Mars is simpler, because it is only needed for science and mission operations.

The season of the year is often given by the Solar Longitude (Ls), which is measured from the Sun and goes from 0° to 360°, where 0° corresponds to the northern spring equinox. It is common to indicate the season of the year referred to an hemisphere (i.e. northern spring equinox), in the context of this synthesis, a different nomenclature based on the solar declination is used to refer to the global climate: northward equinox (equinox in which the sun is moving to the north, i.e. northern spring equinox), northern solstice (solstice in which the sun is in the northern hemisphere), southward equinox, and southern solstice.

Meteorological phenomena on Mars studied with Mars Express VMC images.

Table 1. Compared orbit and rotation parameters of Earth and Mars.



	<b>Earth</b>	<b>Mars</b>
Semimajor axis	1 UA	1.5 UA
Sidereal orbital period	~12 months	~22.5 months
Axial Tilt	~23.4°	~25.2°
Orbital eccentricity	~0.017	~0.093
Mean synodic rotation	~24h 0m	~24h 40m

It is important to remark that given the high orbital eccentricity of Mars, the Ls does not relate linearly to time, that is why sometimes the time of the year is given as the sol of year. Different definitions of Martian months are sometimes used in different contexts. In the case of surface missions time is usually measured as the sol of mission, starting at the day of the landing. These concepts are illustrated in Figure 1.

Martian Years (MY) are measured starting on April 11 1955, which corresponds to the Ls=0 of a year when a great dust storm was registered, commonly known as MY 1, following the proposal by Clancy et al. (2000). We are currently in the MY 36, and the MY37 will start in december 26 2022.

Meteorological phenomena on Mars studied with Mars Express VMC images.

Table 2. List of the most recent Martian Years and their solstices and equinoxes expressed in Earth time for reference.

MY	Ls=0 Northward Equinox	Ls=90 Northern Solstice	Ls=180 Southward Equinox	Ls=270 Southern Solstice
28	Jan 22 2006	Aug 08 2006	Feb 08 2007	Jul 04 2007
29	Dec 10 2007	Jun 24 2008	Dec 25 2008	May 21 2009
30	Oct 26 2009	May 13 2010	Nov 13 2010	Apr 07 2011
31	Sep 14 2011	Mar 30 2012	Sep 29 2012	Feb 23 2013
32	Jul 31 2013	Feb 14 2014	Aug 17 2014	Jan 11 2015
33	Jun 19 2015	Jan 03 2016	Jul 04 2016	Nov 28 2016
34	May 06 2017	Nov 19 2017	May 22 2018	Oct 16 2018
35	Mar 23 2019	Oct 08 2019	Apr 08 2020	Sep 01 2020
36	Feb 08 2021	Aug 25 2021	Feb 24 2022	Jul 21 2022
37	Dec 26 2022	Jul 12 2023	Jan 12 2024	Jun 07 2024

Since no time zones are defined on Mars, the time of the day is often given in Solar True Local Time (LTST), referred to a specific geographic longitude. It is usually given in terms of Martian hours, which result from dividing the duration of the sol by 24, and therefore, slightly longer than Earth hours. Portions of Martian hour can be expressed both as a decimal fraction or using a sexagesimal system. The time of the day can also be expressed in terms of the subsolar longitude, useful for example when studying the polar regions from satellite images.

The accurate parameters and algorithms needed for timekeeping were provided by Allison (1997) and Allison & McEwen (2000).

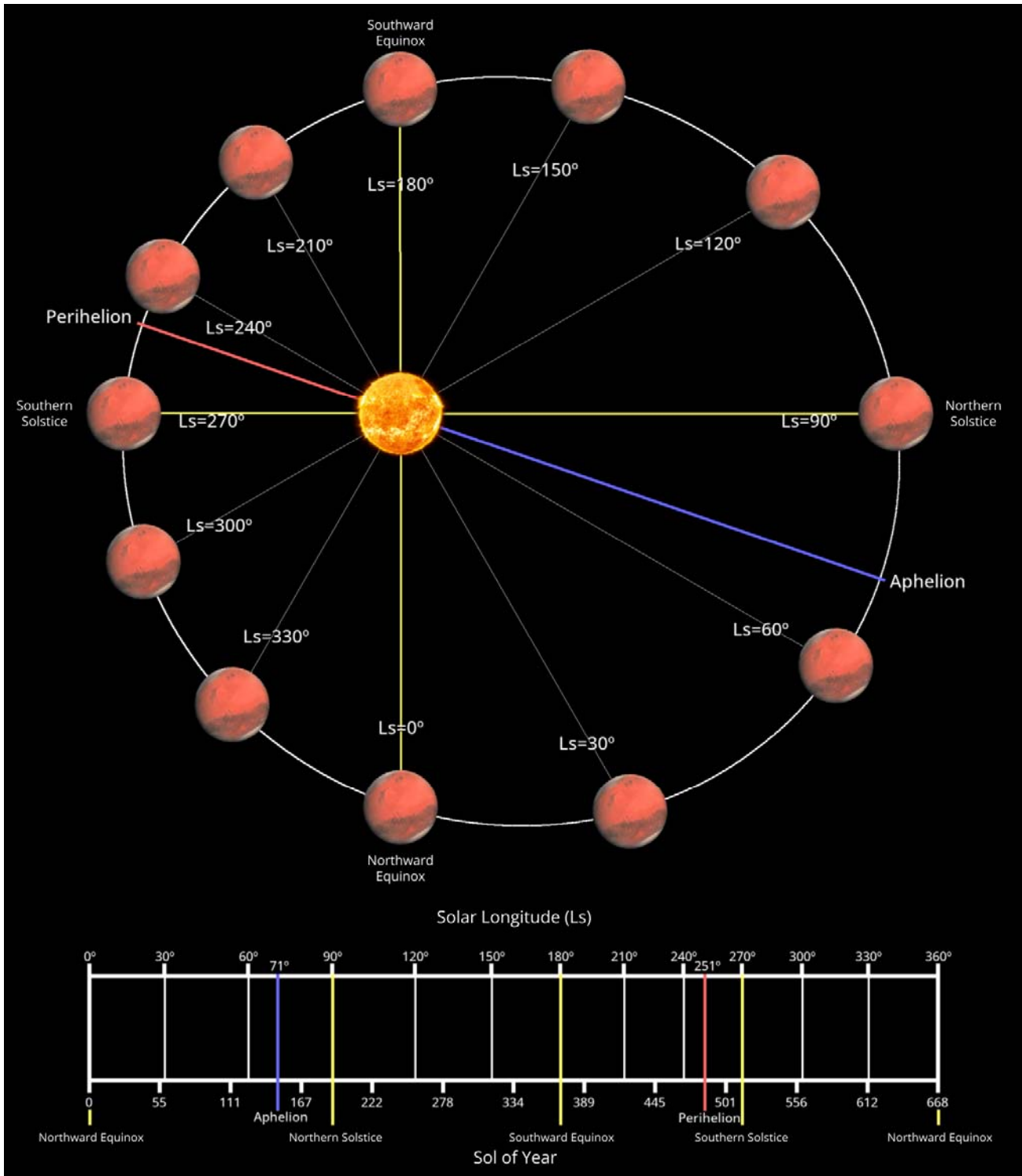


Figure 1. The Martian orbit (top) and basic calendar (bottom). Solar Longitude is indicated every 30°, which corresponds to a common definition of Martian months. The solstices and equinoxes are indicated in yellow, the aphelion is indicated in blue, and the perihelion is indicated in red. It is evident in the bottom diagram that the Solar Longitude is not linear with time (measured as the sol of year), this is due to the orbital eccentricity, overstated in the drawing of the orbit.



Meteorological phenomena on Mars studied with Mars Express VMC images.

### 2.1.3. Topography of Mars

The interaction of the atmosphere with the surface is an important factor to understand the climate and weather on Mars. The surface of Mars interacts with the atmosphere in different ways. The topography of Mars is presented in this section, but the surface also interacts with the atmosphere acting as the source of dust (Kahre et al., 2017), by deposition of water and CO<sub>2</sub> ices (Montmessin et al., 2017; Titus et al., 2017), via exchange of water with regolith (Montmessin et al., 2017), and via exchange of heat due to thermal inertia (Barnes et al., 2017).

The global topography of Mars (Figure 2) was obtained by the MOLA instrument (Mars Orbiter Laser Altimeter; Smith et al., 1999; 2000), and it can be complemented with the HRSC instrument (High Resolution Stereoscopic Camera) to obtain a higher resolution (e.g. Fergason et al., 2018). MOLA also measured the Martian “areoid”, which is the equipotential virtual surface of Mars, equivalent to the Earth geoid; it is in many cases a convenient reference for altitudes in the Martian atmosphere.

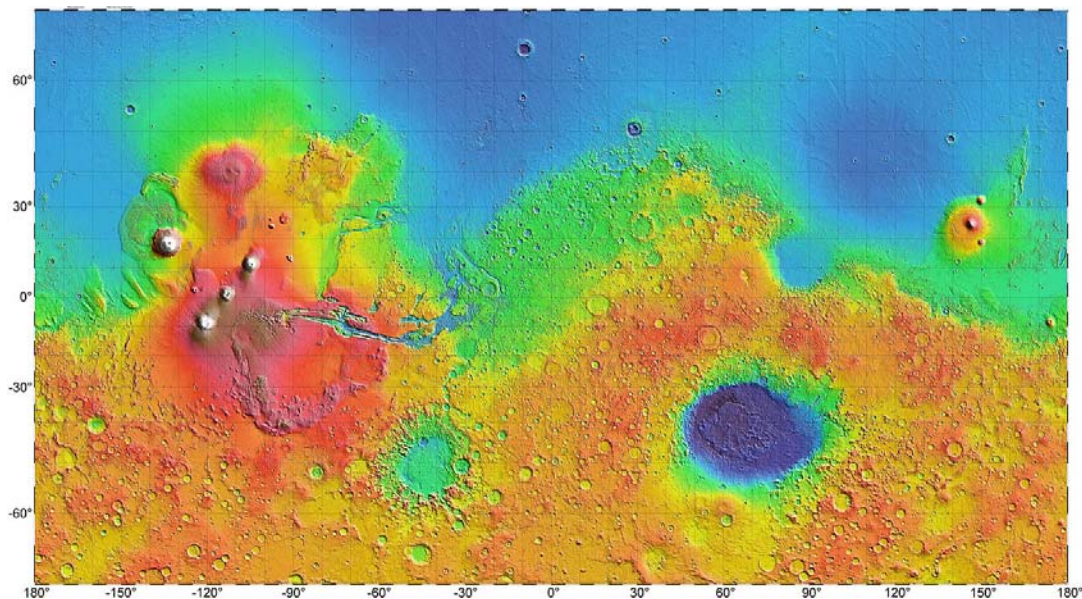


Figure 2. Topographic Mars of Map produced by the MOLA Science Team. NASA/JPL/USGS

Martian topography is more extreme than Earth topography, due in part to the lower gravity. The lowest point is located in Hellas planitia, which is ~6km below the areoid; the highest point is the summit of Olympus Mons, which is ~22km over the areoid. There is an evident difference between the north and the south hemispheres: the north hemisphere is on average lower and flatter, while the south hemisphere is on average higher and

Meteorological phenomena on Mars studied with Mars Express VMC images.

rougher. There is also a dichotomy in terms of longitude, which mostly affects tropical regions: longitudes 0-180°E are lower and less rough than 180-360°E.

The topography affects the climatology, both in the global and the mesoscale scales. The global circulation is affected by the hemispheric differences (Barnes et al., 2017). Local circulations around volcanoes, craters, and other features are responsible for the formation of clouds and the lifting of aerosols due to mesoscale circulations (Michaels et al., 2006).

#### 2.1.4. Atmospheric characteristics and thermal structure

The atmosphere of Mars is massively composed of CO<sub>2</sub> and other components in smaller quantities, as summarized in Figure 3. H<sub>2</sub>O is present with a variable proportion of 15-1500 ppm (Smith et al., 2017; the concentration is highly variable and depends on the altitude, location and season). Both CO<sub>2</sub> and H<sub>2</sub>O can condense in the Martian atmosphere and form clouds and surface deposits. Variable quantities of dust in suspension are also present in the atmosphere (see section 2.1.6).

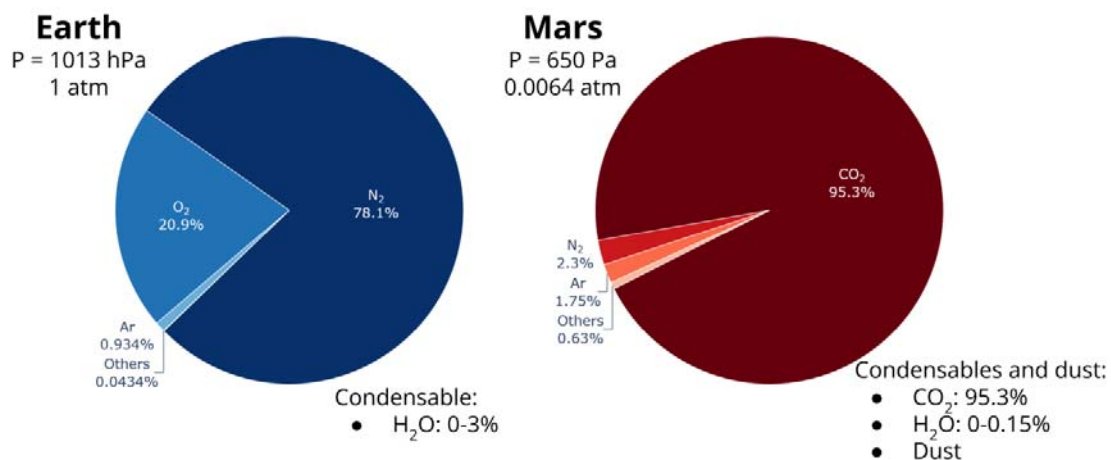


Figure 3. Comparative composition of Earth and Mars atmospheres. Proportions in terms of mole fraction. Mean pressure indicated on top of the pie charts. Relevant condensables and dust are listed below charts. Values for Mars extracted from Smith et al. (2017).

Solar insolation is the main source of energy in the Martian atmosphere, the mean solar power reaching the top of the atmosphere as a function of Ls and latitude is represented in figure 4.

## Meteorological phenomena on Mars studied with Mars Express VMC images.

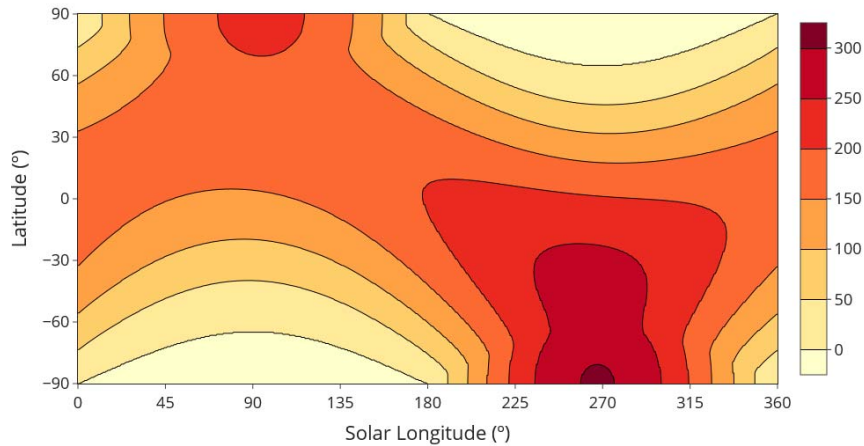


Figure 4. Mean daily insolation at the top of atmosphere (TOA), in  $\text{W/m}^2$  and as a function of latitude and solar longitude. Computed following Liou et al. (2002).

The mean surface pressure is around 650 Pa, which is less than 1% of the surface atmospheric pressure on Earth.  $\text{CO}_2$ , the main atmospheric component, sublimates seasonally into the polar caps, leading to considerable seasonal pressure variations (around 25% of the total pressure). In addition to it, the high orbital eccentricity leads to considerable seasonal global mean temperature variations that have an effect on the pressure cycle too. Figure 5 represents the annual variation of surface pressure as measured by a ground station.

The vertical thermal structure is another important aspect of a planetary atmosphere, because of its relation to dynamics and the transport of aerosols. Different layers (troposphere, stratosphere, mesosphere, thermosphere) are typically present in planetary atmospheres (Sánchez-Lavega, 2010). Earth and Titan atmospheres exhibit a stratosphere (i.e. a region between the troposphere and the mesosphere where temperature increases with altitude due to the presence of some radiatively active compound). This is basically not the case in the atmospheres of Venus and Mars, and that facilitates the vertical transport of water vapor and dust, which has important effects on the vertical distribution of those aerosols.

Figure 6 represents the thermal profiles measured by different landers during their descent. The lowest 50 km, where temperature decreases with altitude, constitute the troposphere or lower atmosphere. In the middle atmosphere or mesosphere, up to approximately 100 km, this tendency is lost, and temperature fluctuates within a range that

Meteorological phenomena on Mars studied with Mars Express VMC images.

remains essentially constant in altitude. The mean thermal profile suffers strong variations as a function of local time, season, and latitude. Thermal tides greatly affect the middle atmosphere, gravity waves produce local variations, and boundary layer convective processes produce large effects on the bottom part of the lower atmosphere.

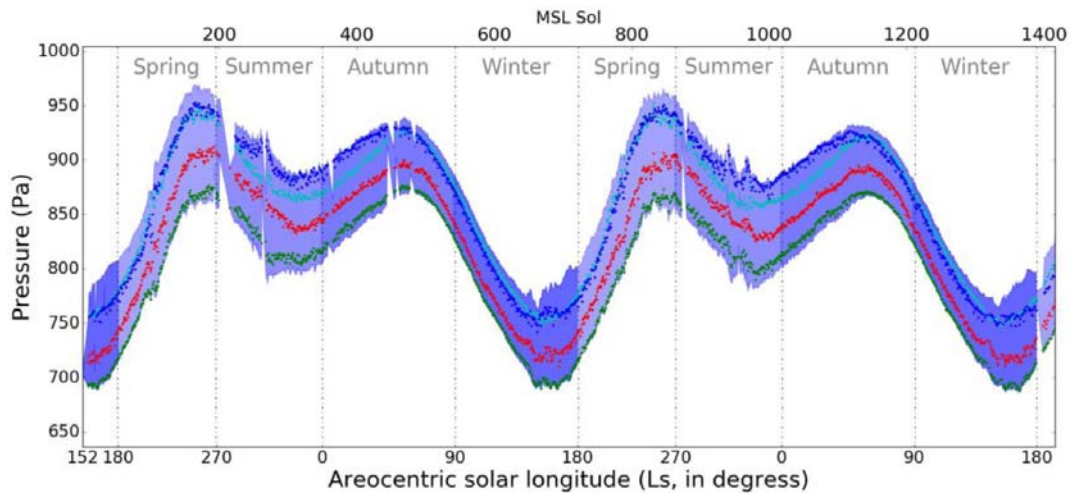


Figure 5. Surface pressure variations measured by the ground based REMS meteorological station on the MSL (Curiosity) rover. Blue shading represents the daily extremes. Cyan, blue, red, and green points correspond to measurements at local time 0, 9, 12, and 15. The annual cycle of pressure due to the sublimation of the polar caps and the orbital eccentricity is apparent. Mean pressure here is higher than the previously mentioned surface global mean of 650 Pa due to the altitude of the rover. Figure reproduced from Ordonez-Etxeberria et al. (2018)

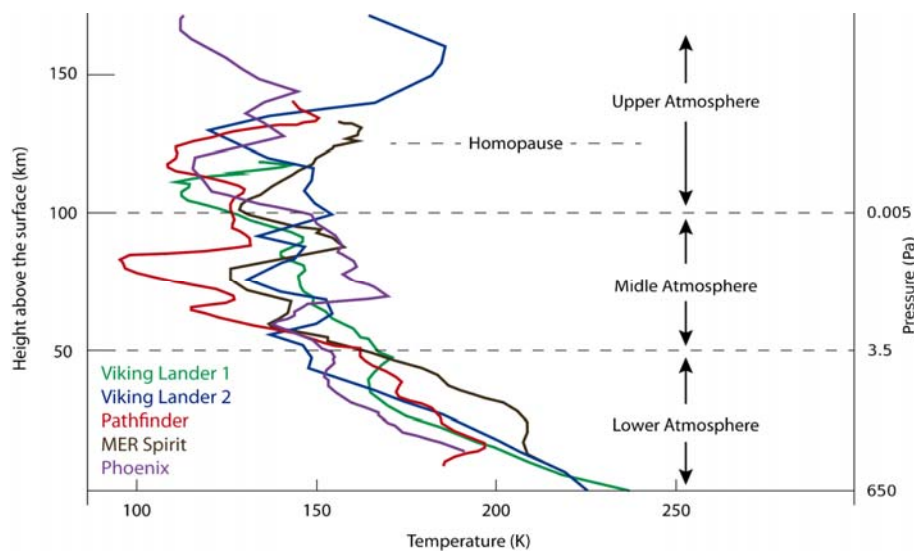


Figure 6. Vertical thermal structure of the atmosphere of Mars as measured by different landers during their descent. Lower, middle, and upper atmosphere are indicated. Figure adapted by Iñaki Ordóñez Etxeberria from Smith et al. (2017).

### 2.1.5. The global circulation

The atmospheric circulation in terrestrial planets is characterized by east-west (zonal) flow dominated by planetary rotation and by the presence of the Hadley cell type (north-south) meridional circulations.

The different insolation in different latitudes produces temperature gradients that produce meridional motions, which redistribute heat and lead to a mean state of equilibrium, in which a gradient of temperatures from tropics to the poles is still present. In the case of rapidly rotating planets, like Earth and Mars, the geostrophic balance dominates the global circulation (Sánchez-Lavega, 2010). Geostrophy implies that there is a relationship between meridional gradients of temperature and vertical gradients of the zonal winds known as the thermal-wind equation:

$$\frac{\partial \bar{u}_g}{\partial \ln p} = -\frac{R}{f} \frac{\partial \bar{T}}{\partial y}$$

Where  $f$  is the Coriolis parameter,  $u$  is the eastwards zonal velocity,  $T$  the temperature and top bars represent the zonal mean value. Assuming that the velocity in the surface is negligible, a decrease in temperature towards the poles implies the existence of winds towards the east at higher altitudes.

The mean global motion of the atmosphere of Mars is summarized in Figure 7. During equinoxes, the warmest temperatures are present over the equator; eastward winds are present in the mid-latitudes as result of the descent of temperature to the poles, and two Hadley cells are present around the equator, where warm air rises as part of their ascending branch. During solstices the warmest temperatures move to high latitudes, and as a result, a strong polar vortex develops in the winter hemisphere, and a single cross-equatorial Hadley cell dominates the meridional circulation. Due to the eccentricity of the orbit of Mars, insolation is higher during the southern solstice, and the corresponding cross-equatorial Hadley cell is stronger at this solstice compared to the opposite one. This situation describes a mean equilibrium during the season, over which perturbations are present in the day to day timescale (for example, due to the radiative effects of dust on the thermal tides).

Given the low humidity, the lack of oceans, and the low atmospheric density, the thermal inertia of the Martian atmosphere is very low compared to that of the Earth, and this translates to bigger temperature oscillations, quick response to the insolation cycles, and rapid dynamical changes. This is a key difference between the atmosphere of Earth and

Meteorological phenomena on Mars studied with Mars Express VMC images.

Mars, it is the reason why warm temperatures reach higher latitudes in the solstices, promoting the existence of the single cross-equatorial Hadley cell.

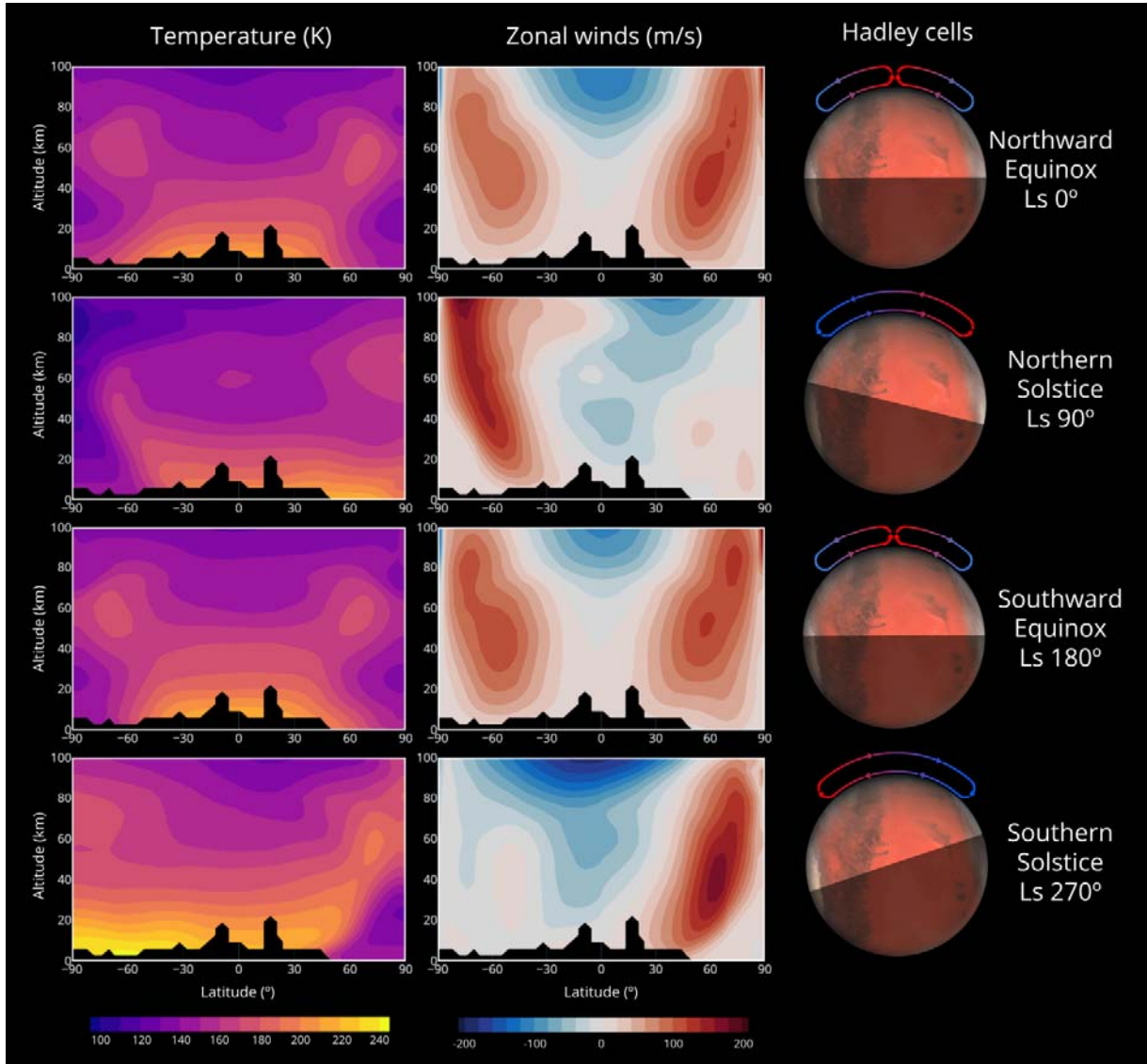


Figure 7. The mean global motion of the atmosphere of Mars. Each row corresponds to a season of the year (two equinoxes and two solstices). Graphs in the left and middle column display zonal averages of temperature and zonal wind as extracted from the Mars Climate Database (see section 2.2.3). The right column displays schemes of the Hadley circulation.

Another consequence of the low thermal inertia is that thermal tides are very important on Mars compared to any other planetary atmosphere in the solar system. Thermal tides are “planetary-scales gravity waves with periods that are harmonics of the solar day” (Barnes et al., 2017). They have a strong effect on the temperatures of the middle atmosphere (and

Meteorological phenomena on Mars studied with Mars Express VMC images.

therefore in the formation of condensate clouds), and they are routinely observed in the pressure field by ground stations.

#### 2.1.6. Aerosols and their climatology

Dust is the main aerosol present in the Martian atmosphere. Some concentration of dust is always present, and the quantity of dust in the atmosphere is much higher during the second half of the year (Ls ~180°-360°). The presence of dust has strong effects on the global circulation via radiative heating and cooling.

In addition to dust, water and CO<sub>2</sub> condensates as ice crystals exist in the Martian atmosphere. Due to the low pressure, both compounds condense directly from gas to ice.

The climatology of dust and condensate clouds is presented in this section.

#### **Dust and dust storms**

Large amounts of dust rest on the surface of the planet, and different loads of it are always present in the atmosphere. Atmospheric phenomena such as surface winds and dust devils contribute to the lifting of dust (Khare et al., 2017), which is then transported by winds, both horizontally and vertically.

The radiative effect of dust is a key factor in the dynamics of the Martian atmosphere, and it plays a role analogous to that of clouds on Earth, causing instabilities in the mean atmospheric state. The distribution of dust has been systematically monitored by different instruments. Montabone et al. (2015; 2020) created dust scenarios based on observational data. These scenarios are used to feed atmospheric models for more realistic simulations.

The global dust activity is much higher during the second half of the year, when the increased insolation due to the proximity of the perihelion season enhances dust lifting. Atmospheric dust content typically starts to increase around Ls 140°, with large interannual variations (see Figure 8).

Meteorological phenomena on Mars studied with Mars Express VMC images.

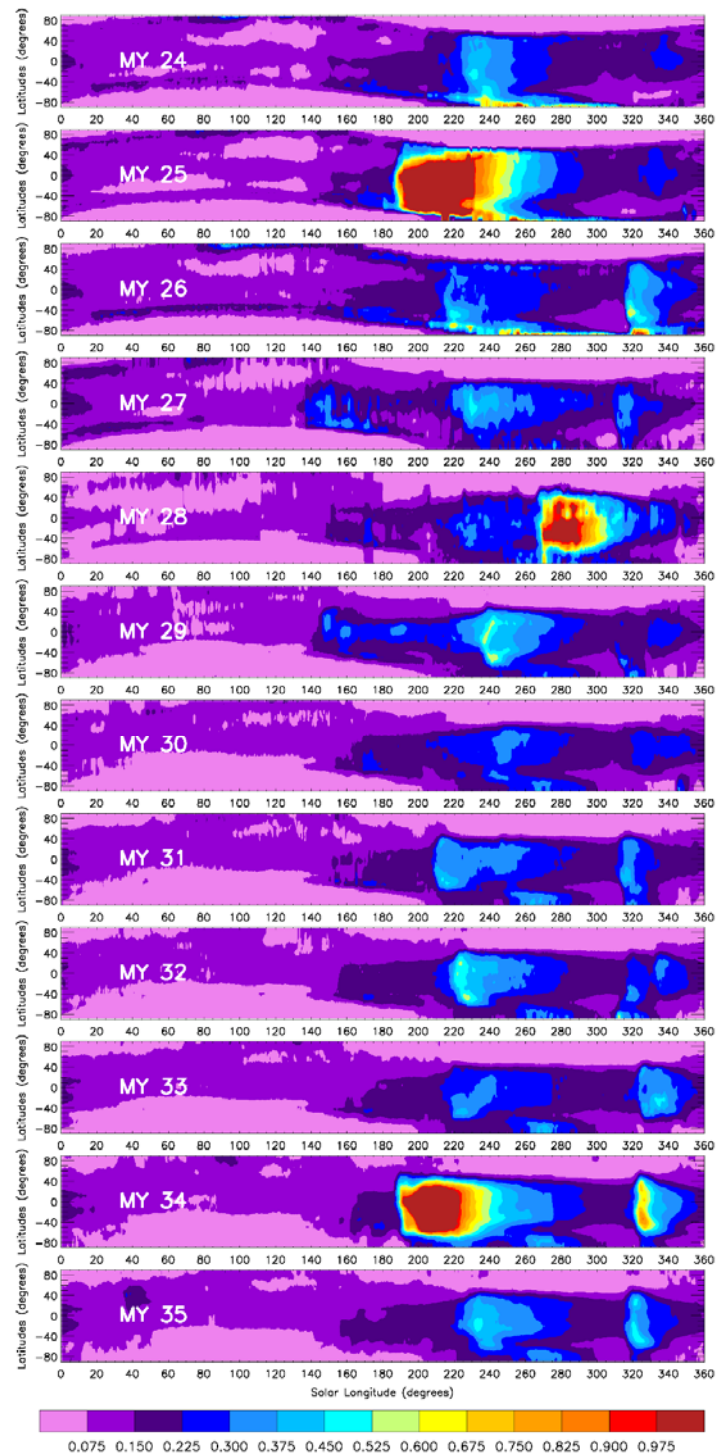


Figure 8. Dust scenarios for Martian years 24-35 provided by Montabone et al. (2015, 2020). The different panels present 9.3 μm absorption column dust optical depth normalized to the reference 610 Pa pressure level in terms of Solar Longitude and Latitude. Reproduced from [http://www-mars.lmd.jussieu.fr/mars/dust\\_climatology/index.html](http://www-mars.lmd.jussieu.fr/mars/dust_climatology/index.html)



## Meteorological phenomena on Mars studied with Mars Express VMC images.

In addition to the background dust in suspension, there are occasional dust storms (Figure 9). They are classified according to their size<sup>1</sup> as local, regional, and global dust storms (GDS<sup>2</sup>). All types of dust storms are most common during the dusty season, and GDSs have only been observed at this season.

Most recent GDSs took place in MYs 25, 28, and 34 (Sánchez-Lavega et al., 2019) leaving an evident signal in Figure 8. These extreme events can blur the view of the planet for months (See eg. Fig. 9a) and have an important impact on global circulation.

In the border of the polar caps, the contrast of temperatures between the ice-free terrain and the polar cap boosts surface winds strong enough to trigger dust storms, and as a result, many local and regional dust storms develop in these areas all year round, including the first half of the year. In the non-dusty season, the borders of the polar caps are the only locations where dust storms are common (Fig. 9c and 9d).

Kass et al. (2016) studied the interannual similarity of the dust activity during the dusty season in non-GDS years. They noticed that three main dust events repeat from year to year, denoted as A, B, and C dust events. All these dust events are clearly seen in Figure 8. The A dust storm typically happens in the Ls range 205°-270°, and reaches a wide range of latitudes. The B dust storm happens around Ls 245°-295° in the south polar latitudes. The C dust storm takes place around Ls 305-335° and it exhibits a latitudinal extension similar to that of A dust storms. On the other hand, it is clear in Figure 8 that the north polar region is almost free of dust during the dusty season, this is caused by the intense polar vortex present in the area, as described in section 2.1.5.

---

<sup>1</sup> An interesting discussion on the historical problem of the classification of dust storms can be found in Cantor (2007). In the review by Khare et al. (2017), two criteria are given to distinguish local and regional dust storms: the size of the long axis of the storm (<2000km for local dust storms), and the area covered by dust (<1.6E6 km<sup>2</sup> for local dust storms)

<sup>2</sup> There is an ongoing discussion about the naming of "global" dust storms, because many authors argue that they are not exactly global, nor are they a single dust storm, an example of this discussion can be found in (Khare et al., 2017). For simplicity, we call them Global Dust Storms (GDSs) in the context of this thesis.

Meteorological phenomena on Mars studied with Mars Express VMC images.

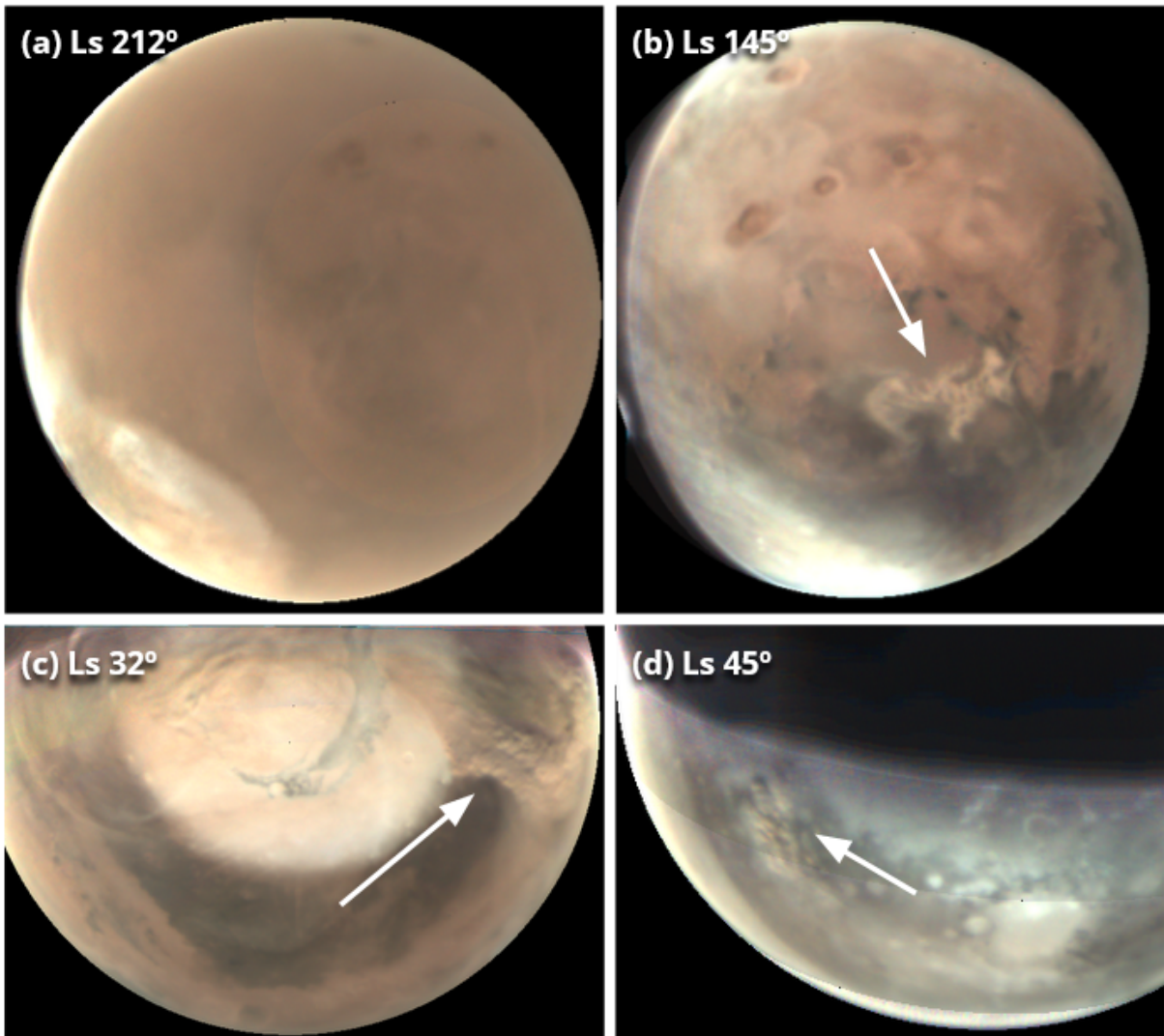


Figure 9. Examples of dust storms as imaged by MEX/VMC (see section 2.2 for details). (a) A full-disk image of Mars during the GDS in MY34 on 2018-07-16, analyzed by Hernández-Bernal et al. (2019). (b) A local dust storm near the equator during the dusty season, observed on 2021-12-21. (c) Local dust storm in the border of the north polar cap during the first half of the year on 2019-05-29, analyzed by Sánchez-Lavega et al. 2022a. (d) Local dust storm in the border of the south polar cap during the first half of the year, on 2010-01-30.

### Condensate clouds

The formation of clouds can happen when temperature is low enough, given a pressure and concentration of the compound (Sánchez-Lavega et al., 2004). Beyond concentration, pressure, and temperature, cloud formation also involves microphysical processes. Indeed, Maltagliati et al. (2011) reported the observation of water vapor in excess of saturation, this

is possible when not enough condensation nuclei are available. Navarro et al. (2014) showed that considering the microphysics of nucleation resulted in improved and more realistic predictions of water ice clouds in a GCM.

In the case of Mars, both water and CO<sub>2</sub> can condense to form clouds (Clancy et al., 2017). Due to the low pressure, such compounds condense directly from gas to solid (ice) phase. Water is present in variable concentrations, and thus the formation of water ice clouds depends strongly on the distribution of water vapor. CO<sub>2</sub> is present everywhere in large quantities, and therefore it only requires suitable conditions of pressure and temperature to condense.

We can differentiate clouds in the lower atmosphere (troposphere), from clouds in the medium atmosphere (mesosphere). In the lower atmosphere CO<sub>2</sub> clouds are only present in the polar night, and contribute to the growth of the polar caps during the winter. Low altitude water ice clouds, and mesospheric clouds are discussed next.

### **Low altitude water ice clouds**

Three main water ice cloud systems are present in the lower atmosphere of Mars: The Aphelion Cloud Belt (ACB), the North Polar Hood (NPH), and the South Polar Hood (SPH). These cloud systems can be seen in simulation results displayed in Figure 10. In addition to this, figure 2 in Wang and Ingersol (2002) provides a very good outline of the distribution and seasonal evolution of the cloud systems on Mars.

Polar Hoods happen during the local autumn and winter over both polar caps. The NPH is optically thicker than the SPH. The NPH covers most of the polar cap and is optically opaque most of the time. The SPH is optically thin, and is usually seen as a haze with occasional isolated clouds.

The ACB is the main cloud system present on Mars. It takes place around the Aphelion season at tropical latitudes, where thin clouds form due to the transient Hadley circulation and the transport of water from the North Polar Cap. The ACB was clearly noticed at the end of the 1990s (eg. James et al. 1996). A first physical explanation was provided by Clancy et al. (1996).

In addition to these large scale cloud systems, other smaller cloud systems are present on Mars. For example, orographic clouds, which are among the subjects of this thesis, and baroclinic spirals, which have been studied among others by Wang and Ingersol (2002), and Sánchez-Lavega et al. (2018b).

Meteorological phenomena on Mars studied with Mars Express VMC images.

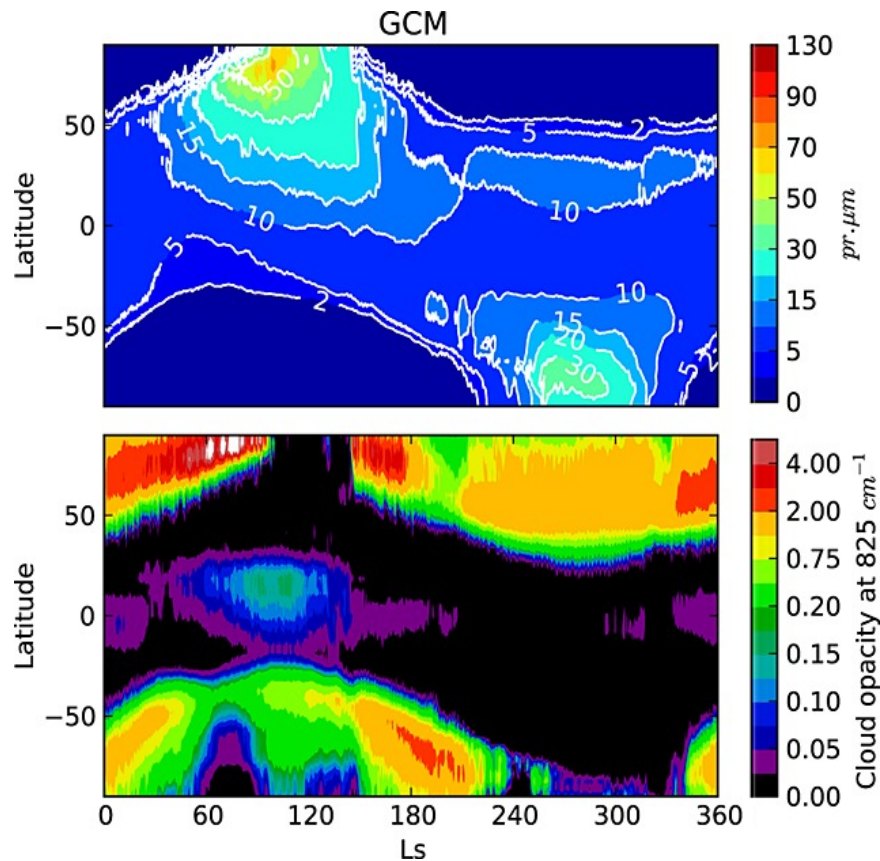


Figure 10. Climatology of water vapor and water ice, extracted from simulations. (top) Precipitable microns of water vapor. (bottom) Cloud opacity at  $825\text{ cm}^{-1}$ . Adapted from Figure 2 in Navarro et al. 2014.

### Mesospheric clouds and dust

High altitude aerosols have been observed on Mars for decades (Anderson and Leovy, 1978). The altitude of mesospheric aerosols is typically below 80 km, although they may occur at higher altitudes (e.g. Sefton-Nash et al., 2013, their figure 9; Clancy et al., 2019, their figures 9 and 10), and even reach altitudes over 100 km (Montmessin et al., 2006). A high altitude plume of unclear nature was observed about 200 km over the limb by ground-based amateur observers in 2012 (Sánchez-Lavega et al., 2015). The mechanisms that lift dust and water vapor to high altitudes are an active area of research.

Many studies have explored high altitude aerosols either in the limb (e.g. Sefton-Nash et al., 2013; Sánchez-Lavega et al., 2018a), or using different types of observations (e.g. Määttä et al., 2010), and nowadays it is well known that dust, water ice, and  $\text{CO}_2$  clouds

## Meteorological phenomena on Mars studied with Mars Express VMC images.

are present at those high altitudes in the middle atmosphere. However, the composition of aerosols in individual observations is often ambiguous due to instrumental limitations.

Dust tends to appear in limb observations in the form of Detached Dust Layers (DDLs). Their origin is often attributed to thermal topographic circulations (Michaels et al. 2006; Heavens et al., 2015), and dust-driven dry convection (Spiga et al., 2013).

The formation of water ice condensates in the mesosphere requires the vertical transport of water vapor from the lower atmosphere, which is currently explained by thermal topographic circulations (Michaels et al., 2006), and Hadley circulation (Shaposhnikov et al., 2019).

CO<sub>2</sub> is naturally present in high quantities at all altitudes. The existence of these clouds was long suspected since the early days of Mars exploration. In 1997 the Mars Pathfinder lander found temperatures below CO<sub>2</sub> condensation during its descent (Schofield et al., 1997), and many studies tried to confirm the existence of such clouds in the following years, it was Montmessin et al. (2007) who provided definitive evidence based on hyperspectral imaging by MEX/OMEGA. Määttänen et al. (2013), and Clancy et al. (2017) provide comprehensive reviews on the history of observations of CO<sub>2</sub> clouds.

The existence of mesospheric CO<sub>2</sub> clouds challenges atmospheric models, both because they require lower temperatures than those initially predicted, and because they require microphysical adjustments. González-Galindo et al. (2011) showed that model predicted temperatures were in general not low enough to trigger CO<sub>2</sub> condensation, but there was a correlation between the location of observed CO<sub>2</sub> clouds and the lowest temperatures predicted by the model. Spiga et al. (2012) showed that observed CO<sub>2</sub> clouds were correlated with areas where the vertical structure of the atmosphere is favorable for the vertical propagation of gravity waves that can produce cold pockets in the mesosphere where subcondensation temperatures could be reached.

Very recently, Määttänen et al. (2022) have implemented a state-of-the-art microphysical model for CO<sub>2</sub> clouds in a GCM. They successfully reproduce many of the observed trends in mesospheric CO<sub>2</sub> clouds. It is worth mentioning that they find that these clouds form in the model by condensing CO<sub>2</sub> on water ice crystals that act as condensation nuclei. Still the reproduced optical depths are lower than observed, which indicates the need for additional condensation nuclei. Määttänen et al. (2022) conclude that these condensation nuclei are possibly provided by meteor ablation.

## Meteorological phenomena on Mars studied with Mars Express VMC images.

Aoki et al. (2018) and Clancy et al. (2019) provided new datasets of observed mesospheric clouds that complement the one produced in the review by Määttä et al. (2013). These datasets indicate that CO<sub>2</sub> mesospheric clouds are mostly common around equatorial latitudes in Solar Longitudes from 0° to 140° (in the aphelion season, when global average temperatures are lower).

The distribution of mesospheric water ice clouds is more extensive, they tend to happen in latitudes lower than 60° through the Martian year. They are constrained to lower altitudes (below 60 km) in the first half of the year, and reach higher altitudes during the second half (Clancy et al., 2019; their figure 10). This is expected since it is known that water vapor reaches higher altitudes during this season (e.g. Fedorova et al., 2021), when global average temperatures are warmer.

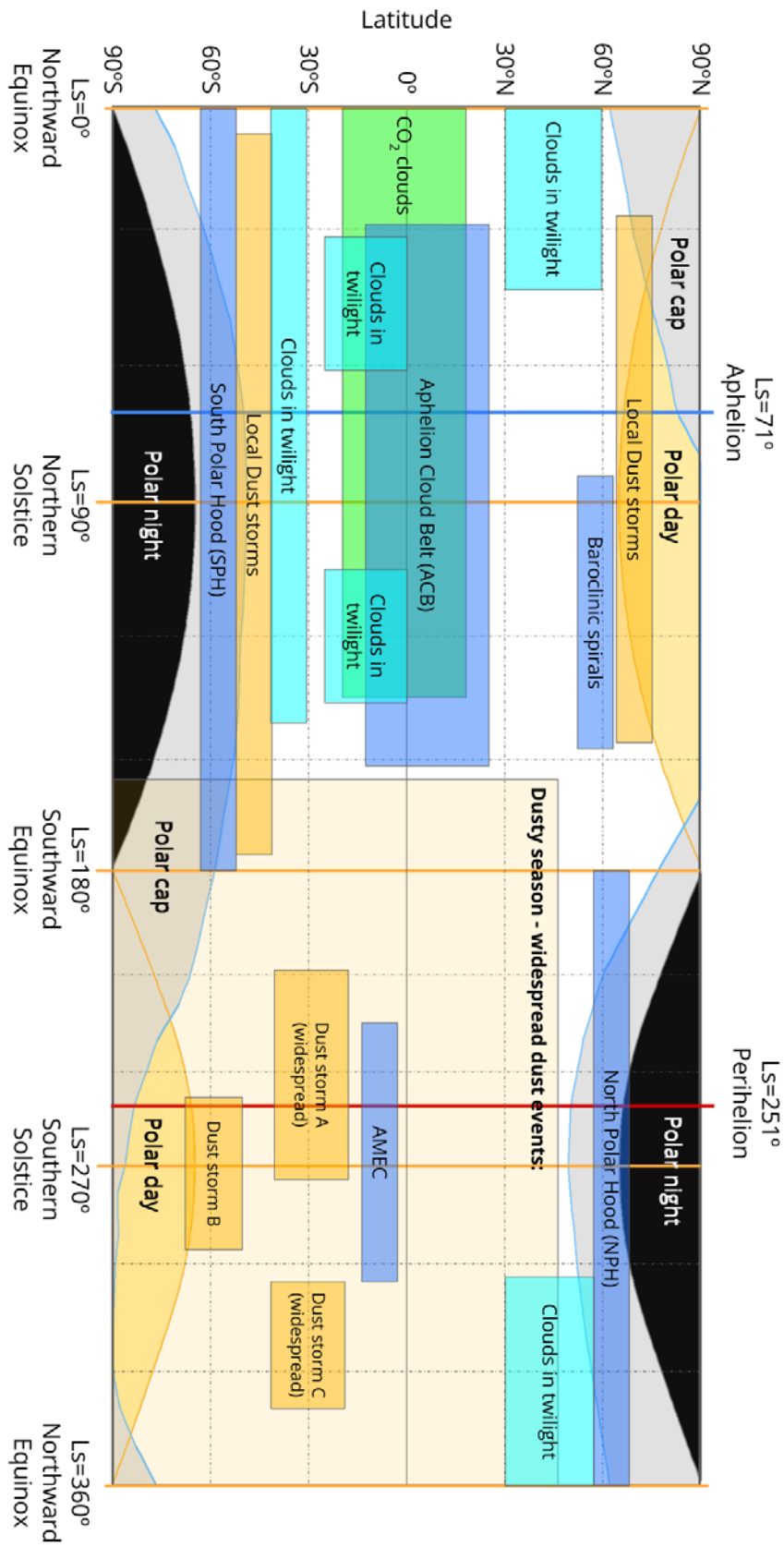
Dust tends to reach higher altitudes and optical opacities during the second half of the year (the dusty season), a trend that has been captured by several observational studies (e.g. Sefton-Nash et al., 2013; Clancy et al., 2019; McCleese et al., 2010).

### 2.1.7. A meteorological calendar of Mars

The phenomena studied in this thesis, together with a non-exhaustive selection of other relevant meteorological phenomena, are presented against time of year in Figure 11. Clouds in twilight and the AMEC have been described for the first time as part of this thesis of this thesis. A brief description of other phenomena is provided in section 2.1.6 above.

Figure 11 (next page). A schematic calendar of meteorological phenomena through the Martian year, inspired by a previous drawing by Agustín Sánchez Lavega. The horizontal axis represents the time of the year and it is scaled with time (i.e. the Ls is not linear, see section 2.1.2), Ls marks are every 30°. Polar nights, polar days, and the extension of the polar caps according to Piqueux et al. (2015) are represented in the background. Most relevant meteorological events are represented with colored squares (orange: dust, blue: water ice, green: CO<sub>2</sub>; cyan: unclear composition of clouds in twilight), the extension of these squares is estimative. The dusty season together with the A and C dust events are widespread events represented in the bottom part of the diagram.

Meteorological phenomena on Mars studied with Mars Express VMC images.





Meteorological phenomena on Mars studied with Mars Express VMC images.

### 2.1.8. Summary of missions and instruments

This section offers a brief summary of the missions and instruments that have explored the low and middle atmosphere of Mars. Ground based and space telescopes, including amateur observers are also a relevant source of data nowadays (e.g. Sánchez-Lavega et al. 2015; 2019; James et al., 1996), but this thesis is focused on data acquired by orbiters.

Figure 12 displays a timeline including most space missions to Mars to date. As part of this thesis, data from many different orbiters has been exploited, including: Mars Express, MAVEN, MOM, MRO, MGS, and Viking.

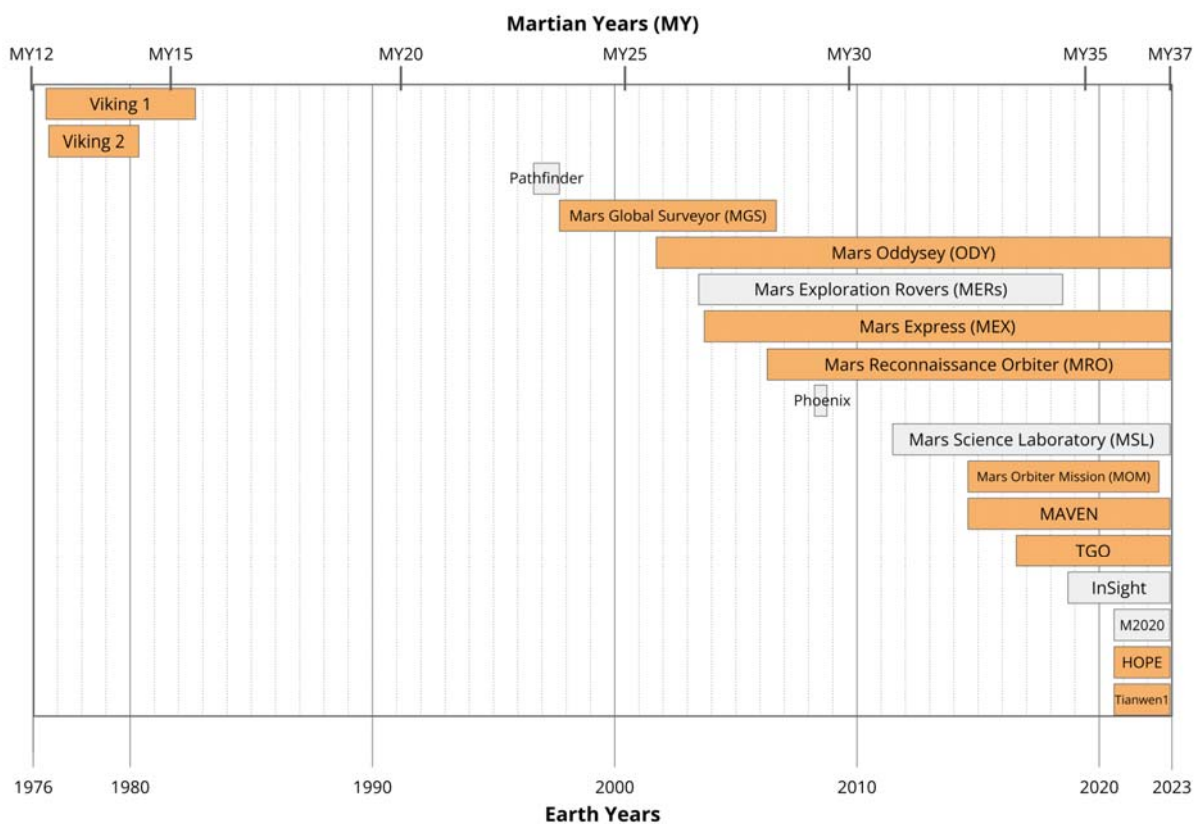


Figure 12. Timeline of missions to Mars. Considering their limited impact in the scientific literature, Mars 2, Mars 3, Mars 5, and Phobos 2 are excluded. Flybys not included. Orange squares represent orbiters and gray squares represent landers, Viking 1 and 2, and Tianwen 1 include an orbiter and a lander.

Science instruments usually included in space missions with the objective of studying the low and middle atmosphere of Mars can be grouped as:

Meteorological phenomena on Mars studied with Mars Express VMC images.

- Instruments aboard orbiters:
  - Imagers
  - Spectrometers
  - Radioscience
  - Radiometers (uncommon)
- Instruments on landers:
  - Acquisition of reentry profiles
  - Meteorological stations
  - Chemical study of the atmosphere or study of dust
  - Cameras

In the case of orbiters, the orbit of the spacecraft must be considered, since it conditions the scientific return of the mission. A number of missions are located in **sun-synchronous** orbits centered on the afternoon local time (with the exception of Mars Odyssey, which shifted to the local time 7AM-7PM for some time; Smith, 2019). Afternoon sun-synchronous orbiters (MGS, MRO, most of its life also ODY) provide a daily coverage of the whole planet at a fixed local time. This enables systematic uniform observations, which facilitates the compilation of statistics and the comparison of meteorological data from different sols, and has allowed the creation of outstanding datasets like those of the instruments MCS and MARCI aboard the MRO mission, and MOC aboard MGS.

Between 1997 and 2014, there were 4 different orbiters on Mars which set the base of our current knowledge of the Martian atmosphere. They were: MGS, ODY, MEX, and MRO. Among them, MEX was the only one not in a sun-synchronous orbit, and ODY only shifted its orbit to a different local time for a couple of Martian years. In more recent years, since 2014, all the new orbiters have entered **non-sun-synchronous** orbits and observations at different local times are more common.

Other relevant characteristic of an orbit is its orbital plane and the altitude. **Polar orbits** enable the monitoring of the polar regions. By definition, sun-synchronous orbiters are polar orbits. **Low orbits**, which provide higher resolution observations and lower orbital periods. **High apocenter** orbits, which provide a privileged point of view that enables a global perspective.

The Mars Orbiter Mission (MOM), and Hope use a **supersynchronous** orbit, which means that its orbital period is longer than the rotation period of the planet. In the case of Hope, the orbit is designed so that in segments of the orbit the spacecraft remains quasi-

Meteorological phenomena on Mars studied with Mars Express VMC images.

stationary over different longitudes, which could be exploited for studies of atmospheric dynamics.

Table 3 is a summary of missions that have orbited Mars, including their orbits and instruments. Table 4 is a more detailed comparison of the imagers aboard such missions. This thesis is based on images acquired by the Visual Monitoring Camera (VMC) aboard Mars Express, and this table provides a context to understand the capabilities of VMC, which are detailed in section 2.2. Also, in addition to VMC, data from other cameras has been exploited as part of this thesis, including: Viking/VIS, MEX/HRSC, MEX/OMEGA, MRO/MARCI, MOM/MCC, and MAVEN/IUVS. Data from MGS/MOC and HOPE/EXI has been analyzed for yet unpublished works. These are all the imagers that have the capability to cover wide areas (coverage column in Table 4), with the only exception of the MoRIC instrument, whose images are not properly stored in a public repository.

Table 3. Relevant orbiters, the characteristics of their orbits, and their instruments suitable for atmospheric science, instrument types in parenthesis (IMG: Imager, SPE: Spectrometer, RAD: Radiocultation, RDM: Radiometer).

Mission (orbiters)	Orbit [orbital parameters] <sup>3</sup>	Atmospheric instruments
Viking orbiters	Non-sun-synchronous High apocenter [1000x40000 km; 55°-80°] <sup>4</sup>	VIS (IMG) MAWD (SPE) IRTM (RDM)
Mars Global Surveyor (MGS)	Afternoon sun-synchronous Polar orbit Low orbit [370x440 km; 93°]	MOC (IMG) TES (SPE) MOLA (other)
Mars Odyssey (ODY)	Afternoon Sun-synchronous (temporarily shifted to 7AM/PM) Polar orbit Low orbit [400 x 400 km; 93°]	THEMIS (IMG)
Mars Express (MEX)	Non-sun-synchronous	VMC (IMG)

<sup>3</sup>Format pericenter X apocenter (km from surface); orbital inclination

<sup>4</sup> The orbits were changed heavily over time, these are indicative values. More details in these links:

Viking 1: <https://nssdc.gsfc.nasa.gov/nmc/spacecraft/display.action?id=1975-075A>

Viking 2: <https://nssdc.gsfc.nasa.gov/nmc/spacecraft/display.action?id=1975-083A>

[https://www.tsgc.utexas.edu/spacecraft/viking/profile\\_vik2orb.html](https://www.tsgc.utexas.edu/spacecraft/viking/profile_vik2orb.html)

Meteorological phenomena on Mars studied with Mars Express VMC images.

	High apocenter Polar orbit [300 x 10000 km; 86°]	HRSC (IMG) OMEGA (IMG) PFS (SPE) SPICAM (SPE) MaRS (RAD)
Mars Reconnaissance Orbiter (MRO)	Afternoon sun-synchronous Low orbit [250x320 km; 93°]	MARCI (IMG) CTX (IMG) HiRISE (IMG) MCS (SPE) CRISM (SPE)
Mars Orbiter Mission (MOM)	Non-sun-synchronous Supersynchronous High apocenter [400x75000 km; 150°]	MCC (IMG) MSM (SPE)
MAVEN	Non-sun-synchronous High apocenter [150x6200 km; 75°]	IUVS (IMG)
Trace Gas orbiter (TGO)	Non-sun-synchronous Low orbit [400x400; 74°]	CaSSIS (IMG) NOMAD (SPE) ACS (SPE)
Hope	Non-sun-synchronous Supersynchronous High apocenter [20000x43000; 25°]	EXI (IMG) EMIRS (SPE)
Tianwen 1	Non-sun-synchronous High apocenter Polar orbit [300x10000; 86°]	MoRIC (IMG) HiRIC (IMG) MMS (SPE; potentially usable for atmosphere)

## Meteorological phenomena on Mars studied with Mars Express VMC images.

Table 4 (next page). Comparative of imagers aboard Mars orbiters. Notes. (1) SS stands for sun-synchronous orbit, NS stands for non-sun-synchronous orbit. (2) This column indicates whether the camera covers or not wide areas, defined as areas with a width in the order of thousands of kilometers imaged over a single observation. This depends on the orbit, the instrument characteristics, and the way it is operated. This kind of coverage is especially useful for the study of the lower and middle atmosphere. (3) Whether or not the instrument can acquire full disk (from limb to limb, not necessarily covering the whole limb) images over timescales of one sol, in some cases the field contains the keyword "Swaths", which means that it makes full disk images by stacking images to make mosaics.

Meteorological phenomena on Mars studied with Mars Express VMC images.

Mission (Orbit <sup>1</sup> ) (years)	Imager	Spectra	Type	Coverage <sup>2</sup>	Full disk <sup>3</sup>
Viking (NS) (1976-1982)	VIS	6 VIS bands	Single shot	Wide	During approach
MGS (SS) (1997-2006)	MOC	Red and Blue	BN single shot Filters pushbroom	Wide	Swaths
ODY (SS) (2001-)	THEMIS	5 VIS bands 10 IR bands	Pushbroom	Narrow	No
MEX (NS) (2003-)	VMC	Low quality RGB bayer	Single shot	Wide	Yes
	HRSC	8 VIS bands 1 NIR band	Pushbroom	Wide	Swaths
	OMEGA	Hyperspectral VIS and IR	Pushbroom	Wide	Swaths
MRO (SS) (2006-)	MARCI	7 VIS bands 2 UV bands	Pushbroom	Wide	Swaths
	CTX	Visual	Single shot	Narrow	No
	HiRISE	14 VIS bands	Pushbroom	Narrow	No
	CRISM	Hyperspectral VIS, NIR, IR	Pushbroom	Narrow	No
MOM (NS) (2014-2022)	MCC	RGB bayer	Single shot	Wide	Yes
MAVEN (NS) (2014-)	IUVS	Hyperspectral UV	Pushbroom	Wide	Swaths
TGO (NS) (2016-)	CaSSIS	4 bands VIS and IR	Pushbroom	Narrow	No
HOPE (NS) (2020-)	EXI	3 VIS bands 3 UV bands	Single shot	Wide	Yes
Tianwen1 (NS) (2020-)	MoRIC	RGB	Single Shot	Wide	Yes?
	HiRIC	VIS and NIR	Pushbroom	Narrow	No

Meteorological phenomena on Mars studied with Mars Express VMC images.

## 2.2. MEX/VMC. Calibration, Data Processing and Operations

This methodological section is devoted to the main instrument used in this thesis, the VMC (Visual Monitoring Camera; figure 13) camera on Mars Express, the first European interplanetary mission, which arrived on Mars in December 2003. VMC was installed on Mars Express as an engineering camera, to confirm the separation of the Beagle 2 lander. In 2007 it was recommissioned to be exploited as an outreach camera (Ormston et al. 2011), and full disk images of Mars captured the attention of the public following ESA media campaigns<sup>5</sup>. In 2016, the scientific recommissioning of VMC started with a contract between ESA and the University of the Basque Country (UPV/EHU), with Agustín Sánchez Lavega as leader of the scientific team (Sánchez-Lavega et al., 2018a).

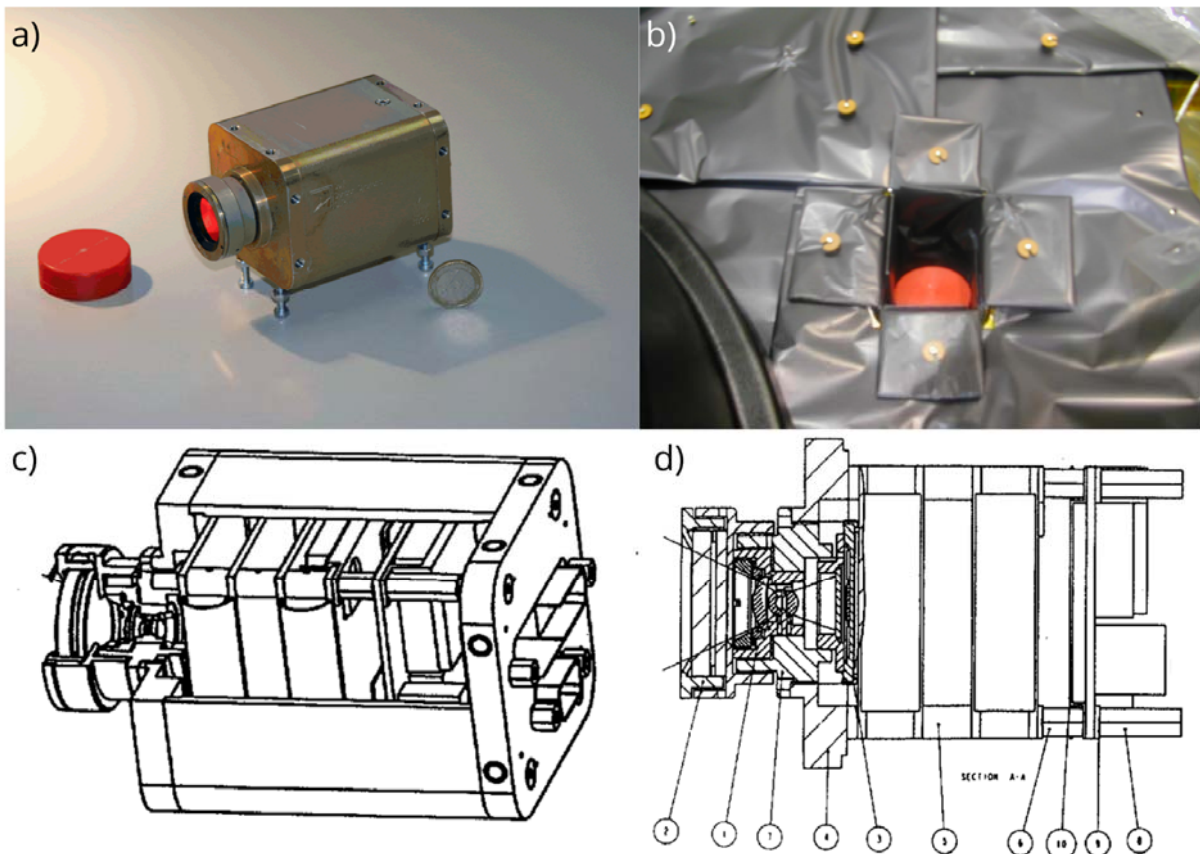


Figure 13. Images and engineering schemes of VMC. Images were obtained on ground, before integration (a) and after integration on the Mars Express body (b). Engineering schemes (c and d) are extracted from the VMC Flight User Manual.

<sup>5</sup> <https://blogs.esa.int/vmc/blog/>

## Meteorological phenomena on Mars studied with Mars Express VMC images.

During the development of this thesis and in collaboration with other team members, VMC has been calibrated, operated, and several pieces of software have been developed which enable data processing and archiving in the ESA Planetary Science Archive (PSA). The main contributions developed for this thesis are described here. Other details about VMC operations and archiving can also be found in the VMC EAICD<sup>6</sup> and in congress abstracts led by Eleni Ravanis (former Graduate Trainee at ESAC; Ravanis et al., 2019;2020).

This section describes the main developments concerning the daily running of VMC as part of the Mars Express mission, summarized in Figure 14. We start in section 2.2.1 by explaining the capabilities that make VMC an interesting instrument for science. Sections 2.2.2 and 2.2.3 describe data processing and the photometric and geometric calibration of VMC. Section 2.2.4 describes the operation of VMC and explains some optimizations for the exposure times developed as part of this thesis. Section 2.2.5 describes the procedures to make experimental level 4 products, which consist in stacking images to improve the dynamic range of the images. Section 2.2.6 describes the hardware and software infrastructure behind the daily running of VMC.

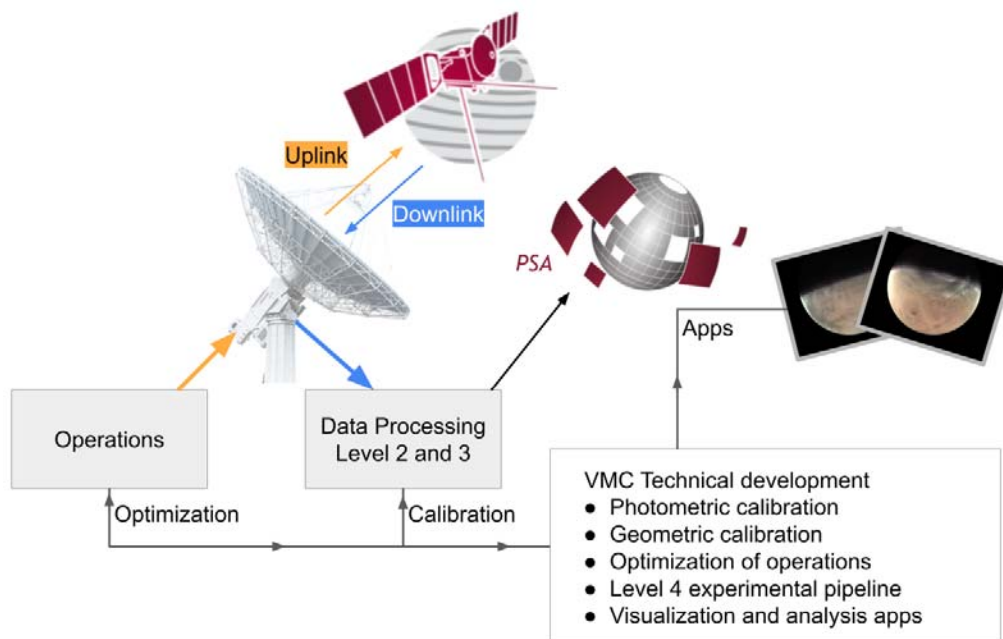


Figure 14. Graphical summary of this section, detailing the developments concerning the daily running of VMC as part of the Mars Express mission.

<sup>6</sup> EAICD stands for “Experiment to Archive Interface Control Document”, which is a descriptive document in the PDS standards. The VMC EAICD can be found in [http://archives.esac.esa.int/psa/ftp/MARS-EXPRESS/VMC/MEX-M-VMC-2-EDR-EXT8-V1.0/DOCUMENT/EAICD\\_VMC.PDF](http://archives.esac.esa.int/psa/ftp/MARS-EXPRESS/VMC/MEX-M-VMC-2-EDR-EXT8-V1.0/DOCUMENT/EAICD_VMC.PDF)



Meteorological phenomena on Mars studied with Mars Express VMC images.

### 2.2.1. The capabilities of VMC

VMC is a simple camera with 640x480 pixels, the typical resolution of a webcam of the 2000s. Indeed, VMC is often called “The Mars Webcam”. The main characteristics of VMC are summarized in table 5.

Table 5. Main VMC characteristics from Flight User Manual (FUM). The FOV (\*) has been determined with higher accuracy as described later, the value cited here is the one given in the FUM, but a slightly different value has been deduced as part of the geometric calibration (section 2.2.3).

Number of pixels	640x480
Color depth	8 bits
Raw image size	307 200 bytes
Spectral capabilities	Low quality RGB Bayer pattern
Pixel size	14 $\mu\text{m}$
Focal length	12.3 mm
Field of View (FOV)	40x31° (*)
Transfer to memory time	38s
Power consumption	<3W (up to 5W during capture)
Exposure times	0.4ms - 90s
Weight	430g
Instrument size	65x60x108mm

Despite the humble origin of VMC, there are three factors that make VMC special compared to most imagers in orbit around Mars (see section 2.1.8 for context):

1. The main outstanding characteristic of VMC is its Field of View (FOV), of around 30°x40°, which is much wider than for other cameras orbiting Mars. This wide FOV combines with the orbit of Mars Express, which is polar and highly elliptical, which allows VMC to image the whole planetary disk from apocenters.
2. The orbit of Mars Express is not Sun-synchronous, a fact that can be exploited by instruments to explore the diurnal variability of atmospheric phenomena. Taking advantage of its capability to obtain full-disk images, this can be specially well exploited by VMC.

Meteorological phenomena on Mars studied with Mars Express VMC images.

3. As VMC is a low resolution single shot camera, its images occupy little space on disk, and sometimes it is possible to perform long observations (lasting around 40–60 minutes and even more) consisting of a large number of images, which enables the production of videos showing atmospheric dynamics. In general this is not possible for pushbroom imagers (MEX/HRSC has become an interesting exception to this with its new operational mode consisting in double brooms).

Considering the VMC pixel resolution ( $\sim 1/16^\circ/\text{px}$ ), it follows that the VMC resolution when imaging Mars is  $\sim 11 \text{ km/px}$  from apocenter (from  $\sim 10000 \text{ km}$ ), and  $\sim 3 \text{ km/px}$  in pericenter (from  $\sim 300 \text{ km}$ ). Intermediate resolutions are possible between the apocenter and the pericenter.

By comparing VMC to other imagers described in section 2.1.8, it can be seen that only MOM/MCC and HOPE/EXI share all these capabilities with VMC. Other instruments, like MAVEN/IUVS and MEX/HRSC are able to obtain full disk images showing different local times that are comparable to those obtained by VMC-like instruments, with the added value that the quality of these instruments specially built for science is far better, and they can cover local times not reachable for VMC. In any case, VMC, being an instrument initially built for a simple mission, has the ability to produce images that increase the observational coverage of the Martian atmosphere and contribute to science.

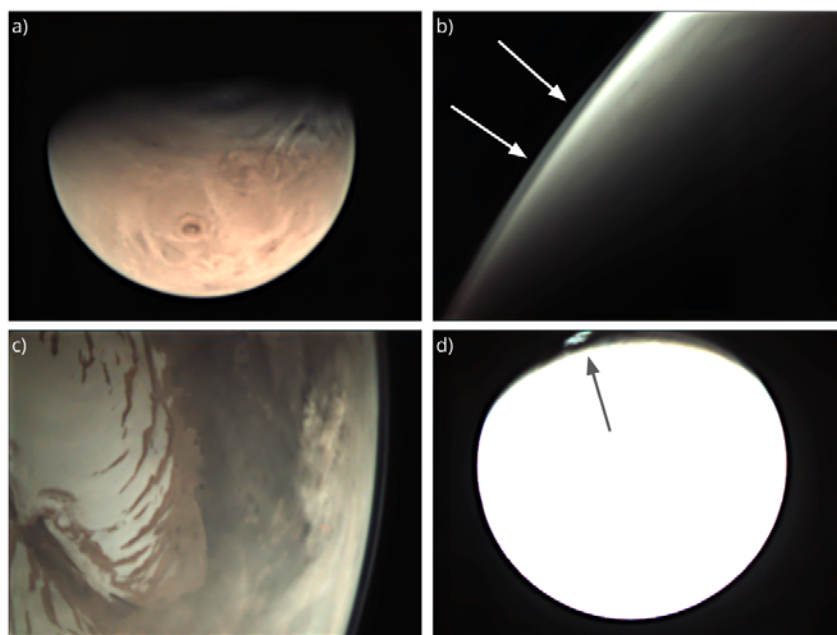


Figure 15. Examples of VMC different VMC observations, displayed images are level 3 products. (a) Full disk image of Mars from apocenter. (b) Aerosols in the limb of Mars imaged in high resolution during a near-pericenter observation. (c) North Polar Cap and a dust storm observed in high resolution near the pericenter. (d) A cloud in twilight seen in an intentionally overexposed full-disk image from apocenter.

Meteorological phenomena on Mars studied with Mars Express VMC images.

### 2.2.2. Photometric calibration and low level data processing

The simple use originally intended for VMC did not need photometric calibration, so the development of a calibration pipeline was needed. The photometric calibration achieved consists of a simple dark current subtraction and flat field correction.

- The dark current was obtained from observations pointing VMC to the area around the constellation of Eridanus, where no bright stars are present. The dark current was stable for the low exposure times typically used to observe Mars (0.4-150ms).
- The flat field was produced by Abel de Burgos Sierra (former Student Trainee at ESAC) based on close-up images acquired by VMC on the northern planitias of Mars from near pericenter. The procedure to create the flat field was based on ideas proposed by space enthusiasts over internet forums<sup>7</sup>, and it is specified in the VMC EAICD.

A calibration pipeline was made as part of this thesis (Figure 16). This pipeline is made with python and based on the software package Luigi<sup>8</sup>, based on an initial structure provided by Dias Almeida Engineering and Systems. The purpose of this pipeline is not just to produce calibrated products, but also to produce metadata LBL files and the directory structure required for the PSA. Level 2 products correspond to uncalibrated images, and level 3 products are calibrated.

This procedure improves the quality of VMC images and enables relative photometry. Although accurate absolute photometry has not yet been achieved, combined observations with HRSC may allow it in the future.

The outputs of the VMC pipeline developed as part of this thesis are regularly archived in ESA Planetary Science Archive (PSA). The process to validate VMC data for the PSA was led by Eleni Ravanis.

### 2.2.3. Geometric calibration

The exploitation of images requires being able to navigate (georeference) pixels, which involves determining the coordinates of the surface point in a pixel, and also any vector and angle related to that point.

---

<sup>7</sup> Team members have been interacting with enthusiasts in the UMSF forum over the years. In the early years of outreach, the suggestions from the public were a source of ideas an inspiration <http://www.unmannedspaceflight.com/index.php?showtopic=5415>

<sup>8</sup> <https://luigi.readthedocs.io/en/stable/>

Meteorological phenomena on Mars studied with Mars Express VMC images.

Any navigation software requires some inputs, like the position, attitude, and characteristics of the camera. The position and attitude of the spacecraft (Mars Express in this case) is given by the technical teams of the mission and publicly archived in the form of SPICE Kernels SPICE (Acton et al., 1996; 2018).

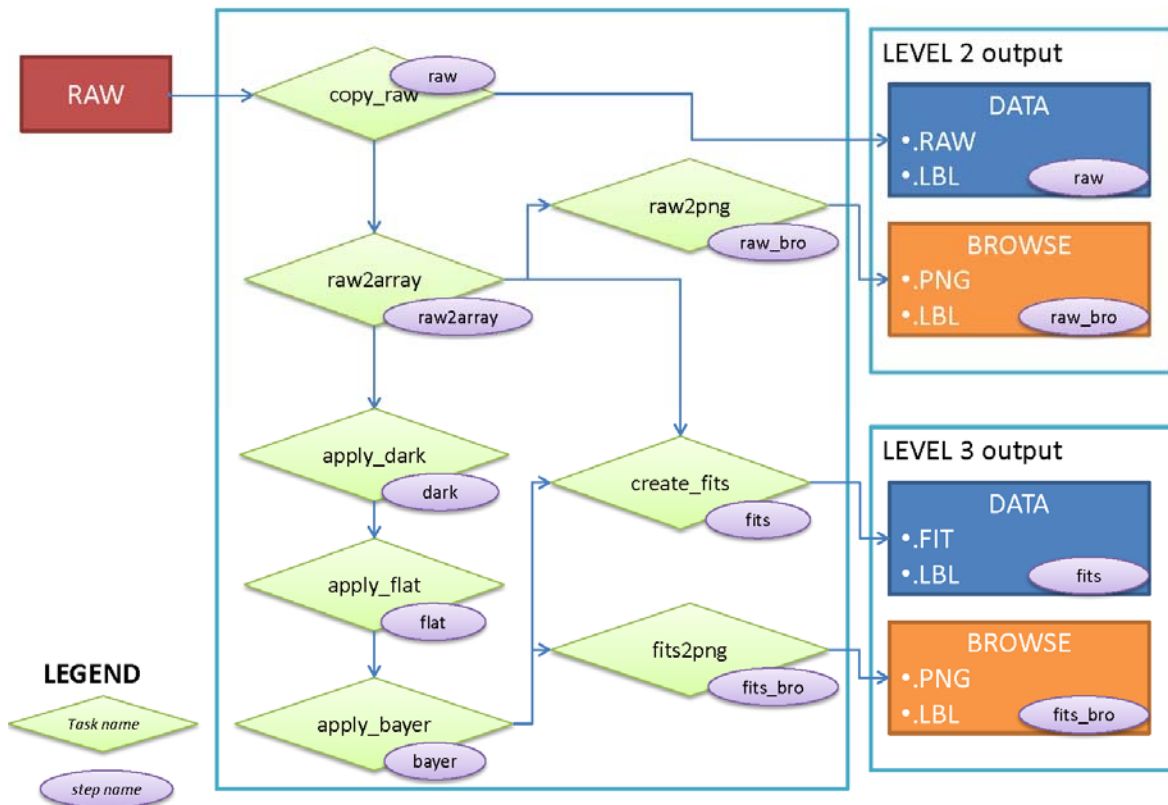


Figure 16. The workflow of the pipeline developed to prepare VMC level 2 and 3 data for the PSA.

Since VMC was never designed for accuracy, the information on the attitude and field of view of VMC was not precise enough (the design values are given in the Flight User Manual; FUM<sup>9</sup>), and there was a need for a geometric calibration. This involved an accurate determination of the attitude of VMC relative to Mars Express, and the characteristics of its field of view. In addition, the timestamp of images (registered after the actual image is captured) suffered a random shift of a few seconds, resulting in new uncertainties.

<sup>9</sup> Publicly available, for example as part of the documents distributed with datasets in the PSA: [https://archives.esac.esa.int/psa/ftp/MARS-EXPRESS/VMC/MEX-M-VMC-2-EDR-EXT8-V1.0/DOCUMENT/MEX-ESA-VMC\\_FLIGHT\\_MANUAL.PDF](https://archives.esac.esa.int/psa/ftp/MARS-EXPRESS/VMC/MEX-M-VMC-2-EDR-EXT8-V1.0/DOCUMENT/MEX-ESA-VMC_FLIGHT_MANUAL.PDF)

Meteorological phenomena on Mars studied with Mars Express VMC images.

As a result, the problem involves 5 free parameters:

- The 3 Euler angles that determine the accurate orientation of VMC relative to the MEX reference frame.
- The axial instantaneous Field of View (iFOV), which defines the pixel angular size and shape.
- The shift in time from the actual image acquisition timestamp to the labeled timestamp.

### **Determination of VMC orientation and iFOV**

In order to determine the orientation of VMC relative to the Mars Express reference frame, we obtained images of fixed stars distributed over the whole sensor. During these observations, the spacecraft maintained a fixed attitude, and therefore the time uncertainty is not present and only 4 free parameters remain: 3 Euler angles, and iFOV.

Long exposures of around 20-30s were used. Such long exposures require a special treatment; the previously described low exposure dark current is not valid anymore, and other images with similar exposure times must be used as dark current. It was determined that the VMC signal to noise ratio was enough to see stars of magnitude up to 2-3, and several observations of stars below that magnitude were performed, many of these in the constellation of Orion.

Only stars with magnitudes lower than 3 and clearly visible in the image were considered. The accurate position of each star was determined by a subpixel Gaussian fit. Due to the noise of the VMC sensor, this Gaussian fit can fail or be inaccurate. In order to reduce this problem, the Gaussian fit result is automatically compared to the positions determined manually, and the star is not considered when the difference is higher than 2 pixels. The result was a set of 54 stars covering the whole VMC sensor. The observed position of stars and an example image showing the constellation of Orion is shown in Figure 17.

A brute-force algorithm was used to test different combinations of the 4 free parameters: Euler angles and iFOV. The best result, which fits the position of 46 stars with an accuracy of less than 1 pixel, was found for the values given in the right column of table 2. The FOV can be calculated from the iFOV, and the corresponding improved estimation is also given in table 6.

Meteorological phenomena on Mars studied with Mars Express VMC images.

The calibrated values are already publicly available as part of the VMC Instrument Kernel<sup>10</sup>, which can be opened and used for geometric calculations using the SPICE software (Acton et al., 1996;2018).

	<b>Value from FUM</b>	<b>Calibrated value</b>
$\alpha_x$	19°	19.2434°
$\alpha_y$	0°	0.2743°
$\alpha_z$	0°	0.4251°
<b>iFOV</b>	0.00113821 rad/pixel	0.00112977 rad/pixel
<b>FOV</b>	40.03° x 30.56°	39.75° x 30.34°

Table 6. VMC geometry parameters, FUM and calibrated values.  $\alpha_x$ ,  $\alpha_y$ ,  $\alpha_z$  stand for the Euler angles. The FUM given FOV has been calculated from the FUM given pixel size and focal length, which explains the difference with the value given in Table 1.

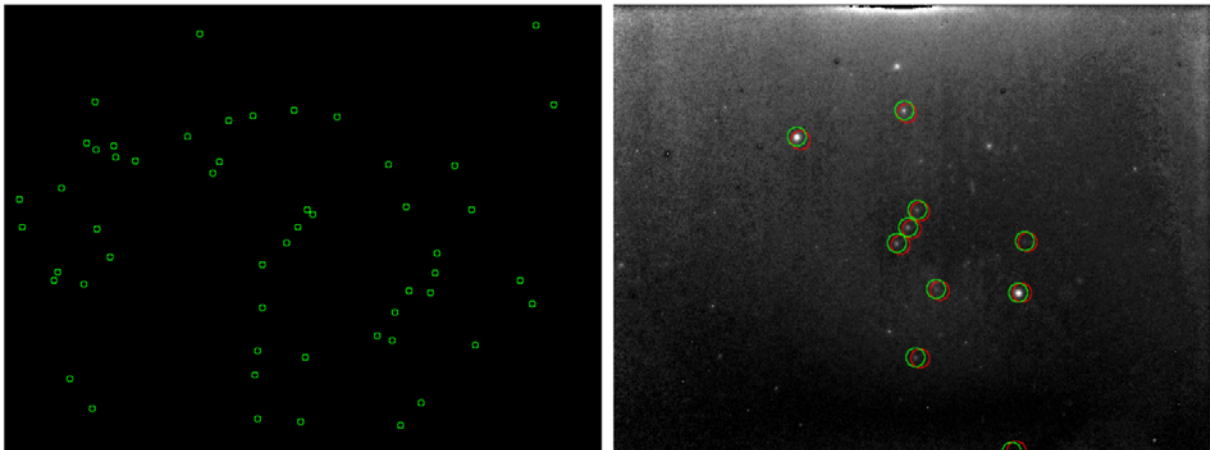


Figure 17. Geometric calibration of VMC. (left) Positions on the sensor of 54 stars used in the analysis. (right) Example of a calibrated image showing the constellation of Orion, the expected position of stars is indicated with red circles (FUM based geometry), and green circles (calibrated geometry).

<sup>10</sup> MEX\_VMC\_V04.TI Mars Express SPICE kernel dataset, distributed by the ESA SPICE service <https://www.cosmos.esa.int/web/spice>

### **Time: Using Phobos as a clock**

The remaining free parameter is the shift in time. The relative orbit of Phobos and Mars Express implies that Phobos is sometimes present in VMC observations from apocenter, moving quickly across the VMC sensor. Using Phobos as a clock, the accurate timestamp of individual images can be determined and compared to the registered timestamp.

37 individual images showing Phobos were used, either with Phobos transiting the disk of Mars or next to it. The observed position of Phobos was manually indicated in each image, and then a specially made program determined the corrected timestamp for each individual image. The process is illustrated in figure 18.

The adjusted timestamps were between 6 and 13 seconds before the registered timestamp, with a mean shift of 9-10 seconds. However, we found no clear pattern for the specific shift of each image within the same observation.

The observed random variations and the limited amount of Phobos observations prevent performing a systematic correction to the whole VMC archive. The effect of this time uncertainty can be neglected in many science analyses, particularly in observations around apocenter, where due to the slow movement of the spacecraft, the fixed attitude during most observations, and the low VMC resolution, ~10 s are not enough to cause significant changes in the observed geometry. Nevertheless, when analyzing images close to pericenter, this shift must be considered. Subtracting ~10 seconds to the registered timestamp can be a good solution when a correction is convenient. Still, an uncertainty of ~4 seconds remains.

Meteorological phenomena on Mars studied with Mars Express VMC images.



Figure 18. Phobos transiting the disk of Mars as seen by VMC on 8 February 2021. The registered timestamp was 18:58:11, but the expected position of Phobos at this time (red circle) is different from the observed position, which is well reproduced by subtracting 10 seconds (timestamp 18:58:01; green circle).

#### 2.2.4. Operations

Part of this thesis has involved the participation in operations and the development of software for that purpose. MEX operations are performed in two main cycles (Merritt, et al., 2018): the Medium Term Planning (MTP), and the Short Term Planning (STP). The Medium Term Planning (MTP), which involves choosing the slots for observations and pointing the spacecraft, is done by Alejandro Cardesín, Eleni Ravanis, and Abel de Burgos Sierra in ESAC, with the science priorities defined by the science team in Bilbao. The Short Term Planning, which involves setting VMC commands including exposure times is fully done by the VMC science team.

The operation of VMC has evolved over time, and the quantity of observations acquired in different times depends on many factors. Figure 19 represents the coverage achieved by VMC over time. It is clear that the achieved coverage has improved a lot since the project to use VMC as a science instrument started (in 2016, MY33). Up to October 2022, 3400 observations containing 80 000 images have been obtained.



Meteorological phenomena on Mars studied with Mars Express VMC images.

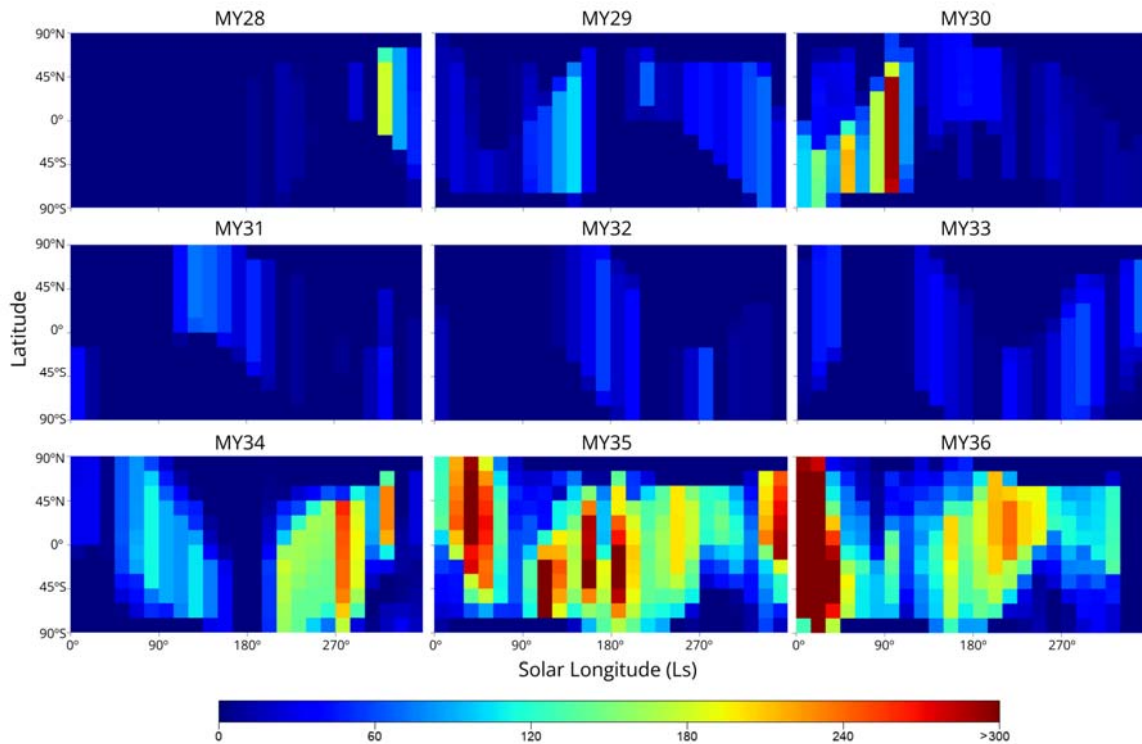


Figure 19. Coverage achieved by VMC over time, up to october 2022. Each panel is a different Martian Year. Horizontal axis corresponds to Ls, Vertical axis corresponds to latitude. The represented quantity is the number of independent observations. Each observation contains a number of images, typically between 10 and 80.

### Medium Term Planning (MTP)

During the MTP, the observation time is distributed between instruments and the pointings of the spacecraft are defined. Due to hardware limitations when VMC is switched on other instruments cannot send data to the mass storage, and thus their data is lost. While most MEX instruments only observe in particular windows, this is a problem for ASPERA, a plasma monitoring experiment that ideally should be always observing.

As a result, most VMC observations take place around Mars Express “maintenance blocks”, performed roughly once a day at apocenter, in which Mars Express turns on its engines to unload the reaction wheels, maintain the orbit trajectory and perform other essential operations. ASPERA cannot observe during maintenance apocenters because particles being expelled by MEX thrusters would affect its measurements, and therefore there is a suitable window a few minutes before and after these maintenance apocenters for VMC to observe.

## Meteorological phenomena on Mars studied with Mars Express VMC images.

Additionally, by agreement with ASPERA, VMC can observe at other locations of the orbit. Finally, VMC can also operate on particular seasons when thermal or data volume issues prevent ASPERA from observing regularly.

VMC is operated trying to not interfere with other instruments, except for campaigns of special scientific interest. VMC images from apocenters are particularly useful, because from that orbital position, Mars is far enough to fit inside the VMC FOV, enabling the monitoring of the global atmosphere on a regular basis. The Mars Express orbit precesses both in the latitude of the apocenters, and the right ascension of the orbital nodes, and thus the phase angle with sun at apocenters can change from very high angles, to very low angles and this has an impact in the possible observations.

Given the characteristics of the MEX orbit, the apocenter is always in the morning side of Mars, and the evening can only be observed from apocenter at polar latitudes. An example of how this biases the local time coverage is shown in supporting material in Hernández-Bernal et al. (2021b; their fig. S2).

### **Short Term Planning (STP)**

During the STP each instrument defines the detailed commanding and observation parameters, which in the case of VMC, involves basically setting the exposure times. The strategy for setting exposure times is a result of the particular way VMC operates, its low dynamic range, and its low signal to noise ratio.

Until 2012, VMC images were commanded manually with variable configuration settings, but in current MEX operation this is no longer possible. In 2012, the VMC commanding was updated, so that each VMC observation consists of a series of consecutive image loops of 6 images. Configurable parameters can be set only for those 6 images and repeats in each loop. Additionally, when VMC is switched on, it takes a “default” image with an exposure of 14ms before entering the loop. Between 2012 and 2018, the length of the loop changed occasionally but no more updates are expected in the future.

The default image exposure of 14ms is hardwired and can not be changed (FUM). The 6-image loop parameters are configurable and can be updated based on the target illumination and/or scientific objective.

VMC requires 38 seconds for each image to be transferred to the memory and an additional margin, which can be partially configured for each image of the loop, is added. Thus, the time between images is typically around 48 seconds. An exception to this is the

## Meteorological phenomena on Mars studied with Mars Express VMC images.

interval between the first (default) and the second image, which is typically around 55 seconds. Additionally, 174 seconds are required to switch on VMC, and up to 60 seconds are required to switch it off. A typical VMC observation is illustrated in figure 20.

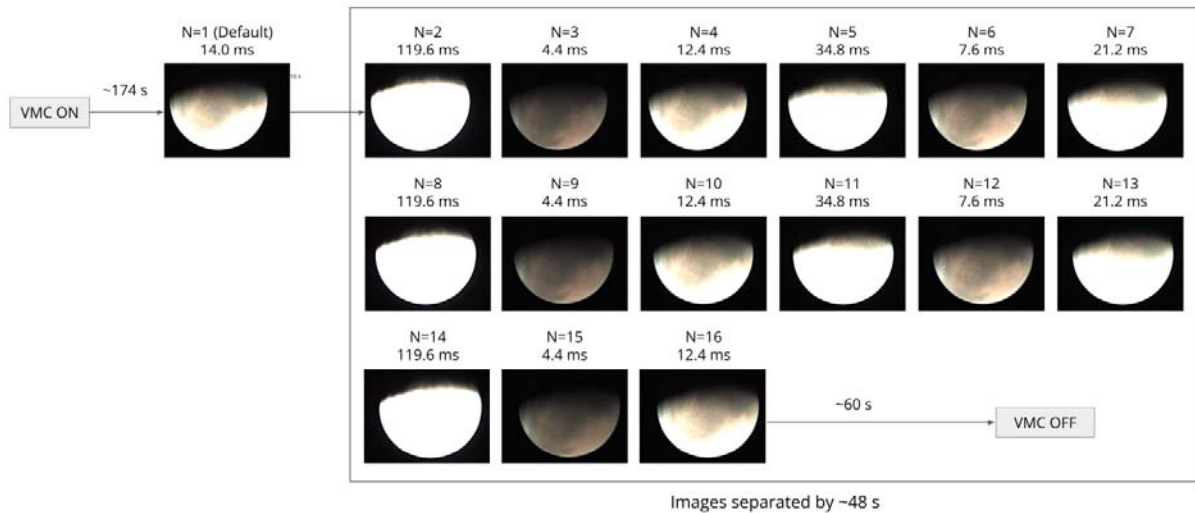


Figure 20. Schematic image loop acquisition of VMC.

The configurable exposure time can range from 0.4 ms to around 90 s, but the thermal noise of the sensor typically overflows the whole sensor even for dark sky observations when the exposure is longer than ~40 s (depending on the temperature of the sensor), and the borders of the field can be already saturated with exposures of 20 s.

As VMC images often cover the whole disk of the planet with a wide variety of incidence, emission, and scattering angles, optimizing exposure times for regular observations constitutes a challenge. Typical exposures for the dayside of Mars are around 2-20 ms, but higher exposures (20 - 120 ms) are usually set to see aerosols over the limb (Sánchez-Lavega et al., 2018a) or in the night side of the terminator (Hernández-Bernal et al., 2021b; Hernández-Bernal et al., 2022b). Even higher exposures, of up to 20 - 30 seconds have occasionally been used to image stars for calibrations (see section 2.2.3) or for particular experiments, for example, to try searching for meteors burning in the atmosphere (Hernández-Bernal et al., 2021c).

### 2.2.5. Level 4 data processing for HDR products

The color depth of only 8 bits (see table 5) implies that the dynamic range and signal to noise ratio of VMC are not very high. In order to overcome this constraint, different

## Meteorological phenomena on Mars studied with Mars Express VMC images.

exposure times are used in different images, to observe both bright targets (e.g. features in the dayside of Mars) and dark targets (e.g. features near the terminator, or dim aerosols high on the limb or far into the night). Those images can be stacked together to obtain High Dynamic Range (HDR) images. The corresponding products are the experimental VMC level 4 products.

The workflow to build HDR products from a group of VMC images involves the following steps:

1. Select source images from the level 3 archive and build a destination projection. Source images should be close in time to avoid large variations in the illumination conditions. Any destination projection is valid.
2. Project source images to the destination projection and normalize the brightness of the projected images by dividing their values by the exposure time of the source image.
3. Map the incidence angle in the destination projection, assuming a timestamp that is typically the average of the timestamps of all the source images.
4. Make regions (defined by a range of incidence angles) in the destination projection for each exposure time.
5. Copy each image to its destination region. When superposition of different exposures is allowed, the brightness is normalized accordingly.

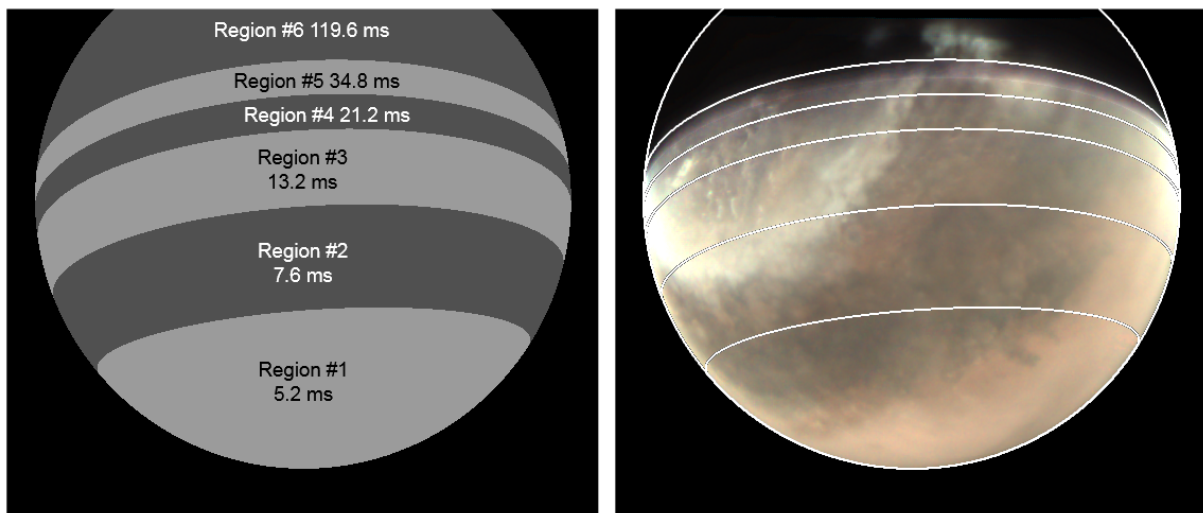


Figure 21. Regions in a destination projection during the process to make an HDR product. The left image is the scheme of the destination projection, where different regions with different optimal exposure times (from 5.2 to 119.6 ms) have been determined. The right image is the output image with the different regions indicated. This image without marks can be seen in the right panel of Figure 23.

Meteorological phenomena on Mars studied with Mars Express VMC images.

These steps result in a product that conserves the relative photometry and contains more information than what can be stored in a typical 8 bit image.

In order to produce images ready to be stored as 8 bit images suitable to be displayed in a standard digital screen two additional steps are needed:

6. Luminosity correction. This is a key step to display the full disk of Mars properly illuminated in a single image. It has been observed that Lambert correction does not provide good results near the terminator, which is often an area of special interest in VMC images. Thus, a modified correction has been developed (Figure 22), which avoids the discontinuity in the terminator and the divergence to infinity of the Lambert correction. Instead, the correction grows slowly to the terminator and keeps a constant value in the night, allowing a proper visualization of clouds in twilight.
7. Histogram adjustment and export to 8 bit image format.

These final steps imply that the relative photometry is lost, but in exchange high quality images with the full disk of Mars uniformly illuminated are obtained.

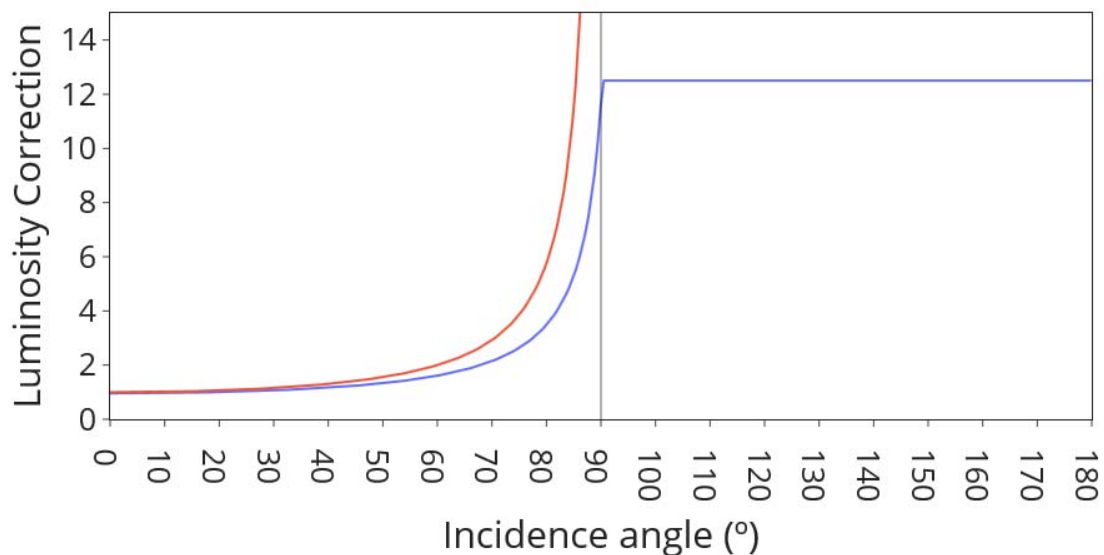


Figure 22. Luminosity correction in developed HDR products. The red curve corresponds to the Lambert correction,  $1/\cos(\alpha)$ , which diverges to infinity at  $\alpha=90^\circ$ . The blue curve represents an alternative correction that produces better results near the terminator and into the night. Right panel in Figure 23 is an example of an image processed using this correction.

## Meteorological phenomena on Mars studied with Mars Express VMC images.

This procedure can be applied with variations for different purposes and specific procedures have been applied in some published papers (e.g. Hernández-Bernal et al., 2019, 2021a). Currently, an experimental pipeline is running operationally (see section 2.2.6), which involves some specific configurations, among others:

- The source images are always loops of 6 images (see section 2.2.4 and figure 20).
- The destination projection is always a spherical projection analogue to the one of the original images.
- Different images are not stacked together in the same region.

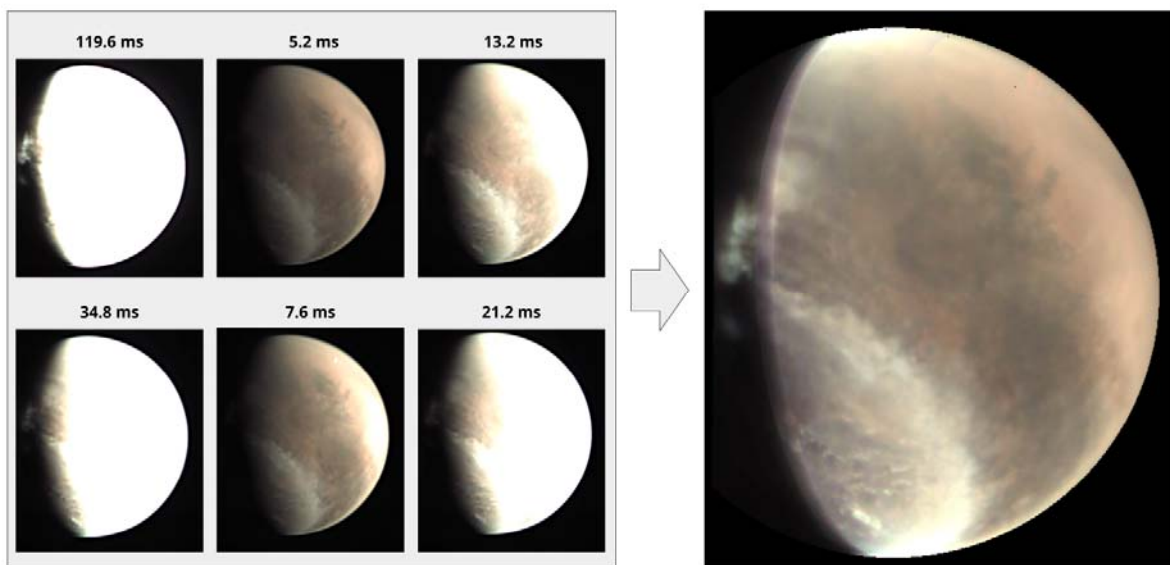


Figure 23. Example of source and output images from the operational pipeline. 6 source images are displayed in the left panel. The output HDR image with the automated luminosity correction and histogram adjustments is displayed in the right panel. Note that the whole diurnal side of the planet and the cloud in twilight can be easily appreciated in the same image. These images were obtained on 2022-01-10.

Meteorological phenomena on Mars studied with Mars Express VMC images.

### 2.2.6. Internal infrastructure and web apps

In practice all the developments and procedures described in this section run operationally over an infrastructure of hardware and software, which involves the synchronized working of three different servers (Figure 24).

- The VMC server at ESAC in Madrid, here the calibration pipeline (see section 2.2.2) runs and all the procedures related to archiving in the PSA are performed. The input files are obtained from the ESA DDS (Data Distribution Service), which distributes data being received by ground antennas from deep space missions.
- Server “Castor” propriety of the Grupo Ciencias Planetarias (GCP) at UPV/EHU in Bilbao hosts the level 4 pipeline, operations software, and other non-graphical analysis tools. A set of jupyter servers supporting analysis, operations, and software development run here.
- Server “Hecate” propriety of the Grupo Ciencias Planetarias (GCP) at UPV/EHU in Bilbao hosts all the galleries and graphical interfaces, including web applications for the VMC team, all of them developed as part of this thesis.

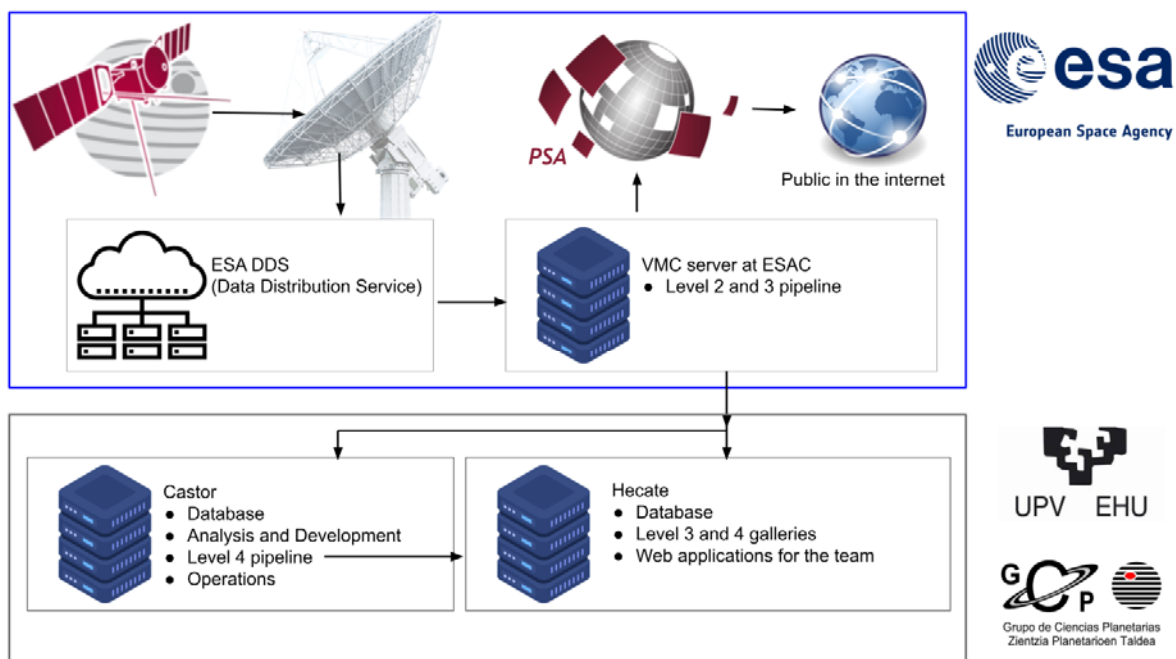


Figure 24. Summary of the servers involved in the daily running of VMC as part of the Mars Express mission. Most of the software was developed as part of this thesis.

A number of web applications have been developed for the VMC team, hosted at the server “Hecate”. They can be accessed by team members at [vmc.ehu.eus](http://vmc.ehu.eus). The main screen of the

Meteorological phenomena on Mars studied with Mars Express VMC images.

system is shown in figure 25. The user can access different applications from the upper menu:

- Calendar. It updates automatically from MEX and VMC databases, and includes MEX MTPs and STPs, VMC planned observations, and planned VMC data downlinks.
- Gallery. The main level 3 gallery, which is described below.
- Grid. A simplified level 3 gallery.
- Loop gallery. A gallery for level 4 HDR data.
- Publications and documents. Sections with useful information for reference.

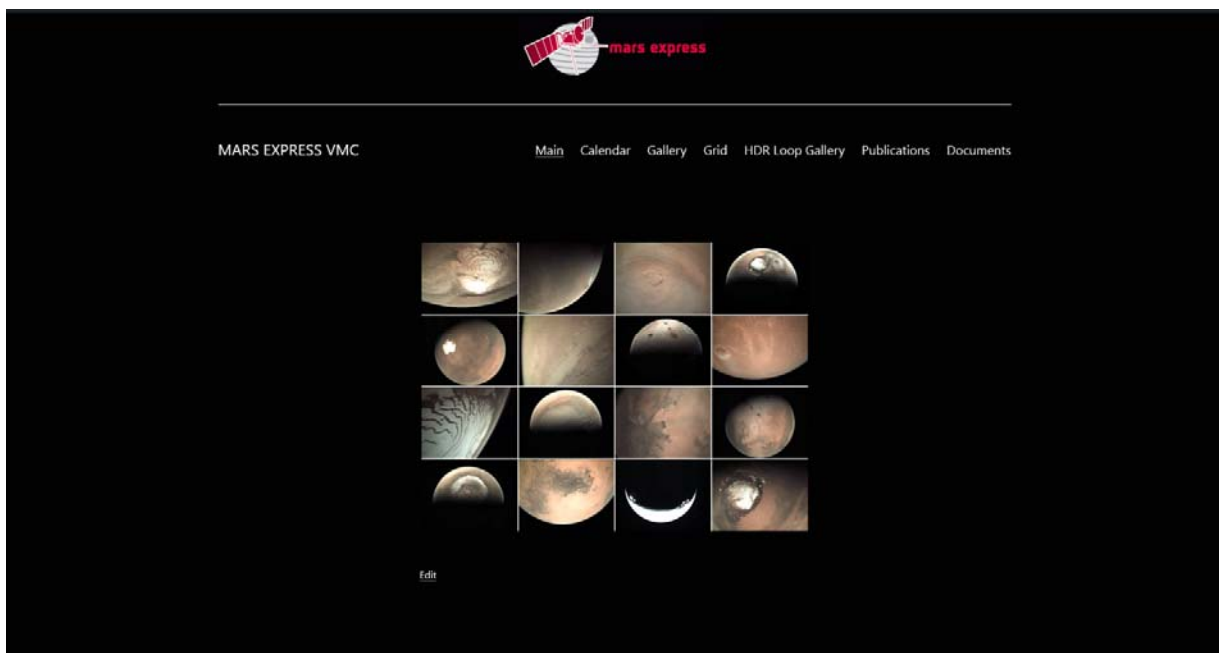


Figure 25. Main screen of the system where the VMC team can access the data.



Meteorological phenomena on Mars studied with Mars Express VMC images.

## The Galleries

Both level 3 and level 4 galleries are based on the same software, made with PHP<sup>11</sup>, javascript<sup>12</sup> with jQuery<sup>13</sup>, and CSS<sup>14</sup> for styling. A base library called “jwindows” was developed to provide a user interface based on windows in the browser. Galleries are able to return basic geometric information, such as coordinates, resolution, and local time at mouse position. Figure 26 shows a screenshot of the level 4 gallery.

In both level 3 and level 4 galleries, each VMC observation is displayed as a thumbnail in the “list of observations” (wide bottom window). The user can move between observations by clicking on the thumbnails or using the right and left arrows of the keyboard. Different images (loops, in the case of the level 4 gallery) within an observation can be accessed using the up and down arrows of the keyboard.

Different lists of observations can be accessed by pushing the magnifying glass icon, which leads to a list of predefined queries (organized by years).



Figure 26. Screenshot of the loop gallery (where HDR level 4 products are displayed), one of the applications internally available to the VMC team members.

<sup>11</sup> <https://www.php.net/>

<sup>12</sup> <https://en.wikipedia.org/wiki/JavaScript>

<sup>13</sup> <https://jquery.com/>

<sup>14</sup> <https://en.wikipedia.org/wiki/CSS>

Meteorological phenomena on Mars studied with Mars Express VMC images.

### Elkano Web App

The Elkano software package that will be described in section 2.3 includes many functions, most of them only available as libraries that can be included in python scripts and notebooks. In order to help users to make simple measurements on level 3 images, a javascript version including the main functions of Elkano was developed, together with a web application that can be accessed easily from the level 3 gallery via the compass sign (it is not yet available for level 4 images). This general-purpose application has been used for example for VMC measurements on Sánchez-Lavega et al. (2022a) and Río-Gaztelurrutia et al. (2021). Other web applications have been developed for different kinds of measurements or with other specific purposes.

Fig. 27 shows a screenshot of the Elkano Web App. Multiple options to display the geometry of the image are available, different maps can be chosen, and by clicking any point of the image the user can define a marker, which is saved on the server with its coordinates and other properties. The list of markers can be downloaded as a CSV<sup>15</sup> file.

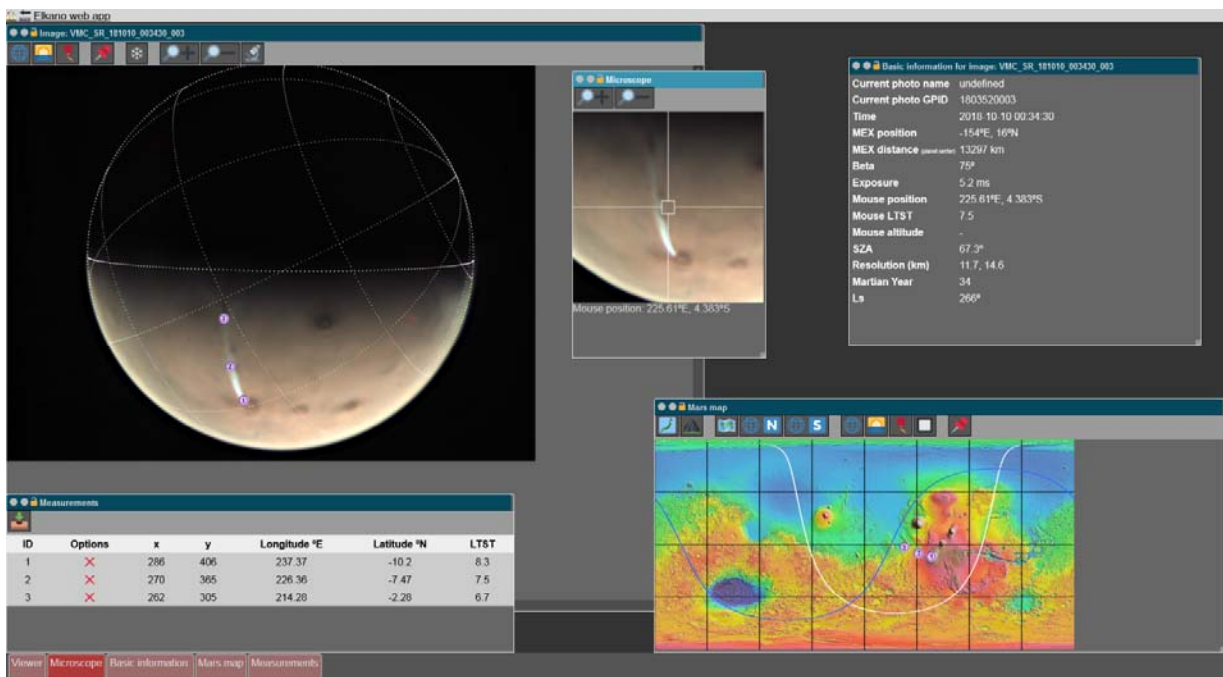


Figure 27. Elkano web application, available to the VMC team members.

<sup>15</sup> [https://en.wikipedia.org/wiki/Comma-separated\\_values](https://en.wikipedia.org/wiki/Comma-separated_values)

Meteorological phenomena on Mars studied with Mars Express VMC images.

### 2.3. Instruments and tools

Although the main source of information for this thesis is the VMC camera, data from other instruments has been exploited, leading to the development of software whose purposes exceeds VMC. In addition, models from the LMD (Laboratoire de Météorologie Dynamique) have been used throughout the thesis.

Section 2.2 focused on developments specific to VMC. In this section, a brief summary of all the other instruments and tools not directly related to VMC will be provided.

#### 2.3.1. Data from other Instruments used in this Thesis

Data from a number of instruments onboard different spacecraft have been used in this thesis:

- HRSC (Jaumann et al., 2007) on board Mars Express is a high resolution pushbroom camera that takes images in 9 different channels at different altitudes along the highly elliptical orbit.
- OMEGA (Bibring et al. 2004) on board Mars Express, is an imaging spectrometer that takes images simultaneously in several spectral bands.
- IUVS (McClintock et al., 2015, Connour et al. 2019) on board MAVEN, is a scanning-slit spectrograph that takes composite false color UV images of Mars. IUVS acquires full disk images of Mars from apocenter during nearly every MAVEN orbit with a cadence of ~4.5 hours.
- MCC (Arya et al. 2015) on board ISRO (Indian Space Research Organization) MOM, is an RGB color camera with a color depth of 10 bit. It acquires images at different altitudes from a highly elliptical orbit, usually with high resolution.
- VIS (Visual Imaging System) (Wellman et al., 1976) on board Viking 2 orbiter was a single channel visible camera of high resolution. Viking orbiters were in highly elliptical non sun-synchronous orbits.
- MARCI (Bell et al., 2009) on board MRO is a pushbroom camera that observes Mars during the afternoon from an afternoon sun-synchronous orbit, achieving high-resolution coverage of the whole planet every Martian sol.

#### 2.3.2. Software

Similar to the software packages developed for VMC as described in section 2.2, other pieces of software were developed for other instruments (for example, a pipeline was created for IUVS data, and some VMC software was adapted to MCC). Software was developed for specific measurements or to cover specific needs of research activities. In

Meteorological phenomena on Mars studied with Mars Express VMC images.

this section, we describe as a sample three of those packages: Elkano, Mars Studio and Marstime.

### **Elkano: broad use for planetary images**

As mentioned before, a highly versatile software for planetary image geometry and navigation called “Elkano” was developed as part of this thesis. This software is programmed in python, and a reduced javascript version has also been developed to be used in web browsers. The main advantage of this software is that it is highly modular and object oriented, which means that planets, cameras, and projections, and the navigation of an image itself are classes for which different instances (objects) can be created. By creating new classes the functionality of the software can be expanded. This software can be used in connection to SPICE (Acton et al., 1996; 2018) to load geometrical information, or it can be used with any other source for geometrical information, making it possible to use the software for planning and operations when SPICE kernels are not available. This was necessary to build operations software for VMC.

So far, the software has been used to navigate original images from VMC, VIS (the visible cameras on the Viking orbiters), and MCC. Amateur ground based telescope images have also been navigated by defining suitable cameras in the system; any telescope and planet could be easily defined.

The software accepts any kind of projection, so projected images from HRSC, MARCI, and other instruments can also be handled using Elkano. Among the currently available projections, there is a “celestial” projection, which allows navigating sky images.

The geometry package includes classes for matrix and vectors, definitions of python operators to work with matrix and vectors, functions to create rotation matrix, recipes to create matrix corresponding to specific orientations of a camera, etc.

A package called “coordsys” provides functions to create grids, limb and terminator curves, and other geometrical forms over the planet.

Synthetic images can be made by projecting a map (typically in cylindrical coordinates) to a photographic spheric projection, but this process takes too much time when done pixel by pixel with Elkano. In order to make synthetic images efficiently, a specific package was made. This package connects to the free software POVray, which is a 3D renderer with hardware acceleration, and creates a synthetic image in a few seconds.

Meteorological phenomena on Mars studied with Mars Express VMC images.

In conclusion, Elkano is a highly modular, versatile, and adaptable geometry and navigation software, that has been fully made as part of this thesis and facilitates working with many instruments and performing geometrical calculations.

```
In [1]: import lib3

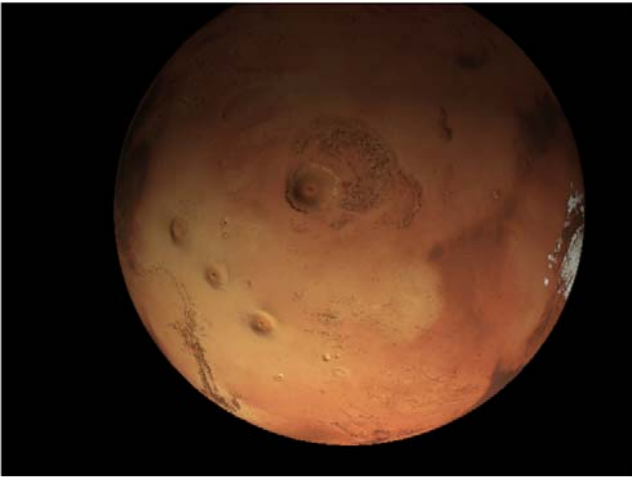
In [2]: from Elkano.navigate import *
        from Elkano.planets import Mars
        from Elkano.cameras import VMC
        from datetime import datetime
        from Elkano import POVray
        texture='Mars_Texture.png'

Construction of a navigate object. SPICE kernels are automatically loaded to acquire the geometry corresponding to the given time

In [3]: nav=navigate(proyeccion=PHOTO,planet=Mars,camera=VMC,datetime=datetime(2019,7,27,18,32,19))

Making a synthetic image with POVray to see what is in this navigate object (what VMC saw at the given time)

In [4]: %%time
        im,a=POVray.synthetic(texture,nav,sun=True,light=0.2)
CPU times: user 3.14 ms, sys: 20.5 ms, total: 23.6 ms
Wall time: 1.7 s

In [5]: im
Out[5]: 
```

Examples of coordinates conversion. From longitude,latitude to pixel

```
In [6]: nav.lonlat2xy([255,10],DEG) #Ascraeus Mons coordinates
Out[6]: ([257.63765179770724, 322.407973654293], True, True)

And from pixel to longitude, latitude

In [7]: nav.xy2lonlat([257,322],DEG)
Out[7]: (array([254.93182133, 9.868698999]), True, True)
```

Figure 28. Screenshot of a python notebook showing some simple examples of use of Elkano.

### Mars Studio

This is a web app designed to work with images from any source. It includes the javascript version of Elkano, so it can perform basic navigation and geometry operations, whether

Meteorological phenomena on Mars studied with Mars Express VMC images.

over original images or over projections (cylindrical, polar, etc.). Images can be loaded as layers and blinked, which is useful to compare images or for cloud tracking. Different kinds of measurements are available. In general, these measurements are stored to a file on the server, which is then opened and processed using python and a specially designed library.

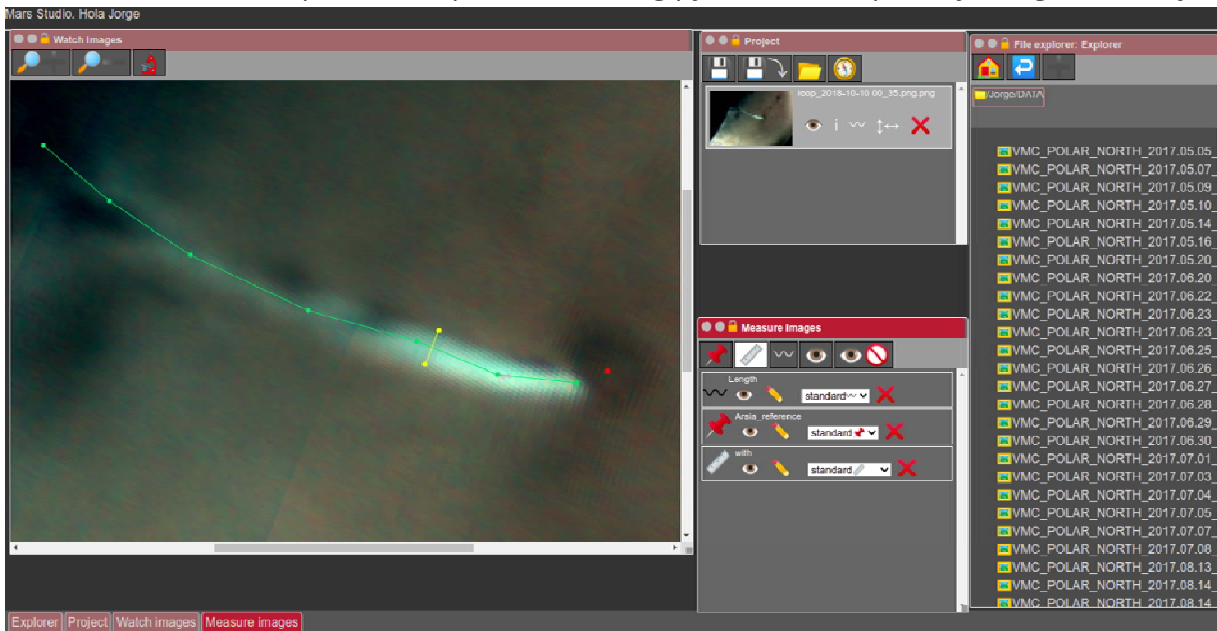


Figure 29. Screen capture displaying an example of use of the application “Mars Studio”.

## Marstime

Making calculations related to the Martian timekeeping is necessary. There are existing applications and software packages for such purposes. There is an existing python library called “pyMarsTime”, which can be found in github<sup>16</sup>. In order to make these calculations simpler, a new python library was made, where the core calculations are made with the functions provided by the original pyMarsTime library (only with slight updates, like adding most recent leap seconds), but a new object oriented interface was made.

With the new library, a marstime object can be easily made from a python datetime object. The marstime object contains attributes, like the MY and Ls. By defining a longitude and a latitude, new attributes like the Local True Solar Time (LTST), or the sun location in the sky become available. An object oriented library is specially useful when many different timestamps are handled in the same program, for example.

<sup>16</sup> <https://github.com/eelsirhc/pyMarsTime>

Meteorological phenomena on Mars studied with Mars Express VMC images.

### 2.3.3. LMD models

The research developed within this thesis uses the support of atmospheric models from the LMD (Laboratoire de Météorologie Dynamique). Their GCM, Mesoscale Model, and the MCD have been used and will be briefly described below. In particular, the work published in the paper Hernández-Bernal et al. (2022a) is based on the use of those models.

#### **GCM**

The LMD developed an advanced GCM (General Circulation Model; Forget et al., 1999) that is widely recognized by the scientific community who work on the atmosphere of Mars. A GCM requires a dynamical core, and a set of physical packages. The dynamical core of a Martian GCM can be adapted from the corresponding dynamical core of Earth GCMs. The resolution of this GCM can be tuned, but it is typically run on a grid of 64x48 cells (64 cells in the longitudinal direction, 48 in the latitudinal direction). In the vertical direction, this GCM uses a system of hybrid coordinates, which means that layers follow the pressure field in high altitudes and are parallel to the ground in low altitudes.

The physical packages of the LMD Martian GCM keep improving over time. Dust radiative processes were improved by Madeleine et al. (2011), and water ice cloud microphysics were improved by Navarro et al. (2014).

As mentioned before, dust has an important radiative effect on the Martian atmosphere, analogous to that of clouds on Earth. This is why the results of this GCM are significantly improved by forcing the presence of dust to follow the actually observed dust optical depth. This is done based on the dust climatologies compiled by Montabone et al. (2015; 2020) for each martian year, which means that GCM simulations can be run specifically for each Martian year, improving the accuracy of the results and the comparability to observations.

#### **Mesoscale model**

The LMD mesoscale model uses the WRF (Weather Research and Forecast model; Skamarock et al. 2008) dynamical core and the same physical packages as the GCM. A mesoscale model runs on a regional domain at higher resolution, using the outputs from a GCM as boundary and initial conditions, and some spin-up simulation time is necessary for the model to converge to valid results from those initial conditions. The LMD Mars Mesoscale Model (MMM; Spiga and Forget, 2009) runs over the outputs of the LMD GCM, this implies that the MMM can be run for the dust scenario of different Martian years.

Meteorological phenomena on Mars studied with Mars Express VMC images.

One of the papers of this thesis (Hernández-Bernal et al., 2022a) has been developed based on the LMD MMM, and the outputs of specially run simulations were analyzed as part of this thesis. The specific configuration of the MMM for that work is described in Hernández-Bernal et al. (2022a)

### **Mars Climate Database (MCD)**

The MCD<sup>17</sup> is a useful tool that opens the LMD Mars GCM to the community in an easy way (Millour et al., 2018). It is a publicly available database containing time-averaged values from the GCM outputs. It can be accessed using a web interface<sup>18</sup>, or a python library<sup>19</sup>.

For many purposes, the MCD provides enough information, since it provides time-averaged values, it is a good approximation to the mean climatological conditions. In many other cases, it is necessary to look at the original GCM outputs, whether because some specific tuning is necessary, because the low resolution and averaged information available in the MCD is not enough, or because it is necessary to see detailed information that is not present in the MCD.

---

<sup>17</sup> The complete documentation can be accessed from:

[http://www-mars.lmd.jussieu.fr/mars/info\\_web/index.html](http://www-mars.lmd.jussieu.fr/mars/info_web/index.html)

<sup>18</sup> [http://www-mars.lmd.jussieu.fr/mcd\\_python/](http://www-mars.lmd.jussieu.fr/mcd_python/)

<sup>19</sup> <https://github.com/aymeric-spiga/mcd-python>



### 3. Objectives and publications

This thesis pursues the study of meteorological events in the atmosphere of Mars based mostly on images provided by MEX/VMC. The general objectives of this thesis can be articulated, following the context about the current knowledge of the Martian atmosphere presented in section 2.1, and the capabilities of VMC described in section 2.2.1 and in the context of available space missions and instruments described in 2.1.8. These general objectives are:

1. Prepare methodologies for VMC to be used as a science instrument and develop techniques and tools for its operation and scientific exploitation.
2. Exploit the particular capabilities of VMC (full disk images, wide local time coverage, video capabilities) to investigate the martian atmosphere and meteorological phenomena.
3. Provide new insights on Martian cloud systems and dust storms based on observations by different instruments and atmospheric models.

In practice the thesis has focused on specific meteorological phenomena for which VMC provided an outstanding coverage not available for other instruments. These meteorological phenomena are: the Global Dust Storm in MY34 and its impact on the south polar region; the Arsia Mons Elongated Cloud (AMEC); and clouds in twilight. The specific objectives for the study of these meteorological phenomena were:

- **Global Dust Storm in MY34** and its impact on the south polar region
  - Analyze the penetration of dust into the south polar cap over the period of the storm.
  - Trace the polar circulation during the dust storm, when it could be affected by the globally changed dynamics due to the widespread presence of dust.
  - Analyze cloud structures appearing over the dust layer
  - Monitor the altitude of aerosols at any latitudes
- **The Arsia Mons Elongated Cloud (AMEC)**
  - Measure the physical characteristics of the cloud and analyze its morphology
  - Determine the diurnal and seasonal evolution and cycles of the cloud and assess the interannual variations of the phenomenon.
  - Understand the formation of this cloud in the context of the second half of the year, which is the dusty season, known for the scarcity of clouds.

Meteorological phenomena on Mars studied with Mars Express VMC images.

- Understand the physical processes leading to the formation of this cloud in the morning and its extreme elongation
- Analyze whether the same physical mechanisms driving the AMEC are behind other observed clouds on Mars that visually resemble the AMEC.
- **Clouds in twilight**
  - Develop advanced techniques to find isolated clouds in twilight and measure their altitude.
  - Analyze the climatology of clouds in twilight in the context of the current knowledge on mesospheric clouds in the Martian atmosphere.
  - Determine the physical processes leading to such climatology
  - Investigate the interannual variations within this climatology in connection to the dust activity and thermal tides
  - Develop new techniques to perform mesospheric cloud-tracking on these clouds.

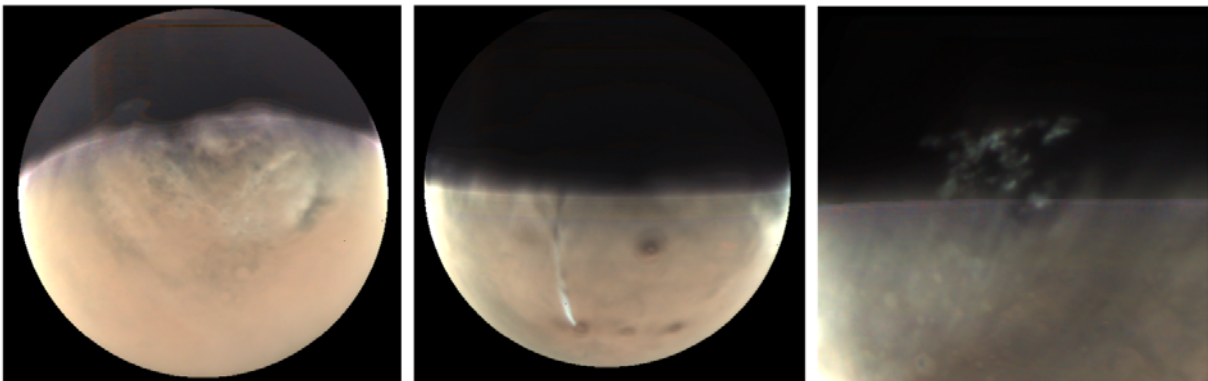


Figure 30. Meteorological phenomena investigated as part of this thesis. (left) GDS MY34 in the south polar region. (middle) The AMEC. (right) Clouds in twilight.

The thesis is supported by 4 first-author papers devoted to the aforementioned meteorological phenomena. Such papers were published in peer reviewed journals . These papers (included in the annex) are:

- **Hernández-Bernal et al. (2019)** The 2018 Martian Global Dust Storm over the South Polar Region studied with MEx/VMC. *Geophysical Research Letters*.
- **Hernández-Bernal et al. (2021a)** An Extremely Elongated Cloud over Arsia Mons Volcano on Mars: I. Life Cycle. *Journal of Geophysical Research: Planets*.

Meteorological phenomena on Mars studied with Mars Express VMC images.

- **Hernández-Bernal et al. (2021b)** A long term study of Mars mesospheric clouds seen at twilight based on Mars Express VMC images. *Geophysical Research Letters*.
- **Hernández-Bernal et al. (2022a)** An Extremely Elongated Cloud over Arsia Mons Volcano on Mars: II. Mesoscale modeling. *Journal of Geophysical Research: Planets*.

Two additional papers led by Agustín Sánchez-Lavega have been published with a coauthor contribution from this thesis:

- Sánchez-Lavega et al. (2019) The onset and growth of the 2018 Martian global dust storm. *Geophysical Research Letters*.
- Sánchez-Lavega et a. (2022a) Cellular patterns and dry convection in textured dust storms at the edge of Mars North Polar Cap. *Icarus*

The development of this thesis has provided new knowledge about some meteorological phenomena in the Martian atmosphere, new observational techniques, and new software. All this work is reflected in the publication of peer reviewed papers, contributions to congresses, and the operation, data processing and archiving of VMC, which is now fully considered and operated as a new scientific instrument onboard Mars Express.

## 4. Summary and discussion

The following subsections include a brief summary and discussion for the three main meteorological phenomena covered in this thesis.

### 4.1. Dust Storms and the Global Dust Storm in Martian Year 34

Dust storms on Mars are an active research topic with many unanswered questions. VMC has observed many dust storms, including dust storms around the polar caps (e.g., Sánchez-Lavega et al., 2022a; Figures 9c and 9d in this thesis), in equatorial latitudes during the dusty season (e.g. Sánchez-Lavega et al., 2022b; Figure 9b), and a Global Dust Storm in MY34 (Hernández-Bernal et al., 2019; Figure 9a). The technical aspects described in section 2.2 have provided support to all those works. This section is devoted to the impact of the GDS 2018 (MY34) over the South Polar Region (SPR), as reported in Hernández-Bernal et al. (2019).

GDSs typically start in the area around Hellas Planitia, where local wind conditions during the dusty season favor dust lifting. Zonal winds and the rising branch of the Hadley cell facilitate the expansion of the dust storm (Kahre et al., 2017). The GDS in MY34 was an exception, and it is the only confirmed GDS that initiated in the northern hemisphere. It started in Acidalia Planitia, at  $\sim 30^\circ\text{N}$  (May 30, Ls  $184^\circ$ ), and reached the south polar cap around 10 days later (June 8, Ls  $189^\circ$ ), as shown by Sánchez-Lavega et al. (2019) using ground-based amateur images. VMC was in the middle of a technical pause due to the transfer of operations from ESOC to ESAC, and operations only resumed in June 18 (Ls  $195^\circ$ ), when the storm was fully developed.

The apocenter of Mars Express was over the SPR at the time, and this allowed VMC to acquire excellent images of the area during the GDS. Four different features were analyzed in this work:

- The covering of the polar cap by dust. The dust distribution was inhomogeneous and evolved from sol to sol.
- The presence of arc-shaped aerosol bands around the pole. These bands were more intense near the terminator, suggestive of water-ice composition
- Cloud tracking allowed wind measurements, showing that winds blew towards the terminator in the morning, a pattern not present in the MCD in dust storm scenario.
- The altitude reached by aerosols (in northern latitudes) was analyzed based on limb images. Aerosols were found at altitudes up to 70km near Alba Mons ( $\sim 250^\circ\text{E}$ ,  $45^\circ\text{N}$ ).



Figure 31. The South Polar Region as observed by VMC on July 1 2018. Aerosols and dust are apparent over the South Polar Cap. Adapted from Figure 2a in Hernández-Bernal et al. (2019)

#### 4.2. Orographic clouds. The Arsia Mons Elongated Cloud (AMEC)

Orographic clouds are very common on Mars. Telescopic observers already noticed that the area of Tharsis was very prominent in “blue clouds” (e.g. Smith & Smith, 1972). Early space missions and radar measurements showed that Tharsis was an elevated area, which led to the idea that clouds present in the area were of orographic origin (Sagan et al., 1971). Orographic clouds on the volcanoes of Tharsis (Olympus, Arsia, Pavonis, Ascraeus, Alba), and Elysium have been widely studied based on images acquired in the afternoon by space probes. They are clearly visible in the MGS/MOC maps provided by Wang & Ingersol (2002; their fig. 2), and in the graphs produced by Benson et al. (2003; 2006). These maps and graphs show that orographic clouds are most common in the first half of the year, as part of the ACB.

The study of orographic clouds in this thesis is built around the Arsia Mons Elongated Cloud (AMEC), which has been investigated and reported for the first time. The

Meteorological phenomena on Mars studied with Mars Express VMC images.

observations of the AMEC were reported in **Hernández-Bernal et al. (2021a)**, and the results of mesoscale simulations were reported in **Hernández-Bernal et al. (2022a)**. The AMEC is a visually striking cloud that repeats regularly in a daily and annual cycle. It forms daily on Arsia Mons (~240°E, 10°S), during the early morning and in the second half of the year. Since orographic clouds during the second half of the year are less common (Benson et al., 2003;2006), and the morning is a poorly observed local time, the existing literature regarding orographic clouds in the morning during the second half of the year is very limited. The study of the AMEC with the aid of the full disk images provided by VMC has led to the investigation of some previously unexplored aspects of orographic clouds on Mars. These investigations are summarized in this section.

#### 4.2.1. The orographic cloud mechanisms on Mars

Mesoscale modeling by Michaels et al. (2006) showed that orographic clouds were the result of upslope winds motivated by insolation. These winds transport water and dust to the upper atmosphere, where water can condensate to form clouds. The study of Michaels et al. addressed clouds in Tharsis (Ascraeus Mons and Olympus Mons) during the first half of the year.

New LMD mesoscale simulations performed for the investigación of the AMEC (Hernández-Bernal et al. 2022a) show that in the second half of the year and at least in low latitudes the mechanism shown by Michaels et al. is not the main driver of orographic clouds. During this season, the hygropause moves to a higher altitude due to the higher temperatures (e.g. Fedorova et al., 2021). As a result, the vertical transport of water motivated by thermal slope winds on mountains does not reach the hygropause efficiently. Instead, at this season and latitude, the main mechanism behind orographic cloud formation involves gravity waves reaching the hygropause. (see section 4 of Hernández-Bernal et al. 2022a, and the supporting material of that paper, with animated videos S1 and S2 showing orographic cloud dynamics).

#### 4.2.2. The Arsia Mons Elongated Cloud (AMEC)

The AMEC takes place next to Arsia Mons during the dusty season (Ls ~220°-320°) on a daily basis, only during the early morning. The cloud is already present at sunrise, when it starts its expansion to the west, reaching a length of up to 1800 km in only about 3 hours. The cloud consists of a head, which is the cloud formation area, next to Arsia Mons, and a tail, which is the result of the expansion. According to observations, the AMEC develops around 45km over the local areoid. The whole cloud dissipates before afternoon, when afternoon sun-synchronous orbiters observe (see section 2.1.8).

Meteorological phenomena on Mars studied with Mars Express VMC images.

Around a thousand images, mostly taken by VMC, were used in the study of the AMEC. The archives of all the imagers with the ability to observe during the early morning were checked, and the observational study of the AMEC included images from 6 different instruments with this ability: VMC, HRSC, and OMEGA onboard Mars Express, IUVS onboard MAVEN, MCC onboard MOM, and the visible camera onboard Viking 2. MRO/MARCI images of Arsia Mons in the afternoon were used as complement to the images acquired during the morning. Figure 32 provides a visual summary of the study reported in **Hernández-Bernal et al. (2021a)**.

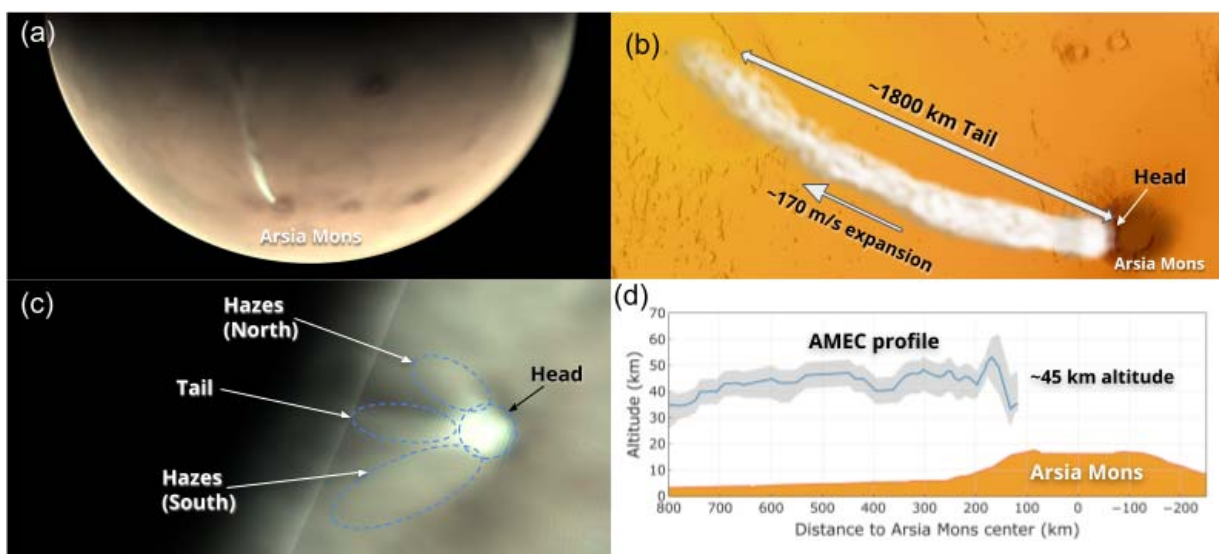


Figure 32. Visual summary of the characteristics of the AMEC as concluded by Hernández-Bernal et al. (2021a). Reproduced from figure 1 in Hernández-Bernal et al. (2022a).

The study of the physical mechanisms behind the AMEC (**Hernández-Bernal et al., 2022a**) is based on GCM and mesoscale simulations using LMD models (Forget et al., 1999; Spiga and Forget, 2009). The models show that the local circulation of winds around Arsia Mons during the morning in the AMEC season produces a strong gravity wave that propagates vertically and leads to the formation of a cold pocket at an altitude of ~45 km where temperatures are down to 30K below the environment temperature (Figure 33). This cold pocket is coincident in space and time with the observed head of the AMEC. However, cloud formation within this cold pocket is not as intense as in observations, and the tail of the AMEC is not reproduced by the model.

In the mechanism shown by Michaels et al., water lifted to the higher atmosphere can be advected horizontally by winds to different areas where condensation conditions are still

## Meteorological phenomena on Mars studied with Mars Express VMC images.

met. However, the AMEC is not formed because water vapor is lifted to a colder atmospheric layer, but because the preexisting water vapor traverses a cold pocket where it condenses. The tail would then form by advection of the water ice formed in the cold pocket. This hints to some unexplained microphysics that might be the cause of the extreme elongation of the AMEC, driven by advection. The full theoretical study of the AMEC is reported in Hernández-Bernal et al. (2022a).

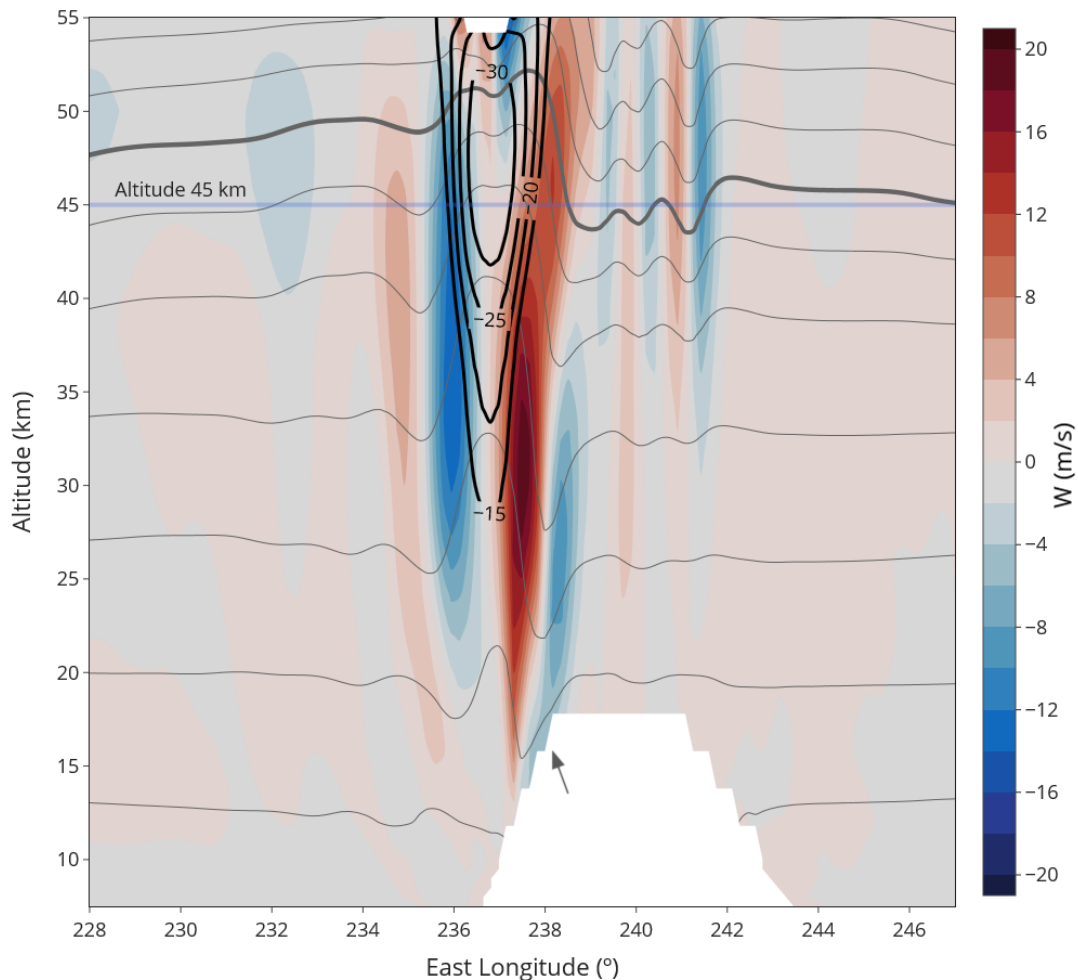


Figure 33. Atmospheric perturbations caused by Arsia Mons in the mesoscale model at 7.6 LT at latitude 8.7°S. Background shade represents vertical winds in m/s (scale at right). Gray curves are potential temperature contours, which correspond to streamlines, with zonal winds blowing westward (i.e. from right to left in this graph). The thick gray curve departing at 45 km shows that there is a positive vertical displacement after the head of the cloud. Thick black contours indicate the area where the temperature is lower than the mean for a given altitude, from -15K to -30K. A horizontal blue line indicates 45km in altitude for



Meteorological phenomena on Mars studied with Mars Express VMC images.

comparison with latter figures. The arrow in the mountain indicates the lee side downslope windstorm. Reproduced from Hernández-Bernal et al. (2022a)

#### 4.2.3. Near CO<sub>2</sub> condensation temperatures in the AMEC

The lowest temperatures predicted by the model in the core of the cold pocket are only a few degrees over CO<sub>2</sub> condensation (figure 34). And mesospheric temperatures in the LMD GCM tend to be higher than actual ones (González-Galindo et al., 2011; Määttä et al., 2022). Taking this into consideration, we can conclude that sub CO<sub>2</sub> condensation temperatures might be reached occasionally or even always in the core cold pocket of the AMEC. Following the conclusions from Määttä et al. (2022), the abundant water ice crystals might act as condensation nuclei for CO<sub>2</sub>, and therefore CO<sub>2</sub> condensates might be present in the AMEC.

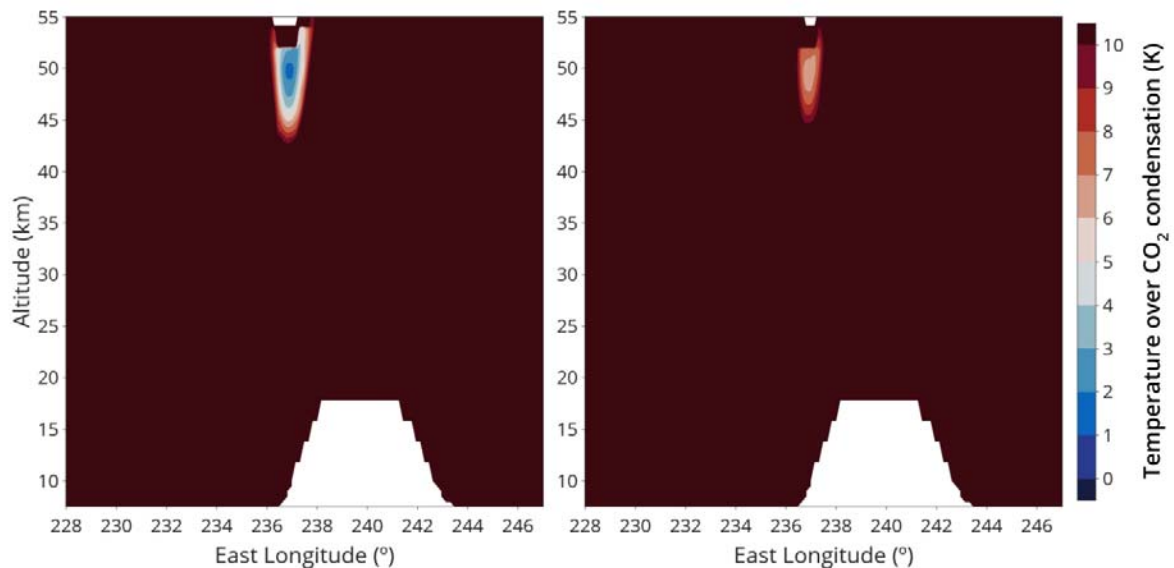


Figure 34. CO<sub>2</sub> condensation conditions in the head of the AMEC. The difference between the temperature of each cell and the CO<sub>2</sub> condensation temperature is represented. Left and right panels correspond respectively to sol 2 and sol 3 in the simulation. Condensation temperature has been computed taking into account the atmospheric pressure of each cell and using the formula given by Sefton-Nash et al. (2013). Both graphs follow a format similar to that of figure 33, for the local time 8.05, when the lowest temperatures are reached (figure 8c in Hernández-Bernal et al., 2022a)

#### 4.2.4. Is the AMEC one of a kind?

Different observations reveal that other clouds resembling the AMEC are present on Mars. Clancy et al. (2009; 2021) have reported observations of “Perihelion Cloud Trails” (PCTs)

Meteorological phenomena on Mars studied with Mars Express VMC images.

around afternoon in the perihelion season, which strongly resemble the aspect and physical characteristics of the AMEC. Viking 2 observed a bright long cloud in sunrise departing from Ascræus Mons in the aphelion season. And VMC observations keep revealing clouds that resemble the AMEC (e.g. figure 35c and 35d).

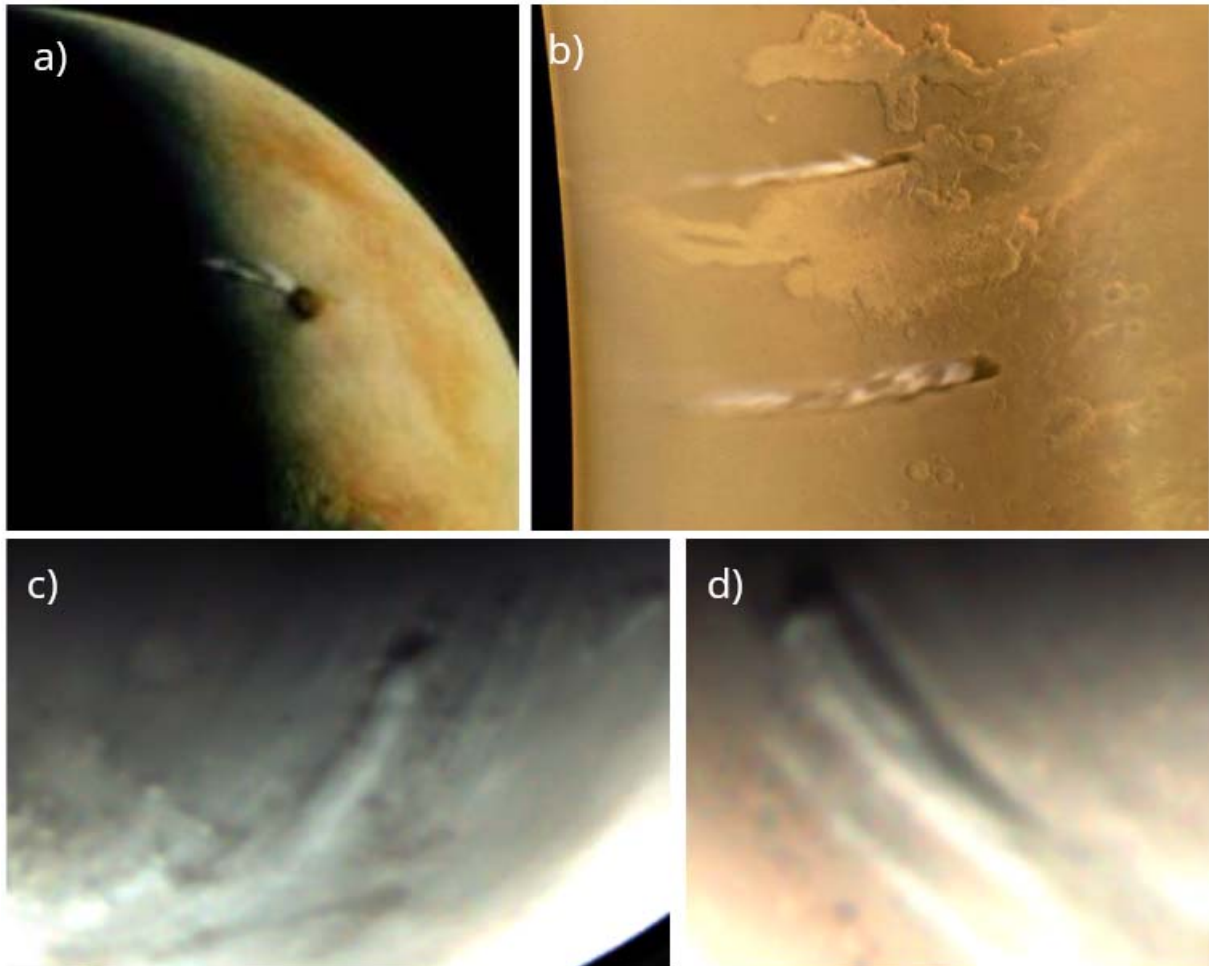


Figure 35. Examples of observed long clouds resembling the AMEC. (a) In Ascræus Mons observed by Viking 2 around aphelion. (b) Near Valles Marineris, adapted from Clancy et al. (2009). (c) In Thaumasia Highlands, observed by VMC in the aphelion season. (d) In Lyot crater, observed by VMC at the end of the dusty season.

Are all the physical mechanisms of these clouds related? A detailed comprehensive observational analysis is yet to be done. So far, only the AMEC and the PCTs have been analyzed in detail and it is clear that the PCTs and the AMEC share several physical parameters (similar altitude, shape, expansion speed, latitude, and season). However, VMC observations reveal other clouds of similar aspect at different latitudes and seasons, where the altitude of the hygropause is different. In those cases, the formation of water ice by

vertical transport of water as in Michaels et al. (2006; see section 4.2.1) could be a simpler explanation to the formation of the cloud when the hygropause is low enough.

Plumes observed during the aphelion season in the western slopes of Tharsis volcanoes were reproduced in the simulations by Michaels et al. (2006). In their mechanism, water is lifted to the higher atmosphere, where it condenses due to the lower temperatures. The formed cloud is then advected by winds that form a long plume that extends over a region in which condensation conditions are still met. However, these plumes exhibit shapes which are more irregular than those observed in the elongated clouds displayed in figure 35.

The striking aspect shared by all the clouds discussed here is the elongated tail, and often a differentiated head is visible. The origin of the tail of the AMEC remains a mystery that was not solved in Hernández-Bernal et al. (2022a). The physics behind the formation of tails might or might not be the same in different seasons, latitudes, and maybe even different altitudes. A detailed study of all these observations may provide new keys to the understanding of this phenomenon.

In conclusion, clouds resembling the AMEC are observed widespread on Mars. There is no simple explanation for the elongated tail of the AMEC, because it forms in a cold pocket when the hygropause is very high. The hygropause is also high in the PCTs, but other observed clouds occur with a lower hygropause, in which case the vertical transport of water as in Michaels et al. could provide a simpler explanation. Nevertheless, it is not clear whether such a process can explain the well defined borders of the elongated clouds discussed here.

Finally, it is worth mentioning that while the AMEC repeats regularly every sol for a long season, these other clouds are more difficult to predict, making it harder to plan observations dedicated to them.

### 4.3. Mesospheric clouds, observing the twilight

High altitude clouds can receive sunlight even during the twilight transition, while the surface below them is in the darkness. These clouds, called noctilucent clouds, are rare on Earth where they form essentially over the polar regions. High altitude clouds on Mars are common and have been observed by orbiters for decades, mostly in limb observations (see section 2.1.6).

Meteorological phenomena on Mars studied with Mars Express VMC images.

High altitude clouds on Mars observed in twilight were probably observed for the first time in the 1890s, when some ground-based observers reported bright patches in the dark side of the terminator (Holden et al., 1890; 1894; Campbell, 1894; Douglass, 1895; 1897).

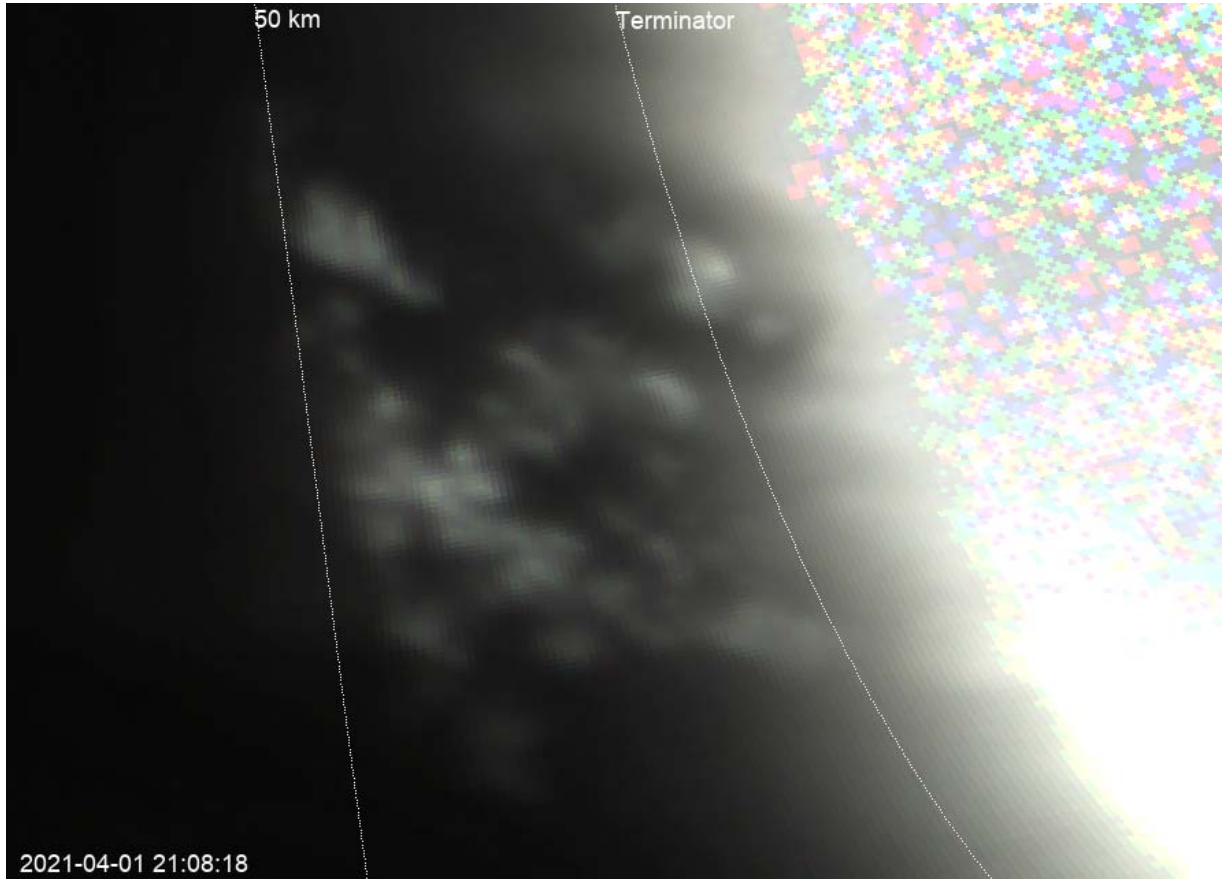


Figure 36. Some clouds observed in twilight by VMC. The distance from the terminator is an indicator of the minimum altitude of the cloud (see also Figure 1 in Hernández-Bernal et al., 2021b). In this case, the clouds are appearing in parallel to the curve indicating 50km, and the observation was a video, which enables the exact determination of the altitude of the clouds.

Modern observers of clouds in twilight include the Hubble Space Telescope (James et al., 1996), the THEMIS instrument on board Mars Odyssey (Inada et al., 2007; McConnochie et al., 2010), and the IUVS instrument on board the MAVEN orbiter (Connour et al., 2020). Other orbiters have observed clouds in twilight (MOM and more recently HOPE) but these observations have not yet been reported in the literature.

From the apocenters of the non-sun-synchronous elliptical orbit of Mars Express, VMC is a privileged observer of the twilight. Its archive includes thousands of images. As part of this

Meteorological phenomena on Mars studied with Mars Express VMC images.

thesis, such VMC capability has been exploited, and the first systematic study of clouds in twilight has been performed, as reported in **Hernández-Bernal et al. (2021b)**, which is the paper to which this subsection is dedicated.

Observing clouds in twilight provides some advantages.

- The minimum cloud altitude can be calculated, and in some cases it is also possible to determine the constrained altitude (see figure 36 here and figure 1 in Hernández-Bernal et al., 2021b)
- Due to the dark background, thin clouds directly illuminated by the sun can be easily detected.

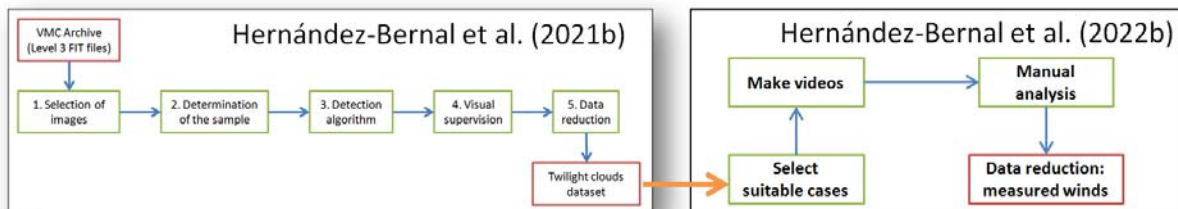


Figure 37. Scheme of the pipelines developed for the work with clouds in twilight in the context of this thesis, note that Hernández-Bernal et al. (2022b) is a congress abstract referring to ongoing work.

#### 4.3.1. A systematic study of clouds in twilight

Left panel in figure 37 is the diagram of the software developed to analyze VMC images and detect clouds in twilight. 407 clouds were detected in a dataset including 1891 independent observations between November 2007 and June 2020. These clouds were archived together with their parameters (longitude, latitude, timestamp, MY, Ls, minimum altitude...).

Second order effects (parallax, non-spherical shape of the planet) can have an effect in the estimation of the cloud altitudes. And thus an algorithm to correct these effects was developed (figure 37). The details are explained in the supporting information of Hernández-Bernal et al. (2021b).

The most relevant results of this work are shown in figure 38 (reproduced from figure 4 in the paper), which displays detected clouds in terms of Solar Longitude (Ls) and Latitude.

Meteorological phenomena on Mars studied with Mars Express VMC images.

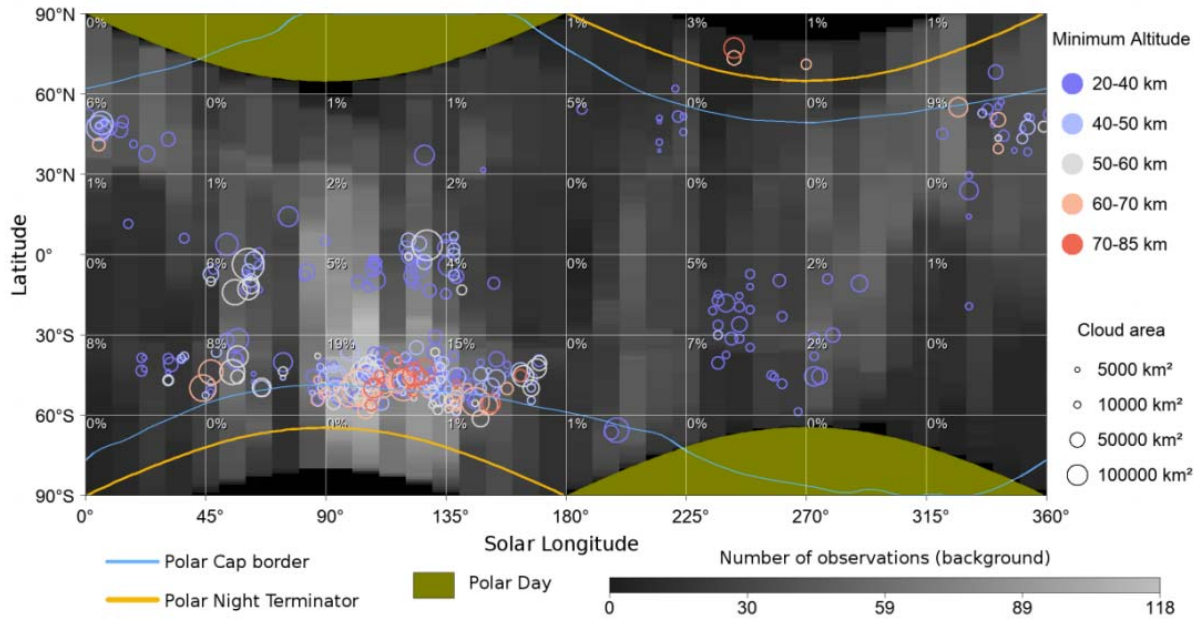


Figure 38. Seasonal distribution of clouds in twilight. Reproduced for quick reference from Hernández-Bernal et al., (2021b)

Figure 38 displays some interesting trends. A large concentration of clouds is present in southern midlatitudes (30°S-60°S) during the southern spring and summer. An analogue but smaller concentration of clouds is also present in the northern midlatitudes in Ls ~320°-30°. These trends were already hinted in early studies on clouds in the mesosphere (Määttä et al., 2013, their figure 6a). In the southern midlatitudes, a couple of CO<sub>2</sub> clouds were detected by MEX/HRSC and MEX/OMEGA and reported by Montmessin et al. (2007) and Määttä et al. (2010). In northern midlatitudes, ODY/THEMIS detected high altitude clouds, as reported by McConnochie et al., 2010). In all the cases, the observations took place near twilight.

Moreover, OMEGA observed some clouds in the morning twilight in southern midlatitudes in March 2016, which were confirmed to be made of water ice (Brigitte Gondet, personal communication).

More recent studies have led to results that keep hinting these trends. Stevens et al. (2017) have used MAVEN/IUVS data to detect mesospheric clouds between 5 and 11 AM, and they found a concentration in the East of Hellas in the same season as the one in Figure 38. Figure 3 in Hernández-Bernal et al. (2021b) displays the distribution of detected clouds in terms of latitude and longitude; indeed, the East of Hellas is one of the most populated areas. Liuzzi et al. (2021) have investigated the distribution of CO<sub>2</sub> clouds using

Meteorological phenomena on Mars studied with Mars Express VMC images.

TGO/NOMAD and using Solar Occultation (which is equivalent to observations in twilight in terms of local time and altitude). They set the East of Hellas as one of their regions of interest (following the results of Stevens et al.), and they found CO<sub>2</sub> clouds there. They also found one CO<sub>2</sub> cloud in northern midlatitudes.

VMC observations do not allow determination of cloud composition. As concluded in Hernández-Bernal et al. (2021b), most of the clouds observed in twilight with VMC are likely to be condensates, and it is a fact that both water ice and CO<sub>2</sub> clouds have been observed in coincidence with the two midlatitude belts observed by VMC and reported as part of this thesis. Considering the recent results by Määttä et al. (2022), in which they reproduce new CO<sub>2</sub> clouds in a GCM by enabling water ice crystals to act as condensation nuclei for CO<sub>2</sub>, it is possible that both water ice and CO<sub>2</sub> are present in the midlatitude mesospheric clouds observed in twilight. Of course, the presence of CO<sub>2</sub> clouds could depend on the season and be subject to strong sol-to-sol variations.

#### 4.3.2. Mesospheric cloud tracking in twilight

The ability of VMC to acquire videos can be exploited to perform cloud tracking in twilight. This is a natural extension of the first work on clouds in twilight. Only a few direct measurements of mesospheric cloud movement have been previously reported using stereo observations by MEX/HRSC and ODY/THEMIS (Määttä et al., 2010; McConnochie et al., 2010; Scholten et al., 2010).

In order to perform cloud tracking on mesospheric clouds seen in twilight over VMC data, we need observations long enough to allow cloud tracking within the observation and exact cloud altitude determination. To identify those observations, a new pipeline has been developed, shown schematically in figure 37. This pipeline makes videos of clouds moving in cases when the observation is long enough to make a video. Only those cases in which the cloud was seen appearing from the night (as in figure 36), and exact cloud altitude can be determined are considered. In the end, only 25 videos gather all the needs of this study.

Cloud tracking is performed manually and uncertainties are estimated from the pixel resolution and the temporal resolution (typically 300s, because only high exposure images show these clouds clearly).

This is an ongoing work and only preliminary results have been reported in the European Planetary Science Congress (EPSC 2022; Hernández-Bernal et al., 2022b).

Meteorological phenomena on Mars studied with Mars Express VMC images.

## 5. References

- Acton Jr, C. H. (1996). Ancillary data services of NASA's navigation and ancillary information facility. *Planetary and Space Science*, 44(1), 65-70.
- Acton, C., Bachman, N., Semenov, B., & Wright, E. (2018). A look towards the future in the handling of space science mission geometry. *Planetary and Space Science*, 150, 9-12.
- Allison, M. (1997). Accurate analytic representations of solar time and seasons on Mars with applications to the Pathfinder/Surveyor missions. *Geophysical Research Letters*, 24(16), 1967-1970.
- Allison, M., & McEwen, M. (2000). A post-Pathfinder evaluation of areocentric solar coordinates with improved timing recipes for Mars seasonal/diurnal climate studies. *Planetary and Space Science*, 48(2-3), 215-235.
- Anderson, E., & Leovy, C. (1978). Mariner 9 television limb observations of dust and ice hazes on Mars. *Journal of Atmospheric Sciences*, 35(4), 723-734.
- Aoki, S., Sato, Y., Giuranna, M., Wolkenberg, P., Sato, T. M., Nakagawa, H., & Kasaba, Y. (2018). Mesospheric CO<sub>2</sub> ice clouds on Mars observed by planetary Fourier spectrometer onboard Mars Express. *Icarus*, 302, 175-190.
- Arya, A. S., Sarkar, S. S., Srinivas, A. R., Moorthi, S. M., Patel, V. D., Singh, R. B., ... & Kumar, A. K. (2015). Mars Colour Camera: the payload characterization/calibration and data analysis from Earth imaging phase. *Current Science*, 109(1076), 1076-1086.
- Barnes, J. R., Haberle, R. M., Wilson, R. J., Lewis, S., Murphy, J. R., & Read, P. L. (2017). The global circulation.
- Bell III, J. F., Wolff, M. J., Malin, M. C., Calvin, W. M., Cantor, B. A., Caplinger, M. A., ... & Thomas, P. C. (2009). Mars reconnaissance orbiter Mars color imager (MARCI): instrument description, calibration, and performance. *Journal of Geophysical Research: Planets*, 114(E8).



Meteorological phenomena on Mars studied with Mars Express VMC images.

Benson, J. L., Bonev, B. P., James, P. B., Shan, K. J., Cantor, B. A., & Caplinger, M. A. (2003). The seasonal behavior of water ice clouds in the Tharsis and Valles Marineris regions of Mars: Mars Orbiter Camera observations. *Icarus*, 165(1), 34-52.

Benson, J. L., James, P. B., Cantor, B. A., & Remigio, R. (2006). Interannual variability of water ice clouds over major Martian volcanoes observed by MOC. *Icarus*, 184(2), 365-371.

Bibring, J. P., Soufflot, A., Berthé, M., Langevin, Y., Gondet, B., Drossart, P., ... & Forget, F. (2004, August). OMEGA: Observatoire pour la Minéralogie, l'Eau, les Glaces et l'Activité. In *Mars Express: the scientific payload* (Vol. 1240, pp. 37-49).

Cantor, B. A. (2007). MOC observations of the 2001 Mars planet-encircling dust storm. *Icarus*, 186(1), 60-96.

Clancy, R. T., Grossman, A. W., Wolff, M. J., James, P. B., Rudy, D. J., Billawala, Y. N., ... & Muhleman, D. O. (1996). Water vapor saturation at low altitudes around Mars aphelion: A key to Mars climate?. *Icarus*, 122(1), 36-62.

Clancy, R. T., Sandor, B. J., Wolff, M. J., Christensen, P. R., Smith, M. D., Pearl, J. C., ... & Wilson, R. J. (2000). An intercomparison of ground-based millimeter, MGS TES, and Viking atmospheric temperature measurements: Seasonal and interannual variability of temperatures and dust loading in the global Mars atmosphere. *Journal of Geophysical Research: Planets*, 105(E4), 9553-9571.

Clancy, R. T., Montmessin, F., Benson, J., Daerden, F., Colaprete, A., & Wolff, M. J. (2017). Mars clouds. *The atmosphere and climate of Mars* (pp. 42-75)

Clancy, R. T., Wolff, M. J., Smith, M. D., Kleinböhl, A., Cantor, B. A., Murchie, S. L., ... & Sandor, B. J. (2019). The distribution, composition, and particle properties of Mars mesospheric aerosols: An analysis of CRISM visible/near-IR limb spectra with context from near-coincident MCS and MARCI observations. *Icarus*, 328, 246-273.

Connour, K., Schneider, N. M., Milby, Z., Forget, F., Alhosani, M., Spiga, A., ... & Wolff, M. J. (2020). Mars's twilight cloud band: A new cloud feature seen during the Mars Year 34 global dust storm. *Geophysical Research Letters*, 47(1), e2019GL084997.

## Meteorological phenomena on Mars studied with Mars Express VMC images.

Fedorova, A., Montmessin, F., Korablev, O., Lefèvre, F., Trokhimovskiy, A., & Bertaux, J. L. (2021). Multi-annual monitoring of the water vapor vertical distribution on Mars by SPICAM on Mars Express. *Journal of Geophysical Research: Planets*, 126(1), e2020JE006616.

Fergason, R. L., Hare, T. M., & Laura, J. (2018). HRSC and MOLA Blended Digital Elevation Model at 200m v2. *Astrogeology PDS Annex*, U.S. Geological Survey. [http://bit.ly/HRSC\\_MOLA\\_Blend\\_v0](http://bit.ly/HRSC_MOLA_Blend_v0)

Forget, F., Hourdin, F., Fournier, R., Hourdin, C., Talagrand, O., Collins, M., ... & Huot, J. P. (1999). Improved general circulation models of the Martian atmosphere from the surface to above 80 km. *Journal of Geophysical Research: Planets*, 104(E10), 24155-24175.

González-Galindo, F., Määttänen, A., Forget, F., & Spiga, A. (2011). The martian mesosphere as revealed by CO<sub>2</sub> cloud observations and general circulation modeling. *Icarus*, 216(1), 10-22.

Hernández-Bernal, J., Sánchez-Lavega, A., del Río-Gaztelurrutia, T., Hueso, R., Cardesín-Moinelo, A., Ravanis, E. M., ... & Wood, S. (2019). The 2018 Martian global dust storm over the South Polar Region studied with MEx/VMC. *Geophysical Research Letters*, 46(17-18), 10330-10337.

Hernández-Bernal, J., Sánchez-Lavega, A., del Río-Gaztelurrutia, T., Ravanis, E., Cardesín-Moinelo, A., Connour, K., ... & Hauber, E. (2021a). An extremely elongated cloud over Arsia Mons volcano on Mars: I. Life cycle. *Journal of Geophysical Research: Planets*, 126(3), e2020JE006517.

Hernández-Bernal, J., Sánchez-Lavega, A., del Río-Gaztelurrutia, T., Hueso, R., Ravanis, E., Cardesín-Moinelo, A., ... & Titov, D. (2021b). A Long-Term Study of Mars Mesospheric Clouds Seen at Twilight Based on Mars Express VMC Images. *Geophysical Research Letters*, 48(7), e2020GL092188.

Hernández-Bernal, J., Sánchez-Lavega, A., Del Río-Gaztelurrutia, T., Hueso, R., Cardesín-Moinelo, A., de la Parra, J. M. Y., ... & Titov, D. (2021c). Looking for Meteors and Fireballs in the atmosphere of Mars from the Visual Monitoring Camera (VMC) on Mars Express (No. EPSC2021-515). *Copernicus Meetings*.

Meteorological phenomena on Mars studied with Mars Express VMC images.

Hernández-Bernal, J., Spiga, A., Sánchez-Lavega, A., Río-Gaztelurrutia, T. D., Forget, F., & Millour, E. (2022a) An Extremely Elongated Cloud over Arsia Mons Volcano on Mars: II. Mesoscale modeling. *Journal of Geophysical Research: Planets*, e2022JE007352.

Hernández-Bernal, J., Sánchez Lavega, A., del Río Gaztelurrutia, T., Hueso Alonso, R., and Cardesín Moinelo, A. (2022b) Cloud tracking and dynamics of Martian mesospheric clouds in twilight as seen by MEX/VMC, Europlanet Science Congress 2022, Granada, Spain, 18–23 Sep 2022, EPSC2022-456, <https://doi.org/10.5194/epsc2022-456>

James, P. B., Bell III, J. F., Clancy, R. T., Lee, S. W., Martin, L. J., & Wolff, M. J. (1996). Global imaging of Mars by Hubble Space Telescope during the 1995 opposition. *Journal of Geophysical Research: Planets*, 101(E8), 18883-18890.

Jaumann, R., Neukum, G., Behnke, T., Duxbury, T. C., Eichertopf, K., Flohrer, J., ... & HRSC Co-Investigator Team. (2007). The high-resolution stereo camera (HRSC) experiment on Mars Express: Instrument aspects and experiment conduct from interplanetary cruise through the nominal mission. *Planetary and Space Science*, 55(7-8), 928-952.

Kahre, M. A., Murphy, J. R., Newman, C. E., Wilson, R. J., Cantor, B. A., Lemmon, M. T., & Wolff, M. J. (2017). The Mars dust cycle. *The atmosphere and climate of Mars*, 18, 295.

Kass, D. M., Kleinböhl, A., McCleese, D. J., Schofield, J. T., & Smith, M. D. (2016). Interannual similarity in the Martian atmosphere during the dust storm season. *Geophysical Research Letters*, 43(12), 6111-6118.

Liou, K.N. (2002). Chapter 2 - Solar Radiation at the Top of the Atmosphere. In *An Introduction to Atmospheric Radiation*. [https://doi.org/10.1016/S0074-6142\(02\)80017-1](https://doi.org/10.1016/S0074-6142(02)80017-1)

Liuzzi, G., Villanueva, G. L., Trompet, L., Crismani, M. M., Piccialli, A., Aoki, S., ... & Vandaele, A. C. (2021). First detection and thermal characterization of terminator CO<sub>2</sub> ice clouds with ExoMars/NOMAD. *Geophysical Research Letters*, 48(22), e2021GL095895.

Määttänen, A., Montmessin, F., Gondet, B., Scholten, F., Hoffmann, H., González-Galindo, F., ... & Bertaux, J. L. (2010). Mapping the mesospheric CO<sub>2</sub> clouds on Mars: MEx/OMEGA and MEx/HRSC observations and challenges for atmospheric models. *Icarus*, 209(2), 452-469.

Meteorological phenomena on Mars studied with Mars Express VMC images.

Määttänen, A., Pérot, K., Montmessin, F., & Hauchecorne, A. (2013). Mesospheric clouds on Mars and on Earth. *Comparative climatology of terrestrial planets*, 393-413.

Määttänen, A., Mathé, C., Audouard, J., Listowski, C., Millour, E., Forget, F., ... & Montmessin, F. (2022). Troposphere-to-mesosphere microphysics of carbon dioxide ice clouds in a Mars Global Climate Model. *Icarus*, 115098.

Madeleine, J. B., Forget, F., Millour, E., Montabone, L., & Wolff, M. J. (2011). Revisiting the radiative impact of dust on Mars using the LMD Global Climate Model. *Journal of Geophysical Research: Planets*, 116(E11).

Maltagliati, L., Montmessin, F., Fedorova, A., Korablev, O., Forget, F., & Bertaux, J. L. (2011). Evidence of water vapor in excess of saturation in the atmosphere of Mars. *science*, 333(6051), 1868-1871.

McClintock, W. E., Schneider, N. M., Holsclaw, G. M., Clarke, J. T., Hoskins, A. C., Stewart, I., ... & Deighan, J. (2015). The imaging ultraviolet spectrograph (IUVS) for the MAVEN mission. *Space Science Reviews*, 195(1), 75-124.

McConnochie, T. H., Bell III, J. F., Savransky, D., Wolff, M. J., Toigo, A. D., Wang, H., ... & Christensen, P.R. (2010). THEMIS-VIS observations of clouds in the martian mesosphere: Altitudes, wind speeds, and decameter-scale morphology. *Icarus*, 210(2), 545-565.

Merritt, D. R., Cardesin Moinelo, A., Marin Yaseli de la Parra, J., Breitfellner, M., Blake, R., Castillo Fraile, M., ... & Titov, D. (2018). Mars Express Science Operations During Deep Eclipse: An Example of Adapting Science Operations On Aging Spacecraft. In *2018 SpaceOps Conference* (p. 2354).

Michaels, T. I., Colaprete, A., & Rafkin, S. C. R. (2006). Significant vertical water transport by mountain-induced circulations on Mars. *Geophysical Research Letters*, 33(16).

Millour, E., Forget, F., Spiga, A., Vals, M., Zakharov, V., & Montabone, L. (2018). Mars climate database. In *From Mars Express to ExoMars*, 27-28 February 2018, Madrid, Spain.

Montabone, L., Forget, F., Millour, E., Wilson, R.J., Lewis, S.R., Cantor, B., Kass, D., Kleinböhl, A., Lemmon, M.T., Smith, M.D., Wolff, M.J., Eight-year Climatology of Dust Optical Depth on Mars. *Icarus* 251, pp. 65-95 (2015), doi: <https://doi.org/10.1016/j.icarus.2014.12.034>

Meteorological phenomena on Mars studied with Mars Express VMC images.

Montabone, L., Spiga, A., Kass, D. M., Kleinböhl, A., Forget, F., Millour, E., Martian Year 34 Column Dust Climatology from Mars Climate Sounder Observations: Reconstructed Maps and Model Simulations. *J. Geophys. Res. - Planets* (2020), doi: <https://doi.org/10.1029/2019JE006111>

Montmessin, F., Bertaux, J. L., Quémerais, E., Korablev, O., Rannou, P., Forget, F., ... & Dimarellis, E. (2006). Subvisible CO<sub>2</sub> ice clouds detected in the mesosphere of Mars. *Icarus*, 183(2), 403-410.

Montmessin, F., Gondet, B., Bibring, J. P., Langevin, Y., Drossart, P., Forget, F., & Fouchet, T. (2007). Hyperspectral imaging of convective CO<sub>2</sub> ice clouds in the equatorial mesosphere of Mars. *Journal of Geophysical Research: Planets*, 112(E11).

Montmessin, F., Smith, M. D., Langevin, Y., Mellon, M. T., & Fedorova, A. (2017). The water cycle. *The atmosphere and climate of Mars*, 18, 338.

Navarro, T., Madeleine, J. B., Forget, F., Spiga, A., Millour, E., Montmessin, F., & Määttänen, A. (2014). Global climate modeling of the Martian water cycle with improved microphysics and radiatively active water ice clouds. *Journal of Geophysical Research: Planets*, 119(7), 1479-1495.

Ordonez-Etxeberria, I., Hueso, R., & Sánchez-Lavega, A. (2018). A systematic search of sudden pressure drops on Gale crater during two Martian years derived from MSL/REMS data. *Icarus*, 299, 308-330.

Ormston, T., Denis, M., Scuka, D., & Griebel, H. (2011). An ordinary camera in an extraordinary location: Outreach with the Mars Webcam. *Acta Astronautica*, 69(7-8), 703-713.

Piqueux, S., Kleinböhl, A., Hayne, P. O., Kass, D. M., Schofield, J. T., & McCleese, D. J. (2015). Variability of the Martian seasonal CO<sub>2</sub> cap extent over eight Mars Years. *Icarus*, 251, 164-180.

Rafkin, S. C., & Michaels, T. I. (2002). Simulation of the atmospheric thermal circulation of a martian volcano using a mesoscale numerical model. *Nature*, 419(6908), 697-699.

## Meteorological phenomena on Mars studied with Mars Express VMC images.

Ravanis, E. M., Cardesín-Moinelo, A., Hernández Bernal, J., Almeida, M., Wood, S., Sánchez-Lavega, A., ... & Martin, P. (2019). Mars Express Visual Monitoring Camera: New Operations and Data Processing for more Science. EPSC2019, 15-20.

Ravanis, E., Hernández-Bernal, J., Cardesín-Moinelo, A., Sánchez-Lavega, A., del Río-Gaztelurrutia, T., Hueso, R., ... & Martin, P. (2020). From engineering to science: Mars Express Visual Monitoring Camera's first science data release (No. EPSC2020-437). Copernicus Meetings.

del Río-Gaztelurrutia, T., Sánchez-Lavega, A., Hernández-Bernal, J., Angulo, A., Hueso, R., Cardesín-Moinelo, A., ... & Titov, D. (2021, April). Analysis of the evolution of Martian polar caps during Martian Years 34-35 from Mars Express Visual Monitoring Camera. In EGU General Assembly Conference Abstracts (pp. EGU21-7787).

Sagan, C., Veverka, J., & Gierasch, P. (1971). Observational consequences of Martian wind regimes. *Icarus*, 15(2), 253-278.

Sánchez-Lavega, A., Pérez-Hoyos, S., & Hueso, R. (2004). Clouds in planetary atmospheres: A useful application of the Clausius–Clapeyron equation. *American Journal of Physics*, 72(6), 767-774.

Sanchez-Lavega, A. (2010). *An introduction to planetary atmospheres*. CRC Press.

Sánchez-Lavega, A., Muñoz, A. G., Garcia-Melendo, E., Perez-Hoyos, S., Gomez-Forrellad, J. M., Pellier, C., ... & Peach, D. (2015). An extremely high-altitude plume seen at Mars' morning terminator. *Nature*, 518(7540), 525-528.

Sánchez-Lavega, A., Chen-Chen, H., Ordonez-Etxeberria, I., Hueso, R., del Rio-Gaztelurrutia, T., Garro, A., ... & Wood, S. (2018a). Limb clouds and dust on Mars from images obtained by the Visual Monitoring Camera (VMC) onboard Mars Express. *Icarus*, 299, 194-205.

Sánchez-Lavega, A., Garro, A., del Río-Gaztelurrutia, T., Hueso, R., Ordoñez-Etxeberria, I., Chen Chen, H., ... & Gondet, B. (2018b). A seasonally recurrent annular cyclone in Mars northern latitudes and observations of a companion vortex. *Journal of Geophysical Research: Planets*, 123(11), 3020-3034.

Meteorological phenomena on Mars studied with Mars Express VMC images.

Sánchez-Lavega, A., del Río-Gaztelurrutia, T., Hernández-Bernal, J., & Delcroix, M. (2019). The onset and growth of the 2018 Martian global dust storm. *Geophysical Research Letters*, 46(11), 6101-6108.

Sánchez-Lavega, A., Erkoreka, A., Hernández-Bernal, J., del Río-Gaztelurrutia, T., García-Morales, J., Ordoñez-Etxeberría, I., ... & Matz, K. D. (2022a). Cellular patterns and dry convection in textured dust storms at the edge of Mars North Polar Cap. *Icarus*, 387, 115183.

Sanchez-Lavega, A., Larsen, E., Hernandez-Bernal, J., del Río-Gaztelurrutia, T., Ordoñez-Etxeberría, I., Ordorika, J., and Cardesín-Moinelo, A. (2022b): Atmospheric disturbances imaged on Mars during the simultaneous operations of four surface stations along 2021 and 2022, Europlanet Science Congress 2022, Granada, Spain, 18–23 Sep 2022, EPSC2022-228, <https://doi.org/10.5194/epsc2022-228>, 2022.

Schofield, J. T., Barnes, J. R., Crisp, D., Haberle, R. M., Larsen, S., Magalhaes, J. A., ... & Wilson, G. (1997). The Mars Pathfinder atmospheric structure investigation/meteorology (ASI/MET) experiment. *Science*, 278(5344), 1752-1758.

Scholten, F., Hoffmann, H., Määttä, A., Montmessin, F., Gondet, B., & Hauber, E. (2010). Concatenation of HRSC colour and OMEGA data for the determination and 3D-parameterization of high-altitude CO<sub>2</sub> clouds in the Martian atmosphere. *Planetary and Space Science*, 58(10), 1207-1214.

Shaposhnikov, D. S., Medvedev, A. S., Rodin, A. V., & Hartogh, P. (2019). Seasonal water “pump” in the atmosphere of Mars: Vertical transport to the thermosphere. *Geophysical Research Letters*, 46(8), 4161-4169.

Skamarock, W. C., & Klemp, J. B. (2008). A time-split nonhydrostatic atmospheric model for weather research and forecasting applications. *Journal of computational physics*, 227(7), 3465-3485.

Smith, M. D. (2019). Local time variation of water ice clouds on Mars as observed by THEMIS. *Icarus*, 333, 273-282.

Smith, D. E., Sjogren, W. L., Tyler, G. L., Balmino, G., Lemoine, F. G., & Konopliv, A. S. (1999). The gravity field of Mars: results from Mars Global Surveyor. *Science*, 286(5437), 94-97.

Meteorological phenomena on Mars studied with Mars Express VMC images.

Smith, D. E., Zuber, M. T., Frey, H. V., Garvin, J. B., Head, J. W., Muhleman, D. O., ... & Sun, X. (2001). Mars Orbiter Laser Altimeter: Experiment summary after the first year of global mapping of Mars. *Journal of Geophysical Research: Planets*, 106(E10), 23689-23722.

Smith, M. D., Bougher, S. W., Encrenaz, T., Forget, F., & Kleinböhl, A. (2017). Thermal structure and composition. *The atmosphere and climate of Mars*, 18, 42.

Smith, S. A., & Smith, B. A. (1972). Diurnal and seasonal behavior of discrete white clouds on Mars. *Icarus*, 16(3), 509-521.

Spiga, A., González-Galindo, F., López-Valverde, M. Á., & Forget, F. (2012). Gravity waves, cold pockets and CO<sub>2</sub> clouds in the Martian mesosphere. *Geophysical Research Letters*, 39(2).

Stevens, M. H., Siskind, D. E., Evans, J. S., Jain, S. K., Schneider, N. M., Deighan, J., et al. (2017). Martian mesospheric cloud observations by IUVS on MAVEN: Thermal tides coupled to the upper atmosphere. *Geophysical Research Letters*, 44(10), 4709–4715. <https://doi.org/10.1002/2017GL072717>

Titus, T. N., Byrne, S., Colaprete, A., & Forget, F. (2017). The CO<sub>2</sub> Cycle. *The atmosphere and climate of Mars*, 18, 374.

Wang, H., & Ingersoll, A. P. (2002). Martian clouds observed by Mars global surveyor Mars orbiter camera. *Journal of Geophysical Research: Planets*, 107(E10), 8-1.

Wang, H., & Ingersoll, A. P. (2003). Cloud-tracked winds for the first Mars Global Surveyor mapping year. *Journal of Geophysical Research: Planets*, 108(E9).

Wellman, J. B., Landauer, F. P., Norris, D. D., & Thorpe, T. E. (1976). The Viking orbiter visual imaging subsystem. *Journal of Spacecraft and Rockets*, 13(11), 660-666.



Meteorological phenomena on Mars studied with Mars Express VMC images.

## Published works

### Lead author papers

Hernández-Bernal, J., Sánchez-Lavega, A., del Río-Gaztelurrutia, T., Hueso, R., Cardesín-Moinelo, A., Ravanis, E. M., ... & Wood, S. (2019). The 2018 Martian global dust storm over the South Polar Region studied with MEx/VMC. *Geophysical Research Letters*, 46(17-18), 10330-10337.

Hernández-Bernal, J., Sánchez-Lavega, A., del Río-Gaztelurrutia, T., Ravanis, E., Cardesín-Moinelo, A., Connour, K., ... & Hauber, E. (2021a). An extremely elongated cloud over Arsia Mons volcano on Mars: I. Life cycle. *Journal of Geophysical Research: Planets*, 126(3), e2020JE006517.

Hernández-Bernal, J., Sánchez-Lavega, A., del Río-Gaztelurrutia, T., Hueso, R., Ravanis, E., Cardesín-Moinelo, A., ... & Titov, D. (2021b). A Long-Term Study of Mars Mesospheric Clouds Seen at Twilight Based on Mars Express VMC Images. *Geophysical Research Letters*, 48(7), e2020GL092188.

Hernández-Bernal, J., Spiga, A., Sánchez-Lavega, A., Río-Gaztelurrutia, T. D., Forget, F., & Millour, E. (2022a) An Extremely Elongated Cloud over Arsia Mons Volcano on Mars: II. Mesoscale modeling. *Journal of Geophysical Research: Planets*, e2022JE007352.

### Coauthored papers

Sánchez-Lavega, A., del Río-Gaztelurrutia, T., Hernández-Bernal, J., & Delcroix, M. (2019). The onset and growth of the 2018 Martian global dust storm. *Geophysical Research Letters*, 46(11), 6101-6108.

Sánchez-Lavega, A., Erkoreka, A., Hernández-Bernal, J., del Río-Gaztelurrutia, T., García-Morales, J., Ordoñez-Etxeberría, I., ... & Matz, K. D. (2022). Cellular patterns and dry convection in textured dust storms at the edge of Mars North Polar Cap. *Icarus*, 387, 115183.

### Lead author contributions to congresses

Hernández-Bernal, J., Sánchez-Lavega, A., del Río-Gaztelurrutia, T., Hueso, R., Ravanis, E., Cardesín-Moinelo, A., ... & Titov, D. (2018). Clouds in the night side of Mars: an analysis using MarsExpress VMC (No. EPSC2018). Copernicus Meetings.

Hernández-Bernal, J., Sánchez-Lavega, A., Río-Gaztelurrutia, D., Hueso, R., Cardesín-Moinelo, A., Ravanis, E. M., ... & Almeida, M. D. (2019, January). The 2018 Martian Global-

Meteorological phenomena on Mars studied with Mars Express VMC images.

Scale Dust Storm over the South Pole studied with VMC onboard Mars Express. In Geophysical Research Abstracts (Vol. 21).

Hernández-Bernal, J., Sánchez-Lavega, A., Río-Gaztelurrutia, D., Hueso, R., Cardesín-Moinelo, A., Ravanis, E. M., ... & Almeida, M. D. (2019, May). The 2018 Martian Global Dust Storm over the Southern Polar Region. Reunión de Ciencias Planetarias y Exploración del Sistema Solar, Torrejón de Ardoz, Comunidad de Madrid, España.

Hernández-Bernal, J., Sánchez-Lavega, A., del Río-Gaztelurrutia, T., Hueso, R., Cardesín-Moinelo, A., Ravanis, E. M., ... & Wood, S. (2019, June) Atmospheric Science with the Visual Monitoring Camera onboard Mars Express: recent results. S-SAIL, Lisbon, Portugal.

Hernández-Bernal, J., Sánchez-Lavega, A., del Río-Gaztelurrutia, T., Hueso, R., Cardesín-Moinelo, A., Ravanis, E. M., ... & Hauber, E. (2019, September). Dynamics of the extremely elongated cloud on Mars Arsia Mons volcano. EPSC 2019, Geneve, Switzerland.

Hernández-Bernal, J., Sánchez-Lavega, A., Río-Gaztelurrutia, T., Hueso, R., I. Ordóñez-Etxeberria, Cardesín-Moinelo, A., Ravanis, E. M., ... & Gondet, B. (2020, April). Dynamics of the extremely elongated cloud on Mars Arsia Mons volcano. EGU 2020, online

Hernández-Bernal, J., Sánchez-Lavega, A., Río-Gaztelurrutia, T., Hueso, R., I. Ordóñez-Etxeberria, Cardesín-Moinelo, A., Ravanis, E. M., ... & Gondet, B. (2020, April). Dynamics of the extremely elongated cloud on Mars Arsia Mons volcano. Reunión Científica de la SEA 2020, online

Hernández-Bernal, J., Sánchez-Lavega, A., del Río-Gaztelurrutia, T., Hueso, R., Cardesín-Moinelo, A., Ravanis, E. M., ... & Titov D. (2020, September). A long term study of twilight clouds on Mars based on MarsExpress VMC images. EPSC 2020, online

Hernández-Bernal, J., Sánchez-Lavega, A., del Río-Gaztelurrutia, T., Hueso, R., Cardesín-Moinelo, A., Ravanis, E. M., ... & Titov D. (2020, September). A long term study of twilight clouds on Mars based on MarsExpress VMC images. AGU 2020, online

Hernández-Bernal, J., Sánchez-Lavega, A., Río-Gaztelurrutia (2021, April). Exploring de formation of the Arsia Mons Elongated Cloud on Mars. EGU 2021, online

Hernandez Bernal, J., Sánchez-Lavega, A., & Del Río-Gaztelurrutia, T. (2021, September). Exploring the formation of the Arsia Mons Elongated Cloud on Mars. In *European Planetary Science Congress* (pp. EPSC2021-487).

Hernández-Bernal, J., Sánchez-Lavega, A., Del Río-Gaztelurrutia, T., Hueso, R., Cardesín-Moinelo, A., de la Parra, J. M. Y., ... & Titov, D. (2021). Looking for Meteors and Fireballs in

Meteorological phenomena on Mars studied with Mars Express VMC images.

the atmosphere of Mars from the Visual Monitoring Camera (VMC) on Mars Express (No. EPSC2021-515). Copernicus Meetings.

Hernández-Bernal, J., Spiga, A., Sánchez-Lavega, A., Del Río-Gaztelurrutia, T., Forget, F., & Millour, E. (2022). *Mesoscale modeling of the Arsia Mons Elongated Cloud (AMEC) on Mars* (No. EGU22-8298). Copernicus Meetings.

Hernández-Bernal, J., Sánchez-Lavega, A., del Río-Gaztelurrutia, T., Spiga, A., Cardesín-Moinelo, A., Hueso, R., ... Wilson, C. (2022, September). Exploring the mysteries of the elongated cloud on the Arsia Mons volcano on Mars. Reunión Científica de la Sociedad Española de Astronomía, Tenerife

Hernández Bernal, J., Cardesín Moinelo, A., Hueso Alonso, R., Ravanis, E., Burgos Sierra, A., Wood, S., Marín Yaseli de la Parra, J., Merrit, D., costa Sitja, M., Escalante, A., Grotheer, E., Esquej, P., Dias Almeida, M., Martin, P., Titov, D., Wilson, C., del Río Gaztelurrutia, T., Sánchez Lavega, A., and Sierra, M.: The Visual Monitoring Camera on Mars Express: calibrating a new science instrument made from an old webcam orbiting Mars, Europlanet Science Congress 2022, Granada, Spain, 18–23 Sep 2022, EPSC2022-684, <https://doi.org/10.5194/epsc2022-684>, 2022.

Hernández-Bernal, J., Sánchez Lavega, A., del Río Gaztelurrutia, T., Hueso Alonso, R., and Cardesín Moinelo, A.: Cloud tracking and dynamics of Martian mesospheric clouds in twilight as seen by MEX/VMC, Europlanet Science Congress 2022, Granada, Spain, 18–23 Sep 2022, EPSC2022-456, <https://doi.org/10.5194/epsc2022-456>, 2022.

### **Coauthored contributions to congresses**

Grotheer, E., Barbarisi, I., Bentley, M., Besse, S., Breittellner, M., Cardesin-Moinelo, A., ... & Voelker, M. (2021, March). Using the ESA's Planetary Science Archive to Search for Mars Express VMC Data of an Elongated Cloud near Arsia Mons. In *52nd Lunar and Planetary Science Conference* (No. 2548, p. 1474).

Montabone, L., Heavens, N., Cardesín-Moinelo, A., François, F., Guzewich, S., Karatekin Ö., Lillis, R., ... Young, B. (2022). The case and approach for continuous, simultaneous, quasi-global weather monitoring on Mars. 44th COSPAR Scientific Assembly 2022

Montabone, L., Heavens, N.G., Pankine, A., Wolff, M., Cardesín-Moinelo, A., Geiger, B., ... Wilson, R.J. (2022) The case and approach for continuous, simultaneous, global Mars weather monitoring from orbit. Mars Atmosphere and Modelling 2022, París

Ravanis, E. M., Cardesín-Moinelo, A., Hernández Bernal, J., Almeida, M., Wood, S., Sánchez-Lavega, A., ... & Martin, P. (2019). Mars Express Visual Monitoring Camera: New Operations and Data Processing for more Science. *EPSC2019*, 15-20.

Meteorological phenomena on Mars studied with Mars Express VMC images.

Ravanis, E., Hernández-Bernal, J., Cardesín-Moinelo, A., Sánchez-Lavega, A., del Río-Gaztelurrutia, T., Hueso, R., ... & Martin, P. (2020, May). The Webcam around Mars: Supporting Science with the Mars Express Visual Monitoring Camera. In *EGU General Assembly Conference Abstracts* (p. 740).

Ravanis, E., Hernández-Bernal, J., Cardesín-Moinelo, A., Sánchez-Lavega, A., del Río-Gaztelurrutia, T., Hueso, R., ... & Martin, P. (2020). *From engineering to science: Mars Express Visual Monitoring Camera's first science data release* (No. EPSC2020-437). Copernicus Meetings.

Ravanis, E., Hueso, R., Sanchez-Lavega, A., Del Rio-Gaztelurrutia, T., Titov, D., Martin, P., ... & Cardesín-Moinelo, A. (2021). Science with small cameras: The Visual Monitoring Camera onboard Mars Express. *43rd COSPAR Scientific Assembly. Held 28 January-4 February, 43*, 231.

Sanchez-Lavega, A., Hernandez-Bernal, J., del Rio-Gaztelurrutia, T., Hueso, R., Cardesín-Moinelo, A., Titov, D. V., ... & de Burgos-Sierra, A. (2018, December). The 2018 Martian global dust storm over the south pole studied with VMC onboard Mars Express. In *AGU Fall Meeting Abstracts* (Vol. 2018, pp. P43K-3885).

Sanchez-Lavega, A., García-Morales, J., Hernandez-Bernal, J., del Río-Gaztelurrutia, T., Hueso, R., Ravanis, E. M., ... & Matz, K. D. (2020). Patterns in textured dust storms in Mars North Pole. EPSC 2020, online.

Sanchez-Lavega, A., García-Morales, J., Hernandez-Bernal, J., del Río-Gaztelurrutia, T., Hueso, R., Ravanis, E. M., ... & Matz, K. D. (2020). Atmospheric spirals in spring time on the edge of the North Pole of Mars. AGU 2020, online

Sanchez-Lavega, A., Leyva, J. M., Erkoreka, A., García-Morales, J., Hernández-Bernal, J., del Río-Gaztelurrutia, T., ... & Matz, K. D. (2021). *Dynamical Phenomena in Martian dust storms* (No. EPSC2021-251). Copernicus Meetings.

Sánchez-Lavega, A. Larsen, E., Hernández-Bernal, J., del Río-Gaztelurrutia, T., Ordóñez-Etxeberría, I., Ordorika, J., Cardesín-Moinelo, A. (2022) Atmospheric disturbances imaged on Mars during the simultaneous operations of four surface stations along 2021 and 2022. EPSC 2022, Granada.

Del Rio Gaztelurrutia, T., Hernandez-Bernal, J., Sanchez-Lavega, A., Hueso, R., Cardesin-Moinelo, A., de Burgos-Sierra, A., ... & Dias Almeida, M. (2018, October). Clouds in the night side of Mars: an analysis using Mars Express VMC. In *AAS/Division for Planetary Sciences Meeting Abstracts# 50* (Vol. 50, pp. 300-05).

Meteorological phenomena on Mars studied with Mars Express VMC images.

del Río-Gaztelurrutia, T., Sánchez-Lavega, A., Hernández-Bernal, J., Angulo, A., Hueso, R., Cardesín-Moinelo, A., ... & Titov, D. (2021, April). Analysis of the evolution of Martian polar caps during Martian Years 34-35 from Mars Express Visual Monitoring Camera. In *EGU General Assembly Conference Abstracts* (pp. EGU21-7787).

Sanchez-Lavega, A., Larsen, E., Hernandez-Bernal, J., del Río-Gaztelurrutia, T., Ordoñez-Etxeberría, I., Ordorika, J., and Cardesín-Moinelo, A.: Atmospheric disturbances imaged on Mars during the simultaneous operations of four surface stations along 2021 and 2022, Europlanet Science Congress 2022, Granada, Spain, 18–23 Sep 2022, EPSC2022-228, <https://doi.org/10.5194/epsc2022-228>, 2022.

**Other articles and contributions to congresses not directly connected to this thesis**

Sánchez-Lavega, A., Almendros, V., Hernández-Bernal, J., Otxoa, I., De Ormaetxea, A. S., & del Río Gaztelurrutia, T. (2019). Basic orbital mechanics from simple observations of the main satellites of Saturn, Uranus and Neptune. *European Journal of Physics*, 40(3), 035601.

Hernández-Bernal, J. (2020). El sol mira a Arrazola a través de los ojos de Anbotu. *Astola: ikerketa eta historia*, (14), 152-161.

Hernández-Bernal, J. (2020). ¿Hay agua en Marte? ¿Y qué podemos aprender de ella? *La Gaceta de Salamanca*, 15 de marzo de 2020.

Hernández-Bernal, J. (2020). Puntual e imposible: la eterna danza de gigantes. *La Gaceta de Salamanca*, 20 de diciembre de 2020.

Hernández-Bernal, J. (2020). De los buenos tiempos. *Crystal Clear*, Logos Elkartea. 30 de diciembre de 2020.

Hernández-Bernal, J. (2021) El cohete chino que iba a estrellarse en Madrid. *The Conversation*, 7 de mayo de 2021.

Hernández-Bernal, J. (2021) ¿Cuál es la huella ecológica del turismo espacial?. *The Conversation*, 21 de julio de 2021.

Pérez-Hoyos, S., Hernández-Bernal, J. (2021). Rusia contra la NASA: por qué la exploración espacial debe contar con todos. *The Conversation*, 17 de noviembre de 2021.

Hernández-Bernal, J., Pérez-Hoyos, S. (2022). Por qué necesitamos una ética espacial. *The Conversation*, 16 de mayo de 2022.

Hernández-Bernal, J. (2022), Ética Espacial: ¿Se convertirán nuestros sueños en distopías?. *Astronomía Magazine* (275, mayo 2022), 22-29

Meteorological phenomena on Mars studied with Mars Express VMC images.

Hernández-Bernal, J., Pérez-Hoyos, S., Almazán, A., Casado A., González-Ferreiro, E., Jilite-Calleja, B., ... Sureda-Anfres, M. (2022, septiembre) Ética espacial: reflexiones sobre un curso de verano interdisciplinar. Reunión Científica de la Sociedad Española de Astronomía, Tenerife

Hernández-Bernal, J., Pérez-Hoyos, S. (2022, octubre) ¿Por qué necesitamos una ética espacial?. Encuentros Transfronterizos de Astronomía Amateur, Pamplona.

Hernández-Bernal, J. (2022), Hacia un sector espacial coherente con la justicia climática. El Periódico, 1 de noviembre de 2022

Hernández-Bernal, J. (2022), La situación no está bajo control. El Correo, 11 de noviembre de 2022

Meteorological phenomena on Mars studied with Mars Express VMC images.



Meteorological phenomena on Mars studied with Mars Express VMC images.

Meteorological phenomena on Mars studied with Mars Express VMC images.

# Conclusions

## Conclusions

This thesis has employed images acquired by the VMC camera onboard the European Mars Express orbiter, together with data from 6 additional instruments, and LMD atmospheric models, to investigate different meteorological phenomena in the atmosphere of Mars.

The methodological developments provided by this thesis (including operations, data processing, and data analysis) have improved the capability to exploit VMC for the investigation of the Martian atmosphere.

The scientific research of the thesis has focused on meteorological phenomena that, due to its particular capabilities, were exceptionally well covered by VMC: the impact of the GDS 2018 on the south polar region, the AMEC, and the clouds in twilight.

All these phenomena have been studied in the context of the existing literature, and some unexpected findings or previously unexplored features have arisen. The cloud tracking performed on south polar latitudes during the GDS 2018 is not coincident with the winds predicted by the LMD Global Circulation Model (GCM) in the context of a dust storm. The study and mesoscale modeling of the AMEC, has revealed that tropical orographic clouds on Mars are the result of different mechanisms in the first and the second halves of the year. And the distribution of mesospheric clouds observed in twilight follows a pattern only hinted by previous observational studies on mesospheric clouds.

Some specific conclusions for these meteorological phenomena are:

- **Global Dust Storm in MY34** and its impact on the south polar region
  - The dust storm penetrated the south polar cap. This penetration was not complete or homogeneous in any of the images acquired by VMC. The weak summer polar vortex on the south pole allowed this penetration, while the strong winter polar vortex in the south prevented the penetration of the storm in the north polar region.
  - The cloud tracking reveals that winds moved towards terminator at high speeds in the morning, a pattern that is not in agreement with the MCD prediction in dust storm scenario.
  - Aerosol bands were observed around the pole in latitudes 60°-80°S. They were likely made of water ice particles. The LMD GMC hints the presence of these bands in the MY34 dust scenario, although the prediction differs from observations in terms of altitude and local time.

Meteorological phenomena on Mars studied with Mars Express VMC images.

- In northern latitudes, aerosols reached an altitude of around 60 km near Alba Patera (latitude 45°N), as seen in VMC images of the limb.
- **The Arsia Mons Elongated Cloud (AMEC)**
  - The AMEC develops every sol during a long season in the (not well constrained) Ls range from 220° to 320°.
  - It follows a daily cycle starting with sunrise, and it expands for 2.5 hours at a velocity of 100-170 m/s, forming a characteristic elongated tail. In MY34 it was observed detached from Arsia Mons once the expansion phase was finished.
  - Tharsis orographic clouds in the second half of the year form due to cold pockets near the hygropause. In contrast, orographic clouds in the first half of the year form by the ascension of water caused by thermal slope winds. The dominance of one mechanism or the other depends on the altitude of the hygropause relative to the ascension of thermal slope winds.
  - Simulations show that the AMEC is the result of a cold pocket (down to 30K below the environment temperature) caused by the ascension of an hydraulic-like jump on the western slope of Arsia Mons, which occurs in coincidence with the fastest winds blowing against the summit of Arsia Mons. Water vapor already present in the higher atmosphere freezes while traversing this cold pocket.
  - In our current knowledge, there is no complete understanding on the formation of the elongated tail of the AMEC. The water ice particles formed in the core cold pocket are most probably advected by winds, but the reason why they do not sublimate as they leave the core cold pocket and reach a hotter region is not yet explained. When advected from the core cold pocket, these particles sublimate very slowly, due to some not yet understood microphysical effects.
  - Other clouds are observed on Mars that exhibit an aspect that resembles the AMEC, including its characteristic elongated tail. The Perihelion Cloud Trails (PCTs), studied by other authors, share many characteristics with the AMEC and are probably originated by a similar mechanism. Other elongated clouds have not been studied in detail, and the fact that they happen in different seasons and longitudes may provide new insights on different possible origins for elongated clouds in Mars.
- **Clouds in twilight**
  - We performed the first systematic study of mesospheric clouds in twilight on Mars. We developed a methodology to detect automatically these clouds in

## Meteorological phenomena on Mars studied with Mars Express VMC images.

images and to determine their minimum altitude, and their constrained altitude for suitable observations.

- These clouds are very common in specific seasons and latitudes, following a distribution that differs from previous observational studies that had been focused in the afternoon. We find an accumulation of clouds in twilight in southern midlatitudes during fall and winter, and a smaller accumulation in the northern midlatitudes around the spring equinox. This distribution was only hinted by previous studies that observed mesospheric clouds around the twilight.
- The extensive dataset of observed clouds in twilight displays interannual variations that deserve further study.
- VMC observations enable cloud-tracking measurements on these clouds and a technique to obtain them is being developed. Measurements of mesospheric winds are scarce in the literature and only a few cases have been reported previously.

In addition to these specific conclusions about the studied meteorological phenomena, a more general conclusion is that the capabilities of VMC (full-disk imaging; coverage of different local times; video acquisition) enable studying phenomena poorly covered by previous instruments. New instruments specially made for science have been starting to cover this gap in recent years, offering high quality images better than those offered by VMC. Still, VMC has the capacity to produce images that increase the observational coverage of the Martian atmosphere, and has demonstrated its ability to contribute to science.

Finally some ideas for future works are summarized below:

- Investigating the AMEC more deeply, using recently acquired observations<sup>20</sup> from VMC and other instruments, including spectrometers (PFS, SPICAM, NOMAD, ACS) and high resolution imagers (HRSC, OMEGA, EXI), that may provide the explanation of the origin of the tail. The rich structure of the head of the cloud, obvious in high-resolution images will also provide insights on the underlying dynamics.
- Investigating the other elongated clouds on Mars. This should start with an analysis of the available images in the context provided by GCM simulations. Then selected

---

<sup>20</sup> For reference of the interested community, this folder gathers a lot of information about the AMEC, and a specially made document with guidelines for planning and analyzing different kinds of observations potentially interesting for the study of the AMEC:

<https://drive.google.com/drive/u/1/folders/1PaLl4E9mmi3r65ooxOGmX-5mPAHz13SF>

Meteorological phenomena on Mars studied with Mars Express VMC images.

locations should be analyzed with the aid of a mesoscale model. Understanding this phenomenon is likely to require observations from spectrometers, and a stronger effort to understand the microphysics potentially enabling the formation of the tail in at least some of the observed cases.

- Investigating the Polar Hoods and their interactions with orography. VMC images reveal a rich variety of morphologies and dynamics in the polar hoods, including different configurations of bands and filaments extending for thousands of kilometers. Also, orographic features near the North Polar Hood interact in striking ways with these polar hoods, especially in the case of Alba Mons, Tempe Terra, Lyot crater, and Phlegra Mons. Such orographic interactions are also present in the South Polar Hood.
- Continue the study of clouds in twilight, complementing VMC images with those acquired by similar instruments, to improve the knowledge of their climatology and interannual variations. Hyperspectral imaging and solar occultation could provide information about their composition and microphysical characteristics. GCM and mesoscale simulations could be used to try to understand and reproduce the observed climatology.
- Investigate the dust spiral observed years ago by MOC and reproduced by Rafkin et al. (2002) in a mesoscale simulation over Arsia Mons. Preliminary analysis of MARCI images reveals different configurations of occurrence of this spiral and its random occurrence in different sols over a long season. GCM and mesoscale simulations could be used to learn more about this phenomenon and understand what are the elements from the global circulation that activate it only in specific sols.

Meteorological phenomena on Mars studied with Mars Express VMC images.

Meteorological phenomena on Mars studied with Mars Express VMC images.

# Annex



Meteorological phenomena on Mars studied with Mars Express VMC images.

## Annex

The four papers that are part of this thesis are provided separately and can be accessed in the following links. Some of them are also available in sci-hub.

- **Hernández-Bernal et al. (2019)** The 2018 Martian Global Dust Storm over the South Polar Region studied with MEx/VMC. *Geophysical Research Letters*.
  - <https://doi.org/10.1029/2019GL084266>
  - <https://arxiv.org/abs/2102.13521>
- **Hernández-Bernal et al. (2021a)** An Extremely Elongated Cloud over Arsia Mons Volcano on Mars: I. Life Cycle. *Journal of Geophysical Research: Planets*.
  - <https://doi.org/10.1029/2020JE006517>
  - <https://arxiv.org/abs/2103.03919>
- **Hernández-Bernal et al. (2021b)** A long term study of Mars mesospheric clouds seen at twilight based on Mars Express VMC images. *Geophysical Research Letters*.
  - <https://doi.org/10.1029/2020GL092188>
  - <https://arxiv.org/abs/2104.02355>
- **Hernández-Bernal et al. (2022a)** An Extremely Elongated Cloud over Arsia Mons Volcano on Mars: II. Mesoscale modeling. *Journal of Geophysical Research: Planets*.
  - (open access) <https://doi.org/10.1029/2022JE007352>

# Geophysical Research Letters

## RESEARCH LETTER

10.1029/2019GL084266

### Special Section:

Studies of the 2018/Mars Year  
34 Planet-Encircling Dust  
Storm

### Key Points:

- The 2018 global dust storm propagated unevenly over the South Polar Region, not covering it fully, and forming elongated narrow dust arcs
- Overall, dust moved toward the terminator, reaching velocities up to 100 m/s in the morningside
- During June–July 2018, the top altitude of dust showed both spatial and temporal variability, ranging from 10–70 km

### Supporting Information:

- Supporting Information S1
- Data Set S1
- Data Set S2
- Data Set S3

### Correspondence to:

J. Hernández-Bernal,  
jorge.hernandez@ehu.eus

### Citation:

Hernández-Bernal, J., Sánchez-Lavega, A., del Río-Gaztelurrutia, T., Hueso, R., Cardesín-Moinelo, A., Ravanis, E. M., et al. (2019). The 2018 Martian global dust storm over the South Polar Region studied with MEx/VMC. *Geophysical Research Letters*, 46, 10,330–10,337. <https://doi.org/10.1029/2019GL084266>

Received 24 JUN 2019







Accepted 7 AUG 2019

Accepted article online 13 AUG 2019

Published online 24 SEP 2019

©2019. American Geophysical Union.  
All Rights Reserved.

## The 2018 Martian Global Dust Storm Over the South Polar Region Studied With MEx/VMC

J. Hernández-Bernal<sup>1,2</sup> , A. Sánchez-Lavega<sup>1,2</sup> , T. del Río-Gaztelurrutia<sup>1,2</sup>, R. Hueso<sup>1</sup> , A. Cardesín-Moinelo<sup>3</sup> , E. M. Ravanis<sup>3</sup> , A. de Burgos-Sierra<sup>3</sup> , D. Titov<sup>4</sup>, and S. Wood<sup>5</sup>

<sup>1</sup>Dpto. Física Aplicada I, EIB, Universidad País Vasco UPV/EHU, Bilbao, Spain, <sup>2</sup>Aula Espazio Gela, Escuela de Ingeniería de Bilbao, Universidad del País Vasco UPV/EHU, Bilbao, Spain, <sup>3</sup>ESAC, European Space Agency, Madrid, Spain, <sup>4</sup>ESTEC, European Space Agency, Noordwijk, Netherlands, <sup>5</sup>ESOC, European Space Agency, Darmstadt, Germany

**Abstract** We study the 2018 Martian global dust storm (GDS 2018) over the Southern Polar Region using images obtained by the Visual Monitoring Camera (VMC) on board Mars Express (MEx) during June and July 2018. Dust penetrated into the polar cap region but never covered the cap completely, and its spatial distribution was nonhomogeneous and rapidly changing. However, we detected long but narrow aerosol curved arcs with a length of ~2,000–3,000 km traversing part of the cap and crossing the terminator into the nightside. Tracking discrete dust clouds allowed measurements of their motions that were toward the terminator with velocities up to 100 m/s. The images of the dust projected into the Martian limb show maximum altitudes of ~70 km but with large spatial and temporal variations. We discuss these results in the context of the predictions of a numerical model for dust storm scenario.

**Plain Language Summary** Dust storms of different scales (local, regional, etc.) are common on Mars. Some Martian years a regional storm activates secondary storms and dust encircles the planet, in a dust event usually called a global dust storm. The last global dust storm took place in 2018, and we are not currently able to predict when a new one will occur. Global dust storms affect the global dynamics of the Martian atmosphere, and the dynamics of the polar regions is a good proxy to the global situation. In this paper, we take advantage of the polar orbit of Mars Express to study the Southern Polar Region during 2018 global dust storm using the Visual Monitoring Camera onboard the spacecraft. We show how the dust penetrated into the polar cap, the apparition of aerosol arcs curved around the pole, and the presence of winds blowing up to 100 m/s, not following the usual patterns expected with no global dust storm.

## 1. Introduction

Mars global dust storms (GDS) are uncommon and nowadays unpredictable aperiodic events (Kahre et al., 2017; Montabone & Forget, 2018, and references therein for recent reviews). On 30 May 2018 (Martian Year MY 34), a dust storm started in Acidalia Planitia, rapidly evolving to become a planet encircling dust storm (GDS 2018), as described from ground-based observations (Sánchez-Lavega et al., 2019) and from in situ measurements by Curiosity rover (Mars Science Laboratory; Guzewich et al., 2019). Ground-based images show that the storm reached the south polar cap edge at 60°S on 6 June and that by mid-June dust had penetrated the polar cap (Sánchez-Lavega et al., 2019). However, the nearly equatorial viewing geometry from ground-based telescopes prevented a detailed study of the dust propagation in the Southern Polar Region (SPR) and its interaction with the south polar cap.

Mars Express (MEx) polar orbit allows a nearly nadir view of the poles, and images of both polar regions are regularly obtained using the Visual Monitoring Camera (VMC; Ormston et al., 2011; Sánchez-Lavega, Chen-Chen, et al., 2018). Due to a technical pause in VMC operations, monitoring of the 2018 GDS started on 18 June, approximately 20 sols after its onset (Sánchez-Lavega et al., 2019). During the rest of June, and in July and August, VMC obtained a large set of images showing the SPR (Figure 1) at a typical resolution in the range of 9–13 km/pixel (details on the list of observations are given in the supporting information). The period under study spans from 18 June to 3 August 2018 ( $L_s \sim 195\text{--}220^\circ$ ). The propagation of the GDS over the SPR is a unique opportunity to study the interaction of a planetary-scale phenomenon with the particular dynamics of the polar atmosphere such as the polar vortex, katabatic winds, and condensate clouds (Smith et al., 2018). The behavior of dust from GDS 2018 over the SPR

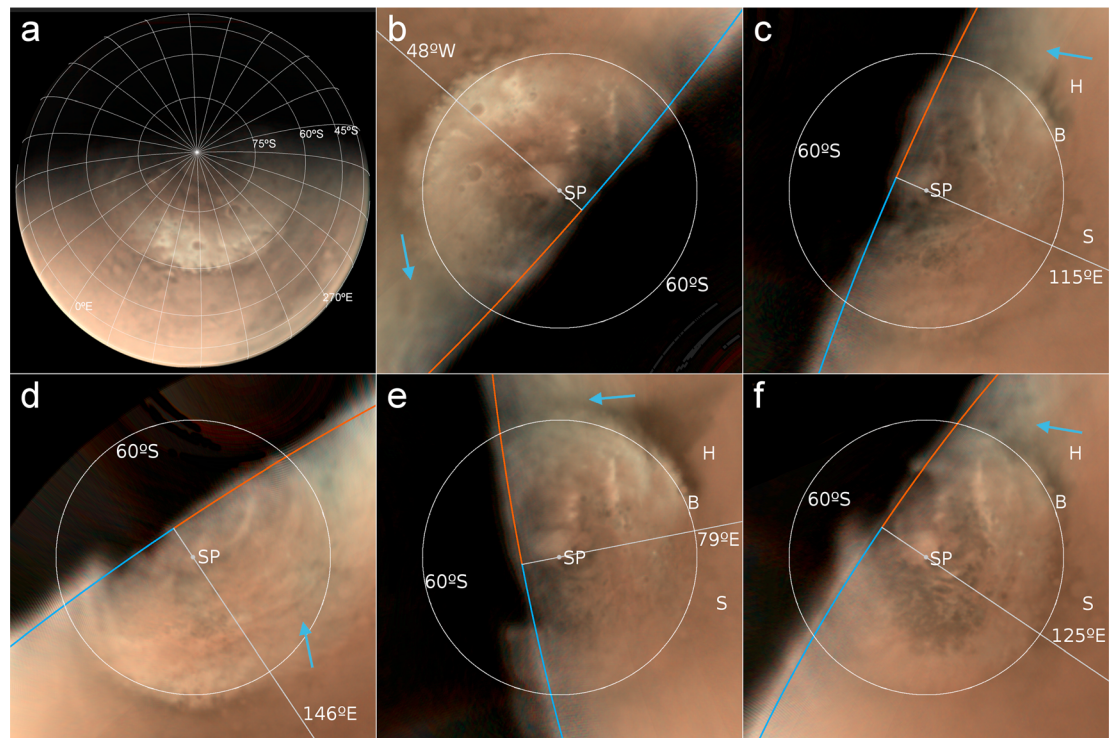


**Figure 1.** Images of the SPR during GDS 2018. (a) Direct polar view: 18 June, 21.50 UT and its polar projection (b). (b–f) Polar projections covering latitudes 50–90°S; (c) 21 June, 12.40 UT; (d) 23 June, 11.50 UT; (e) 26 June, 18.25 UT; and (f) 11 July, 00.35 UT. Orange and blue curves indicate, respectively, the morning and the evening terminator, and the gray line represents the subsolar meridian. In all projections, longitude 0°E points upward and east longitude increases clockwise. Hellas planitia, and Barnard and Secchi craters are identified by the letters H, B, and S, respectively. SP stands for South Pole. The blue arrows indicate morning hazes. See supporting information for further details on observations and image processing. GDS = global dust storm.

is the main subject of study in this paper. In addition, VMC also performed dedicated limb observations when MEX was near pericenter which allowed us to measure aerosol top altitude and horizontal distribution (Sánchez-Lavega, Chen-Chen, et al., 2018).

For geometry calculations and navigation of images, two software packages were used: PLIA (Hueso et al., 2010) and a new package named Elkano (see supporting information). Geometry parameters were extracted using SPICE (Acton, 1996; Acton et al., 2018), from publicly available SPICE Kernels provided by the ESA SPICE Service (Costa, 2018). MOLA topographic data (Smith et al., 1999) were taken into account when necessary. For time calculations, we use algorithms and definitions described by Allison (1997) and Allison and McEwen (2000). See supporting information for further methodological details.

## 2. Dust Distribution in the SPR

In mid-June 2018, the edge of the southern polar cap (the area of the SPR covered by ice) was at latitude 60°S, in good agreement with previous measurements in this season ( $L_s \sim 195^\circ$ ) of the MY (Schmidt et al., 2009). Ground based observations indicate that the propagation of the GDS 2018 into the Southern Polar Cap region started on 8–9 June, reaching latitude 70°S at longitudes 0° to 60°E (Sánchez-Lavega et al., 2019). The dust further penetrated on 11 June to latitude 75°S, at two or more different longitudes (0° to 60°E and  $\sim 225^\circ$ E), according to a National Aeronautics and Space Administration image animation PIA22519, based on image sequences obtained with the Mars Color Imager on board Mars Reconnaissance Orbiter (Malin et al., 2001; <https://photojournal.jpl.nasa.gov/catalog/PIA22519>).

VMC started taking images of the SPR on 18 June. The dust distribution was clearly nonhomogenous and showed daily changes throughout June (Figures 1b–1e). Images taken on the 18 and 23 June show

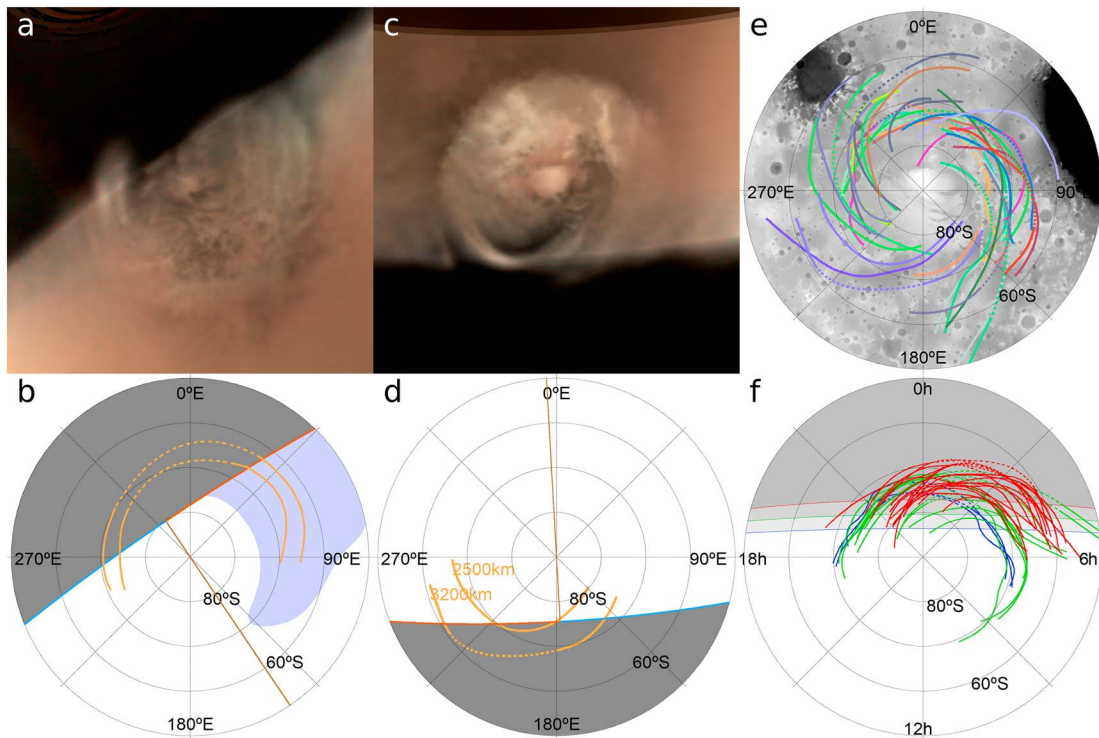


**Figure 2.** Images and structure of the arc bands around the south pole. (a, c) Polar projected images of the Southern Polar Region on 1 July, 17:30 UT and 22 July, 16:40 UT, respectively. (b, d) Schematic representations of previous images showing the nightside (dark gray), the morning hazes (blue lilac), and the observed bands, with continuous orange lines indicating visible parts and dotted sections indicating the potential location in the nightside. Numbers in orange indicate the estimated length of arcs. Red and blue lines indicate morning and evening terminators, and the brown line indicates the subsolar meridian. Notice the absence of morning hazes and the presence of a fully visible band on 22 July. (e) Areographic distribution of measured bands over a gray topographic map made from MOLA data (Smith et al., 1999) (different colors represent different observations). (f) Graph showing the latitude-local time distribution of all the observed bands. Different band colors indicate different periods starting on 18 June (blue), 1 July (green), and 18 July (red). Gray areas represent the night.

longitude sectors from 270° to 0°E (Figures 1a and 1b) and 150° to 200° (Figure 1d), respectively. In those images, surface features of the SPR are clearly seen, indicating a limited presence of dust. On 21 and 26 June the presence of thick dust is noticeable at longitudes eastward 90°E (Figures 1c and 1e). Much clearer regions are seen westward of Hellas where surface details, such as crater Barnard, are easily identified. This region is imaged again on 11 July (Figure 1f) showing that the dust is still present although in smaller quantities. Various surface features can be identified in Figures 1c, 1e, and 1f, especially in the 90–180° range of longitudes, with different degrees of contrast that indicate a variable coverage by dust. Nevertheless, dust rarely hides surface features completely in the southernmost regions. It is worth noticing that morning hazes are usually present about 3–6 hr after sunrise (blue arrows in Figure 1) and mix with the dust. Since they appear in the morning hours to disappear later, these hazes are most likely water ice condensates of relatively low optical depth. In summary, VMC image sequences in June–July show that dust entered the polar cap region, but penetration was irregular, and it never covered the entire polar cap. Additional images of the SPR are presented in the supporting information Figure S1.

### 3. Arc-Shaped Aerosol Bands Over the SPR Seen in Twilight

The season under study follows the southern spring equinox ( $L_s \sim 195\text{--}220^\circ$ ), hence at any given time, a part of the SPR was not illuminated by the Sun. High-altitude aerosols can get direct illumination by the setting Sun in the night and thus become visible against a dark background. MEX/VMC observations included some high-exposure images, which enabled visualizing bright structures in the nightside beyond the terminator (Figure 2). These features are organized in one or more arc-shaped parallel bands (Figure 2a), curving around the pole, and extending from the evening terminator to the morning terminator. In some cases the features are not completely visible, with bands captured in the nightside of the terminator both in the

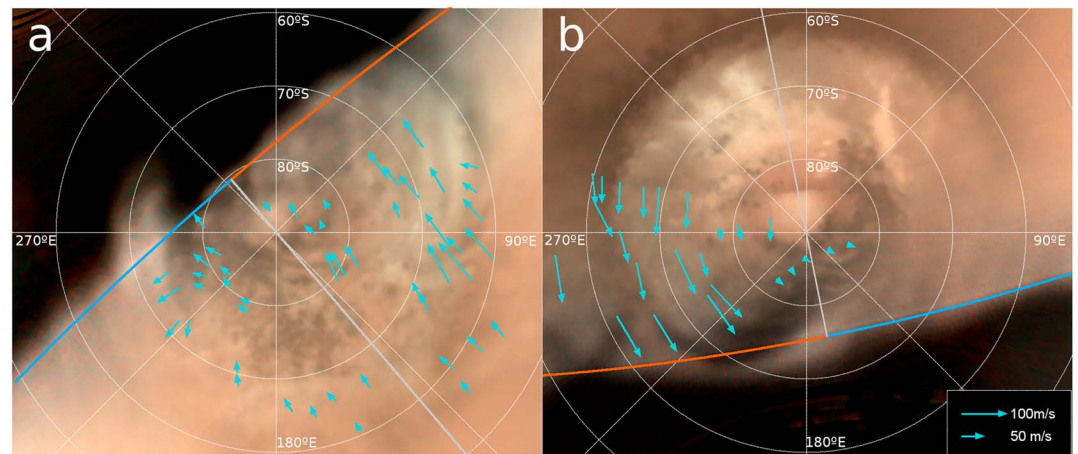


**Figure 3.** Velocity vectors retrieved tracking discrete features in two different dates: (a) 1 July, 17:20 UT and (b) 18 July, 14:40 UT. Morning terminator, evening terminator, and subsolar meridian are indicated in the same format as in Figure 1.

evening and morning terminators, but not in regions at local midnight (Figures 2a and 2b). In other cases, the bands are seen in full length (Figures 2c and 2d). In the morning terminator, the bands are harder to distinguish since they mix with the morning hazes (Figures 2a–2b). In Figure 2e we show the location of all measured bands against a map of the SPR.

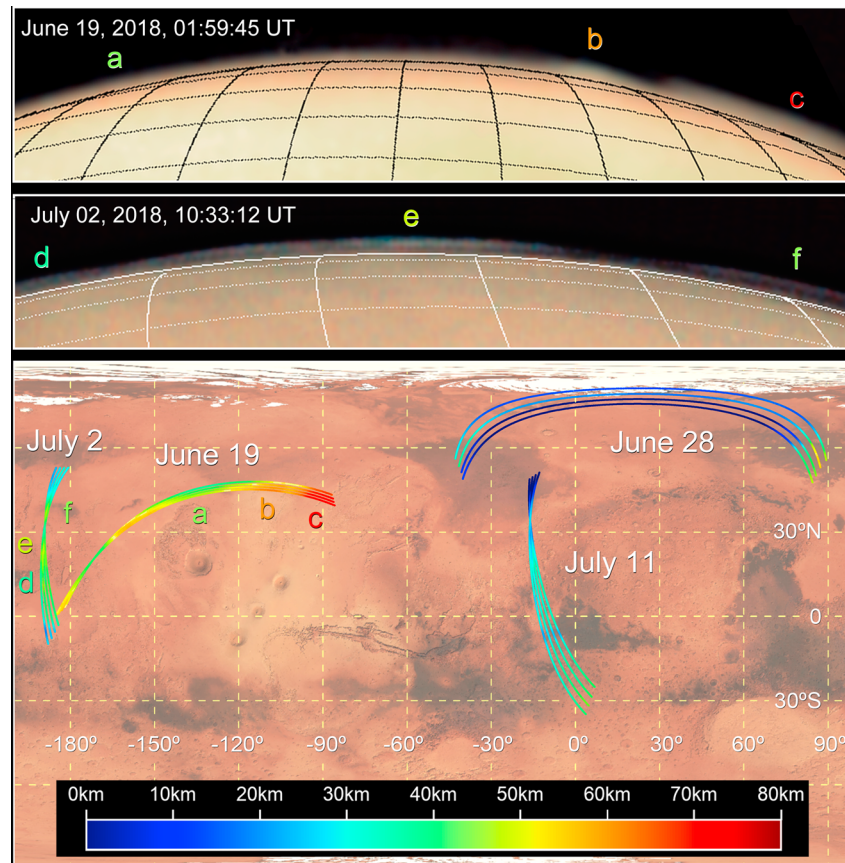


**Figure 4.** (upper two panels) Dust projected at limb in two different dates corresponding to a planet-wide expansion of the GDS 2018 (Sánchez-Lavega et al., 2019). (lower panel) Location of the limb observations over a map of Mars. Top altitudes are indicated using a color code.

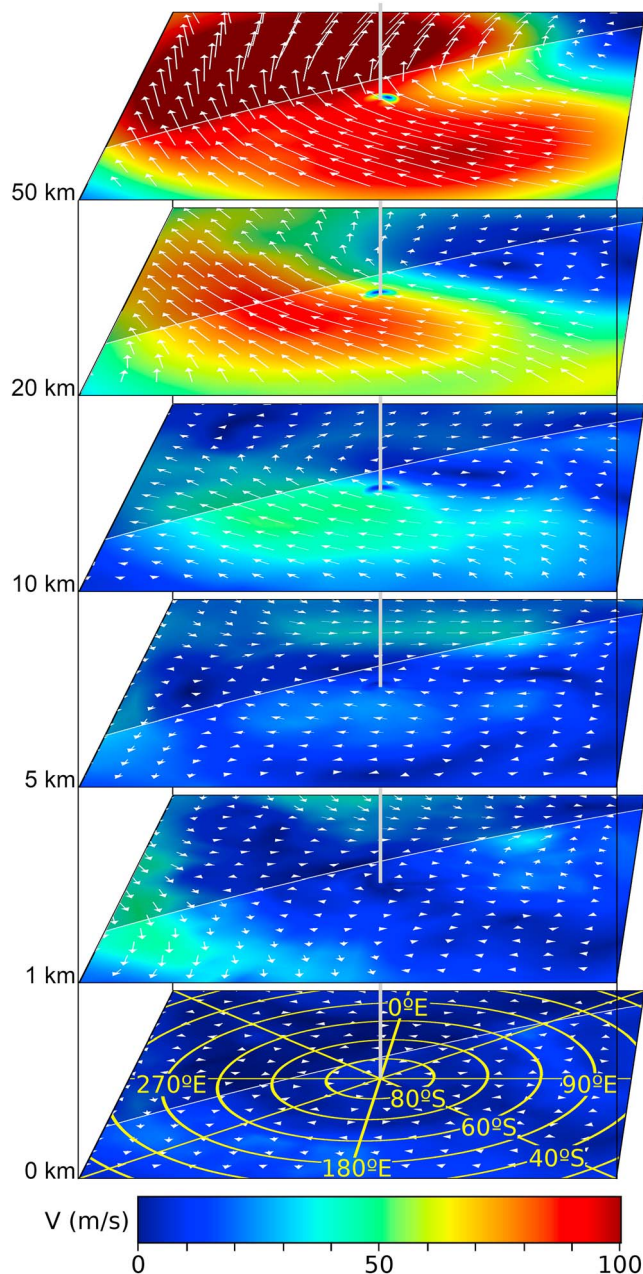


**Figure 5.** Wind field retrieved from MCD for dust storm solar minimum scenario, showing winds over the South Pole on 1 July at 17:10 (same time as for Figure 3a) at different altitudes. Equivalent figure for Figure 3b is available in the supporting information. A white line in the maps shows the terminator. The darker area corresponds to the nightside and the lighter are to dayside.

than in the evening. Winds are slower over the polar cap, with typical velocities of 60 m/s in the morning (reaching 80–100 m/s only in exceptional cases), and still lower (~20–40 m/s) around the pole and in the afternoon side. It is quite remarkable that the pattern of the wind field changes with date. Figure 3a, corresponding to 1 July, shows no hint of circulation around the pole, and the wind vectors are not oriented in the direction of the bands. On the contrary, on 18 July (Figure 3b) wind vectors are suggestive of a circulation around the pole (longitudes ~135°E and 225°E and latitudes ~70–90°S), although the lack of measurements in the evening side means we should exercise caution when making this inference. In addition, the vectors

At the evening terminator, the bands are closer to the pole, at distances ranging between 300 and 1,100 km from it. They extend across a typical length of 2,000–3,000 km, ending further from the pole, at about 500–1,500 km in the morning terminator. The bands show irregular morphology with widths in the range ~200–500 km. Additionally, an image from 1 July shows two or three parallel curved bands in the dayside, separated by ~100–200 km and extending up to a thousand kilometers in length at a mean latitude of 70°S, 1,200 km from the pole (Figure 2a). The visibility of the bands in the nightside is an indication of their altitude, which we determine by simple geometry (Hernández-Bernal et al., 2018) to be in the range of  $10\text{--}35 \pm 5$  km, higher in the evening side than in the morning side. The presence of banding becomes more frequent as the season progresses, and after 18 July, at least one band is fully visible in the night in most cases. As can be seen in Figure 2f, this is mainly a consequence of the change in the position of the terminator with the advancing season. Moreover, as the season advances, the bands become less curved, their centers recede from the terminator and they move toward the morningside. Unfortunately, the lack of reliable spectral information from VMC prevents us from determining the nature of the aerosol forming the bands, although it is very likely that this is dust from the GDS. The shape and distribution of the bands suggests that they are organized by the polar atmospheric dynamics. One possibility is that the polar vortex causes the organization of these bands, a possibility discussed in section 7.

#### 4. Tracking Motions Over the SPR

Previous wind measurements of the SPR in a period ( $L_s = 337\text{--}10^\circ$ ) with no dust storms were obtained by Wang and Ingersoll (2003) who analyzed Mars Obiter Camera images finding velocities from 10 to 20 m/s. Here we use VMC images to track motions of the dust during the 2018 dust storm (Figure 3). Previous wind measurements associated to cloud features using VMC images can be found in Sánchez-Lavega, Garro, et al. (2018). We have measured 10 pairs of VMC images taken between 1 July and 3 August separated by 20–40 min at a spatial resolution of ~11 km/pixel that allows us to retrieve velocities with an estimated error of 10 m/s. We use animations and blinking between the two images of a selected pair to identify moving features, and then point manually to their centers to track their motion. Sharpest aerosol features (suitable for cloud tracking) are mostly found in regions at morning local true solar time. We assume that features act as passive tracers and that their motions mark the velocity of the underlying winds. Although other possibilities cannot be excluded, the short time interval in each pair makes advection the most likely cause of motion in features that do not change much in shape or area.

The main trend visible in our measurements is that features move toward the terminator (Figure 3). The highest velocities occur at the edge of the polar cap, where they reach up to 110 m/s (Figure 3a and supporting information Figure S5). At equal latitudes, velocities in the morning are higher

show some orientation along the arc band that extends from latitude 80°S and longitude 150° to latitude 60°S and longitude 250°. These contradictory measurements of motions between the two dates show the complexity of the polar dynamics under a global dust storm condition.

### 5. Altitude Reached by Dust During GDS 2018

In addition to apocenter observations of the SPR, some VMC images were programmed to observe the limb of the planet from a closer distance. The orbit of MEx during this period allowed limb images of equatorial and northern latitudes with resolutions of  $\sim 7$  km/pixel (Figure 4). At the limb, aerosols reflect sunlight against the dark background, and the maximum height and horizontal structure over the surface can be easily estimated once the geometry of the observation is determined (Sánchez-Lavega, Chen-Chen, et al., 2018). Figure 4 shows two examples of high-altitude aerosols at the limb, most likely dust from the GDS according to the area occupied by the expanding storm (Sánchez-Lavega et al., 2019), reaching up to 60–70 km over the surface. Figure 4 also shows the location of all limb observations for the reported period and the dust top altitude. The maximum altitude,  $\sim 60$  km, was observed on 19 June around Alba Patera. Scans of the limb show significant top altitude differences (from  $\sim 10$  to 70 km) depending on the date and location, reflecting the complex dynamics involved in the GDS 2018.

### 6. Comparison With Model Predictions

The Mars Climate Database (MCD; Forget et al., 1999; Millour et al., 2015) provides easy access to a statistical summary of results of the global climate model of Mars developed by the Laboratoire de Météorologie Dynamique under different dust and solar activity scenarios. In order to find out how the GDS affected the dynamics of the SPR, we have compared our measurements with the predictions from the model. Since the GDS developed under solar minimum, we considered two solar minimum scenarios: climatology (low dust) and dust storm. The dust storm scenario is not expected to describe the situation with accuracy, but it might be a first approach to the actual dynamics of the atmosphere during the dust storm.

For the orbital solar longitude and time of the day in Mars corresponding to the observation on 1 July at 17:20 UT (Figure 3a) the MCD winds are shown in Figure 5. Since our cloud-tracking measurements lack altitude information, we present the velocity field from the model in the altitude range of 0–50 km, which is consistent with the altitude measurements in the previous section. Above 10 km, the MCD predicts winds moving toward the terminator, mostly in the eveningside; winds in the morningside are slower. These winds seem to result from a displacement of a predicted polar vortex in the direction of the morningside, relative to the terminator. In fact, a similar shift of the north polar vortex was observed in a reanalysis of a regional dust storm in MY 26,  $L_s \sim 320^\circ$  (Mitchell et al., 2015). The prediction of motions toward the terminator above 10 km is globally consistent with our measurements shown in Figure 3a, although our measured values do not agree with the predicted velocities, as MCD predicts faster winds in the eveningside than in the morningside at any altitude over 10 km, while we observe faster winds in the morningside.

### 7. Conclusions

The GDS 2018 penetrated the southern polar cap region, as already reported by Sánchez-Lavega et al. (2019), but dust coverage was not complete or homogeneous and we do not observe the south polar cap fully covered by dust in any image. In the north, the GDS expansion apparently stopped at  $\sim 45$ – $50^\circ$ N (Sánchez-Lavega et al., 2019). This asymmetric behavior of the GDS between the two poles can probably be explained by the presence of a strong polar vortex in the northern hemisphere, and a weak one in the south. This is in agreement with the observations that Martian polar vortices are stronger in the winter and that the north polar vortex is stronger than the south polar one (Mitchell et al., 2015; Waugh et al., 2016).

The wind speeds and measured directions of the dust motions show differences when compared with the MCD predictions for a dusty scenario, particularly in the relative intensity of evening and morning winds, suggesting that the GDS 2018 altered the polar dynamics significantly. A proper account of the observed dust load and its spatial distribution in MY 34 have been described elsewhere in this number (Montabone et al., 18 July 2019), and its inclusion in the Laboratoire de Météorologie Dynamique Mars global climate

model will probably lead to a better agreement. One possible interpretation of the circumpolar banding organization reported in section 3 is that it results from an alignment of dust masses by the winds blowing with the polar vortex. When we compare the bands with our measured winds (Figure 3a), or with the MCD wind field prediction at 10- to 50-km height (Figure S4), we do not find correspondence between the bands and the circulation, or even a clear presence of a polar vortex. As an alternative explanation, recent numerical simulations of the polar dynamics with a shallow water model, which include diabatic effects (Rostami et al., 2018), show that, under normal conditions, the potential vorticity field organizes in patches that sometimes form bands and arcs around the pole resulting from nonlinear instabilities in the flow.

A good understanding of polar dynamics during this major dust storm event, when the dust penetrates the polar area, requires additional observations to the ones presented here. Studies from other instruments will surely provide data on the dust mass load (Montabone et al., 18 July 2019), temperature, chemical composition, and other physical properties that will serve as a reference input to numerical models of polar dynamics.

#### Acknowledgments

This work has been supported by the Spanish project AYA2015-65041-P (MINECO/FEDER, UE) and Grupos Gobierno Vasco IT-1366-19. J. H. B. was supported by ESA Contract 4000118461/16/ES/JD, Scientific Support for Mars Express Visual Monitoring Camera. We acknowledge support from the Faculty of the European Space Astronomy Centre (ESAC). VMC raw images used in this study can be accessed through VMC raw file gallery <http://blogs.esa.int/ftp/vmc/raw> and calibrated images will be available in ESA PSA in the near future. A list of observations used in this paper is provided in the supporting information. MCD database files are available in <http://www-mars.lmd.jussieu.fr/mars.html>.

#### References

- Acton, C., Bachman, N., Semenov, B., & Wright, E. (2018). A look towards the future in the handling of space science mission geometry. *Planetary and Space Science*, *150*, 9–12. <https://doi.org/10.1016/j.pss.2017.02.013>
- Acton, C. H. Jr. (1996). Ancillary data services of NASA's navigation and ancillary information facility. *Planetary and Space Science*, *44*(1), 65–70. [https://doi.org/10.1016/0032-0633\(95\)00107-7](https://doi.org/10.1016/0032-0633(95)00107-7)
- Allison, M. (1997). Accurate analytic representations of solar time and seasons on Mars with applications to the Pathfinder/Surveyor missions. *Geophysical Research Letters*, *24*(16), 1967–1970. <https://doi.org/10.1029/97GL01950>
- Allison, M., & McEwen, M. (2000). A post-Pathfinder evaluation of areocentric solar coordinates with improved timing recipes for Mars seasonal/diurnal climate studies. *Planetary and Space Science*, *48*(2-3), 215–235. [https://doi.org/10.1016/S0032-0633\(99\)00092-6](https://doi.org/10.1016/S0032-0633(99)00092-6)
- Costa, M. (2018, September). SPICE for ESA planetary missions: Geometry and visualization support to studies, operations and data analysis. In European Planetary Science Congress (Vol. 12).
- Forget, F., Hourdin, F., Fournier, R., Hourdin, C., Talagrand, O., Collins, M., et al. (1999). Improved general circulation models of the Martian atmosphere from the surface to above 80 km. *Journal of Geophysical Research*, *104*(E10), 24,155–24,175. <https://doi.org/10.1029/1999JE001025>
- Guzewich, S. D., Lemmon, M., Smith, C. L., Martínez, G., Vicente-Retortillo, Á., Newman, C. E., et al. (2019). Mars Science Laboratory observations of the 2018/Mars year 34 global dust storm. *Geophysical Research Letters*, *46*, 71–79. <https://doi.org/10.1029/2018GL080839>
- Hernández-Bernal, J., Sánchez Lavega, A., del Río Gaztelurrutia, T., Hueso, R., Cardesín Moineiro, A., de Burgos Sierra, A., & Dias Almeida, M. (2018, September). Clouds in the night side of Mars: An analysis using Mars Express VMC. In European Planetary Science Congress (Vol. 12).
- Hueso, R., Legarreta, J., Rojas, J. F., Peralta, J., Pérez-Hoyos, S., del Río-Gaztelurrutia, T., & Sánchez-Lavega, A. (2010). The planetary laboratory for image analysis (PLIA). *Advances in Space Research*, *46*(9), 1120–1138. <https://doi.org/10.1016/j.asr.2010.05.016>
- Kahre, M. A., Murphy, J. R., Newman, C. E., Wilson, R. J., Cantor, B. A., Lemmon, M. T., & Wolff, M. J. (2017). The Mars dust cycle. *The Atmosphere and Climate of Mars*, *18*, 295.
- Malin, M. C., Bell, J. F., Calvin, W., Clancy, R. T., Haberle, R. M., James, P. B., et al. (2001). Mars Color Imager (MARCI) on the Mars Climate Orbiter. *Journal of Geophysical Research*, *106*(E8), 17,651–17,672. <https://doi.org/10.1029/1999JE001145>
- Millour, E., Forget, F., Spiga, A., Navarro, T., Madeleine, J. B., Montabone, L., & Lopez-Valverde, M. A. (2015, September). The Mars climate database (MCD version 5.2). In European Planetary Science Congress (Vol. 10).
- Mitchell, D. M., Montabone, L., Thomson, S., & Read, P. L. (2015). Polar vortices on Earth and Mars: A comparative study of the climatology and variability from reanalyses. *Quarterly Journal of the Royal Meteorological Society*, *141*(687), 550–562. <https://doi.org/10.1002/qj.2376>
- Montabone, L., & Forget, F. (2018, July). On forecasting dust storms on Mars. 48th International Conference on Environmental Systems. Montabone, L., Spiga, A., Kass, D.M., Kleinböhl A., Forget, F., & Millour E. Martian year 34 column dust climatology from Mars Climate Sounder observations: reconstructed maps and model simulations, arXiv\_1907.08187v1 (18 July 2019)
- Ormonston, T., Denis, M., Scuka, D., & Griebel, H. (2011). An ordinary camera in an extraordinary location: Outreach with the Mars Webcam. *Acta Astronautica*, *69*(7-8), 703–713. <https://doi.org/10.1016/j.actaastro.2011.04.015>
- Rostami, M., Zeitlin, V., & Montabone, L. (2018). On the role of spatially inhomogeneous diabatic effects upon the evolution of Mars' annular polar vortex. *Icarus*, *314*, 376–388. <https://doi.org/10.1016/j.icarus.2018.05.026>
- Sánchez-Lavega, A., Chen-Chen, H., Ordonez-Etxeberria, I., Hueso, R., del Río-Gaztelurrutia, T., Garro, A., & Wood, S. (2018). Limb clouds and dust on Mars from images obtained by the Visual Monitoring Camera (VMC) onboard Mars Express. *Icarus*, *299*, 194–205. <https://doi.org/10.1016/j.icarus.2017.07.026>
- Sánchez-Lavega, A., Del Río-Gaztelurrutia, T., Hernández-Bernal, J., & Delcroix, M. (2019). The onset and growth of the 2018 Martian global dust storm. *Geophysical Research Letters*, *46*, 6101–6108. <https://doi.org/10.1029/2019GL083207>
- Sánchez-Lavega, A., Garro, A., del Río-Gaztelurrutia, T., Hueso, R., Ordoñez-Etxeberria, I., Chen Chen, H., et al. (2018). A seasonally recurrent annular cyclone in Mars northern latitudes and observations of a companion vortex. *Journal of Geophysical Research: Planets*, *123*, 3020–3034. <https://doi.org/10.1029/2018JE005740>
- Schmidt, F., Douté, S., Schmitt, B., Vincendon, M., Bibring, J. P., Langevin, Y., & Team, O. (2009). Albedo control of seasonal South Polar cap recession on Mars. *Icarus*, *200*(2), 374–394. <https://doi.org/10.1016/j.icarus.2008.12.014>
- Smith, D. E., Sjogren, W. L., Tyler, G. L., Balmimo, G., Lemoine, F. G., & Konopliv, A. S. (1999). The gravity field of Mars: Results from Mars Global Surveyor. *Science*, *286*(5437), 94–97. <https://doi.org/10.1126/science.286.5437.94>



- Smith, I. B., Diniega, S., Beaty, D. W., Thorsteinsson, T., Becerra, P., Bramson, A. M., & Spiga, A. (2018). 6th international conference on Mars polar science and exploration: Conference summary and five top questions. *Icarus*, *308*, 2–14. <https://doi.org/10.1016/j.icarus.2017.06.027>
- Wang, H., & Ingersoll, A. P. (2003). Cloud-tracked winds for the first Mars Global Surveyor mapping year. *Journal of Geophysical Research*, *108*(E9), 5110. <https://doi.org/10.1029/2003JE002107>
- Waugh, D. W., Toigo, A. D., Guzewich, S. D., Greybush, S. J., Wilson, R. J., & Montabone, L. (2016). Martian polar vortices: Comparison of reanalyses. *Journal of Geophysical Research: Planets*, *121*, 1770–1785. <https://doi.org/10.1002/2016JE005093>

This article is a companion to Hernández-Bernal et al. (2022), <https://doi.org/10.1029/2022JE007352>

**Key Points:**

- We report a new phenomenon consisting of an extremely elongated water ice cloud (up to 1,800 km) extending westward from the Arsia Mons volcano
- The cloud reaches the mesosphere (45 km), and expands at a velocity of around 170 m/s in Martian Year 34.
- This cloud repeatedly forms in the early mornings, and repeats in a daily cycle between Ls 220° and 320° every Martian year

**Supporting Information:**

- Supporting Information S1
- Figure S1
- Figure S2
- Figure S3
- Figure S4
- Figure S5
- Figure S6
- Figure S7
- Figure S8
- Table S1
- Table S2
- Table S3
- Table S4
- Table S5
- Table S6
- Movie S1
- Movie S2
- Movie S3

**Correspondence to:**

J. Hernández-Bernal,  
[jorge.hernandez@ehu.eus](mailto:jorge.hernandez@ehu.eus)













**Citation:**

Hernández-Bernal, J., Sánchez-Lavega, A., del Río-Gaztelurrutia, T., Ravanis, E., Cardesín-Moinelo, A., Connour, K., et al. (2021). An extremely elongated cloud over Arsia Mons volcano on Mars: I. Life cycle. *Journal of Geophysical Research: Planets*, 126, e2020JE006517. <https://doi.org/10.1029/2020JE006517>

Received 5 MAY 2020  
 Accepted 9 DEC 2020

© 2020. American Geophysical Union.  
 All Rights Reserved.

## An Extremely Elongated Cloud Over Arsia Mons Volcano on Mars: I. Life Cycle

J. Hernández-Bernal<sup>1,2</sup> , A. Sánchez-Lavega<sup>1</sup> , T. del Río-Gaztelurrutia<sup>1</sup> , E. Ravanis<sup>3</sup> , A. Cardesín-Moinelo<sup>3,4</sup> , K. Connour<sup>5</sup> , D. Tirsch<sup>6</sup> , I. Ordóñez-Etxeberria<sup>1</sup> , B. Gondet<sup>7</sup>, S. Wood<sup>8</sup>, D. Titov<sup>9</sup>, N. M. Schneider<sup>5</sup> , R. Hueso<sup>1</sup> , R. Jaumann<sup>10</sup> , and E. Hauber<sup>6</sup> 

<sup>1</sup>Dpto. Física Aplicada I, EIB, Universidad País Vasco UPV/EHU, Bilbao, Spain, <sup>2</sup>Aula Espazio Gela, Escuela de Ingeniería de Bilbao, Universidad Del País Vasco UPV/EHU, Bilbao, Spain, <sup>3</sup>European Space Agency, ESAC, Madrid, Spain, <sup>4</sup>Instituto de Astrofísica e Ciências Do Espaço, Obs. Astronómico de Lisboa, Portugal, <sup>5</sup>Laboratory for Atmospheric and Space Physics, University of Colorado, Boulder, USA, <sup>6</sup>German Aerospace Center (DLR), Institute of Planetary Research, Berlin, Germany, <sup>7</sup>Institut D'Astrophysique Spatiale, CNRS/University Paris Sud, Orsay, France, <sup>8</sup>European Space Agency, ESOC, Darmstadt, Germany, <sup>9</sup>European Space Agency, ESTEC, Noordwijk, The Netherlands, <sup>10</sup>Freie Universität Berlin, Institute of Geological Sciences, Berlin, Germany

**Abstract** We report a previously unnoticed annually repeating phenomenon consisting of the daily formation of an extremely elongated cloud extending as far as 1,800 km westward from Arsia Mons. It takes place in the solar longitude (Ls) range of ~220°–320°, around the Southern solstice. We study this Arsia Mons Elongated Cloud (AMEC) using images from different orbiters, including ESA Mars Express, NASA MAVEN, Viking 2, MRO, and ISRO Mars Orbiter Mission (MOM). We study the AMEC in detail in Martian year (MY) 34 in terms of local time and Ls and find that it exhibits a very rapid daily cycle: the cloud growth starts before sunrise on the western slope of the volcano, followed by a westward expansion that lasts 2.5 h with a velocity of around 170 m/s in the mesosphere (~45 km over the areoid). The cloud formation then ceases, detaches from its formation point, and continues moving westward until it evaporates before the afternoon, when most sun-synchronous orbiters make observations. Moreover, we comparatively study observations from different years (i.e., MYs 29–34) in search of interannual variations and find that in MY33 the cloud exhibits lower activity, while in MY34 the beginning of its formation was delayed compared with other years, most likely due to the Global Dust Storm. This phenomenon takes place in a season known for the general lack of clouds on Mars. In this paper we focus on observations, and a theoretical interpretation will be the subject of a separate paper.

**Plain Language Summary** In September and October 2018, the Visual Monitoring Camera onboard Mars Express observed a spectacular water ice cloud extending as far as 1,800 km westward from the Arsia Mons Volcano on Mars. This curious extremely elongated cloud caught the attention of the public ([http://www.esa.int/Science\\_Exploration/Space\\_Science/Mars\\_Express/Mars\\_Express\\_keeps\\_an\\_eye\\_on\\_curious\\_cloud](http://www.esa.int/Science_Exploration/Space_Science/Mars_Express/Mars_Express_keeps_an_eye_on_curious_cloud)). We study this Arsia Mons Elongated Cloud (AMEC) with the aid of several instruments orbiting Mars. We find that the AMEC repeated regularly each morning for a number of months, and that it is an annually repeating phenomenon that takes place every Martian year around the Southern Hemisphere during spring and summer. The AMEC follows a rapid daily cycle: it starts to expand from Arsia Mons at dawn at an altitude of about ~45 km, and for ~2.5 h it expands westward as fast as 170 m/s (around 600 km/h). The cloud then detaches from Arsia Mons and evaporates before noon. In previous Martian years, few observations of this phenomenon are available because most cameras orbiting Mars are placed in orbits where they can only observe during the afternoon, whereas this cloud takes place in the early morning, when the observational coverage is much lower.

### 1. Introduction

Water ice clouds are present throughout the Martian year (MY) with large temporal and spatial variability (R. Clancy et al., 2017; Wang & Ingersoll, 2002; Wolff et al., 2019). They have been observed from ground-based telescopes (Herschel, 1784; Slipher, 1927; S. A. Smith & Smith 1972), orbiting spacecraft (Curran et al., 1973; Leovy et al., 1973, 1971), and rovers (Kloos, 2016; Wolff et al., 2005).

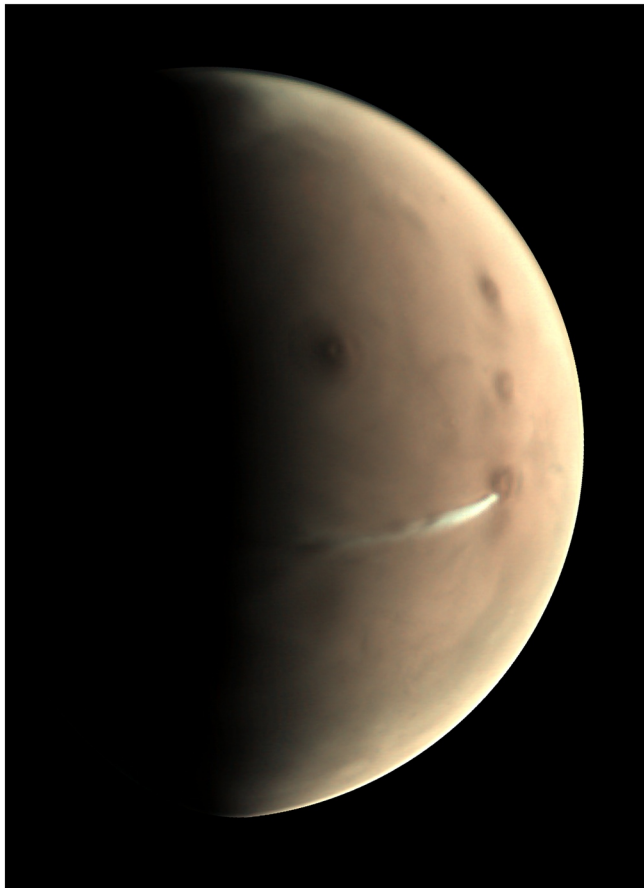


**Figure 1.** The elongated cloud extending around 1,800 km to the west from Arsia Mons volcano on October 10, 2018 (MY34). Image acquired by the VMC camera onboard MEX. ESA press release: [http://www.esa.int/Science\\_Exploration/Space\\_Science/Mars\\_Express/Mars\\_Express\\_keeps\\_an\\_eye\\_on\\_curious\\_cloud](http://www.esa.int/Science_Exploration/Space_Science/Mars_Express/Mars_Express_keeps_an_eye_on_curious_cloud).

Prominent clouds are commonly found in the region of Tharsis, and have been noticed since the telescopic era (Slipher, 1927; S. A. Smith & Smith, 1972). Based on early topographic maps, Sagan et al. (1971) proposed a topographic origin for these clouds over Tharsis and other high-altitude regions. The observations of the Mariner and Viking missions supported this idea and confirmed the water ice composition (Curran et al., 1973; Peale et al., 1973). More recently, Michaels et al. (2006) have shown in a mesoscale model how the circulation induced by giant volcanoes injects large amounts of aerosols into the global circulation.

Water ice clouds on Mars, including the topographic ones, are most commonly seen as part of the Aphelion Cloud Belt (ACB) in the season around the solar longitude ( $L_s$ )  $\sim 40^\circ$ – $140^\circ$  (R. Clancy et al., 2017, 1996; James et al., 1996). Benson et al. (2003, 2006) studied the seasonal distribution of clouds around the giant volcanoes on Mars using afternoon observations, and found that the volcanoes usually lack clouds during the dusty season, in the  $L_s$  range  $\sim 200^\circ$ – $360^\circ$ . Arsia Mons is an exception to this, as it shows cloud activity in the  $L_s$  range  $245^\circ$ – $322^\circ$ , while in general little cloud activity is found on Mars in this season (Benson et al. 2006, 2003; Wang & Ingersoll, 2002).

There is a bias in the local time of observations made by orbiting spacecraft that could affect our knowledge of the life cycle of Martian water ice cloud systems, which is that most observations in the past 2 decades of Mars exploration have been acquired by spacecraft in afternoon sun-synchronous orbits (whose observations are centered at local afternoon). This is the case for the Mars Global Surveyor (MGS), Mars Odyssey (later shifted to 7 a.m.–7 p.m. local times; M. D. Smith, 2019a), and Mars Reconnaissance Orbiter (MRO). Until 2014, when MAVEN (Mars Atmosphere and Volatile Evolution) and the Mars Orbiter Mission (MOM) arrived at Mars, Mars Express (MEX) was the only mission in a non-sun-synchronous orbit. The ExoMars Trace Gas Orbiter (TGO), which arrived in 2016 and began science operations in 2018, is also in a non-sun-synchronous orbit.

Given this observational bias, few authors have researched the daily evolution of water ice clouds. Hunt et al. (1980) studied the daily evolution of several orographic clouds based on Viking images, and Akabane et al. (2002) used ground-based telescopic observations (see also Glenar et al., 2003). Other authors (e.g., Wilson et al., 2007) took advantage of the night side observations of afternoon sun-synchronous missions to analyze the behavior of clouds during the night. More recently, Smith et al. (2019a) compared THEMIS observations from before and after the shift in the local time of the Mars Odyssey sun-synchronous orbit. Afternoon sun-synchronous orbiters can only be used to study variations within a few hours around the afternoon, given the narrow range of different local times covered by their field of view (Benson et al., 2003, 2006; Wolff et al., 2019). Landers and rovers are also suitable observers of the diurnal variations (Kloos et al., 2018; Sutton et al., 1978). More observations from non-sun-synchronous orbiters (e.g., Giuranna et al., 2019) are necessary to achieve a full comprehension of the diurnal variability of the Martian climate.

We report the observation of a previously observed but unnoticed phenomenon, that is, the formation of an extremely Elongated Cloud extending to the west from the Arsia Mons volcano (Figure 1). We first noticed this phenomenon in 2018 (MY34), as a result of the better observational conditions favored by the MEX and MAVEN orbits. We then found this phenomenon in archived images from previous years, always around the same season, in the  $L_s$  range  $220^\circ$ – $320^\circ$ , which included the Southern solstice ( $L_s$   $270^\circ$ ) and the perihelion ( $L_s$   $251^\circ$ ). This Arsia Mons Elongated Cloud (AMEC) develops in the early morning and dissipates before afternoon; this is why it was seldom observed by the instruments on missions in afternoon sun-synchronous orbits, such as the Mars Color Imager (MARCI) on MRO or Mars Orbiter Camera (MOC) on MGS.

**Table 1**  
*Spacecraft and Instruments Temporal Coverage*

Instrument	Spacecraft	Number of observations	Spatial resolution (km px <sup>-1</sup> )	MY
VMC	MEX	63	12	29,30,31,33,34
HRSC	MEX	3	1	33,34
OMEGA	MEX	1	5	34
IUVS	MAVEN	29	10	34
MCC	MOM	3	1	32
VIS	Viking 2	2	1	12
MARCI	MRO	*	1	*

*Notes.* Table 1: For each instrument, we specify the number of observations, the typical spatial resolution of the images in our dataset, and the MY. Refer to Tables S1–S6 in the supporting material for further details. In the case of VMC, the actual number of images is much larger than the number of observations, since each observation consists of a number of similar images with different exposure times. \*Since MARCI is used only for support and performs daily systematic observations, we do not indicate the number of observations or the MYs covered.

The occurrence of the AMEC in this particular season is likely related to a specific coincidence of atmospheric conditions such as winds, temperatures, pressure, and water vapor content in the region. Since the cloud seems to occur at every MY, we are interested in the interannual variability of the phenomenon, and its possible value as a proxy for the general state of the atmosphere in different MYs (Sánchez-Lavega et al., 2018b). We note that the 2018 observations of the AMEC were after the Martian Global Dust Storm (GDS) of 2018 (Guzewich et al., 2019; Sánchez-Lavega et al., 2019), and GDSs are the most conspicuous Martian events that exhibit interannual variability. In fact, Benson et al. (2006), based on afternoon observations, reported lower cloud activity over Arsia Mons following the 2001 GDS, compared to the previous MY.

In this first paper, we analyze observations of the AMEC. We start our analysis by focusing on MY34 (which corresponds to observations in 2018), as most available observations of the AMEC correspond to this year. Then, we compare the characteristics of the AMEC in MY34 with all available observations from previous years, in search of interannual variations. A theoretical analysis of the phenomenon will be the subject of a separate paper.

In Section 2, we describe our observations and methods. In Section 3, we briefly describe the Tharsis region and the topographic profiles of the four giant volcanoes, including Arsia Mons. In Section 4, we describe the

daily cycle followed by the AMEC, from twilight to noon and afternoon, as inferred from observations in MY34. In Section 5, we show several morphologic and dynamic features of the cloud and describe its seasonal evolution. In Section 6, we measure the altitude of the cloud. In Section 7, we compare MY34 with observations from previous years, with a special interest in interannual variations. Finally, in Section 8 we summarize our observations and present our conclusions.

## 2. Observations and Methods

In this study, we have taken advantage of a variety of imaging systems onboard different spacecraft (Table 1 and Figure 3):

1. VMC (visual monitoring camera) (Ormston et al., 2011; Sánchez-Lavega et al. 2018a), onboard MEX, is a low-resolution RGB color camera that usually observes from the apoapsis of the MEX orbit at 10,500 km (details on the orbit and VMC operations can be found in Ravanis et al., 2020). Images are usually taken in a series covering several minutes, enabling the measurement of atmospheric motions from the tracking of clouds and dust features (Hernández-Bernal et al., 2019)
2. HRSC (high-resolution stereo camera) (Jaumann et al., 2007) onboard MEX is a high-resolution pushbroom camera that takes images in nine different channels at different altitudes along the highly elliptical orbit
3. OMEGA (Observatoire pour la Minéralogie, l'Eau, les Glaces et l'Activité) (Bibring et al., 2004) onboard MEX, is an imaging spectrometer that takes images simultaneously in several spectral bands
4. IUVS (imaging ultraviolet spectrograph) (Connour et al., 2020; McClintock et al., 2015) onboard MAVEN is a scanning-slit spectrograph that takes composite false color UV images of Mars. IUVS acquires data during nearly every MAVEN orbit with a cadence of ~4.5 h, enabling it to image recurring phenomena
5. MCC (Mars color camera) (Arya et al., 2015) onboard ISRO (Indian Space Research Organization) MOM, is an RGB color camera that acquires images at different altitudes from a highly elliptical orbit, usually with high resolution
6. VIS (visual imaging system) (Wellman et al., 1976) onboard Viking 2 orbiter was a single-channel visible camera of high resolution. Viking orbiters were in highly elliptical non-sun-synchronous orbits
7. MARCI (Mars color imager) (Bell et al., 2009) onboard MRO is a pushbroom camera that observes Mars during the afternoon from an afternoon sun-synchronous orbit, achieving high-resolution coverage of

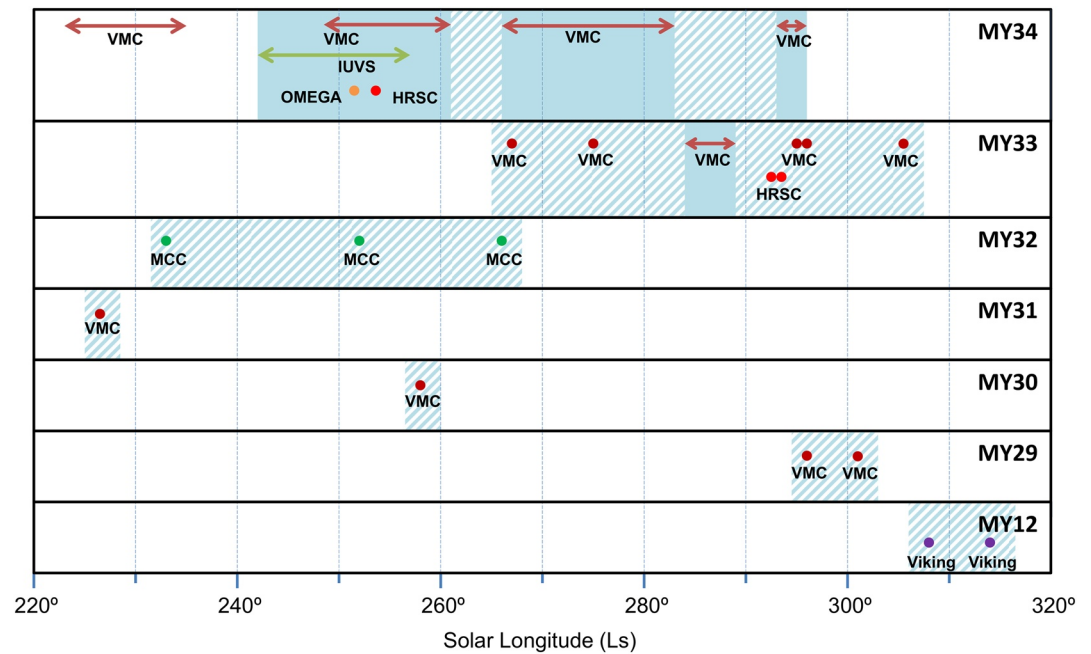


**Figure 2.** Seasonal coverage of Arsia Mons observations by different instruments. Colored points represent single observations and arrows represent periods with continuous observations (at least every few sols). Only observations between 5 and 10 LTST (local true solar time) are included. Positive observations (i.e., with the AMEC present) are indicated by the background color. Flat colored areas indicate continuous observations, and striped areas infer the probable minimum duration of the phenomenon. Single positive observations are indicated by a small striped area. The actual duration of the phenomenon is very likely longer than shown here for most MYs, as few suitable observations are available before MY34, and they are all positive. This figure will be discussed again in Section 7, as part of the interannual comparison. Refer to Tables S1–S6 in the supporting material for further details.

the whole planet every Martian sol. As MARCI only observes during the afternoon, it has never imaged the AMEC itself; therefore, we use MARCI for support in the understanding of the AMEC daily cycle (Section 4)

This includes all current missions in non-sun-synchronous orbits, except TGO. We have excluded TGO since its only camera, CASSIS (color and stereo surface imaging system), has a narrow field of view and thus it is not likely to have imaged the AMEC.

The largest set of observations corresponds to MY34, spanning the orbital longitude range from Ls 223° to Ls 296°. This set comprises about 75 observations obtained with the instruments VMC, IUVS, HRSC, and OMEGA, together with some MARCI observations. The use of this set of instruments has allowed us to follow the evolution of the phenomenon in MY34, both throughout the season and at a broad range of local times. There are far fewer observations from other MYs. Examples of images obtained by the various instruments used here are shown in Figure 3. Details of how the images from different instruments were processed and measured can be found in the supporting information. In general, we consider that a detection is positive if we find a morning cloud near the volcano or an elongated cloud west to the volcano, even if the volcano is not present in the image.

We used the geometry package Elcano (Hernández-Bernal et al., 2019, see for example Figure 1) for the navigation of VMC, Viking/VIS, and MCC images and for geometrical calculations in general. When necessary, spacecraft geometric information was extracted from SPICE (C. H. Acton 1996; C. Acton et al., 2018), with SPICE kernels provided by NASA NAIF in the case of MAVEN, MRO, and Viking, and ESA SPICE Service in the case of MEX (Costa, 2018). In the case of MCC, we used kernels distributed by ISRO, and gaps in these kernels were covered through geometric information provided in the labels of MCC publicly available products. MARCI images were navigated and projected with the aid of the ISIS3 software package

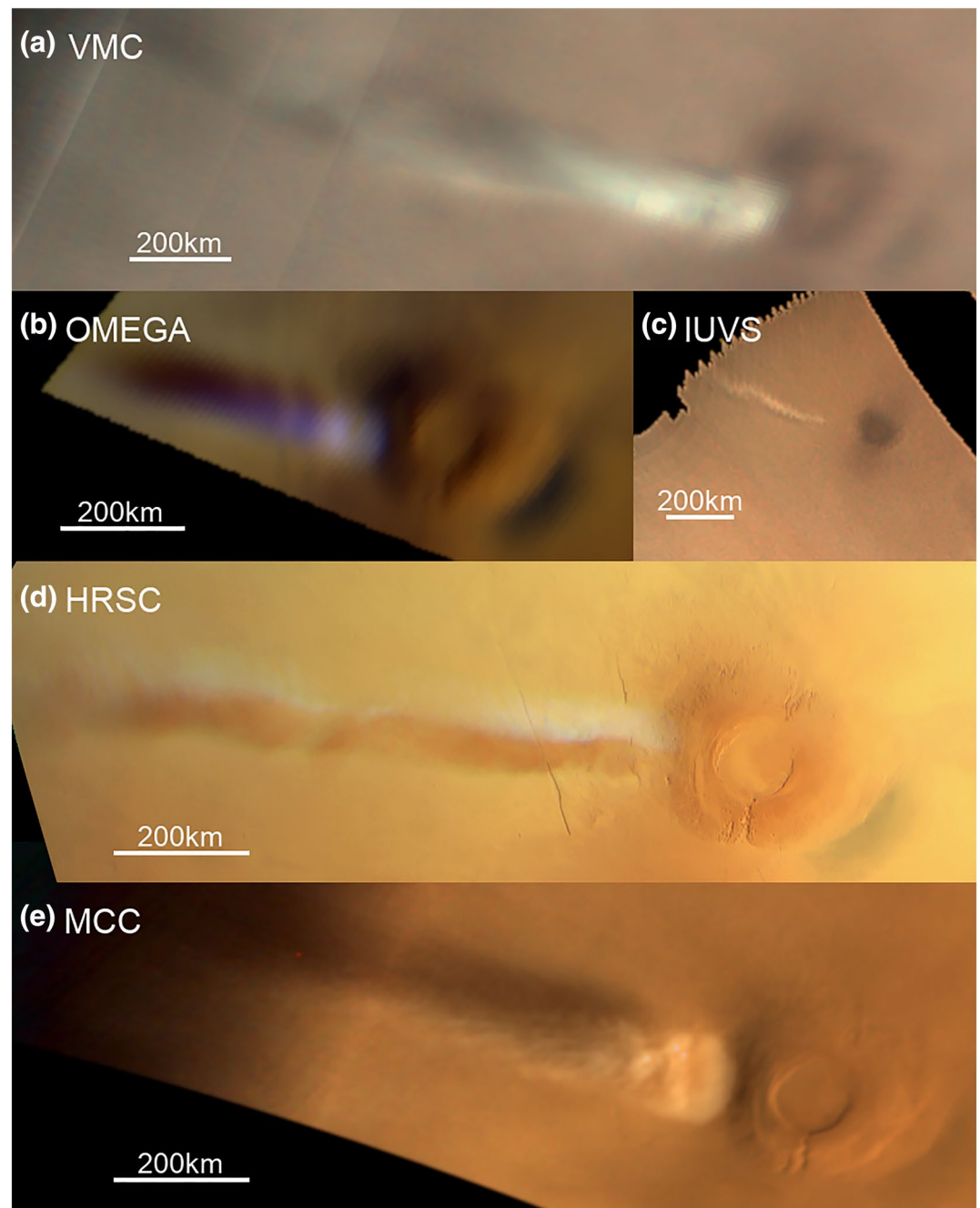


**Figure 3.** Examples of images from different instruments. Panels (a)–(e) show cylindrical projections of images displaying the AMEC at Arsia Mons. (a) VMC observation; October 22, 2018, MY34, Ls 274°, LTST 7.8 (VMC observation 180371). (b) OMEGA observation; September 17, 2018, MY34, Ls 252°, LTST 7.5 (MEX orbit 18612). (c) IUVS observation from apocenter; September 7, 2018, MY34, Ls 245°, LTST 8.9 (MAVEN orbit 7673). (d) HRSC observation; September 21, 2018, MY34, Ls 254°, LTST 8.5 (MEX orbit 18627). (e) MCC observation; December 13, 2014, MY32, Ls 252°, LTST 6.7 (MCC product MCC\_MRD\_20141213T134802312\_D\_GDS).

(Edwards, 1987). We projected the images onto cylindrical maps after correction of their luminosity (for uniformity near the terminator) before making measurements (see details in supporting material).

For topographic calculations (precise geometry calculations, and shadow measurements) we used Mars Orbiter Laser Altimeter (MOLA) data (D. E. Smith et al., 2001), and for topographic maps we use the topog-

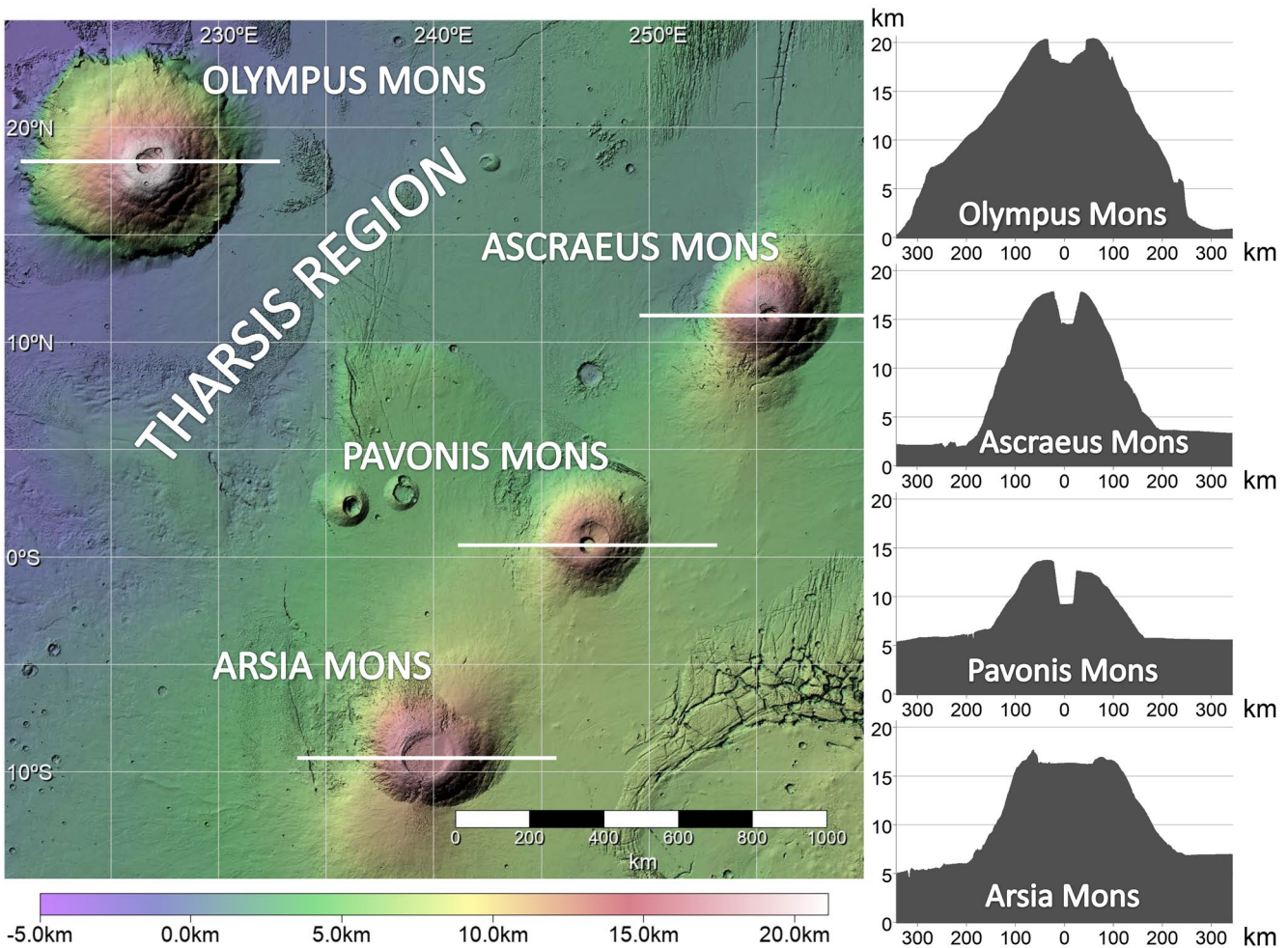


**Figure 4.** Topography of the Tharsis region from the MOLA–HSRC data plot with hillshading (Ferguson et al., 2018). The four giant volcanoes are apparent. The right panels show topographic profiles for each volcano from MOLA. Altitudes are relative to the areoid.

topography produced by Ferguson et al. (2018) from MOLA and HRSC data. All altitudes in this paper are given relative to the areoid as defined in the MOLA data. For time calculations, we used algorithms and definitions described by Allison (1997) and Allison and McEwen (2000), and the enumeration of MYs proposed by R. T. Clancy et al. (2000). All local true solar times (LTSTs) mentioned in this paper refer to the position of the volcanic rim of Arsia Mons volcano (239.5°E, 9.2°S), unless otherwise indicated.

Linear regressions shown in Figures 6, 7, and 12 are calculated using orthogonal distance regression, which takes into account error in both the variables.

### 3. Topography of the Tharsis Region

The most prominent volcanic provinces on Mars are the Elysium region, Alba Mons, and the Tharsis Region, which contains the four tallest volcanoes on Mars: Olympus Mons, Ascaeus Mons, Pavonis Mons, and Arsia Mons (Figure 4). The entire Tharsis area is considerably higher than the mean altitude of the Martian surface.

Figure 4 shows a topographic map and the vertical profiles along the central axis of the four Tharsis volcanoes. The summits of the four volcanoes are ~8–20 km above their surrounding area, and at their base they extend ~300–500 km in diameter. All of the volcanoes also have depressed calderas in the range of ~50–100 km in diameter and 1–4 km in depth.

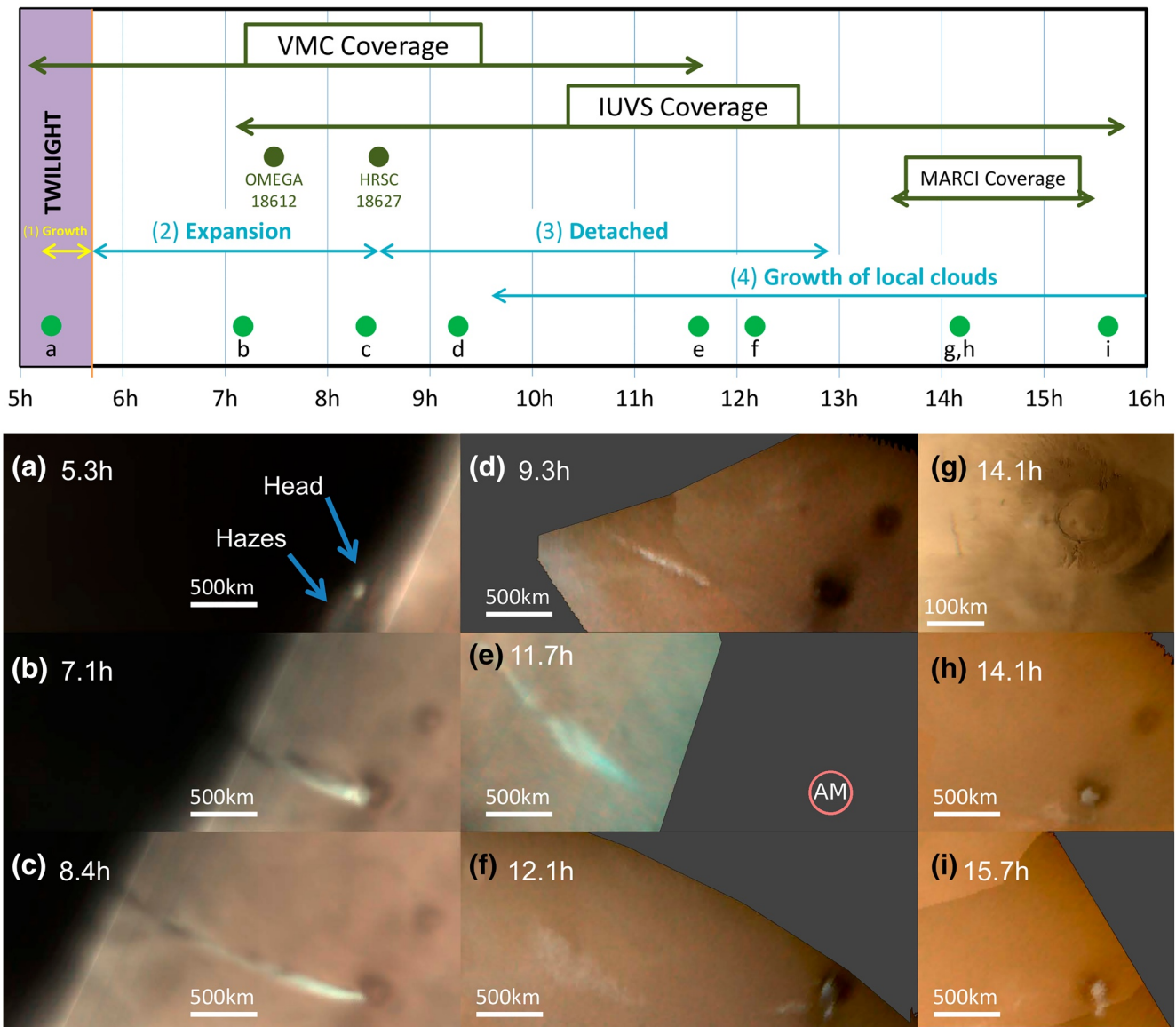


**Figure 5.** Daily cycle of the AMEC in MY34. Top panel: Phases of the cloud evolution and instrument coverage as a function of LTST indicated in Martian hours. Transition time between phases is represented at a fixed time for simplicity, but there is obviously a degree of sol-to-sol variability (see main text for details). Local times of the images in the bottom panel are indicated by green marks. Bottom panel: examples showing the appearance of the cloud at different local times on cylindrical projections. Gray areas represent non-imaged regions, dark areas correspond to the night. (a) Phase 1. Cloud in twilight, around 30 km above the local areoid; October 1, 2018, Ls 261° (VMC observation 180340). (b) Phase 2. The cloud is around 1,000 km in length; October 16, 2018, Ls 270° (VMC observation 180362). (c) Phase 2. The cloud is around 1,800 km in length; October 10, 2018, Ls 266° (VMC observation 180352). (d) Phases 3 and 4. The cloud is detached and thin clouds are visible on the western slope of Arsia Mons; September 22, 2018, Ls 255° (IUVS, MAVEN orbit 7757). (e) Phase 3. Detached AMEC, Arsia Mons was not imaged and its position is indicated; October 11, 2018, Ls 267° (VMC observation 180354). (f) Phases 3 and 4; September 21, 2018, Ls 254° (IUVS, MAVEN orbit 7752). (g) Phase 4; October 1, 2018, Ls 260° (MARCI product K09\_057091\_2603\_MA\_00N118W). (h) Phase 4; August 31, 2018, Ls 241° (IUVS, MAVEN orbit 7635). (i) Phase 4; August 27, 2018, Ls 238° (IUVS, MAVEN orbit 7613).

#### 4. Daily Cycle of the Cloud in MY34

The AMEC daily cycle was observed in detail in MY34. In the Ls range of 242°–296°, the AMEC was always present in the early morning. The first observation of the AMEC was performed by IUVS on September 2, 2018 (Ls 242°). Prior to that date, the cloud was not present in suitable observations by VMC in August, in the Ls range 223°–235°. The last image of the AMEC was obtained by VMC on 28 November (Ls 296°) and the region was not observed by VMC later in the season. Orbital and operational constraints prevented



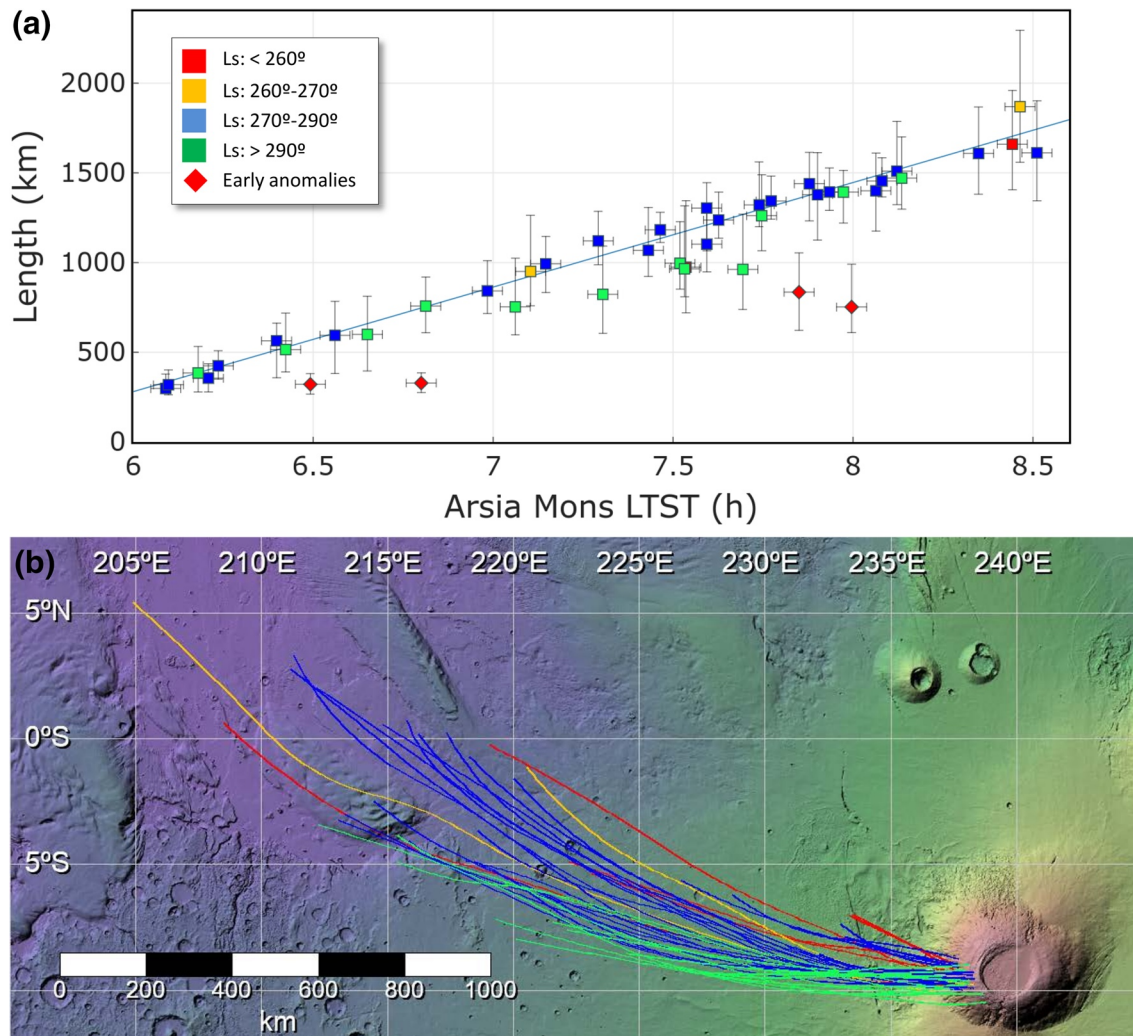


**Figure 6.** Expansion phase of the AMEC. (a) Length of the cloud as a function of LTST. Point uncertainties are calculated as explained in Supplementary Text S3. For long observations, only a representative part of all the available images are represented, separated by  $\sim 15$  min. Linear fit (early anomalies excluded) gives an expansion velocity of  $170 \pm 10 \text{ ms}^{-1}$ . (b) Cloud trajectories (traced manually) on a topographic map (the same map as seen in Figure 4). Color codes indicate the Ls ranges given in the legend in (a).

observations of Arsia Mons by MAVEN after Ls  $\sim 260^\circ$ . While more than 80 Martian sols separate the first and last observations, the AMEC phenomenon is likely to have started earlier (sometime between Ls  $235^\circ$ , when there is a negative observation, and Ls  $242^\circ$ , when there is a positive observation) and to have continued later than Ls  $296^\circ$ , since it was observed in an equivalent season in previous years (Figure 2).

In what follows, we use the word “tail” to refer to the elongated part of the AMEC, and “head” to refer to the easternmost side of the cloud, next to the volcano where it starts developing. Further details on the morphology of the cloud are given in Section 5.

During the period studied, the AMEC showed remarkable repeatability in its morphological evolution, following a well-defined daily cycle with different phases that are summarized in Figure 5. We identified the following phases, which we will describe in detail below:

1. Cloud head formation: Before sunrise, the head of the cloud forms and grows in area, probably due to ascending motions (Figure 5a). As the observation period is around the southern solstice, there were no notable variations of sunrise time at 5.7 LTST, and thus insolation as a function of LTST was practically non-variable during the season

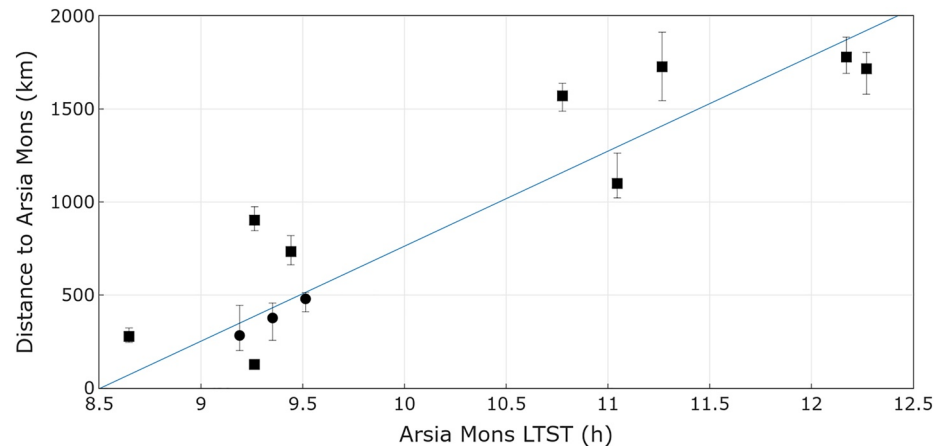


**Figure 7.** Distance of the cloud head to Arsia Mons as a function of LTST during the detachment phase. Point uncertainties are calculated as in Figure 6a. Circles correspond to three measurements within the same VMC observation. Squares represent IUVS observations, each corresponding to a different sol. Due to the coverage limitations, all these observations correspond to the Ls range 240°–260°.

2. Tail expansion: After sunrise, the cloud rapidly expands westward to generate the distinctive elongated tail (Figures 5b and 5c)
3. Detachment and decay: At around 8.3–8.7 LTST, the cloud formation ceases, detaches from its formation point, and the complete cloud moves westward due to advecting winds until it evaporates before afternoon. Throughout the rest of the morning, the tail keeps moving to the west while slowly fading, probably due to evaporation (Figures 5d–5f)
4. Local clouds: At around 11 LTST, and simultaneously with a decay of the tail in (3), new local clouds, distinct from the AMEC, distributed around the volcano, and smaller in area, begin to form around Arsia Mons. The formation of these clouds always starts on the western slope, and then grows to cover the volcano. A few observations show the presence of local clouds earlier than 11 LTST (for example, in Figure 5d), but they do not grow significantly until 11 LTST. Similar clouds are observed later in the day by MARCI and IUVS (Figure 5d and 5f–5i), and are well known (Benson 2003,2006; Wang & Ingersoll, 2002), but they may not be associated with the occurrence of the AMEC elongated cloud

#### 4.1. Phase 1. Cloud Head Formation in Twilight

VMC images of Arsia Mons taken some minutes before sunrise show the formation of a “twilight cloud” west of the volcano caldera, at  $\sim 237^\circ\text{E}$  and  $9.5^\circ\text{S}$  (Figure 5a). The cloud forms during nighttime, and sunlight starts illuminating the cloud tops before sunrise because of their altitude of  $30 \pm 5$  km above the Martian areoid (Hernández-Bernal et al., 2018). Diffuse hazes extending to the south of the cloud accompany the head during this twilight phase (Figure 5a).

#### 4.2. Phase 2. Westward Expansion of the Tail

For  $\sim 3$  h after sunrise, the cloud grows rapidly in length forming the AMEC phenomenon (Figures 5b and 5c). We measured the length of the cloud (following its curvature) from available VMC images throughout the season and corresponding to different local times (Figure 6). When a VMC series was long enough, we measured several images in the series, always separated by at least 15 min to make sure that the variation between images was significant.

Figure 6a shows the tail length against local time (from 6 to 8.5 h LTST). Only observations where the whole cloud is visible are included (discarding those images where the cloud penetrates the terminator). The growth is approximately linear, and a linear fit gives an apparent expansion velocity of  $170 \pm 10\text{ms}^{-1}$ . Assuming a constant rate, and considering the initial size of the head to be around 125 km (see section 5.1),

the linear fit indicates that the expansion from that size initiates at around  $5.8 \pm 0.2$  LTST (the local sunrise is at 5.7 LTST). The maximum length of the AMEC was measured on 10 October (Ls 266°), with a tail of around 1,800 km in length.

In some of the early sols (September 2018), the cloud was shorter than the value expected at the corresponding local time from the general trend, pointing toward some sol-to-sol and/or seasonal variability. These early anomalies are indicated by the diamonds in Figure 6a, and could be due to the fact that GDS 2018 was in its decaying stage throughout that period (Guzewich et al., 2019).

Figure 6b illustrates the extension of the cloud tail at different local times and epochs. The concavity of the curved trajectories is always to the north, suggesting advection of the cloud by persistent combined zonal (westward) and meridional (northward) winds. Due to variations of existing winds, the curvature of the tail varies from sol-to-sol, with local time, and with Ls.

### 4.3. Phase 3. Detachment and Decay

At some point around 8.3–8.7 LTST, the cloud detaches from its formation point in Arsia Mons. For example, we see the cloud attached at 8.4 LTST in Figure 5c, and already detached at later local times in Figures 5d and 5e. Some VMC images show that the cloud head narrows before its detachment (Figure 5c, supplementary animation S3), and IUVS observations capture detached clouds after 8.7 LTST (Figure 5d). At the beginning of this phase, there is no remnant cloud activity in the vicinity of Arsia Mons, as the whole cloud moves away from the volcano. Figure 7 shows the distance of the head of the cloud from the location on Arsia Mons where it formed, as measured in the IUVS and VMC images. It shows a linear trend, with large dispersion indicating sol-to-sol variability. A linear fit gives a detachment velocity of  $150 \pm 30 \text{ ms}^{-1}$ . All observations represented in this graph were acquired before Ls 260°, that is, in the period of the early anomalies mentioned in Section 4.2, since due to limited coverage, there are no images of a detached cloud later in the season.

As the sol progresses, both IUVS and VMC observations of the detached cloud reveal a fainter and more turbulent elongated cloud (Figures 5e and 5f). The AMEC eventually disappears, and is no longer visible in IUVS observations at 13 LTST.

### 4.4. Phase 4. New Clouds at Arsia Mons

As the head of the AMEC continues to move away from the base of the volcano, new clouds form over Arsia Mons. A few IUVS images show the development of faint clouds on the western slope of the volcano as early as 9.3 LTST (Figure 5d), but most clouds develop after 11 LTST, and they continue to be present until the last IUVS observation at 15.7 LTST (Figures 5h and 5i). Higher resolution images obtained by MARCI at around 14.0 LTST also show those clouds (Figure 5g). These afternoon clouds appearing around Arsia Mons in this season were also reported in Wang & Ingersoll (2002) and Benson et al. (2003, 2006) and may not be related to the AMEC elongated cloud.

## 5. Morphology and Dynamic Features in MY34

In this section, we describe the morphology of the AMEC, and some further dynamical aspects of the phenomenon.

### 5.1. Position and Size of the Head of the AMEC before Detachment

We measured the position and size of the head of the cloud throughout different local times and sols (Ls) in the VMC images (Figures 8a and 8b). Error was estimated manually, taking into account the limited quality of the images and the diffuse boundaries of the clouds. Approximating the eastern boundary of the head to a semicircle, we determined its diameter and center, and used them as a measure of size and location, respectively. Examples of actual head morphologies can be found in Figure 9. The head diameter ranged from 50 to 250 km with a typical value of about 125 km. Because of the dispersion of the data, it is difficult to retrieve a clear temporal evolution of the head size as a function of LTST or Ls (Figures 8c and 8d). There

are hints of a quick head formation early in the morning, reaching a maximum size of  $\sim 175$  km at  $\sim 7$  LTST, and then decreasing to around 75–100 km at 8.5 LTST, with no clear trend as the season evolves.

The central latitude of the head was most often in the range of  $8.5^{\circ}$ – $10^{\circ}$ S, within the range of latitudes of the Arsia Mons caldera. The easternmost longitude, related to the presence of the cloud on the flank of the volcano, was always lower than  $238.5^{\circ}$ E, that is, not reaching the caldera (Figure 8f). The easternmost longitude of the head center occurred in the range  $L_s \sim 270^{\circ}$ – $275^{\circ}$ . Although measurements of the position of the cloud might be biased by the effect of parallax, given the estimated height of the cloud (see Section 6), this effect is always within the range of error of our measurements.

## 5.2. Morphology of the AMEC during the Expansion Phase

VMC reveals a rich variety of morphologies, particularly in the head of the cloud, during the expansion phase of the AMEC from 6.5 to 8.5 LTST, when the cloud morphology is already well developed. A scheme of the different features that we observe is presented in Figure 9a.

The earliest occurrences of the AMEC in the season show a small head and a tail with an approximately constant width, similar to the size of the head, and with no signs of turbulence (Figure 9b). This morphology (Type I) was commonly observed before  $L_s 256^{\circ}$ , and different observations differ mainly in the brightness of the tail. Following a gap with no suitable observations for this classification until  $L_s 266^{\circ}$  (see Figure 2), different morphologies are observed at different LTSTs. In the early hours ( $\sim 6.9$ – $7.6$  LTST) the AMEC shows a Type II morphology (Figure 9c), with a bright textured head and smooth narrowing of the neck into a tail of decreasing width. Later in the day ( $\sim 7.3$ – $8.4$  LTST), we find Type III morphology, with a darker region separating the tail from a still bright head (Figure 9d). This morphology is often associated with a more undulating tail. Finally, prior to detachment ( $\sim 8.2$ – $8.6$  LTST), we often observe Type IV morphology, with a diminishing head and a broad tail that narrows away from Arsia Mons (Figure 9e).

## 5.3. Other Features

Although the AMEC can be generally described with the four typologies defined above, there are some variations and extra features worth mentioning.

In some images taken early in the season ( $L_s 249^{\circ}$  and  $253^{\circ}$ ) of appearance of the AMEC phenomenon, the tail of a cloud of Type I morphology is very thin, and the bright head and the dark elongated shadow of the tail dominate the image (Figure 9f). The brightness of the cloud and the visibility of the shadow might be affected by the observation geometry.

Images often show the presence of hazes close to the AMEC. At dawn, the hazes are already visible on the night side of the terminator (see Figure 5a) and they persist into the early hours (see animations in supporting information). Later in the season (after  $L_s 275^{\circ}$ ) the AMEC is sometimes accompanied by less diffuse structures, forming cones that extend from its head at an angle of  $30^{\circ}$ – $60^{\circ}$  relative to the tail axis (Figure 9g).

In Figure 9h, the tail splits into two sections with slightly different directions (see animation S2 in supporting material), probably due to changes in the intensity and direction of the winds. Finally, the morphology of the tail is sometimes suggestive of bursts of cloud activity in the head advected by winds. Figure 9i shows a  $\sim 50$  km wide blob detaching from the head to the tail at 8.0 LTST, in a configuration that can be described as Type III. This observation continued with a transition to morphology IV, as can be seen in animation S3 in the supporting information.

## 5.4. Evolution throughout MY34

In addition to the marked daily cycle, the AMEC showed a longer term variability throughout the MY34. The phases of the daily cycle discussed in Section 4.2 were quite regular during the majority of the period studied, with the exception of some early anomalies, marked as red diamonds in Figure 6a. Cloud Type I occurs only in this early season, and in these anomalies the cloud usually develops later in the sol, and the cloud length is shorter at any given LTST. For example, on the 19 September there was no cloud at 6.1 LTST,

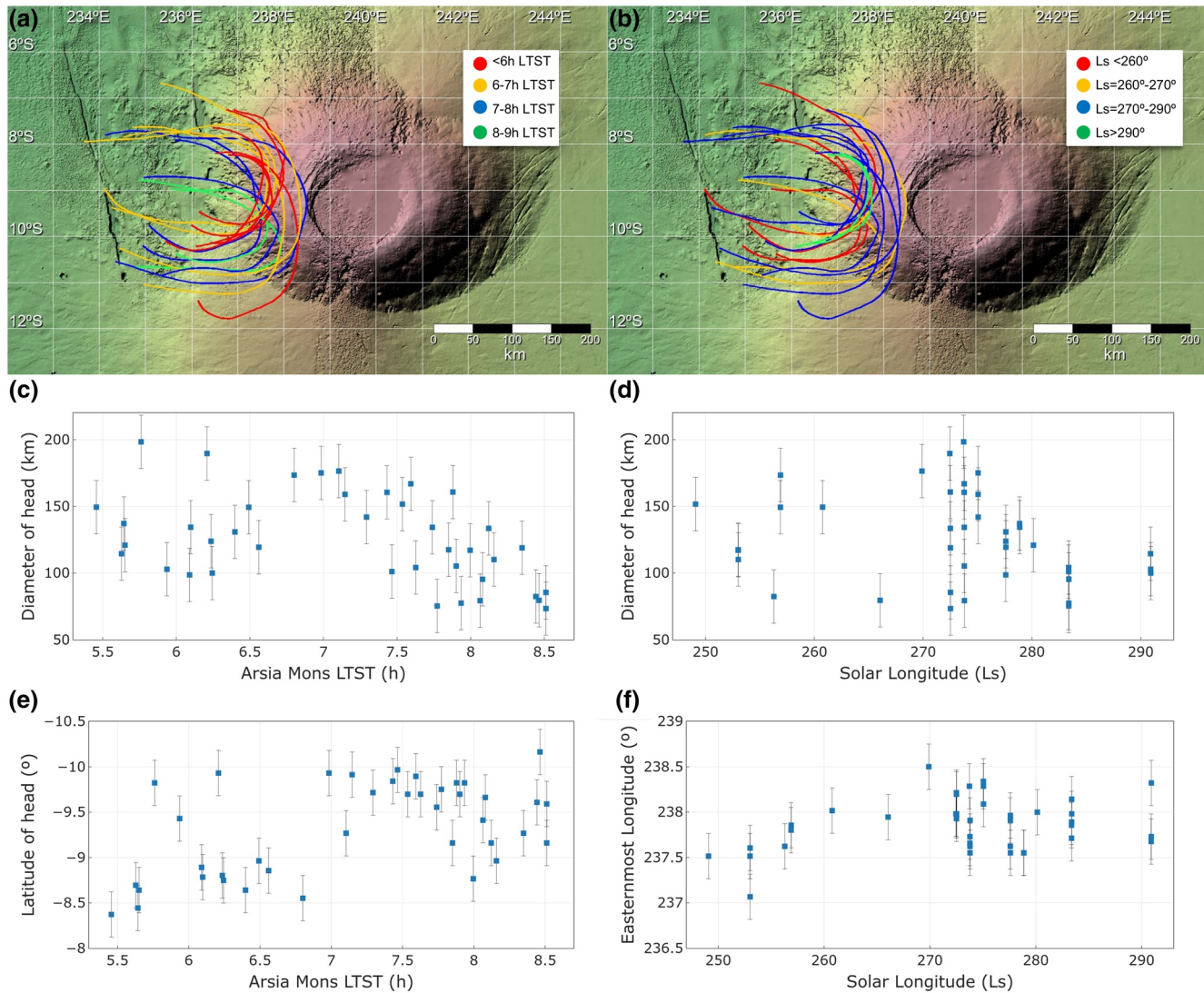


**Figure 8.** (a) and (b): Position and size of the head of the AMEC as a function of LTST and solar longitude (Ls). The curves (traced manually) represent the head contour and colors identify LTST in (a) and Ls in (b). (c) and (d) Head diameter as a function of LTST and Ls. (e) Latitude of the head center as a function of LTST. (f) Longitude of the head center as a function of Ls.

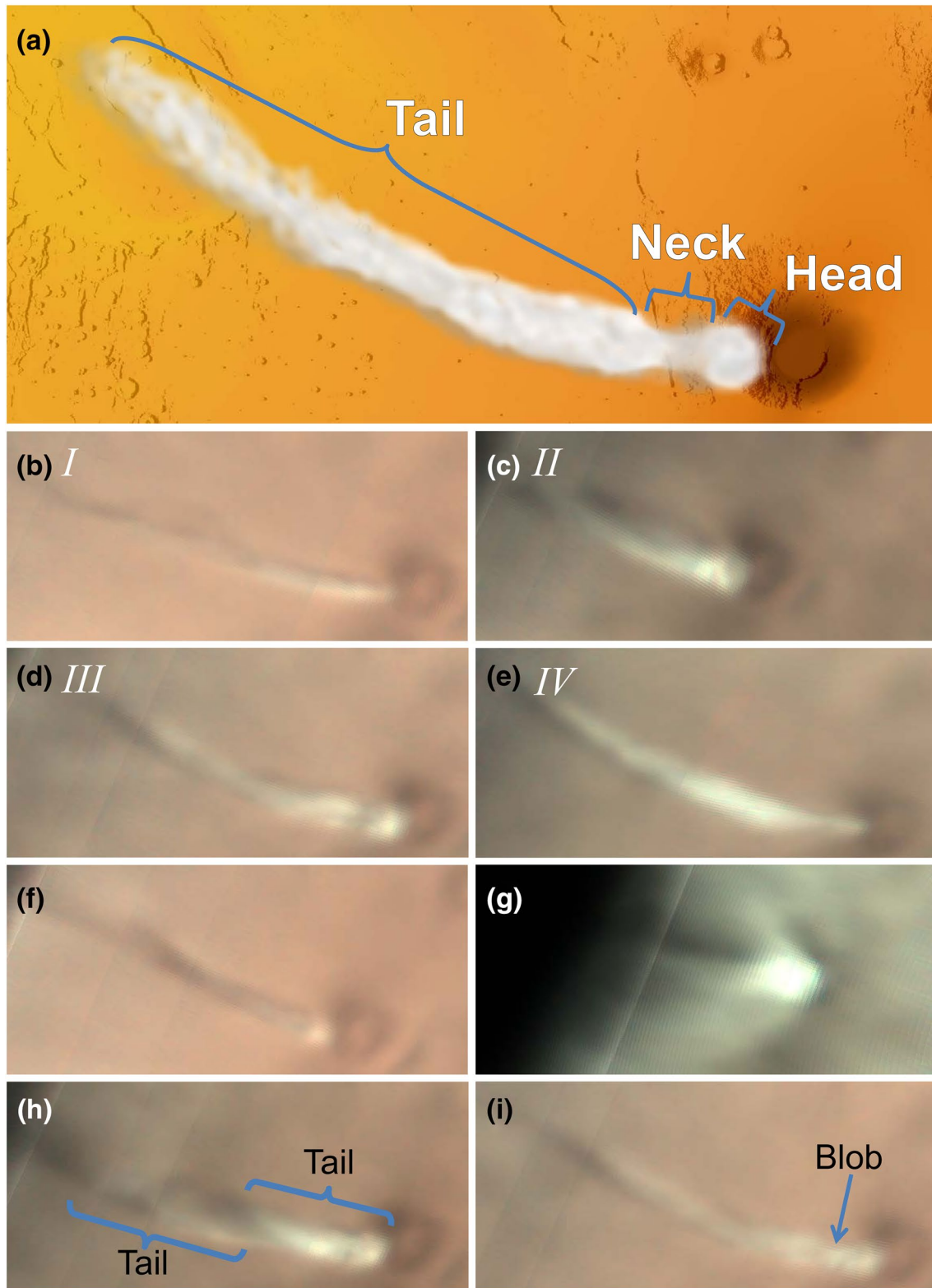
and the cloud was shorter than usual at 8.0 LTST (VMC observations 180317 and 180318). We also find clouds shorter than usual in VMC observation 180329 on 25 September at 6.9 LTST (Figure 10f), and in the OMEGA observation in orbit 18612 on 17 September at 7.5 LTST (Figure 3b). This difference in behavior at the beginning of the season was possibly due to the remaining presence of abundant dust from GDS 2018 (Guzewich et al., 2019).

## 6. Altitude of the Cloud and Limb Observation in MY34

We use three different methods to determine the AMEC altitude:

1. Analysis of shadows and illumination conditions
2. Visibility of the cloud tops during twilight (Hernández-Bernal et al., 2018)
3. Direct measurement from images of the AMEC phenomenon at the limb of Mars

The observations used in the analysis of the cloud altitude in MY34 are presented in Figure 10. All altitudes in this section are relative to the Martian areoid as defined by MOLA data. The accuracy of these measure-



ments is highly dependent on how sharp the border of the clouds is, as detailed in supporting material text S4.

Figures 10a and 10f shows the shadow projected by the cloud in two different stages of the phenomenon and with different illumination conditions. Figure 10a shows the cloud and its shadow as seen in high resolution by HRSC. We studied this shadow in three dimensions, taking into account the parallax effect due to the high altitude of the cloud, the position of the observer, and the local topography. We found that the tail of the cloud was around 40–50 km in altitude. The profile of heights along the tail is indicated by the blue line in Figure 10g. The uncertainty of these measurements is mostly due to the difficulty of determining the limits of the cloud and the shadow, because of the presence of surrounding hazes. It is interesting to note that, within measurement uncertainties, the head of the cloud is higher than the tail, and the farthest extreme of the tail is at a lower altitude.

Figure 10f is a low-resolution image acquired by VMC taken on a sol when the expansion of the cloud was delayed with respect to the trend established in Section 4 (an early anomaly). Local time at Arsia Mons is 6.8 LTST and the low solar elevation angle ( $\sim 15^\circ$ ) results in a long shadow that extends to the terminator. Simple geometry calculations indicate a minimum altitude of 45 km for the cloud tops and a vertical extension of the cloud of at least 5–10 km. The extension and altitude of this cloud is represented by the green area in Figure 10g.

Figures 10b and 10c shows images obtained with VMC of the AMEC cloud at the limb of Mars. The curves corresponding to the limb in these images are shown with white lines in Figure 10d. The limb observation shows aerosols around Arsia Mons and on its eastern side. Note that this observation was performed at Ls  $281^\circ$ , a season where hazes are also commonly observed in nadir observations of the region (Section 5.3). On the eastern side of Arsia Mons (yellow arrows in Figure 10c), optically thick aerosols are present up to an altitude of  $35 \pm 10$  km, and an optically thinner detached layer is present at altitudes of  $45 \pm 10$  km. On the western side of the volcano (cyan arrows in Figure 10c), the head appears at a slightly higher altitude next to Arsia Mons ( $\sim 50 \pm 10$  km) in agreement with measurements of the shadow in the HRSC image (see Figure 10g for comparison).

Figure 10e is a good example of a twilight observation by VMC. From an analysis of image sequences like this one, we constrained the top altitude of the cloud to be  $30 \pm 5$  km.

Finally, Figure 10g summarizes the results of our altitude measurements. Our results suggest that the cloud head rises during twilight, when we measure lower heights for the head cloud tops than at the start of expansion.

## 7. Interannual Comparison

We searched for the AMEC phenomenon in a survey of available images taken by Mars orbiters. We only found suitable observations (in the expected ranges of LTST and Ls) in MYs 29–33 (see Figure 2). We also include an observation in MY12, corresponding to the Viking 2 spacecraft. Poor coverage of earlier observations does not allow us to reveal the full seasonal cycle of the cloud appearance, but a conservative estimation from our observations is that it takes place between Ls =  $220^\circ$ – $320^\circ$ , although its lifespan might be longer (see Figure 2).

Figure 11 shows examples of images of the cloud in different MYs and in the following subsections we explore the potential interannual variability of the AMEC features.

**Figure 9.** Morphology of the AMEC cloud: (a) Scheme of different AMEC features over a synthetic representation, including the head, neck, and tail. (b)–(e) Examples of different morphologies. (b) Type I morphology; September 18, 2018, Ls  $256^\circ$ , LTST 8.5 (VMC observation 180326). (c) Type II morphology; October 18, 2018, Ls  $270^\circ$ , LTST 7.1 (VMC observation 180362). (d) Type III morphology; October 20, 2018, Ls  $272^\circ$ , LTST 7.9 (VMC observation 180366). (e) Type IV morphology; November 6, 2018, Ls  $283^\circ$ , LTST 8.1 (VMC observation 180397). (f)–(i) Examples of other features. (f) Bright head with a long dark tail that is, probably the shadow projected by the optically thin tail; September 13, 2018, Ls  $249^\circ$ , LTST 7.5 (VMC observation 180306). (g) Hazes in almost symmetrical angles occur  $\sim 50^\circ$  relative to the cloud tail; November 28, 2018, Ls  $296^\circ$ , LTST 6.6 (VMC observation 180424). (h) Two tails at once; October 22, 2018, Ls  $274^\circ$ , LTST 7.4 (VMC observation 180371). (i) Blob in the head being torn off from the head of the cloud (see animation S1 in supporting information); October 20, 2018, Ls  $273^\circ$ , LTST 8.1 (VMC observation 180366).

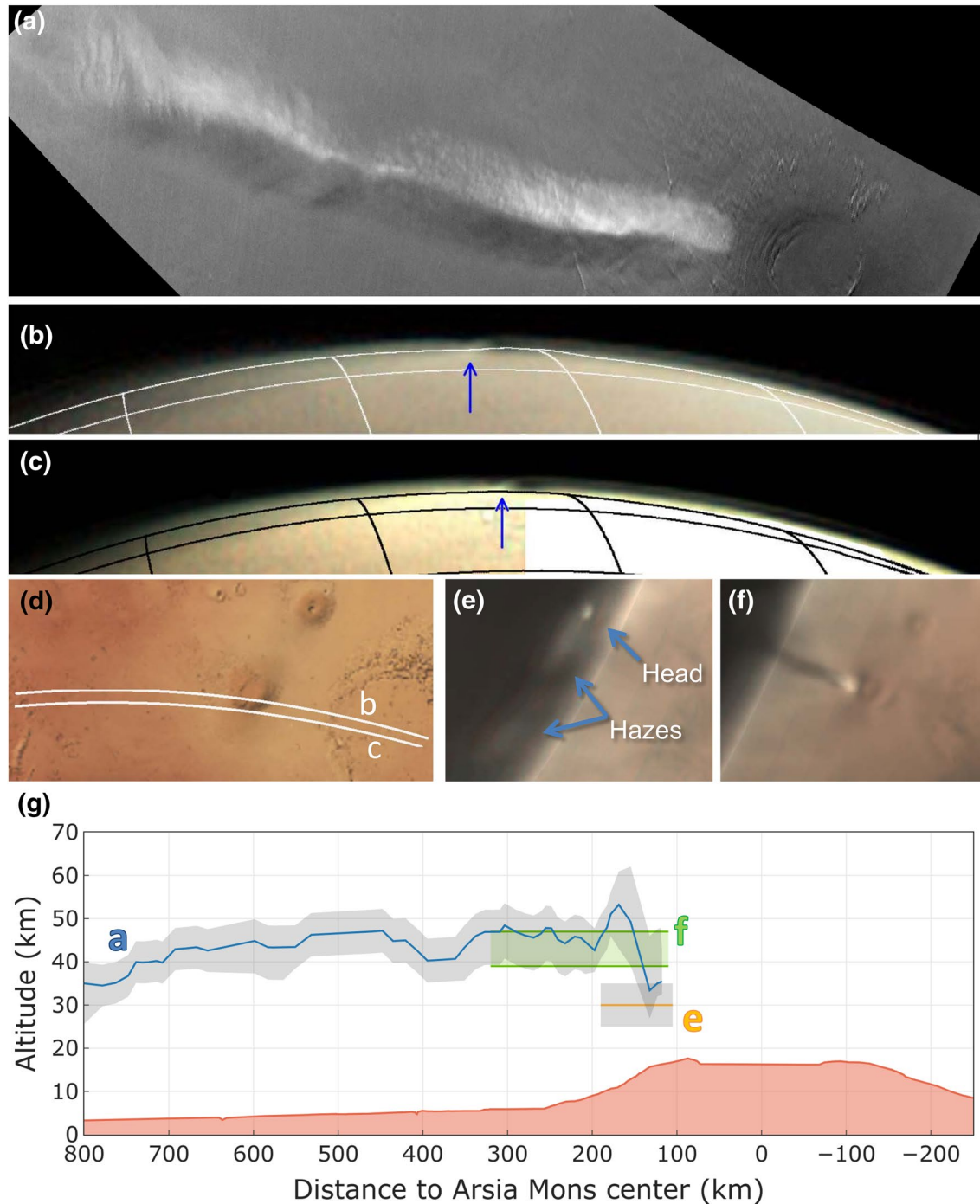


**Figure 10.** Altitude of the AMEC relative to the areoid from different observations. (a) Shadow of the cloud at high resolution as observed by HRSC. This image has been enhanced to improve shadow visibility (for the equivalent color image refer to Figure 3d); acquired on September 21, 2018, Ls 254°, LTST 8.5 (orbit 18627). (b) and (c) AMEC cloud seen at the limb, clearly visible on the western flank (left of the volcano position, indicated with dark blue arrows), with hazes and a detached layer of aerosols east of the Arsia Mons (right of the blue arrow). These images were acquired 48 s apart on November 3, 2018, Ls 281°, LTST 6.5 (VMC observation 180390). (d) Map of the region showing limb trajectories for (b) and (c). (e) Head of the cloud imaged during twilight. Hazes also appear around the head in twilight (indicated with arrows); October 1, 2018, Ls 261°, LTST 5.3 (VMC observation 180340). (f) Shadow of the cloud shortly after dawn; September 25, 2018, Ls 257°, LTST 6.9 (VMC image 180329). (g) Graph showing the topographic profile (red profile at the bottom) as well as the altitude of the cloud shown in panels (a) (blue line) and (e) (orange line), where gray areas indicate the uncertainty in altitude. Also shown is the altitude and minimum thickness of the cloud shown in (f).



When comparing the onset date of the phenomenon for the available MYs (see Figure 2), we see that the earlier appearances were in MY31 (Ls 226°) and MY32 (Ls 233°). In MY34, we have suitable VMC observations at these Ls that do not show the AMEC phenomenon (see Figure 2 and Table S1), suggesting that the onset of the AMEC season that year was delayed in comparison with MYs31 and 32. This delay is possibly related to the occurrence of the MY34 GDS, and the progressive clearing of dust in the atmosphere (Guzewich et al., 2019; Sánchez-Lavega et al., 2019).

### 7.1. Daily Cycle: Expansion and Detachment

Figure 12a shows the length of the AMEC as a function of LTST for MYs29–33, measured only in the images where the complete cloud was visible. The global trend of growth with LTST is similar in MYs29–32, and a linear fit to data corresponding to those 4 years indicates an expansion velocity of  $130 \pm 20 \text{ ms}^{-1}$ , slower than in MY34. The fit is not as good as in Figure 6 (which contains data from MY34 only), as it must reflect a degree of interannual variability. The trend in MY33 is different, and the AMEC is often considerably shorter in length than expected from the general trend in other years, resembling the “early anomalies” reported for MY34 in Section 4.2 (e.g., compare Figures 11g with 10f). The expansion direction of the cloud is similar to MY34, initially to the west, and curving toward the north (Figure 12b). An exception to this is MY33, when the cloud expanded initially southward of Arsia Mons, but keeping its northward pointing concavity.

A few observations in previous years were acquired after 9 LTST and before noon, the local time around which the AMEC had always detached from Arsia Mons in MY34. MY33 is an exception to this, as VMC observed past 9 LTST on several occasions. Unlike in MY34, in images before 10 LTST, the cloud had not clearly detached from Arsia Mons, and no elongated cloud was found between 10 and 12 LTST.

### 7.2. AMEC Morphology

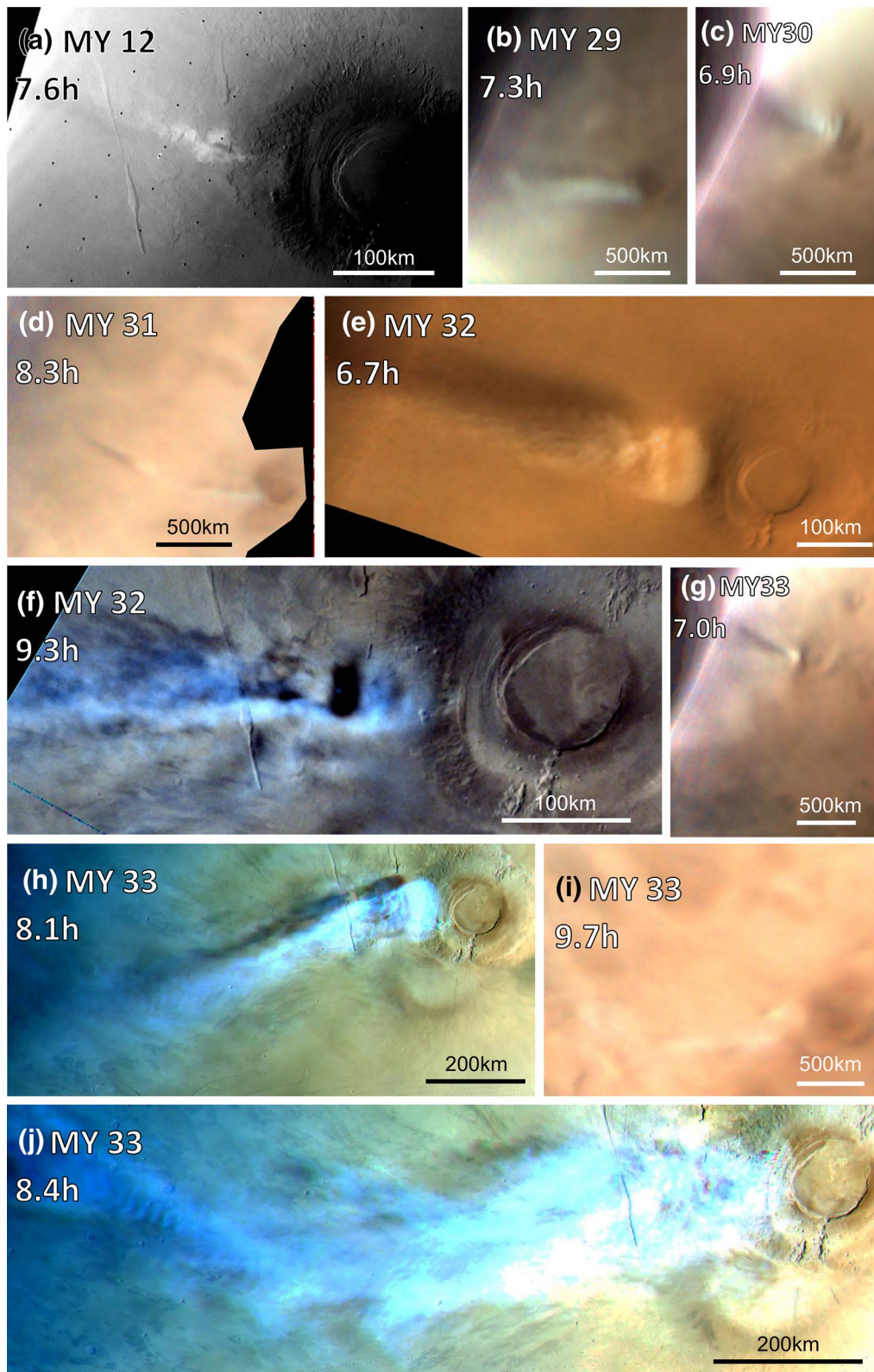
In general, morphologies of the cloud in all years are similar to those reported in Section 5.2 for MY34. For example, Figure 11c shows a morphology resembling Types II or III discussed in Section 5.2; Figure 11d shows a clear case of Type I and Figure 11e resembles Type II. Figure 11h corresponds to Type III, indicating that the dark feature usually observed in the neck in low-resolution images of this morphology is the result of a lack of thick clouds in the area. Figure 11g closely resembles the early anomaly depicted in Figure 10f. Figures 11f and 11i have no clear equivalent in MY34, and it is worth mentioning that both were obtained at a local time when the cloud was usually detached in MY34.

Hazes and conical shapes such as those reported in Section 5.3 are also found in VMC images from the previous years, as in Figure 11b and 11c, which shows hazes southward of the AMEC. The high-resolution images in Figure 11f and 11h shows hazes southward of the elongated cloud, and extended hazes in the west in the vicinity of the terminator.

If we concentrate on the specific features of the AMEC observed at high resolution, the sol-to-sol variability prevails over the seasonal evolution, as is apparent in Figure 11h and 11j, obtained by HRSC only four sols apart and almost at the same local time.

### 7.3. Cloud Altitude in Previous Years

We do not have any limb or twilight observations from previous years, and thus all our estimations of height are obtained by analyzing the shadow of the cloud in high-resolution images. The HRSC image obtained in orbit 16486 in MY33 (Figure 11h) shows the AMEC casting a prominent shadow at 8.1 LTST, which gives a cloud altitude of 40–45 km above the areoid. The MCC observations of the shadow at Ls 252° (Figure 11e) at 6.7 LTST gives an altitude of  $34 \pm 3$  km above the areoid. Another MCC observation on January 4, 2015 (Figure 10f) at 9.2 LTST shows the projected shadow from the head from which we derive an altitude of  $45 \pm 2$  km. All these altitudes are in very good agreement with those reported previously in Section 6 for MY34.



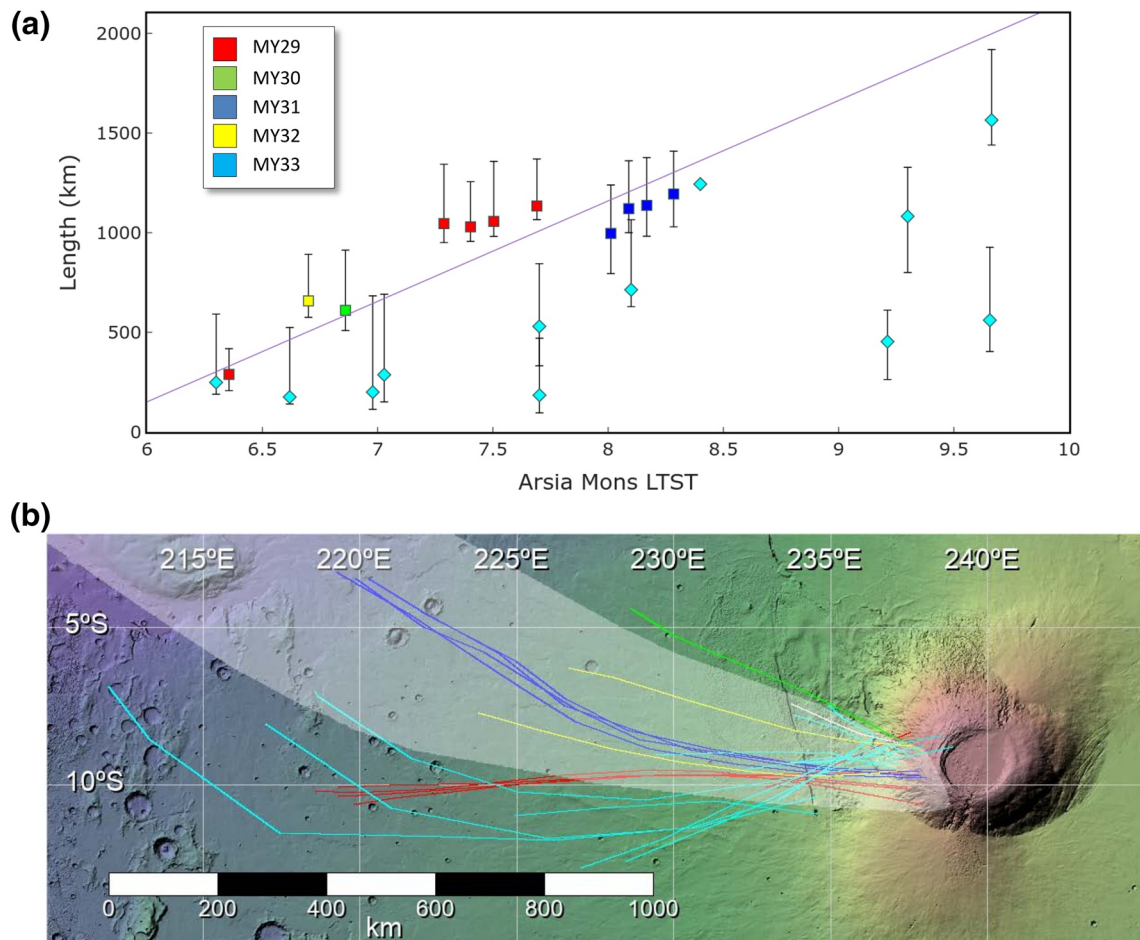


**Figure 12.** Length and curvature of the AMEC in MYs 29–33 (analogous to Figure 6). (a) Length of the AMEC as a function of local time. Color code indicates MY. The linear fit corresponds to all data except for MY33 (indicated with diamond-shaped markers). (b) Outline of the tail of the cloud over a topographic map as in Figure 6b. The area occupied by the cloud trajectories in MY34 (Figure 6b) is indicated by a background white shadow for comparison.

## 8. Discussion and Conclusion

In this paper, we report the formation of an extremely Elongated Cloud in the early hours of the morning, extending to the west from the Arsia Mons volcano (AMEC, Arsia Mons Elongated Cloud). We analyze several features of this cloud phenomenon and its changes as a function of Local Time, Ls, and MY. In our study, we have focused on the occurrence of the AMEC phenomenon during MY34, which started during the decaying phase of a GDS (2018), and we have also presented observations of the phenomenon in previous MYs.

Morphologically, the AMEC has two main regions (Figure 9a): first, the head, a bright cloud approximately round in shape but with texture, of an average size of  $\sim 125$  km in diameter that forms above the western flank of the volcano at longitude  $237^\circ\text{E}$  and latitude  $8.5^\circ\text{S}$ – $10^\circ\text{S}$ ; and second the long tail that grows and expands westward toward the terminator during the morning hours at speeds of around  $170\text{ ms}^{-1}$  in MY 34 (slower in other years) The elongated cloud attains a maximum length of 1,800 km but its width typically remains below 200 km. The head reaches maximum altitudes of 40–50 km above the areoid. We find that

**Figure 11.** Images of the AMEC phenomenon seen in different MYs. All images are projected onto cylindrical maps. Spatial scale is indicated in each panel. (a) MY12; August 11, 1977, Ls  $314^\circ$  (Viking Orbiter 2 observation 356b33). (b) MY29; July 2, 2009, Ls  $296^\circ$  (VMC observation 090025). (c) MY30; March 21, 2011, Ls  $258^\circ$  (VMC observation 110005). (d) MY31; December 15, 2012, Ls  $226^\circ$  (VMC observation 120060). (e) MY32. December 13, 2014, Ls  $252^\circ$  (MCC product MCC\_MRD\_20141213T134802312\_D\_GDS). (f) MY32; January 4, 2015, Ls  $266^\circ$  (MCC product MCC\_MRD\_20150104T063053645\_D\_D32). (g) MY33; December 25, 2016, Ls  $287^\circ$  (VMC observation 160150). (h) MY33; January 5, 2017, Ls  $294^\circ$  (HRSC observation in orbit 16486). (i) MY33; January 8, 2017, Ls  $296^\circ$  (VMC observation 170010). (j) MY33; January 1, 2017, Ls  $291^\circ$  (HRSC observation in orbit 16472).

the AMEC follows a daily cycle with head formation around sunrise (5.7 LTST), followed by its expansion and detachment from the volcano point origin at  $\sim 8.5$  LTST. In the following hours, the cloud becomes thinner and more turbulent, evaporating while new thin clouds grow locally over Arsia Mons, as observed in the afternoon in previous MYs (Benson et al., 2003; 2006; Wang & Ingersoll, 2002).

Due to the fact that the AMEC phenomenon occurs at the Martian sunrise, we have few observations that show the details of the head formation in high resolution. One of the best images of the earlier head morphology was obtained by Viking Orbiter 2 in MY12 (Ls 308°) (Figure 5 in Hunt & Pickersgill, 1984). The image, obtained at LTST 6.6, shows a high dynamical richness in the head, and another image (Figure 6 in the same reference) at Ls 314° shows the plume growing some hundred kilometers to the west of Arsia Mons at 7.6 LTST, in good agreement with what we have observed in recent years.

The pattern traced by the AMEC during its development and expansion typically exhibited a curved shape with its concavity pointing toward the north (Figures 6 and 12), as driven by the ambient zonal and meridional winds. We found evidence suggesting seasonal changes and interannual variations, but we also observed strong sol-to-sol variations. Thus, the tail length and orientation are a good proxy to characterize the ambient wind field structure and its variability.

With these data in hand, the scenario we propose is that the cloud head formation takes place when moist air is forced to ascend in updrafts along the volcano slopes, and the head forms when water ice condenses due to low temperatures at higher altitudes. We suggest that after the head formation, high-altitude westward winds expand and drag the cloud to the west. The vertical ascent of air parcels into the Martian mesosphere driven by anabatic winds along the slopes of the giant Mars volcanoes has been studied by means of mesoscale models (Michaels et al., 2006; Rafkin et al., 2017, 2002). These studies show that water vapor may be transported up to altitudes higher than 40 km (Michaels et al., 2006). On the contrary, recent works have shown that the hygropause can reach up to 90 km during a GDS (Heavens et al., 2018). In a second paper, we will present a full theoretical study of the AMEC phenomenon based on its orographic nature and numerical models.

Observations in the afternoon show that Arsia Mons is the only location on Mars where water ice clouds are usually found in the season of occurrence of the AMEC (Benson et al., 2006, 2003; Wang & Ingersoll, 2002). The AMEC takes place in the early morning and thus it was not part of the mentioned studies. Previous works have studied the water vapor concentration on the slopes of the Tharsis giant volcanoes (Maltagliati et al., 2008; Titov et al., 1994). This topic together with other aspects regarding the AMEC formation will be discussed in the second part of this work.

The AMEC phenomenon develops during the season of maximum insolation at the volcano (daily average at the Top of the Atmosphere (TOA) ranges from  $\sim 200$  to  $225 \text{ Wm}^{-2}$  (see Figure 3 in Sánchez-Lavega et al., 2019) with the perihelion occurring at Ls 251° and the southern solstice at Ls 270°. The AMEC season is also the period when dust injection in the atmosphere and the development of dust storms on Mars take place (Kahre et al., 2017; see also bottom panel of Figure 3, in Sánchez-Lavega et al., 2019). Therefore, the two phenomena, the AMEC and dust (via GDS and regional storms), occur simultaneously, making the AMEC a good case study for the effect of dust on the dynamics and distribution of water vapor, and the microphysics of orographic cloud formation.

There is possible evidence of the effects of dust storms on afternoon cloud development at Arsia Mons. Benson et al. (2003) reported no afternoon cloud activity in Arsia Mons between Ls 227° and 235° during MY24 at the time of a regional dust storm (Cantor et al., 2001). Later, Benson et al. (2006) also reported less cloud formation over Arsia Mons during the GDS 2001 that took place in MY25 (Cantor, 2007; Montabone 2015; Strausberg et al., 2005). We have explored the AMEC cases in MYs with GDS (MY12, MY34) and without (MYs 29–33). We use the earliest AMEC observations among all the MYs studied, which corresponds to Ls 226° in MY31 (December 2012), as a reference. The Viking Orbiter images of the AMEC described above (MY12, Ls 307° and 317°, July 1977) were obtained during the GDS 1977B that took place between May and October 1977 (Ls 268°–349°; Pollack et al., 1979), indicating that both phenomena coexisted. In MY34, we find a faster expansion compared with previous years, and a seasonal delay in the Ls of the onset of the AMEC phenomenon, compared with MYs 31 and 32, and some “early anomalies” occurring at the beginning of the season (captured at Ls 240°–260°), consisting of a later formation of the cloud head and a shorter

development of its tail. These features are possibly related to the fact that the onset of the AMEC coincided with the decline of GDS 2018 (Guzewich et al., 2019; Montabone et al., 2020; M. D. Smith 2019b).

How rare is the AMEC phenomenon? The presence of the Valles Marineris Cloud Trails (VMCT) reported by R. T. Clancy et al. (2009; 2014) strongly resembles the AMEC. These VMCT are observed recurrently at each MY in the Valles Marineris and Noctis Labyrinthus areas around the perihelion season (Ls around 230°–260°) in the afternoon hours (13–15 LTST). Observed in MY28, the clouds were quite elongated, with lengths of 400–1,000 km and widths of 25–75 km, and altitudes as deduced from shadows of around 40–50 km, with the cloud expansion requiring winds over 100 ms<sup>-1</sup> (Clancy, 2009). Another feature that might be similar to the AMEC is an elongated cloud that has been reported over Ascraeus Mons (the northern Tharsis volcano), first observed by the Viking orbiters (Carr et al., 1980, Figure 141).

Future observations of the AMEC should focus on detailed and systematic images by spacecraft in non-sun-synchronous orbits in order to track the evolution of the phenomenon as a function of local time and, in the long-term, to monitor its interannual variability (current available orbiters are MEX, MAVEN, MOM, and TGO). Wide-angle cameras like VMC and MCC are well suited to cover large areas at once and obtain sequences of images that enable the study of the phenomenon globally as a function of LTST, and the EXI instrument onboard the Emirates Mars Mission (EMM) will also have this capability. Some pushbroom scanners, like IUVS or HRSC, can also obtain regular images of large spatial areas that could show this kind of phenomenon. Narrow-angle cameras can give details of the cloud morphology at its onset, and spectral imagers (e.g., MEX/OMEGA, TGO/CASSIS, EMM/EXI) and other instruments (e.g., MEX/PFS) can give information on cloud particle sizes and optical depths and retrieve temperatures and water vapor abundances. A good characterization of dust in the atmosphere can help in understanding the connection between dust storms and the varied behavior of the AMEC. All these parameters will enable the future modeling of this outstanding Martian meteorological phenomenon.

## Data Availability Statement

A list of observations used in this paper is provided in the Supporting Information. All observations are available in ESA PSA, NASA PDS, and ISRO ISSDC. Specific links are given in the supporting material. We uploaded the images as they were used in this study to a repository publicly available: <https://doi.org/10.6084/m9.figshare.c.5212793>. We acknowledge the use of data from the Mars Orbiter Mission (MOM), first interplanetary mission of the Indian Space Research Organization (ISRO), archived at the Indian Space Science Data Center (ISSDC).

## Acknowledgments

This work has been supported by the Spanish project AYA2015-65041-P and PID2019-109467GB-I00 (MINECO/FEDER, UE) and Grupos Gobierno Vasco IT-1366-19. JHB was supported by ESA Contract No. 4000118461/16/ES/JD, Scientific Support for Mars Express Visual Monitoring Camera. The Aula Espazío Gela is supported by a grant from the Diputación Foral de Bizkaia (BFA). We acknowledge support from the Faculty of the European Space Astronomy Center (ESAC). Special thanks are due to the Mars Express Science Ground Segment and Flight Control Team at ESAC and ESOC. The contributions by K.C and N.M.S were supported by NASA through the MAVEN project. We acknowledge Claus Gebhardt and an anonymous reviewer whose comments helped improve and clarify this manuscript.

## References

- Acton, C., Bachman, N., Semenov, B., & Wright, E. (2018). A look towards the future in the handling of space science mission geometry. *Planetary and Space Science*, *150*, 9–12.
- Acton, C. H., Jr (1996). Ancillary data services of NASA's navigation and ancillary information facility. *Planetary and Space Science*, *44*(1), 65–70.
- Akabane, T., Nakakushi, T., Iwasaki, K., & Larson, S. M. (2002). Diurnal variation of Martian water-ice clouds in Tharsis region of the low latitude cloud belt: Observations in 1995–1999 apparitions. *Astronomy & Astrophysics*, *384*(2), 678–688.
- Allison, M. (1997). Accurate analytic representations of solar time and seasons on Mars with applications to the Pathfinder/Surveyor missions. *Geophysical Research Letters*, *24*(16), 1967–1970. <https://doi.org/10.1029/97GL01950>
- Allison, M., & McEwen, M. (2000). A post-Pathfinder evaluation of areocentric solar coordinates with improved timing recipes for Mars seasonal/diurnal climate studies. *Planetary and Space Science*, *48*(2–3), 215–235.
- Arya, A. S., Sarkar, S. S., Srinivas, A. R., Moorthi, S. M., Patel, V. D., Singh, R. B., et al. (2015). Mars Colour Camera: The payload characterization/calibration and data analysis from Earth imaging phase. *Current Science*, *109*, 1076–1086.
- Bell, J. F., III, Wolff, M. J., Malin, M. C., Calvin, W. M., Cantor, B. A., Caplinger, M. A., et al. (2009). Mars reconnaissance orbiter Mars color imager (MARCI): Instrument description, calibration, and performance. *Journal of Geophysical Research*, *114*(E8). <https://doi.org/10.1029/2008JE003315>
- Benson, J. L., Bonev, B. P., James, P. B., Shan, K. J., Cantor, B. A., & Caplinger, M. A. (2003). The seasonal behavior of water ice clouds in the Tharsis and Valles Marineris regions of Mars: Mars Orbiter Camera observations. *Icarus*, *165*(1), 34–52.
- Benson, J. L., James, P. B., Cantor, B. A., & Remigio, R. (2006). Interannual variability of water ice clouds over major Martian volcanoes observed by MOC. *Icarus*, *184*(2), 365–371.
- Bibring, J. P., Soufflot, A., Berthé, M., Langevin, Y., Gondet, B., Drossart, P., et al. (2004). OMEGA: Observatoire pour la Minéralogie, l'Eau, les Glaces et l'Activité. Mars express: The scientific payload. (Vol. 1240, pp. 37–49).
- Cantor, B. A. (2007). MOC observations of the 2001 Mars planet-encircling dust storm. *Icarus*, *186*(1), 60–96.

- Cantor, B. A., James, P. B., Caplinger, M., & Wolff, M. J. (2001). Martian dust storms: 1999 Mars orbiter camera observations. *Journal of Geophysical Research*, *106*(E10), 23653–23687. <https://doi.org/10.1029/2000JE001310>
- Carr, M. H., Baum, W. A., Blasius, K. R., Briggs, G. A., Cutts, J. A., Duxbury, T. C., et al. (1980). *Viking orbiter views of Mars: NASA SP-441*. <https://history.nasa.gov/SP-441/contents.htm>
- Clancy, R. T., Grossman, A. W., Wolff, M. J., James, P. B., Rudy, D. J., Billawala, Y. N., et al. (1996). Water vapor saturation at low altitudes around Mars aphelion: A key to Mars climate?. *Icarus*, *122*(1), 36–62.
- Clancy, R., Montmessin, F., Benson, J., Daerden, F., Colaprete, A., & Wolff, M. (2017). Mars Clouds. In R. Haberle, R. Clancy, F. Forget, M. Smith, & R. Zurek (Eds.), *The Atmosphere and Climate of Mars* (Cambridge planetary science (pp. 76–105). Cambridge: Cambridge University Press. <https://doi.org/10.1017/9781139060172.005>
- Clancy, R. T., Sandor, B. J., Wolff, M. J., Christensen, P. R., Smith, M. D., Pearl, J. C., et al. (2000). An intercomparison of ground-based millimeter, MGS TES, and Viking atmospheric temperature measurements: Seasonal and interannual variability of temperatures and dust loading in the global Mars atmosphere. *Journal of Geophysical Research*, *105*(E4), 9553–9571. <https://doi.org/10.1029/1999JE001089>
- Clancy, R. T., Wolff, M. J., Cantor, B. A., Malin, M. C., & Michaels, T. I. (2009). Valles Marineris cloud trails. *Journal of Geophysical Research*, *114*(E11). <https://doi.org/10.1029/2008JE003323>
- Clancy, R. T., Wolff, M. J., Smith, M. D., Cantor, B. A., & Spiga, A. (2014). The Global and Local Characters of Mars Perihelion Cloud Trails. *AGUFM*, P53D–P07.
- Connour, K., Schneider, N. M., Milby, Z., Forget, F., Alhosani, M., Spiga, A., & Wolff, M. J. (2020). Mars's Twilight Cloud Band: A new cloud feature seen during the Mars year 34 global dust storm. *Geophysical Research Letters*, *47*(1), e2019GL084997. <https://doi.org/10.1029/2019GL084997>
- Costa, M. (2018). SPICE for ESA Planetary Missions: Geometry and visualization support to studies, operations and data analysis. European planetary science congress. (Vol. 12).
- Curran, R. J., Conrath, B. J., Hanel, R. A., Kunde, V. G., & Pearl, J. C. (1973). Mars: Mariner 9 spectroscopic evidence for H<sub>2</sub>O ice clouds. *Science*, *182*(4110), 381–383.
- Edwards, K. (1987). Geometric processing of digital images of the planets. *Photogrammetric Engineering and Remote Sensing*, *53*(9), 1219–1222.
- Ferguson, R. L., Hare, T. M., & Laura, J. (2018). *HRSC and MOLA Blended digital elevation model at 200m v2*. *Astrogeology PDS Annex*. U.S. Geological Survey. [http://bit.ly/HRSC\\_MOLA\\_Blend\\_v0](http://bit.ly/HRSC_MOLA_Blend_v0)
- Giuranna, M., Wolkenberg, P., Grassi, D., Aronica, A., Aoki, S., Scaccabarozzi, D., et al. (2019). The current weather and climate of Mars: 12 years of atmospheric monitoring by the Planetary Fourier Spectrometer on Mars Express. *Icarus*, *113*, 406.
- Glenar, D. A., Samuelson, R. E., Pearl, J. C., Bjoraker, G. L., & Blaney, D. (2003). Spectral imaging of Martian water ice clouds and their diurnal behavior during the 1999 aphelion season (Ls= 130). *Icarus*, *161*(2), 297–318.
- Guzewich, S. D., Lemmon, M., Smith, C. L., Martínez, G., de Vicente-Retortillo, Á., Newman, C. E., et al. (2019). Mars science laboratory observations of the 2018/Mars year 34 global dust storm. *Geophysical Research Letters*, *46*(1), 71–79. <https://doi.org/10.1029/2018GL080839>
- Heavens, N. G., Kleinböhl, A., Chaffin, M. S., Halekas, J. S., Kass, D. M., Hayne, P. O., et al. (2018). Hydrogen escape from Mars enhanced by deep convection in dust storms. *Nature Astronomy*, *2*, 126–132.
- Hernández-Bernal, J., Sánchez Lavega, A., del Río Gaztelurrutia, T., Hueso, R., Cardesin Moinelo, A., de Burgos Sierra, A., et al. (2018). Clouds in the night side of Mars: An analysis using Mars Express VMC. EPSC abstracts. (Vol. 12). European Planetary Science Congress EPSC2018-337.
- Hernández-Bernal, J., Sánchez-Lavega, A., del Río-Gaztelurrutia, T., Hueso, R., Cardesin-Moinelo, A., Ravanis, E. M., et al. (2019). The 2018 Martian global dust storm over the south Polar region studied with MEx/VMC. *Geophysical Research Letters*, *46*(17–18), 10330–10337. <https://doi.org/10.1029/2019GL084266>
- Herschel, W. (1784). On the remarkable appearance of the polar regions of the planet Mars, the inclination of its axis, the position of its poles, and its spheroidal figure; with a few hints relating to its real diameter and its atmosphere. *Philosophical Transactions of the Royal Society of London*, *24*, 233–273.
- Hunt, G. E., & Pickersgill, A. O. (1984). Some observations of Martian cloud systems. *Vistas in Astronomy*, *27*, 131–148.
- Hunt, G. E., Pickersgill, A. O., James, P. B., & Johnson, G. (1980). Some diurnal properties of clouds over the Martian volcanoes. *Nature*, *286*(5771), 362.
- James, P. B., Bell, J. F., III, Clancy, R. T., Lee, S. W., Martin, L. J., & Wolff, M. J. (1996). Global imaging of Mars by Hubble Space Telescope during the 1995 opposition. *Journal of Geophysical Research*, *101*(E8), 18883–18890. <https://doi.org/10.1029/96JE01605>
- Jaumann, R., Neukum, G., Behnke, T., Duxbury, T. C., Eichentopf, K., Flohrer, J., et al. (2007). The high-resolution stereo camera (HRSC) experiment on Mars Express: Instrument aspects and experiment conduct from interplanetary cruise through the nominal mission. *Planetary and Space Science*, *55*(7–8), 928–952.
- Kahre, M. A., Murphy, J. R., Newman, C. E., Wilson, R. J., Cantor, B. A., Lemmon, M. T., et al. (2017). The Mars Dust Cycle. *The Atmosphere and Climate of Mars*, *18*, 295.
- Kloos, J. L. (2016). *Cloud observations from the Mars science laboratory mission: Seasonal variability, scattering phase function, and validation of optical depths using lidar measurements of terrestrial cirrus clouds*. Retrieved from <https://yorkspace.library.yorku.ca/xmlui/handle/10315/33436>
- Kloos, J. L., Moores, J. E., Whiteway, J. A., & Aggarwal, M. (2018). Interannual and diurnal variability in water ice clouds observed from MSL over two Martian years. *Journal of Geophysical Research: Planets*, *123*(1), 233–245. <https://doi.org/10.1002/2017JE005314>
- Leovy, C. B., Briggs, G. A., & Smith, B. A. (1973). Mars atmosphere during the Mariner 9 extended mission: Television results. *Journal of Geophysical Research*, *78*(20), 4252–4266. <https://doi.org/10.1029/JB078i020p04252>
- Leovy, C. B., Smith, B. A., Young, A. T., & Leighton, R. B. (1971). Mariner Mars 1969: atmospheric results. *Journal of Geophysical Research*, *76*(2), 297–312. <https://doi.org/10.1029/JB076i002p00297>
- McClintock, W. E., Schneider, N. M., Holsclaw, G. M., Clarke, J. T., Hoskins, A. C., Stewart, I., et al. (2015). The imaging ultraviolet spectrograph (IUVS) for the MAVEN mission. *Space Science Reviews*, *195*(1–4), 75–124.
- Michaels, T. I., Colaprete, A., & Rafkin, S. C. R. (2006). Significant vertical water transport by mountain-induced circulations on Mars. *Geophysical Research Letters*, *33*(16). <https://doi.org/10.1029/2006GL026562>
- Montabone, L., Forget, F., Millour, E., Wilson, R. J., Lewis, S. R., Cantor, B., et al. (2015). Eight-year climatology of dust optical depth on Mars. *Icarus*, *251*, 65–95.
- Montabone, L., Spiga, A., Kass, D. M., Kleinböhl, A., Forget, F., & Millour, E. (2020). Martian Year 34 column dust climatology from Mars climate sounder observations: Reconstructed maps and model simulations. *Journal of Geophysical Research: Planets*, *125*, e2019JE006111. <https://doi.org/10.1029/2019JE006111>

- Ormston, T., Denis, M., Scuka, D., & Griebel, H. (2011). An ordinary camera in an extraordinary location: Outreach with the Mars Webcam. *Acta Astronautica*, 69(7–8), 703–713.
- Peale, S. J. (1973). Water and the Martian W cloud. *Icarus*, 18(3), 497–501.
- Pollack, J. B., Colburn, D. S., Flasar, F. M., Kahn, R., Carlston, C. E., & Pidek, D. (1979). Properties and effects of dust particles suspended in the Martian atmosphere. *Journal of Geophysical Research*, 84(B6), 2929–2945. <https://doi.org/10.1029/JB084iB06p02929>
- Rafkin, S. C., Maria, M. R. S., & Michaels, T. I. (2002). Simulation of the atmospheric thermal circulation of a martian volcano using a mesoscale numerical model. *Nature*, 419(6908), 697.
- Rafkin, S. C., Spiga, A., & Michaels, T. I. (2017). Mesoscale Meteorology. *The Atmosphere and Climate of Mars*, 18, 203.
- Ravanis, E., Hernández-Bernal, J., Cardesín-Moinelo, A., Sánchez-Lavega, A., del Río-Gaztelurrutia, T., Hueso, R., et al. (2020). From engineering to science: Mars express visual monitoring camera's first science data release. European planetary science congress. (Vol. 14).
- Sagan, C., Veveřka, J., & Gierasch, P. (1971). Observational consequences of Martian wind regimes. *Icarus*, 15(2), 253–278.
- Sánchez-Lavega, A., Chen-Chen, H., Ordóñez-Etxeberria, I., Hueso, R., del Río-Gaztelurrutia, T., Garro, A., et al. (2018a). Limb clouds and dust on Mars from images obtained by the Visual Monitoring Camera (VMC) onboard Mars Express. *Icarus*, 299, 194–205.
- Sánchez-Lavega, A., Del Río-Gaztelurrutia, T., Hernández-Bernal, J., & Delcroix, M. (2019). The onset and growth of the 2018 Martian global dust storm. *Geophysical Research Letters*, 46, 6101–6108. <https://doi.org/10.1029/2019GL083207>
- Sánchez-Lavega, A., Garro, A., Río-Gaztelurrutia, T., Hueso, R., Ordóñez-Etxeberria, I., Chen-Chen, H., et al. (2018b). A seasonally recurrent annular cyclone in Mars northern latitudes and observations of a companion vortex. *Journal of Geophysical Research: Planets*, 123, 3020–3034. <https://doi.org/10.1029/2018JE005740>
- Slipher, E. C. (1927). In: Atmospheric and Surface Phenomena on Mars (Vol. 39(230), 209–216). Publications of the Astronomical Society of the Pacific. Retrieved from <https://www.jstor.org/stable/40692693?seq=1>
- Smith, M. D. (2019a). Local time variation of water ice clouds on Mars as observed by THEMIS. *Icarus*, 333, 273–282.
- Smith, M. D. (2019b). THEMIS observations of the 2018 Mars global dust storm. *Journal of Geophysical Research: Planets*, 124(11), 2929–2944. <https://doi.org/10.1029/2019JE006107>
- Smith, S. A., & Smith, B. A. (1972). Diurnal and seasonal behavior of discrete white clouds on Mars. *Icarus*, 16(3), 509–521.
- Smith, D. E., Zuber, M. T., Frey, H. V., Garvin, J. B., Head, J. W., Muhleman, D. O., et al. (2001). Mars Orbiter Laser Altimeter: Experiment summary after the first year of global mapping of Mars. *Journal of Geophysical Research: Planets*, 106(E10), 23689–23722. <https://doi.org/10.1029/2000JE001364>
- Strausberg, M. J., Wang, H., Richardson, M. I., Ewald, S. P., & Toigo, A. D. (2005). Observations of the initiation and evolution of the 2001 Mars global dust storm. *Journal of Geophysical Research*, 110(E2). <https://doi.org/10.1029/2004JE002361>
- Sutton, J. L., Leovy, C. B., & Tillman, J. E. (1978). Diurnal variations of the Martian surface layer meteorological parameters during the first 45 sols at two Viking lander sites. *Journal of the Atmospheric Sciences*, 35(12), 2346–2355.
- Wang, H., & Ingersoll, A. P. (2002). Martian clouds observed by Mars global surveyor Mars orbiter camera. *Journal of Geophysical Research*, 107(E10), 8–1. <https://doi.org/10.1029/2001JE001815>
- Wellman, J. B., Landauer, F. P., Norris, D. D., & Thorpe, T. E. (1976). The Viking orbiter visual imaging subsystem. *Journal of Spacecraft and Rockets*, 13(11), 660–666.
- Wilson, R. J., Neumann, G. A., & Smith, M. D. (2007). Diurnal variation and radiative influence of Martian water ice clouds. *Geophysical Research Letters*, 34(2). <https://doi.org/10.1029/2006GL027976>
- Wolff, M. J., Clancy, R. T., Banfield, D., & Cuzzo, K. (2005). Water ice clouds as seen from the Mars Exploration Rovers. *AGU fall meeting abstracts*.
- Wolff, M. J., Clancy, R. T., Kahre, M. A., Haberle, R. M., Forget, F., Cantor, B. A., et al. (2019). Mapping water ice clouds on Mars with MRO/MARCI. *Icarus*, 332, 24–49.

# Geophysical Research Letters

## RESEARCH LETTER

10.1029/2020GL092188

### Key Points:

- We present a new methodology to detect clouds at twilight and measure their altitude. We find 407 cases, some at altitudes over 80 km
- High altitude clouds appear most often in mid-latitudes during the local winter. This is a new trend when compared to previous studies
- High altitude clouds concentrate aerographically in a southern belt that includes Terra Cimmeria, and in clusters on northern planitias

### Supporting Information:

Supporting Information may be found in the online version of this article.

### Correspondence to:

J. Hernández-Bernal,  
[jorge.hernandez@ehu.eu](mailto:jorge.hernandez@ehu.eu)

### Citation:

Hernández-Bernal, J., Sánchez-Lavega, A., del Río-Gaztelurrutia, T., Hueso, R., Ravanis, E., Cardesin-Moinelo, A., et al. (2021). A long-term study of Mars mesospheric clouds seen at twilight based on Mars Express VMC images. *Geophysical Research Letters*, 48, e2020GL092188. <https://doi.org/10.1029/2020GL092188>

Received 18 DEC 2020  
Accepted 10 MAR 2021

## A Long-Term Study of Mars Mesospheric Clouds Seen at Twilight Based on Mars Express VMC Images

J. Hernández-Bernal<sup>1,2</sup> , A. Sánchez-Lavega<sup>1,2</sup> , T. del Río-Gaztelurrutia<sup>1,2</sup> , R. Hueso<sup>1</sup> , E. Ravanis<sup>3,4</sup> , A. Cardesin-Moinelo<sup>3,5</sup> , S. Wood<sup>6</sup>, and D. Titov<sup>7</sup>

<sup>1</sup>Departamento Física Aplicada I, Escuela de Ingeniería de Bilbao Universidad del País Vasco UPV/EHU, Bilbao, Spain, <sup>2</sup>Aula Espazio Gela, Escuela de Ingeniería de Bilbao, Universidad del País Vasco UPV/EHU, Bilbao, Spain, <sup>3</sup>European Space Agency, ESAC, Madrid, Spain, <sup>4</sup>Department of Earth Sciences, University of Hawai'i, Honolulu, HI, USA, <sup>5</sup>Instituto de Astrofísica e Ciências do Espaço, Obs. Astronómico de Lisboa, Libson, Portugal, <sup>6</sup>European Space Agency, ESOC, Darmstadt, Germany, <sup>7</sup>European Space Agency, ESTEC, Noordwijk, Netherland

**Abstract** We present the first systematic study of clouds observed during twilight on Mars. We analyze images obtained by the Visual Monitoring Camera on Mars Express between 2007 and 2020. Using an automated retrieval algorithm, we found 407 cases of clouds observed at twilight, in which the geometry of the observations allows to derive the minimum altitude, revealing that many of these clouds are in the mesosphere (above 40 km and up to 90 km). The majority of these mesospheric clouds were detected in mid-latitudes at local autumn and winter, a new trend only hinted at by previous studies. In particular, we find a massive concentration of clouds in the southern mid-latitudes between Terra Cimmeria and Aonia, a region where high altitude events have been previously observed. We propose that there is an unknown mechanism in these regions that enhances the probability to host high altitude clouds around the southern winter solstice.

**Plain Language Summary** During twilight, when the sun is below the horizon, its light can still reach clouds or mountains high above the surface, making them bright features on the dark background. This effect is sometimes seen on noctilucent clouds on Earth, and also in the mountains on the Moon. On Mars, it was first observed by ground based observers in the 1890s, and occasional observations have been later reported. We present here the first systematic study of such clouds on Mars as observed from space by the Visual Monitoring Camera (also known as the Mars webcam) onboard Mars Express. The study of clouds at twilight reveals information about their altitude, and the state of the atmosphere at this moment of the daily cycle. We analyze the occurrence of these clouds and find some new trends that previous observations had only hinted at.

## 1. Introduction

During twilight, when the sun is below the horizon, high altitude structures like mountains or clouds can receive the light of the sun, and appear bright over the dark of the night. On Earth, we can see this effect from the ground in high altitude noctilucent clouds (Gadsden & Schröder, 1989). On Mars, bright patches at the terminator were first observed by telescopic observers in the 1890s (Campbell, 1894; Douglass, 1895; 1897; Holden et al., 1890; 1894), but due to the lack of topographic models at the epoch it was not clear whether they were due to topography or atmospheric aerosols. Today, current topographic data (Smith et al., 2001) allow us to deduce that most of these observations of bright features in the night side of the terminator of Mars are atmospheric aerosols (water ice, CO<sub>2</sub> ice, and dust, see e.g., Zurek 2017 or Clancy et al., 2017). For simplicity, we refer in this paper to all the aerosol patches as “clouds,” no matter whether they are made of condensates or dust, as we cannot determine the composition of aerosols from our observations.

Clouds at twilight on Mars have been detected by the Hubble Space Telescope (HST; James et al., 1996), the Thermal Emission Imaging System (THEMIS; Inada et al., 2007; McConnochie et al., 2010) onboard Mars Odyssey, and the Imaging Ultraviolet Spectrograph (Connour et al., 2020) on board the MAVEN (Mars Atmosphere and Volatile Evolution) mission. However, until 2014 most orbiters on Mars were placed in afternoon sun-synchronous orbits, and thus, few orbital observations of regions in twilight are available (Hernández-Bernal et al., 2020). Among the surface missions, Viking landers performed observations of



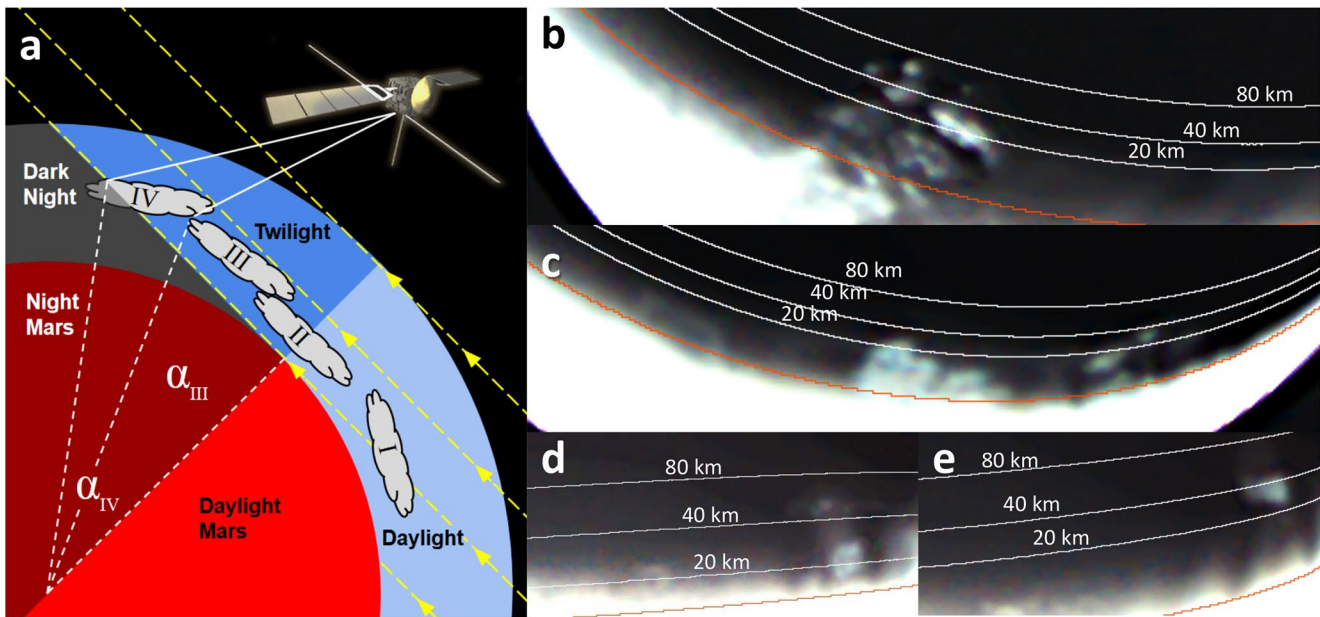


**Figure 1.** Scheme of cloud detection from orbit (left), and cloud examples from VMC images (right). (a) The daylight, twilight, and dark night regions of the atmosphere are indicated. Clouds III and IV are visible from space as isolated bright patches over the dark of the night, while II is seen as a bright patch connected to the terminator. Note that  $\alpha$  is the incidence angle minus  $90^\circ$ ; (b) A cluster of clouds over Terra Cimmeria on Ls  $123^\circ$  (MEXVMC\_1800430001, 2018-02-01); (c) Some discrete clouds (right) and a cloud connected to the terminator (left) around Alba Patera at Ls  $343^\circ$  (MEXVMC\_1700560001, 2017-04-04); (d and e) A recurrent cloud observed on 2020-03-08 and 2020-03-10 at Ls  $164^\circ$ , around Terra Sirenum (MEXVMC\_2000970003 and MEXVMC\_2001010003). In (b–e) minimum-altitude curves are drawn in gray and the terminator in red.

the brightness of the twilight, but did not find clouds (Kahn et al., 1981), and the Pathfinder lander found a cloud 60–100 km over the surface early before sunrise (Clancy & Sandor, 1998; Smith et al., 1997). More recently, the Curiosity rover has also imaged clouds at twilight (Newman, 2019).

In this paper, we study twilight clouds (Figure 1) with the aid of the Visual Monitoring Camera (VMC; Sánchez-Lavega et al., 2018; see also Ravanis et al., 2020) onboard Mars Express (MEX). VMC is probably the best suited among available instruments for this kind of study, as it has a wide field of view, takes regular full disk images showing the terminator of Mars, and its archive covers 6 Martian Years (MY; from MY 29 to MY 35).

While different types of twilight are clearly defined for the case of Earth (e.g., Seidelmann et al., 1992), no formal definitions exist for the twilight on Mars. In this paper, we consider for statistical purposes the region from the terminator to  $15^\circ$  into the night (incidence angle  $90^\circ$ – $105^\circ$ ) as twilight. This distance from the terminator corresponds to a minimum altitude of 120 km (see Section 2, and supporting information S1) and while high altitude events might overtake this altitude (Sánchez-Lavega et al., 2015), we did not find such high altitude events in this work.

The Martian Climate is characterized by a “cloudy season” (Solar Longitude, Ls  $\sim 0^\circ$ – $180^\circ$ ), and a “dusty season” (Ls  $\sim 135^\circ$ – $360^\circ$ ). Dust storms of different scales predominate in the dusty season (Kahre et al., 2017) and water ice clouds are most common in the “cloudy season,” but both water clouds and dust storms can be found during the whole year in different locations. Most water ice clouds can be classified in two main regimes (Clancy et al., 2017; see also Figure 2 in Wang & Ingersoll, 2002): (1) the Aphelion Cloud Belt (ACB; Clancy et al., 1996), which dominates the cloudy season; (2) and the Polar Hoods (PHs; Benson et al., 2010; 2011), which appear around the polar regions mostly during the local autumn and winter.

Clouds bright at twilight are necessarily high above the surface. Following the discoveries by Clancy et al. (2007), Montmessin, Bertaux et al. (2006), Montmessin et al. (2007), Montmessin, Quémerais

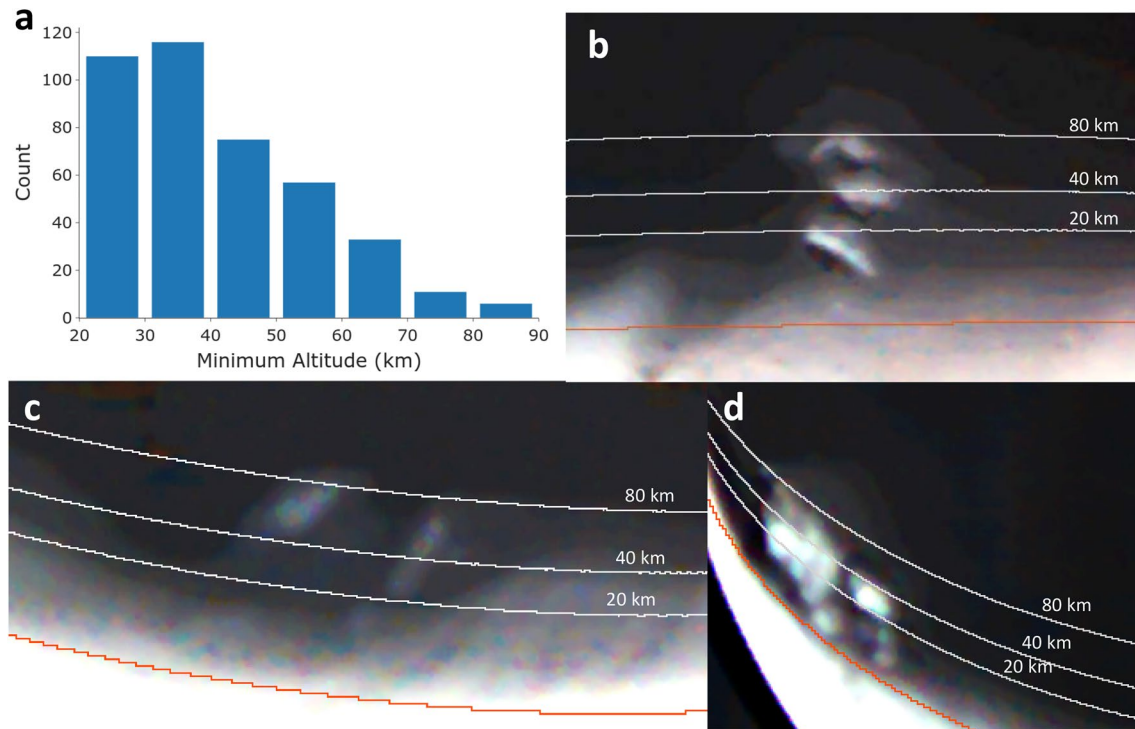


**Figure 2.** Minimum altitude of detected clouds. (a) Statistical distribution of the detected minimum altitudes. (b) Cloud with altitude  $\sim 81$  km over Terra Cimmeria (MEXVMC\_0800560021, 2008-09-07). (c) Cloud  $\sim 82$  km at  $80^\circ\text{N}$  (MEXVMC\_0900110028, 2009-04-09). (d) Cloud  $\sim 89$  km over Argyre Planitia (MEXVMC\_1904350006, 2019-11-25).

et al. (2006), Vincendon et al. (2011) and others, Martian mesospheric clouds (40 km and above) have been widely investigated in recent years. They are typically found at maximum altitudes of 80–90 km, and are more common in equatorial regions in the cloudy season, and in mid-latitudes in the dusty season. They can be made of dust, water ice, or  $\text{CO}_2$  ice, and the climatology of different compounds is not always clear from observational studies, due to observational limitations. Based on afternoon and mid-night systematic observations from MRO, Clancy et al. (2019) find that dust is rare in the mesosphere,  $\text{CO}_2$  aerosols are more common in equatorial regions at  $\text{Ls } 0^\circ\text{--}160^\circ$ , and  $\text{H}_2\text{O}$  aerosols prevail at  $\text{Ls } 160^\circ\text{--}360^\circ$ , in the latitude range  $50^\circ\text{N--}50^\circ\text{S}$ , with a minimum at low latitudes, in agreement with the trends found by Sefton-Nash et al. (2013). The formation of  $\text{CO}_2$  clouds, which seems to be common in the mesosphere, is still challenging for models.  $\text{CO}_2$  ice requires very low temperatures to condense, and thus the diurnal cycle is a relevant factor for their study (González-Galindo et al., 2011). There have been some reports of mesospheric clouds around twilight, in the evening by THEMIS (Inada et al., 2007; McConnochie et al., 2010), and in the early morning by MEX/OMEGA and MEX/HRSC (Montmessin et al., 2007; Määttänen et al., 2010), often in mid-latitudes during the local autumn. For reviews on mesospheric clouds see Määttänen et al. (2013) and Clancy et al. (2017)

The systematic study of aerosols in the twilight presented here provides information about the state of the atmosphere at different altitudes in different locations and seasons of Mars. In Section 2, we explain our data set and methods, in Section 3, we show our results, and in Section 4, we discuss our results and conclusions.

## 2. Data Set and Methods

We base our study on the MEX/VMC image data set (Ravanis et al., 2020), which includes more than 2,000 independent observations (each observation lasts several minutes and contains a number of consecutive images) in MYs 29–35, mostly from MEX apocenters, where VMC captures full disk images of the planet.

A first estimation of the minimum altitude necessary for the clouds at twilight to be illuminated, deduced from simple geometry (Figure 1a), is:  $h_{\min} = R_{\text{Mars}} \tan(\alpha) \tan(\alpha / 2)$ . This corresponds to actual altitude for clouds that are at the limit of the twilight (cloud example IV in Figure 1a). However, this simple calculation of minimum altitudes ignores the nonspherical shape of the planet and the parallax of the observations. To include these effects, we have developed a numerical method, detailed in the supporting information S1. For image navigation, geometry, topography, and Mars time calculations, we used the methods described in Hernández-Bernal et al. (2020).

We performed an automated search of bright patches in the dark (night) side of the terminator considering only isolated patches (i.e., bright areas disconnected from the terminator) at least 20 km over the areoid. Therefore, we only detect discrete clouds (e.g., cloud examples III and IV in Figure 1a), and bright hazes crossing the terminator into the dark side of Mars are ignored (e.g., cloud example II in Figure 1a). In our automated search, MEX/VMC images showing the dark (night) side of Mars with appropriate exposure are first selected. Then, the selected images are analyzed in search of bright features in the dark side of the planet (clouds). The results from the automated analysis are supervised visually to discard false positives. Finally, the parameters for each cloud, including minimum altitude, location, area, date, Ls, and MY, are stored. The details of our analysis pipeline are presented in the supporting information S1. The low quality RGB Bayer pattern of VMC color images (Ormston et al., 2011) is not sufficient to determine the composition of these clouds.

### 3. Results

We have analyzed 4,621 images in 1,891 independent observations spanning from MY28, Ls 344°, to MY35, Ls 229° (November 2007 to June 2020). The coverage through time is not homogeneous (Ravanis et al., 2020), and it is especially low in MYs 31 and 32. Due to the MEX orbit, most of the observed areas correspond to morning twilight (see Figure S1 for local time bias). In total, we have detected 407 clouds.

#### 3.1. Altitude of the Clouds

In Figure 2, we show the statistical distribution of clouds at twilight according to their minimum altitude, and we provide some examples of the highest detected features. Typically, the uncertainty of our calculated minimum altitudes is below 5–10 km (the uncertainty is higher for higher altitudes). The highest clouds detected have a minimum altitude of around 80 km over the areoid, which is in agreement with previous studies on high altitude aerosols (Määttä et al., 2013).

#### 3.2. Areographic and Seasonal Distribution

The areographic distribution of clouds at twilight shows that they are more common in specific areas, grouped in three latitudes (Figure 3). The southern group forms a prominent belt around 45°S, and most clouds there seem to concentrate in three regions distributed in the longitude range 120°–360°E (Terra Cimmeria, Terra Sirenum, and Aonia Terra). Other concentrations appear to the west of Noachis Terra and on the southern border of Hellas Planitia. In the equatorial group, most clouds are around the Tharsis area and also in the regions of Margaritifer Terra and Tyrrhena Terra. It is worth noticing that we do not find clouds higher than 60 km in equatorial latitudes, and most detected clouds in this region are below 40 km. Fewer clouds are found in the northern latitudes, around 45°N, mostly in the regions of Acidalia and Arcadia Planitia. In general clouds are more common in the longitude range 180°–360°E at all latitudes, and in the case of the southern belt, this limit shifts westward to 130°E including Terra Cimmeria.

In Figure 4, we show the seasonal distribution of clouds from observations in different years, including morning and evening twilight. The plot shows that clouds at twilight are more common in the cloudy season (Ls 0°–180°). The southern belt shows an intense activity in the Ls range 40°–180°. Clouds from the equator are observed in the Ls range 45°–140° whereas a northern cloud concentration at mid-latitudes takes place in the Ls range 330°–20°, at the end of the dusty season. We detected several clouds at lower minimum altitudes on latitudes 0°–60°S in Ls 225°–290°, which might correspond to dust activity, since

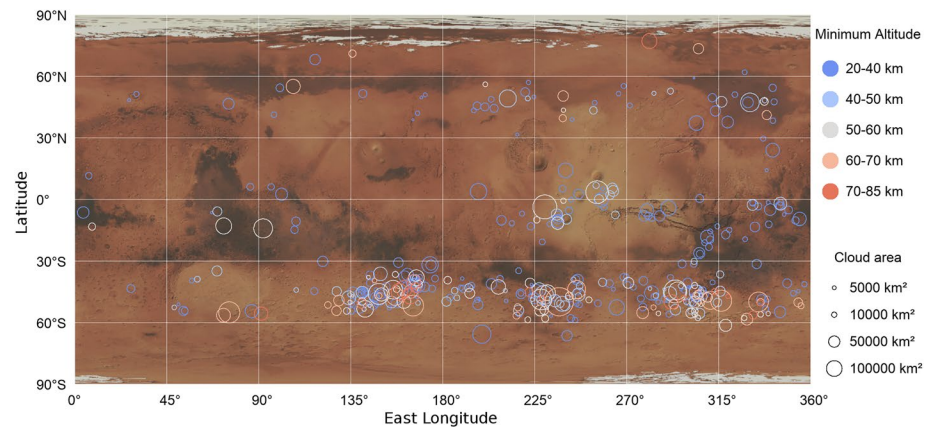


**Figure 3.** Areographic distribution of detected clouds with minimum altitude above 20 km. Clouds are indicated with circles. Color code indicates minimum altitude and size of the circle indicates area. The coverage of the different areas can be found in Figure S1.

this range of Latitude and Ls was only observed in MY34, which was characterized by a global dust storm in Ls 185°–280° (Montabone et al., 2020; Sánchez-Lavega et al., 2019). In the supporting information, we separate the results for the morning (Figure S3) and evening (Figure S4) twilight. We find that the southern belt is present at both morning and evening. However, the sampling of the evening is poor in other regions, preventing us from extracting further conclusions on LTST dependence.

The north polar night was only observed in MY29, between Ls 240° and 270°. Three high clouds were detected (two of them shown in Figure 2c), with minimum altitudes of 60–80 km.

#### 4. Discussion and Conclusions

Aerosols observed in twilight are distributed mainly in three groups: one over the equator (Ls 40°–140°), one at northern mid-latitudes around 45°N at the end of the local winter (Ls 330°–30°), and the southern belt around 45°S during the local autumn and winter (Ls 40°–160°). A considerable fraction of the detected

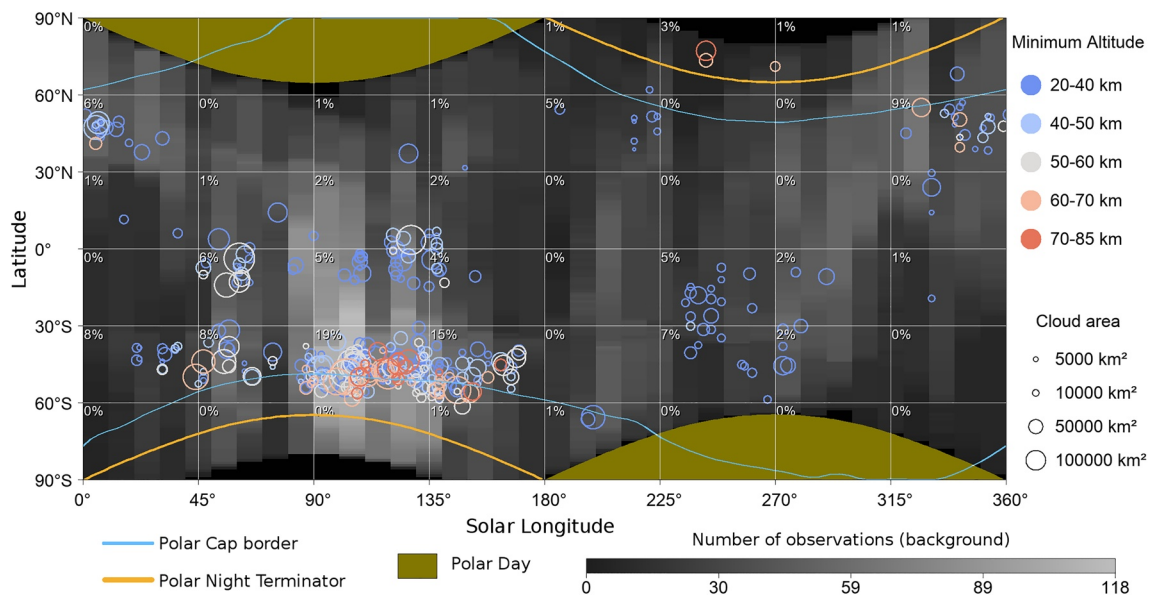


**Figure 4.** Seasonal distribution of detected clouds with minimum altitude over 20 km and from MYs 29–35. For each rectangle of the grid, the percentage of positive observations (containing at least one cloud over 20 km) is indicated in the corner. The border of the polar caps was plotted from data presented in Piqueux et al. (2015).

clouds is at minimum altitudes of 40 km or more, and thus we consider them to be in the mesosphere. When the minimum altitude is lower, clouds could be located in the troposphere, where the ACB and the PHs dominate cloud trends.

The equatorial group could be related to the ACB, which takes place in the same latitude range and season. The detected clouds in equatorial latitudes are not very high (most cloud tops are below 40 km), which is in agreement with the altitudes reported by McCleese et al. (2010) for the ACB. The mid-latitude groups might have some relation with the PHs, that take place in autumn and winter. Our southern twilight belt appears at the same time as the south polar hood (SPH). Benson et al. (2010) reported top altitudes of 30–40 km for the SPH, but we find a considerable number of clouds in the mesosphere, higher than 40 km, in the Ls range 90°–150°. Our northern group only starts at the end of the northern winter (Ls > 330°). Again, Benson et al. (2011) reported top altitudes of ~40 km for the NPH, and we find a number of clouds at higher altitudes.

Our study reveals that mesospheric clouds (with minimum altitudes of at least 40 km) are common in the southern belt during the local winter. Previous studies, which occasionally reported clouds at mid-latitudes during the local autumn around twilight (Määttä et al., 2010; Montmessin et al., 2007; McConnochie et al., 2010; Sánchez-Lavega et al., 2018; Scholten et al., 2010, see also Figure 6 in the review by Määttä et al., 2013), constitute hints of the trend we report here. In the case of the northern belt, we only detect high clouds after Ls 330°, but this result must be taken with caution, since the sampling of the region is poorer, particularly earlier in the season. McConnochie et al. (2010) reported the presence of high clouds at northern mid-latitudes in an earlier Ls range 200°–300° suggestive of a similar trend as in the Southern belt. It must be noted that McConnochie et al. (2010) detected clouds in the evening twilight, while our northern detections correspond to morning twilight, but this is probably not significant since our data is clearly biased toward morning twilight, as can be seen in Figure S2. In Figures S3 and S4, we show respectively morning and evening twilight detections, showing the presence of the southern belt at both morning and evening twilight. In agreement with the review by Määttä et al. (2013), we find lower mesospheric cloud activity around the aphelion (see Figure 4, around Ls 70°), this trend is also apparent in Clancy et al. (2019, their Figure 10).

It is worth noting that our southern belt is very prominent, both in terms of the quantity of detected clouds, especially in the Ls range 90°–180°, when we find twilight clouds in ~19% of our observations, and because of the frequency of high altitude apparitions (Figure 4).

We cannot determine the aerosol nature of our detections from our observations alone. However, given the seasonal distribution of these clouds, and by comparison to the studies of limb spectra by Sefton-Nash et al. (2013) and Clancy et al. (2019) from data obtained by the Mars Climate Sounder, most of these clouds are likely to be condensates, and some of them might be made of CO<sub>2</sub>. Montmessin et al. (2007) and Määttä et al. (2010) reported two mid-latitude mesospheric clouds at latitudes 49°S and 47°N confirmed to be made of CO<sub>2</sub> by OMEGA. Temperatures predicted by atmospheric models such as the LMD-MGCM are not low enough for CO<sub>2</sub> to condense, but observed CO<sub>2</sub> clouds occur in regions where temperatures predicted by models are closest to condensation (González-Galindo et al., 2011). Those models could indicate that CO<sub>2</sub> condensation is possible in our southern belt (see Figure 3 in González-Galindo et al., 2011).

H<sub>2</sub>O clouds have also been observed at mesospheric altitudes (e.g., Clancy et al., 2019; Vincendon et al., 2011). While not much water vapor is expected at mesospheric altitudes in the southern latitudes during the aphelion season (Federova et al., 2020 report low concentrations, and the LMD-MCD (Forget et al., 1999; Millour et al., 2009) predicts concentrations around 1–3 ppmv), and temperatures are low enough to produce water-ice condensates. Another possibility is that the water concentration is actually enhanced due to the upward branch of the Hadley cell around the northern solstice, injecting water vapor coming from the northern latitudes (Heavens et al., 2011). The northern group occurs in the dusty season, and thus the presence of high altitude dust is expected. It is also coincident with the H<sub>2</sub>O mesospheric cloud trends reported by Clancy et al. (2019) and temperatures and water-mixing ratios predicted by the LMD-MCD are consistent with water ice condensation.

Dust is not very common in the aphelion season and thus our southern belt is not likely to contain dust, but several clouds observed around Ls 225°–290° in MY35 in the southern hemisphere (Figure 4), might

correspond to dust activity during the Global Dust Storm GDS 2018 (Montabone et al., 2020; Sánchez-Lavega et al., 2019).

Regarding the distribution in longitude, our detected clouds are more common around longitudes 180°–360° E, in good agreement with previous works (review by Aoki et al., 2018; Clancy et al., 2019; Määttä et al., 2013; Sánchez-Lavega et al., 2018). The longitudinal distribution of twilight clouds is inhomogeneous (Figure 3) despite a quite homogeneous sampling of each latitude (see Figure S1); they are most common on Terra Cimmeria, Terra Sirenum, and Aonia Terra. An extremely high-altitude plume was observed ~200 km over Terra Cimmeria, also in the early morning around the northern solstice (Sánchez-Lavega et al., 2015). This region seems to be a common scenario of high altitude events, especially in the early morning, as shown in Figure 7 of Pellier (2012), using HST data. We propose that the regions of Terra Cimmeria, Terra Sirenum, and Aonia Terra, might have some unknown mechanism to produce high altitude hazes around the southern winter solstice.

The observation of the twilight can provide valuable information about water vapor distribution and the temperature structure required to form condensates. Currently available orbiters suitable for this kind of study are MEX (e.g., Määttä et al., 2010; Montmessin et al., 2007; this work), MAVEN (e.g., Connour et al., 2020), MOM (Arya et al., 2015), and Mars Odyssey (McConnochie et al., 2010). The new Tianwen-1 (Wan et al., 2020) and HOPE (Sharaf et al., 2020) orbiters will also be able to perform such investigations.

## Data Availability Statement

The VMC data set used in this investigation is available in the ESA PSA (Planetary Science Archive) at: [https://archives.esac.esa.int/psa/#!/Table%20View/VMC%20\(Mars%20Express\)=instrument](https://archives.esac.esa.int/psa/#!/Table%20View/VMC%20(Mars%20Express)=instrument)

## Acknowledgments

This work has been supported by the Spanish project AYA2015-65041-P and PID2019-109467GB-I00 (MINECO/FEDER, UE) and Grupos Gobierno Vasco IT-1366-19. J.H.B. was supported by ESA Contract No. 4000118461/16/ES/JD, Scientific Support for Mars Express Visual Monitoring Camera. The Aula Espazío Gela is supported by a grant from the Diputación Foral de Bizkaia (BFA). The authors acknowledge support from the Faculty of the European Space Astronomy Centre (ESAC). Special thanks are due to the Mars Express Science Ground Segment and Flight Control Team at ESAC and ESOC.

## References

- Aoki, S., Sato, Y., Giuranna, M., Wolkenberg, P., Sato, T. M., Nakagawa, H., & Kasaba, Y. (2018). Mesospheric CO<sub>2</sub> ice clouds on Mars observed by planetary Fourier spectrometer onboard Mars Express. *Icarus*, 302, 175–190. <https://doi.org/10.1016/j.icarus.2017.10.047>
- Arya, A. S., Sarkar, S. S., Srinivas, A. R., Moorthi, S. M., Patel, V. D., Singh, R. B., et al. (2015). Mars colour camera: The payload characterization/calibration and data analysis from Earth imaging phase. *Current Science*, 109. <https://doi.org/10.18520/cs/v109/i6/1076-1086>
- Benson, J. L., Kass, D. M., & Kleinböhl, A. (2011). Mars' north polar hood as observed by the Mars Climate Sounder. *Journal of Geophysical Research*, 116(E3), E03008. <https://doi.org/10.1029/2010je003693>
- Benson, J. L., Kass, D. M., Kleinböhl, A., McCleese, D. J., Schofield, J. T., & Taylor, F. W. (2010). Mars' south polar hood as observed by the Mars Climate Sounder. *Journal of Geophysical Research*, 115(E12), E12015. <https://doi.org/10.1029/2009je003554>
- Campbell, W. W. (1894). An explanation of the bright projections observed on the terminator of Mars. *Publication of the Astronomical Society of the Pacific*, 6(35), 103–112. <https://doi.org/10.1086/120795>
- Clancy, R. T., Grossman, A. W., Wolff, M. J., James, P. B., Rudy, D. J., Billawala, Y. N., et al. (1996). Water vapor saturation at low altitudes around Mars aphelion: A key to Mars climate? *Icarus*, 122(1), 36–62. <https://doi.org/10.1006/icar.1996.0108>
- Clancy, R. T., Montmessin, F., Benson, J., Daerden, F., Colaprete, A., & Wolff, M. J. (2017). *Mars clouds* (pp. 42–75). The Atmosphere and Climate of Mars.
- Clancy, R. T., & Sandor, B. J. (1998). CO<sub>2</sub> ice clouds in the upper atmosphere of Mars. *Geophysical Research Letters*, 25(4), 489–492. <https://doi.org/10.1029/98gl00114>
- Clancy, R. T., Wolff, M. J., Smith, M. D., Kleinböhl, A., Cantor, B. A., Murchie, S. L., et al. (2019). The distribution, composition, and particle properties of Mars mesospheric aerosols: An analysis of CRISM visible/near-IR limb spectra with context from near-coincident MCS and MARCI observations. *Icarus*, 328, 246–273. <https://doi.org/10.1016/j.icarus.2019.03.025>
- Clancy, R. T., Wolff, M. J., Whitney, B. A., Cantor, B. A., & Smith, M. D. (2007). Mars equatorial mesospheric clouds: Global occurrence and physical properties from Mars Global Surveyor Thermal Emission Spectrometer and Mars Orbiter Camera limb observations. *Journal of Geophysical Research*, 112(E4), E04004. <https://doi.org/10.1029/2006je002805>
- Connour, K., Schneider, N. M., Milby, Z., Forget, F., Alhosani, M., Spiga, A., et al. (2020). Mars's twilight cloud band: A new cloud feature seen during the Mars Year 34 Global Dust Storm. *Geophysical Research Letters*, 47(1), e2019GL084997. <https://doi.org/10.1029/2019gl084997>
- Douglass, A. E. (1895). A cloud-like spot on the terminator of Mars. *The Astrophysical Journal*, 1, 127. <https://doi.org/10.1086/140022>
- Douglass, A. E. (1897). Projections on the terminator of Mars and martian meteorology. *Astronomische Nachrichten*, 142, 363–366. <https://doi.org/10.1002/asna.18971422205>
- Fedorova, A., Montmessin, F., Korabiev, O., Lefèvre, F., Trokhimovskiy, A., & Bertaux, J. L. (2020). Multi-annual monitoring of the water vapor vertical distribution on Mars by SPICAM on Mars Express. *Journal of Geophysical Research: Planets*, 126, e2020JE006616. <https://doi.org/10.1029/2020JE006616>
- Forget, F., Hourdin, F., Fournier, R., Hourdin, C., Talagrand, O., Collins, M., et al. (1999). Improved general circulation models of the Martian atmosphere from the surface to above 80 km. *Journal of Geophysical Research*, 104(E10), 24155–24175. <https://doi.org/10.1029/1999je001025>
- Gadsden, M., & Schröder, W. (1989). Noctilucent clouds. In *Noctilucent clouds* (pp. 1–12). Berlin, Heidelberg: Springer.
- González-Galindo, F., Määttä, A., Forget, F., & Spiga, A. (2011). The martian mesosphere as revealed by CO<sub>2</sub> cloud observations and general circulation modeling. *Icarus*, 216(1), 10–22. <https://doi.org/10.1016/j.icarus.2011.08.006>

- Heavens, N. G., McCleese, D. J., Richardson, M. I., Kass, D. M., Kleinböhl, A., & Schofield, J. T. (2011). Structure and dynamics of the Martian lower and middle atmosphere as observed by the Mars Climate Sounder: 2. Implications of the thermal structure and aerosol distributions for the mean meridional circulation. *Journal of Geophysical Research*, *116*(E1), E01010. <https://doi.org/10.1029/2010je003713>
- Hernández-Bernal, J., Sánchez-Lavega, A., del Río-Gaztelurrutia, T., Ravanis, E., Cardesin-Moinelo, A., Connour, K., et al. (2020). An extremely elongated cloud over Arsia Mons volcano on Mars: I. Life cycle. *Journal of Geophysical Research*, *126*, e2020JE006517. <https://doi.org/10.1029/2020JE006517>
- Holden, E. S. (1894). *Bright projections at the terminator of Mars*. Publications of the Astronomical Society of the Pacific.
- Holden, E. S., Schaeberle, J. M., & Keeler, J. E. (1890). *White spots on the terminator of Mars*. Publications of the Astronomical Society of the Pacific.
- Inada, A., Richardson, M. I., McConnochie, T. H., Strausberg, M. J., Wang, H., & Bell, J. F., III. (2007). High-resolution atmospheric observations by the Mars Odyssey thermal emission imaging system. *Icarus*, *192*(2), 378–395. <https://doi.org/10.1016/j.icarus.2007.07.020>
- James, P. B., Bell, J. F., III, Clancy, R. T., Lee, S. W., Martin, L. J., & Wolff, M. J. (1996). Global imaging of Mars by Hubble Space Telescope during the 1995 opposition. *Journal of Geophysical Research*, *101*(E8), 18883–18890. <https://doi.org/10.1029/96je01605>
- Kahn, R., Goody, R., & Pollack, J. (1981). The Martian twilight. *Journal of Geophysical Research*, *86*(A7), 5833–5838. <https://doi.org/10.1029/ja086ia07p05833>
- Kahre, M. A., Murphy, J. R., Newman, C. E., Wilson, R. J., Cantor, B. A., Lemmon, M. T., & Wolff, M. J. (2017). The Mars dust cycle. *The Atmosphere and Climate of Mars*, *18*, 295.
- Määttänen, A., Montmessin, F., Gondet, B., Scholten, F., Hoffmann, H., González-Galindo, F., et al. (2010). Mapping the mesospheric CO<sub>2</sub> clouds on Mars: MEX/OMEGA and MEX/HRSC observations and challenges for atmospheric models. *Icarus*, *209*(2), 452–469. <https://doi.org/10.1016/j.icarus.2010.05.017>
- Määttänen, A., Pérot, K., Montmessin, F., & Hauchecorne, A. (2013). Mesospheric clouds on Mars and on Earth. In *Comparative climatology of terrestrial planets* (pp. 393–413). The University of Arizona Press.
- McCleese, D. J., Heavens, N. G., Schofield, J. T., Abdou, W. A., Bandfield, J. L., Calcutt, S. B., & Paige, D. A. (2010). Structure and dynamics of the Martian lower and middle atmosphere as observed by the Mars Climate Sounder: Seasonal variations in zonal mean temperature, dust, and water ice aerosols. *Journal of Geophysical Research*, *115*(E12), E12016. <https://doi.org/10.1029/2010je003677>
- McConnochie, T. H., Bell, J. F., III, Savransky, D., Wolff, M. J., Toigo, A. D., Wang, H., et al. (2010). THEMIS-VIS observations of clouds in the martian mesosphere: Altitudes, wind speeds, and decameter-scale morphology. *Icarus*, *210*(2), 545–565. <https://doi.org/10.1016/j.icarus.2010.07.021>
- Millour, E., Forget, F., González-Galindo, F., Spiga, A., Lebonnois, S., Lewis, S. R., & Huot, J. P. (2009). *The mars climate database (version 4.3)*. SAE Technical Paper. (No. 2009-01-2395).
- Montabone, L., Spiga, A., Kass, D. M., Kleinböhl, A., Forget, F., & Millour, E. (2020). Martian Year 34 column dust climatology from Mars climate sounder observations: Reconstructed maps and model simulations. *Journal of Geophysical Research: Planets*, *125*, e2019JE006111. <https://doi.org/10.1029/2019JE006111>
- Montmessin, F., Bertaux, J.-L., Quémerais, E., Korablev, O., Rannou, P., Forget, F., et al. (2006). Subvisible CO<sub>2</sub> ice clouds detected in the mesosphere of Mars. *Icarus*, *183*(2), 403–410. <https://doi.org/10.1016/j.icarus.2006.03.015>
- Montmessin, F., Gondet, B., Bibring, J. P., Langevin, Y., Drossart, P., Forget, F., & Fouchet, T. (2007). Hyperspectral imaging of convective CO<sub>2</sub> ice clouds in the equatorial mesosphere of Mars. *Journal of Geophysical Research: Planets*, *112*(E11), E11S90. <https://doi.org/10.1029/2007je002944>
- Montmessin, F., Quémerais, E., Bertaux, J. L., Korablev, O., Rannou, P., & Lebonnois, S. (2006). Stellar occultations at UV wavelengths by the SPICAM instrument: Retrieval and analysis of Martian haze profiles. *Journal of Geophysical Research: Planets*, *111*(E9), E09S09. <https://doi.org/10.1029/2005je00266>
- Newman, C. (2019). *Sols 2400-2401: Just a cloud at twilight...—NASA's mars exploration program*. Retrieved from <https://mars.nasa.gov/msl/mission-updates/sols-2400-2401-just-a-cloud-at-twilight/>
- Ormonston, T., Denis, M., Scuka, D., & Griebel, H. (2011). An ordinary camera in an extraordinary location: Outreach with the Mars Webcam. *Acta Astronautica*, *69*(7–8), 703–713. <https://doi.org/10.1016/j.actaastro.2011.04.015>
- Pellier, C. (2012). Martian terminator projections observed by the HST. In *Communications in Mars observations No. 400*. International Society of Mars Observers. <https://www.kwasan.kyoto-u.ac.jp/~cmo/cmomn4/CMO400.pdf>
- Piqueux, S., Kleinböhl, A., Hayne, P. O., Kass, D. M., Schofield, J. T., & McCleese, D. J. (2015). Variability of the Martian seasonal CO<sub>2</sub> cap extent over eight Mars Years. *Icarus*, *251*, 164–180. <https://doi.org/10.1016/j.icarus.2014.10.045>
- Ravanis, E., Hernández-Bernal, J., Cardesin-Moinelo, A., Sánchez-Lavega, A., del Río-Gaztelurrutia, T., Hueso, R., et al. (2020). From engineering to science: Mars Express Visual Monitoring Camera's first science data release 14 Europlanet Science Congress. <https://doi.org/10.5194/epsc2020-437>
- Sánchez-Lavega, A., Chen-Chen, H., Ordoñez-Etxebarria, I., Hueso, R., del Río-Gaztelurrutia, T., Garro, A., et al. (2018). Limb clouds and dust on Mars from images obtained by the Visual Monitoring Camera (VMC) onboard Mars Express. *Icarus*, *299*, 194–205. <https://doi.org/10.1016/j.icarus.2017.07.026>
- Sánchez-Lavega, A., del Río-Gaztelurrutia, T., Hernández-Bernal, J., & Delcroix, M. (2019). The onset and growth of the 2018 Martian global dust storm. *Geophysical Research Letters*, *46*(11), 6101–6108. <https://doi.org/10.1029/2019GL083207>
- Sánchez-Lavega, A., Muñoz, A. G., García-Melendo, E., Pérez-Hoyos, S., Gómez-Forrellad, J. M., Pellier, C., et al. (2015). An extremely high-altitude plume seen at Mars' morning terminator. *Nature*, *518*(7540), 525–528. <https://doi.org/10.1038/nature14162>
- Scholten, F., Hoffmann, H., Määttänen, A., Montmessin, F., Gondet, B., & Hauber, E. (2010). Concatenation of HRSC colour and OMEGA data for the determination and 3D-parameterization of high-altitude CO<sub>2</sub> clouds in the Martian atmosphere. *Planetary and Space Science*, *58*(10), 1207–1214. <https://doi.org/10.1016/j.pss.2010.04.015>
- Sefton-Nash, E., Teanby, N. A., Montabone, L., Irwin, P. G. J., Hurley, J., & Calcutt, S. B. (2013). Climatology and first-order composition estimates of mesospheric clouds from Mars Climate Sounder limb spectra. *Icarus*, *222*(1), 342–356. <https://doi.org/10.1016/j.icarus.2012.11.012>
- Seidelmann, P. K. (1992). *Explanatory supplement to the astronomical almanac*. University Science Books.
- Sharaf, O., Amiri, S., Aldhafri, S., Withnell, P., & Brain, D. (2020). Sending hope to Mars. *Nature Astronomy*, *4*(7), 722. <https://doi.org/10.1038/s41550-020-1151-y>
- Smith, D. E., Zuber, M. T., Frey, H. V., Garvin, J. B., Head, J. W., Muhleman, D. O., et al. (2001). Mars Orbiter Laser Altimeter: Experiment summary after the first year of global mapping of Mars. *Journal of Geophysical Research*, *106*(E10), 23689–23722. <https://doi.org/10.1029/2000je001364>

- Smith, P. H., Bell, J. F., Bridges, N. T., Britt, D. T., Gaddis, L., Greeley, R., et al. (1997). Results from the Mars Pathfinder camera. *Science*, 278(5344), 1758–1765. <https://doi.org/10.1126/science.278.5344.1758>
- Vincendon, M., Pilorget, C., Gondet, B., Murchie, S., & Bibring, J. P. (2011). New near-IR observations of mesospheric CO<sub>2</sub> and H<sub>2</sub>O clouds on Mars. *Journal of Geophysical Research*, 116(E11), E00J02. <https://doi.org/10.1029/2011je003827>
- Wan, W. X., Wang, C., Li, C. L., & Wei, Y. (2020). China's first mission to Mars. *Nature Astronomy*, 4(7), 721. <https://doi.org/10.1038/s41550-020-1148-6>
- Wang, H., & Ingersoll, A. P. (2002). Martian clouds observed by Mars global surveyor Mars orbiter camera. *Journal of Geophysical Research*, 107(E10), 8–1. <https://doi.org/10.1029/2001je001815>
- Zurek, R. W. (2017). Understanding Mars and its atmosphere. *The Atmosphere and Climate of Mars*, 18.



This article is a companion to Hernández-Bernal et al. (2020), <https://doi.org/10.1029/2020JE006517>

**Key Points:**

- We performed mesoscale model dynamic simulations of the Arsia Mons Elongated Cloud observed in the Martian southern solstice
- Topography-induced circulation causes temperatures to drop by about 30 K at the observed origin location and local time of the cloud
- The cloud tail is much more elongated in the observations than in the model, which challenges our understanding of winds and microphysics

**Supporting Information:**

Supporting Information may be found in the online version of this article.

**Correspondence to:**

J. Hernández-Bernal,  
[jorge.hernandez@ehu.es](mailto:jorge.hernandez@ehu.es)

**Citation:**

Hernández-Bernal, J., Spiga, A., Sánchez-Lavega, A., del Río-Gaztelurrutia, T., Forget, F., & Millour, E. (2022). An extremely elongated cloud over Arsia Mons volcano on Mars: 2. Mesoscale modeling. *Journal of Geophysical Research: Planets*, 127, e2022JE007352. <https://doi.org/10.1029/2022JE007352>

Received 28 APR 2022

Accepted 20 SEP 2022

**Author Contributions:**

**Conceptualization:** J. Hernández-Bernal, A. Spiga

**Data curation:** A. Spiga, F. Forget, E. Millour

**Formal analysis:** J. Hernández-Bernal, A. Spiga

**Funding acquisition:** A. Sánchez-Lavega, T. del Río-Gaztelurrutia

© 2022 The Authors.

This is an open access article under the terms of the [Creative Commons Attribution-NonCommercial License](#), which permits use, distribution and reproduction in any medium, provided the original work is properly cited and is not used for commercial purposes.

# An Extremely Elongated Cloud Over Arsia Mons Volcano on Mars: 2. Mesoscale Modeling

J. Hernández-Bernal<sup>1,2</sup> , A. Spiga<sup>3</sup> , A. Sánchez-Lavega<sup>1</sup> , T. del Río-Gaztelurrutia<sup>1</sup> , F. Forget<sup>3</sup>, and E. Millour<sup>3</sup>

<sup>1</sup>Departamento de Física Aplicada, EIB, Universidad País Vasco UPV/EHU, Bilbao, Spain, <sup>2</sup>Aula Espazio Gela, Escuela de Ingeniería de Bilbao, Universidad del País Vasco UPV/EHU, Bilbao, Spain, <sup>3</sup>Laboratoire de Météorologie Dynamique/Institut Pierre Simon Laplace (LMD/IPSL), Sorbonne Université, Centre National de la Recherche Scientifique (CNRS), École Polytechnique, École Normale Supérieure (ENS), Paris, France

**Abstract** In a previous work (Hernández-Bernal et al., 2021, <https://doi.org/10.1029/2020je006517>) we performed an observational analysis of the Arsia Mons Elongated Cloud (AMEC), which stands out due to its impressive size and shape, quick dynamics, and the fact that it happens during the Martian dusty season. Observations show that its morphology can be split in a head, on the western slope of the volcano of around 120 km in diameter; and a tail, that expands to the west reaching more than 1,000 km in length, making the AMEC the longest orographic cloud observed so far in the solar system. In this work we run the Laboratoire de Météorologie Dynamique Mesoscale Model to gain insight into the physics of the AMEC. We note that it is coincident in terms of local time and seasonality with the fastest winds on the summit of Arsia Mons. A downslope windstorm on the western slope is followed by a hydraulic-like jump triggering a strong vertical updraft that propagates upwards in the atmosphere, causing a drop in temperatures of down to 30 K at 40–50 km in altitude, spatially and temporarily coincident with the observed head of the AMEC. However the model does not reproduce the microphysics of this cloud: the optical depth is too low and the expansion of the tail does not happen in the model. The observed diurnal cycle is correctly captured by the model for the head of the cloud. This work raises new questions that will guide future observations of the AMEC.

**Plain Language Summary** This is the second paper of our research on the Arsia Mons Elongated Cloud (AMEC), which is a visually impressive cloud on Mars. It appears on the western flank of the Arsia Mons volcano during a specific season right at sunrise. For 3 hr it grows, developing a thin elongated tail that has been observed to be as long as 1,800 km. In our previous work we described available observations. In this work we run a high resolution atmospheric model that captures the effect of the Arsia Mons volcano on the atmosphere. This model shows that due to the presence of the volcano and its effect on the wind, air is forced upwards next to the volcano, leading to a drop in temperatures of 30°C, which causes the formation of the cloud under extreme conditions of humidity. This is a success of the model that provides a new understanding of this outstanding cloud, however, the accurate physics behind the extreme expansion of the AMEC are not fully understood yet. This work solves some questions and raises many new ones, which will be an aid in the planning of new observations.

## 1. Introduction

In a recent work (Hernández-Bernal et al., 2021; henceforth Part 1 paper) we reported the existence of the Arsia Mons Elongated Cloud (AMEC), and we performed a comprehensive observational analysis of this unusual cloud. It forms every morning on the western slope of the Arsia Mons volcano on Mars, in a not well constrained period within the dusty season, potentially lasting from Ls (Solar Longitude) 220° to Ls 320°, which includes the perihelion (Ls 251°) and the southern solstice (Ls 270°). This orographic cloud starts its expansion from the western slope of Arsia Mons around local sunrise (5.7 local time), and it grows to the west for 2–3 hr. The expansion velocity was observed to be around 130 m/s in most Martian Years (MY), and 170 m/s in MY34. Its maximum observed length was 1,800 km. The altitude of the cloud was measured to be around 45 km. Figure 1 is a visual summary of Part 1 paper featuring its main characteristics.

Arsia Mons is part of the volcanic region of Tharsis, where other volcanoes are also present (see e.g., Figure 2). This area has been known for the frequent presence of thick clouds since the early telescopic observations

**Investigation:** J. Hernández-Bernal, A. Spiga, A. Sánchez-Lavega, T. del Río-Gaztelurrutia, F. Forget  
**Methodology:** J. Hernández-Bernal, A. Spiga, E. Millour  
**Project Administration:** A. Sánchez-Lavega, T. del Río-Gaztelurrutia  
**Resources:** A. Sánchez-Lavega, T. del Río-Gaztelurrutia  
**Software:** J. Hernández-Bernal, A. Spiga, F. Forget, E. Millour  
**Supervision:** A. Spiga, A. Sánchez-Lavega, T. del Río-Gaztelurrutia  
**Validation:** A. Spiga  
**Visualization:** J. Hernández-Bernal, A. Spiga, A. Sánchez-Lavega, T. del Río-Gaztelurrutia, F. Forget, E. Millour  
**Writing – original draft:** J. Hernández-Bernal  
**Writing – review & editing:** J. Hernández-Bernal, A. Spiga, A. Sánchez-Lavega, T. del Río-Gaztelurrutia

(Slipher, 1927; Smith & Smith, 1972). Later on, new observations made obvious that Tharsis is an elevated area hosting high topographic features and that those clouds were of orographic origin (Peale, 1973; Sagan et al., 1971).

The spatial and seasonal distribution of water ice clouds through the Martian Year, and the seasonal trends of orographic clouds on the volcanoes of Tharsis were clearly described by Wang and Ingersoll (2002), and Benson et al. (2003, 2006) based on daily observations during the local afternoon by the Mars Orbiter Camera (MOC). They showed that orographic clouds are regularly present at the Tharsis volcanoes during the first half of the Martian year (Ls 0°–180°), when tropical clouds are very common as part of the Aphelion Cloud Belt (ACB; Clancy et al., 1996). However, during the dusty season at the second half of the year (Ls 180°–360°), clouds are not common in low latitudes. Systematic observations usually take place in the afternoon, and Arsia Mons is the only low-latitude location with frequent clouds in these observations. The AMEC occurs at Arsia Mons during this season in the early morning, a local time not covered by MOC and other instruments and therefore it is not included in the aforementioned works (see Part 1 paper).

Several authors have used Mesoscale Models (MM) to study orographic clouds on Tharsis during the first half of the year (Ls ~100°). Michaels et al. (2006) explored the formation of orographic clouds on Olympus and Ascraeus Mons based on the MRAMS mesoscale model (Rafkin et al., 2001). They showed that the main mechanism behind these orographic clouds is the pumping of water from lower to higher altitudes by insolation driven wind on the slopes of the volcanoes. Water vapor is elevated to higher layers, and it condenses into water-ice clouds that are usually advected to the west by the predominant winds. Spiga and Forget (2009) tested the Laboratoire de Meteorologie Dynamique (LMD) Mars Mesoscale Model on different meteorological phenomena, including orographic clouds on Tharsis at Ls 90° and 120°, and they reached similar conclusions to those of Michaels et al. (2006).

Due to the proximity to the aphelion (Ls 71°), in the current climate global average temperatures on Mars are lower during the first half of the year than during the second half. As a result, during that season the low-latitude hygropause (the layer where conditions for water condensation are met, typically confining water beneath) is located at a relatively low altitude (about 10–20 km), favoring the occurrence of the ACB (Clancy et al., 1996; Montmessin et al., 2004). During the second half of the year, the hygropause raises to 30–60 km and as a result, clouds form at higher altitudes (Clancy et al., 1996), and water vapor is no longer confined to the lower atmosphere (e.g., Fedorova et al., 2021).

In this work we used a hierarchy of multiscale modeling, from global climate simulations to regional “mesoscale” simulations of the area of Tharsis during the second half of the year, and gained insight into the atmospheric physics driving the AMEC. We also use this modeling framework to put the AMEC in perspective with the orographic cloud formation mechanism described by Michaels et al. (2006) and the relationship to seasonal variability of the hygropause.

In Section 2 we describe our simulations. We present our results for the AMEC analysis in Sections 3–6. In Section 3 we overview the environment conditions as extracted from the global-scale model. In Section 4 we show the prediction of the MM for the AMEC, and describe the general dynamics and microphysics that very probably lead to the occurrence of this unusual cloud. In Section 5 we show the diurnal cycle of the AMEC as predicted by the model. In Section 6 we explore sol-to-sol, seasonal, and interannual variations based on the GCM predictions from Section 3 and the knowledge about the AMEC acquired in Section 4. In Section 7 we provide some conclusions and perspectives.

## 2. Methodology

In this study, we use the Mars Mesoscale Model (MMM; or MM, for Mesoscale Model) initially described by Spiga and Forget (2009), which consists in coupling an adapted version of the terrestrial Weather Research and Forecast model (Skamarock & Klemp, 2008) with the Martian physical packages developed at LMD: radiative transfer (Forget et al., 1999), dust processes (Madeleine et al., 2011), and water-ice clouds formation including microphysics (Navarro et al., 2014). The MMM uses initial and boundary conditions from the LMD Global Climate Model (GCM) with which most of the physical parameterizations are shared. The mesoscale modeling methodology deployed in this paper is similar to mesoscale simulations developed in Spiga et al. (2017).

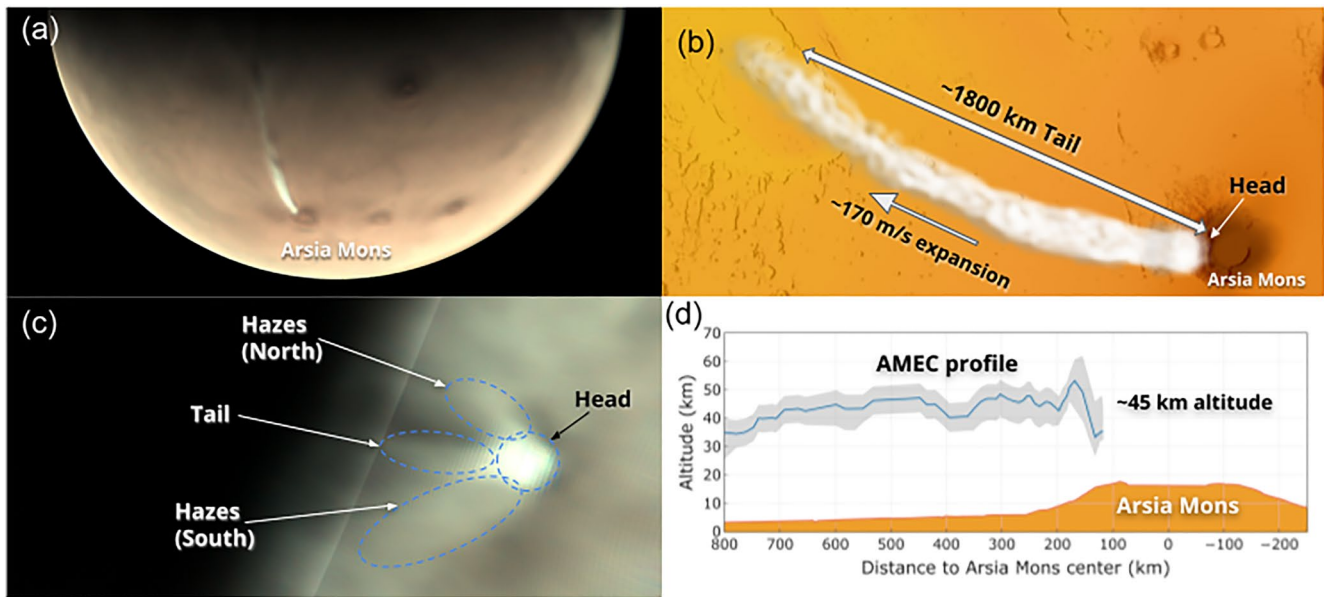


**Figure 1.** Visual summary of the main Arsia Mons Elongated Cloud (AMEC) features as reported in Part 1 paper. (a) The AMEC as imaged by VMC onboard Mars Express. (b) Idealized artistic impression of the AMEC featuring its main morphological parts (head and tail), its expansion velocity, and tail length. (c) Annotated image of the AMEC (extracted from panel 9g from Part 1 paper) showing the hazes occasionally observed around the tail. (d) Vertical profile of the AMEC as reported in Part 1 paper.

Specifics of the simulations carried out to explore AMEC-like phenomena are detailed as follows. The horizontal domain comprises  $321 \times 321$  grid points with mesh spacing of 10 km, encompassing the large region of the Tharsis volcanoes around Arsia Mons (see Figure 2). Along the vertical, 101 levels were included with a model top at 1 Pa (approximately 60 km above the local surface) and mesh spacing progressively increasing from 5 m in the lowermost layer to 1,300 m at model top; vertical resolution within the altitudes of interest for this study (20 and 45 km) are respectively about 700 and 900 m. Integration timestep is 20 s and the WRF dynamical core uses the non-hydrostatic option. All simulations were run for three full Martian sols; as is usually done for mesoscale simulations, the first sol is considered as model spin-up and the second and third sols are retained for analysis. Results from the second and third simulated sols are very similar and we chose to perform our analysis on the second simulated sol. Plots refer to this second sol, except otherwise indicated.

Our reference simulation to analyze AMEC-like signatures is constrained by the dust scenario for MY34 detailed in Montabone et al. (2020). We chose this scenario because most observations in Part 1 paper were in MY34. Note that the GCM predictions for this MY34, which were used for mesoscale simulations as initial and boundary conditions, are also discussed in our Section 3 to discuss the global-scale conditions relevant for our analysis. To put MY34 in a broader context, this discussion in Section 3 also includes GCM runs using dust scenarios at other MY (Montabone et al., 2015). The 3-sol MMM simulation is done at the northern winter solstice at  $L_s = 270^\circ$ . In this paper, all local times (LT) are Local True Solar Time at the meridian  $240^\circ\text{E}$ , which crosses Arsia Mons and all altitudes are expressed as being above the reference areoid defined with MOLA topography (Smith et al., 2001).

The LMD MMM predicts the observed daytime and nighttime cloud covers for the aphelion season around  $L_s = 120^\circ$  (Spiga & Forget, 2009, their Figure 10; Spiga et al., 2017, their Supplementary Figure 5), similarly to predictions discussed for example, in Michaels et al., 2006 (their Figure 1). Previous reports of mesoscale modeling of water-ice clouds for Tharsis did not discuss the perihelion season  $L_s = 270^\circ$  considered here. The AMEC takes place in the morning, when not many observations are available, probably all of them analyzed in Part 1 paper. On the other hand, systematic observations in the afternoon by sun-synchronous orbiters have enabled a very good knowledge of that local time. Based on such observations, Wang and Ingersoll (2002) and Benson et al. (2003, 2006) showed that during the perihelion season Arsia Mons is the only Tharsis volcano that exhibits prominent clouds in the afternoon, which is in qualitative agreement with the MM results shown in Figure 2 for the same local time. This strengthens the reliability of our results.

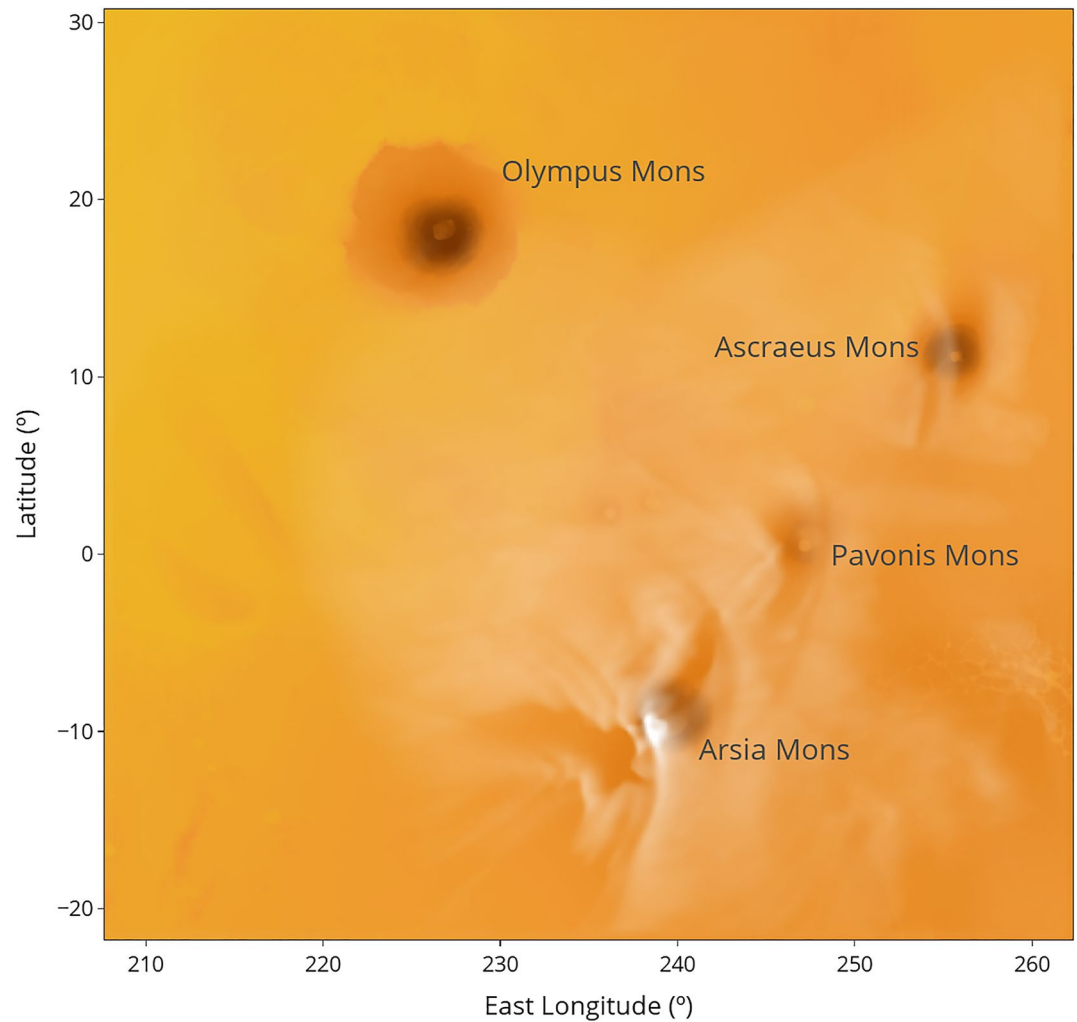


**Figure 2.** Representation of visible clouds predicted by the Mesoscale Model in the afternoon in the reference simulation, in MY34 at Ls 270°. The maximum predicted optical depth is around 0.2. Refer to Figure S1 in Supporting Information S1 for the equivalent quantitative representation of optical depth.

### 3. Environment Conditions From the GCM

We show in this section the relevant unperturbed environment conditions at the time and season of the AMEC, as extracted from the GCM. We expect winds to be a key for the dynamics of the AMEC, and temperature and water content to affect the microphysics of the cloud. These large scale variables are given by the global circulation, which also involves the relevant effects of thermal tides (e.g., Barnes et al., 2017). Since the AMEC occurs at a particular season and local time, we show these variables in terms of altitude, local time, and solar longitude.

Figure 3a shows zonal winds at 20 km (over the summit of Arsia Mons) plotted in terms of Solar Longitude and Local Time for MY34. It is apparent that the AMEC season and local time (marked by a white rectangle) is coincident with the fastest zonal winds on the summit of Arsia. This trend repeats annually, although there are obvious interannual variations (see Figure 3d). The early onset of strong westward winds in MY 34 is particularly noticeable. Vertical zonal wind profiles show westward winds higher up, peaking at approximately 45 km (Figure 3b shows the profile at 7 LT and Ls270, when the cloud is fully developed), and winds at 45 km are also faster during the AMEC season compared to other seasons (Figure 3d).

As expected, temperature is higher during the perihelion season, due to the higher insolation (Figure 3f). This leads to a rise of the hygropause, which enables higher concentrations of water in the mesosphere (Figures 3c and 3g).

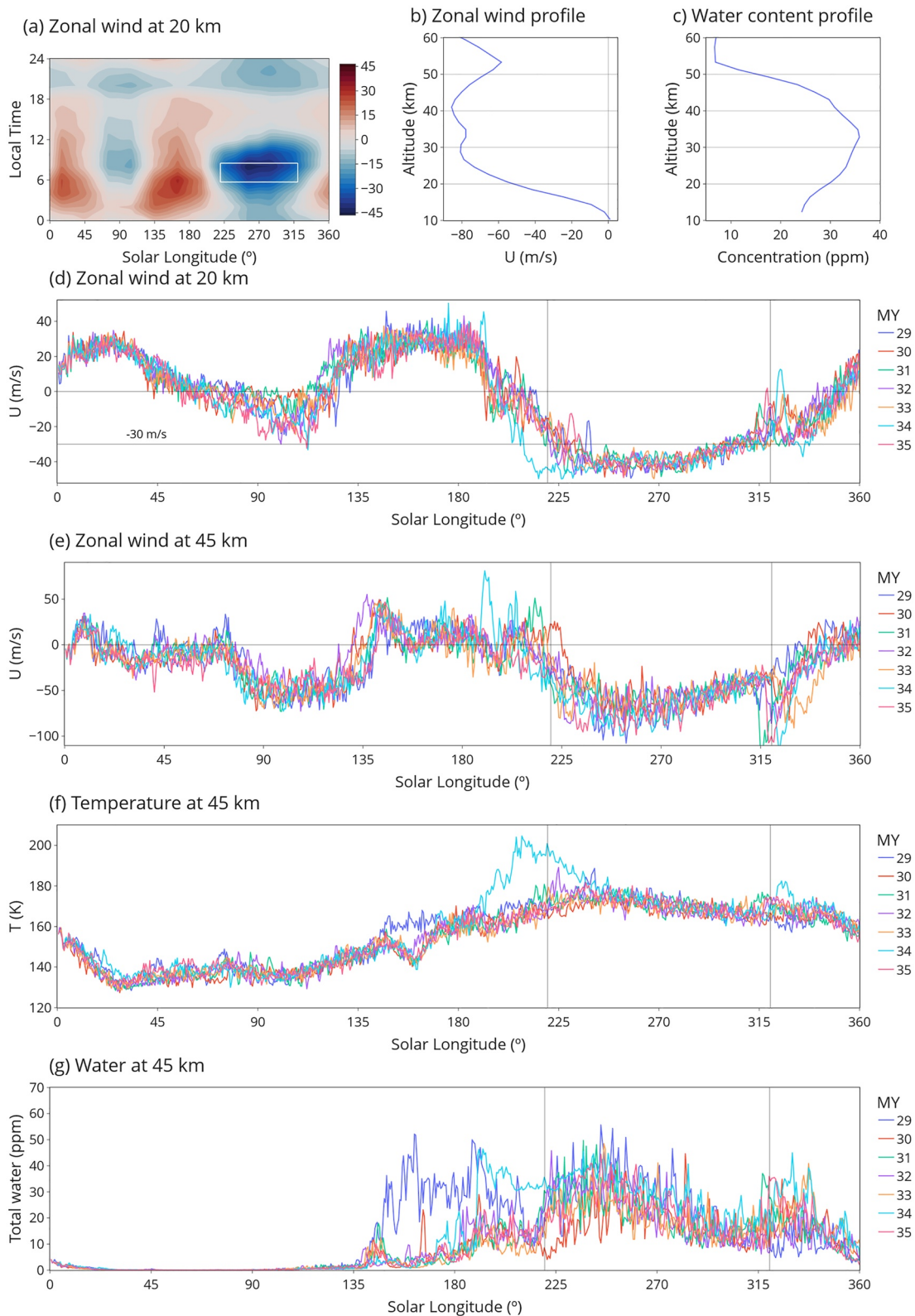


Figure 3.

#### 4. Dynamics and Microphysics of the AMEC

In this section, we use results from the MM to identify the main physical processes that lead to the occurrence of the AMEC.

As shown in Part 1 paper, the AMEC occurs in the season around Ls 220–320°, and its daily expansion starts around 5.7 LT, finishing around 8.5 LT. For simplicity, in order to explore the general mechanisms of the phenomenon, we use in this section a fixed local time, 7.6 LT, a local time when the AMEC is well developed in observations. The diurnal cycle is explored in Section 5.

Water pumping by volcanoes from lower altitudes (by upslope anabatic winds) is an efficient mechanism to form orographic clouds at low latitudes during the aphelion season (Michaels et al., 2006). Our simulations show that this is not the main mechanism behind the AMEC (or other orographic clouds taking place on Tharsis during the perihelion season), because the hygropause moves to higher altitudes during this season compared to the colder aphelion season (e.g., Fedorova et al., 2021). As a result, at the perihelion season, less water is available at low altitudes to be transported upwards by volcanoes (see e.g., Figures 3c and 6d), and the altitudes reached by transported water are not high enough to trigger condensation. Instead, gravity waves produced by the volcanoes, which perturb the hygropause, are the main driver of orographic clouds during the perihelion season. This is illustrated in Videos S1 and S2 in Supporting Information S1. Taking this into consideration, we base our following discussion about the AMEC on the fact that the vertical transport of water from the surface is negligible.

##### 4.1. Perturbation of the Atmosphere by Arsia Mons During the AMEC

The MM shows how Arsia Mons perturbs the local atmosphere at all altitudes during the AMEC season (Figure 4). Easterly winds are perturbed by the volcano, triggering orographic gravity waves, creating ascending and descending cells, with the strongest updraft on lee side (red cell in the left side of the volcano in Figure 4), at the western side of the volcano. Typical gravity wave perturbations of vertical wind simulated by the model reach 8 m/s, while the strongest updraft reach a much larger vertical velocity of 20 m/s with no corresponding down-draft of this amplitude. This Strong Vertical Updraft (SVU from now onwards) causes a drop in temperatures (a cold pocket; represented by thick black contours in Figure 4) of down to  $-30\text{K}$  at altitudes around 40–50 km. The longitude, latitude and altitude of the center of this cold pocket are coincident with the position of what we called the head of the AMEC in Part 1 paper (see Figure 1). The PFS instrument onboard Mars Express has recently observed cold pockets over Tharsis volcanoes in this season that resemble the one found in our simulation (P. Wolkenberg, private communication).

This SVU in the lee side is strongly reminiscent of a hydraulic jump. Upstream the hydraulic-like jump, on the slope of the mountain, we see a downslope windstorm (blue cell on the left slope of the volcano in Figure 4, indicated with an arrow). Downslope windstorms on Earth mountains have received strong interest because they can be very fast near the surface, potentially posing a risk, and they are sometimes followed a hydraulic jump. Different theoretical approaches have been proposed to characterize this kind of flow around mountains (e.g., Durran, 1990; Lott, 2016). In our case, the fast winds blowing on the summit of Arsia Mons (Figure 3a), the vertical shear of winds, and the presence of a critical level near the surface (Figure 3b), are conditions that favor the occurrence of the downslope windstorm followed by the hydraulic-like jump.

The SVU grows with altitude (in terms of wind speed and flow perturbation) as a result of the lowering of pressure, as expected from gravity-wave theory. The adiabatic ascent of air masses in the SVU is the cause of the temperature drop, which is larger for higher vertical ascent of air parcels. The thick gray streamline shown in Figure 4, reveals a net ascent of up to 8 km at the altitude where the AMEC forms ( $\sim 45\text{ km}$ ), coincident with the largest drop in temperature. It is followed by much slower descent that retains colder temperatures in the whole area, as we show in Section 4.2. The total vertical ascent of parcels is not just a result of vertical wind speed, the width of the ascending cells, and the horizontal wind speeds are also important.

**Figure 3.** Environment conditions. Negative zonal winds are westward. (a) Zonal winds (m/s) over the summit of Arsia Mons (at 20 km), extracted from the Mars Climate Database. The strongest winds are coincident with observations of the Arsia Mons Elongated Cloud: at Ls  $\sim 220^\circ$ – $320^\circ$ , and Local Time 5.7–8.5 (squared area). (b) Vertical profile of zonal winds on Arsia at 7 LT and Ls  $270^\circ$ . (c) Vertical profile of water content (vapor and ice) on Arsia at 7 LT and Ls  $270^\circ$ . (d–g) Variables at relevant altitudes for each sol of different years in the GCM, at 7 LT at Arsia Mons; seasonal trends, sol-to-sol variations, and interannual variations are apparent. Potential AMEC season indicated between two vertical lines. (d) Zonal winds at 20 km (over the summit of Arsia). (e) Zonal wind at 45 km (cloud altitude). (f) Temperature. (g) Total water (vapor and ice) volume mixing ratio (ppm).

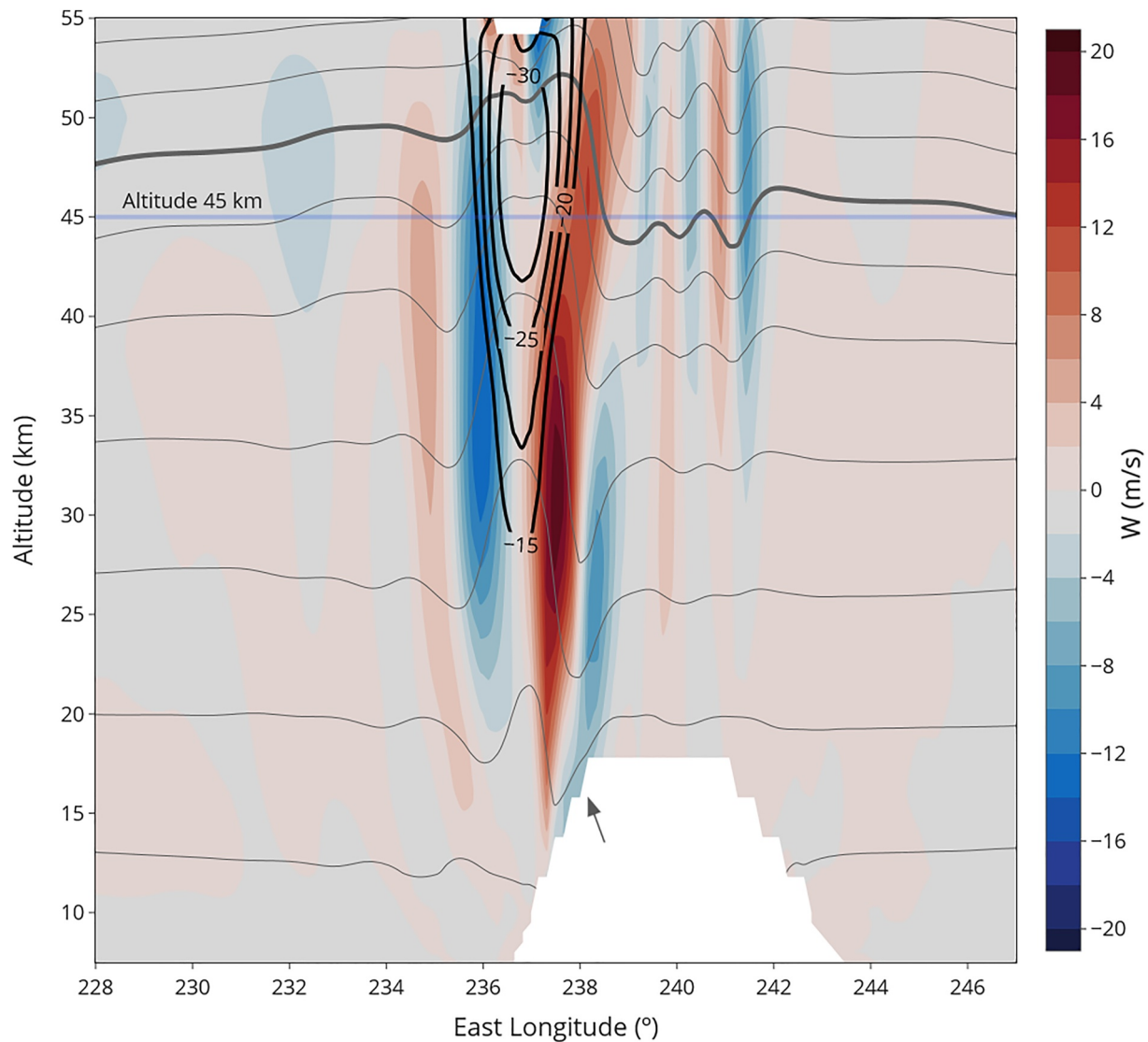


**Figure 4.** Atmospheric perturbations caused by Arsia Mons in the reference run of the mesoscale model at 7.6 LT at latitude 8.7°S. Background shade represents vertical winds in m/s (scale at right). Gray curves are potential temperature contours, which correspond to streamlines, with zonal winds blowing westward (i.e., from right to left in this graph). The thick gray curve departing at 45 km shows that there is a positive vertical displacement after the head of the cloud. Thick black contours indicate the area where the temperature is lower than the mean for a given altitude, from  $-15$  to  $-30$  K. A horizontal blue line indicates 45 km in altitude for comparison with latter figures. The arrow in the mountain indicates the lee side downslope windstorm.

As we noted in Section 3, the AMEC season coincides with the fastest zonal winds on the summit of Arsia Mons (Figure 3a). We cannot establish a definitive connection between these transient fast winds and the occurrence of the SVU leading to the AMEC. Other variables, like the specific vertical profile of winds or potential temperature might play a significant role.

In summary of this section, the occurrence of the AMEC is coincident with the presence of fastest winds on the summit of Arsia Mons (Figure 3a). This, together with the characteristics of the wind profile is probably the cause of the onset of the SVU on the lee of the volcano. At higher altitudes, at the altitude of the cloud, the adiabatic ascent of air parcels for up to 8 km creates a cold pocket with temperatures down to 30K below the environment temperature (Figure 4), coincident in space and time with what we called the head of the AMEC in Part 1 paper.

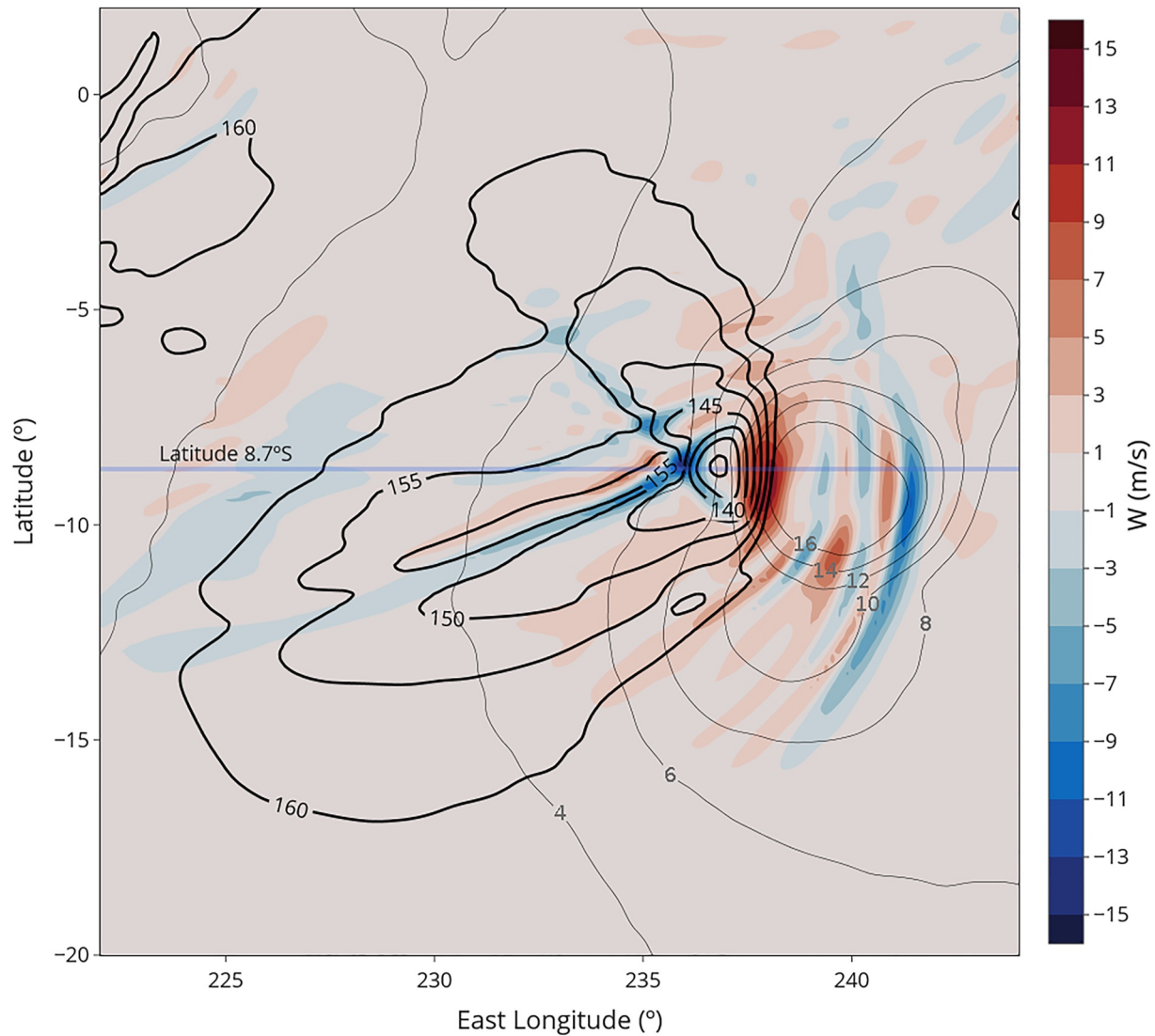


**Figure 5.** Anatomy of the cold pocket at 45 km in altitude. Background shade shows vertical winds in m/s, thin gray curves are contours of topography (altitude indicated in gray numbers), bold contours are isotherms below 160 K, which is around the environment temperature. The core of the cold pocket ( $T = 130\text{--}140\text{ K}$ ) is coincident with the head of the Arsia Mons Elongated Cloud, and is located right over the Strong Vertical Updraft. From this position, two branches with temperatures below 155 K depart to the northwest and southwest. A bigger area below 160 K extends to the west for almost 1,000 km. A horizontal blue line indicates latitude  $8.7^\circ\text{S}$  for comparison with Figure 4.

#### 4.2. Anatomy of the Cold Pocket

In Figure 4, thick contour lines mark the position of the cold pocket corresponding to the head of the AMEC at  $8.7^\circ\text{S}$ . The perturbations caused by Arsia Mons in the atmosphere extend in latitude in an asymmetric way that we describe in this subsection. Figure 5 shows the extent of the cold pocket at 45 km. The environment temperature at this altitude is around 160 K in the MM.

Next to the SVU, where the ascent of air parcels as traced by streamlines in Figure 4 is maximum, the cold pocket reaches its lowest temperature, below 140 K ( $\Delta T = -20\text{ K}$ ), and down to 130 K ( $\Delta T = -30\text{ K}$ ). This lowest-temperature area has a round shape that visually resembles the aspect of the head of the AMEC in observations. Its diameter is around 120 km, its center latitude is  $8.7^\circ\text{S}$ , and its easternmost longitude is  $237.5^\circ\text{E}$ ; all these parameters are in agreement with the measurements shown in Figure 8 of Part 1 paper, and therefore we consider that this feature predicted by the model corresponds to the actual head of the AMEC in observations.



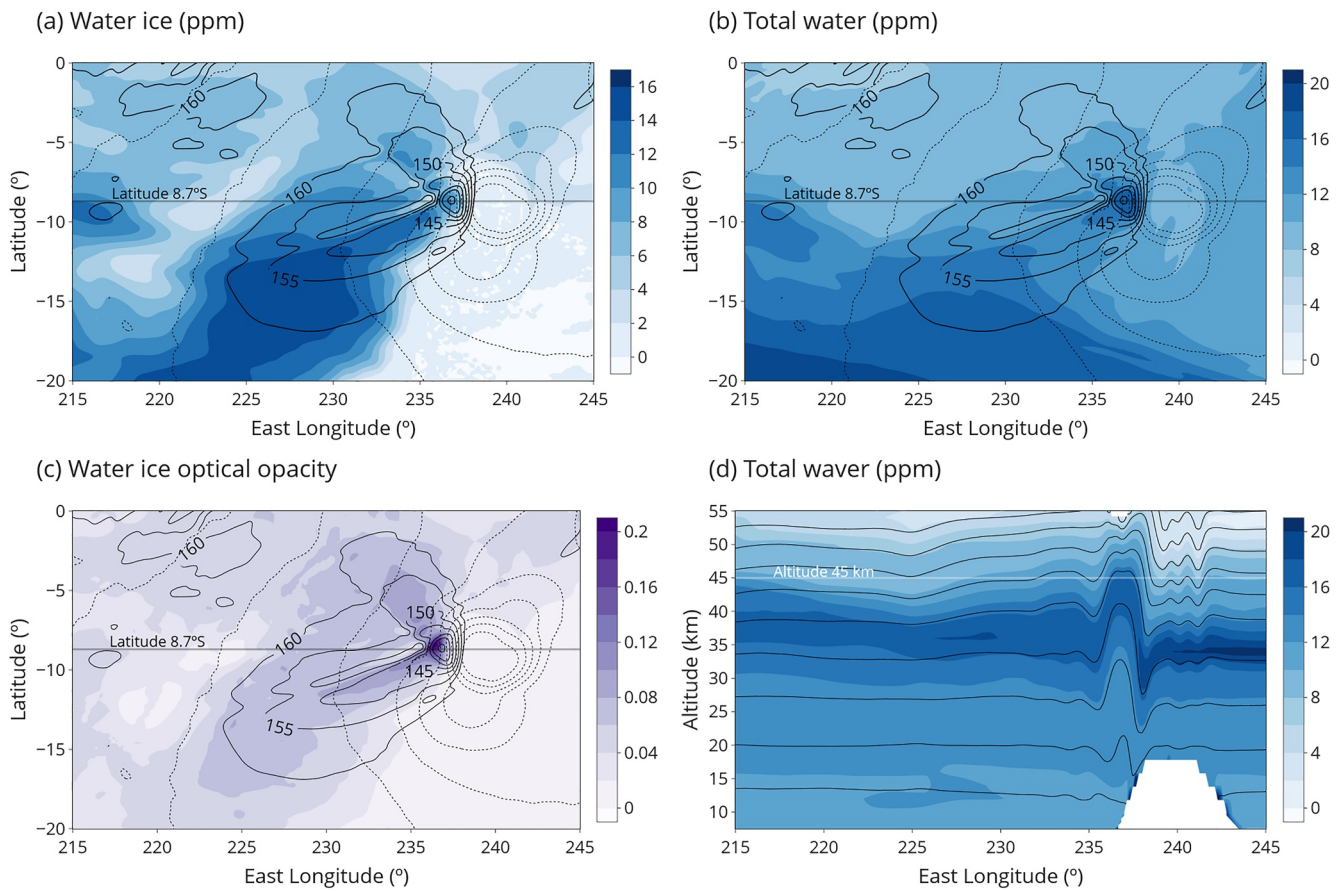


**Figure 6.** Water and clouds around Arsia Mons during the Arsia Mons Elongated Cloud at 7.6 LT as predicted by the mesoscale model. Color scales represent the magnitude indicated at the top of each panel. In panels (a–c) thick contour lines are isotherms, and in panel (d) lines of constant potential temperature, which correspond to streamlines. (a) Water ice concentration at 45 km. (b) Total water concentration at 45 km. (c) Water ice optical depth. (d) Total water volume mixing ratio (ppm) at latitude 8.7°S.

The contour below 155 K ( $\Delta T < -5$  K) exhibits the shape of two branches extending to the northwest and southwest. The southern branch has a narrow inner region of lower temperatures  $T < 150$  K that extends for around 500 km, with a width of only around 100 km. It is tempting to consider that this branch of the cold pocket corresponds to the tail of the AMEC, but we will show in Section 4.3 that the tail is more likely caused by advection. Both branches of the cold pocket extend to the West, which is the approximate direction of horizontal winds at this altitude. It is likely that the shape of this cold pocket with its two branches is related to the U shaped patterns found in the theoretical work by Smith (1980) on the flow past an isolated mountain.

Finally, the area where the temperature is below the unperturbed 160 K ( $\Delta T < 0$  K), extends up to 1,000 km to the West, due to the slow descent of air parcels after the SVU described above.

### 4.3. Cloud Formation and Expansion of the AMEC

In this subsection, we explore the cloud formation in the head of the AMEC and the formation of the characteristic tail.

We start by analyzing the water vapor and ice distributions in the model. Figures 6a and 6b show water ice distribution and total amount of water respectively, at 45 km altitude. The total amount of water is increased in the head of the AMEC compared to other areas at the same altitude. The vertical distribution of total water (Figure 6d) shows that this is a result of the vertical displacement of moist parcels following the SVU, which transports water from lower layers of the atmosphere, where water concentration is higher.

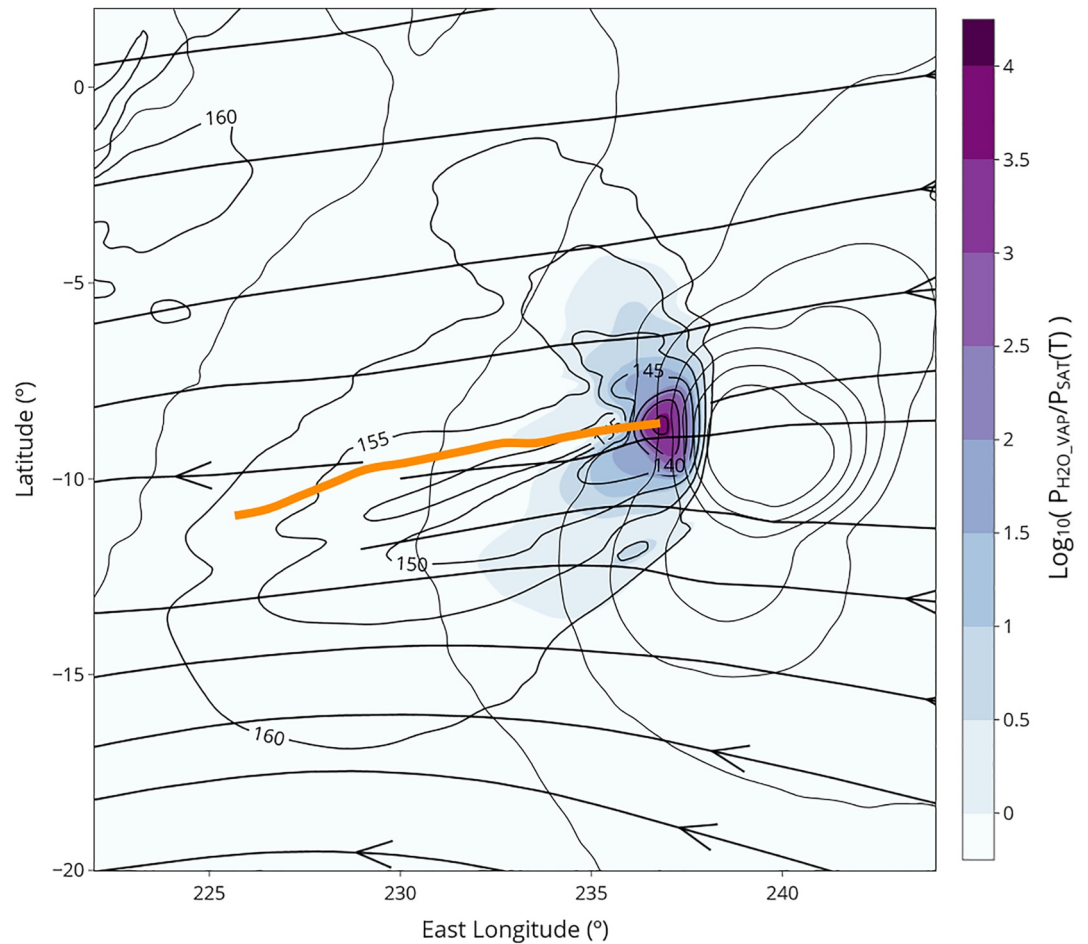


**Figure 7.** Relative humidity index at 45 km: water vapor partial pressure divided by the saturation pressure at a given temperature:  $P_{\text{H}_2\text{O\_VAP}}/P_{\text{SAT}}(T)$ . Represented in  $\log_{10}$  scale, as extracted from the mesoscale model at 7.6 LT. Superimposed streamlines of winds (arrows), and advection trajectory traced by hypothetical cloud particles from 5.7 to 7.6 LT (thick orange curve departing from the head). Cold pocket in the same format as in previous figures for reference.

Figures 6a and 6c show that water ice and optical depth are higher in the position of the head. However, the model does not directly reproduce the observed tail of the AMEC. Additionally, the maximum optical depth at the core of the cold pocket is 0.2, a low value, considering the brightness of the AMEC in the images by different instruments shown in Part 1 paper.

In the following subsections we discuss the microphysics of cloud formation in the head (Section 4.3.1), the microphysics that might enable the existence of the tail (Section 4.3.2), and the sensibility of the microphysics with the contact parameter (Section 4.3.3).

#### 4.3.1. Microphysics of the Head

Figure 7 shows the relative humidity index at 45 km in logarithmic scale. Water vapor in excess of saturation exists wherever this index is higher than 1 (0 in logarithmic scale), therefore this figure reveals that a large amount of water remains in excess of saturation around the head of the AMEC in the model. The area where  $\Delta T < -20$  K, which is the area that we identify as the head of the AMEC, is characterized by a relative humidity index over 200 (2.3 in logarithmic scale). The relative humidity index reaches values as high as 5,000 in the core of this area (3.7 in logarithmic scale).

Water vapor in excess of saturation was first observed on Mars by the SPICAM (Spectroscopy for Investigation of Characteristics of the Atmosphere of Mars) spectrometer onboard Mars Express (Maltagliati et al., 2011). Early models of the Martian atmosphere considered a simplified cloud microphysics that assumed that all water vapor

in excess of saturation condenses into water ice, and thus could not account for supersaturated vapor. Microphysics of LMD Mars models (including the MM used in this work) was improved by Navarro et al. (2014). Among other things, they considered nucleation processes, allowing condensation only when suitable condensation nuclei are present and therefore enabling the model to predict the presence of water vapor in excess of saturation. Indeed, Navarro et al. found in their GCM runs supersaturation indexes in the order of  $\sim 5,000$  (their Figure 10).

Cloud particles generated within the core of the cold pocket must be small, because they only stay for a few minutes in the coldest area where  $\Delta T = -20$  K. The zonal wind speed at 45 km is  $\sim 100$  m/s, so an air parcel crosses this coldest region, of  $\sim 100$  km, in  $\sim 10^3$  s, while the characteristic timescale for particle growth by condensation is in the order of  $10^4$  s (Clancy et al., 2017, their Figure 5.18). We do not count with measurements of particle size for the AMEC, however, the cloud trails reported by Clancy et al. (2009, 2021), which share many characteristics with the AMEC, exhibit particle sizes below  $1 \mu\text{m}$ .

If cloud particles are small, and so much water vapor remains in excess of saturation, the optical depth will be very sensitive to the availability of condensation nuclei. Thus an enhanced concentration of condensation nuclei (dust particles) in the head of the AMEC, might be able to reduce the water vapor in excess of saturation and increase the cloud optical depth in the model.

#### 4.3.2. Microphysics and Expansion of the Tail

There are at least two different mechanisms that could be involved in the expansion of the AMEC: Advection and in-situ condensation.

The morphology of the southern branch of the cold pocket shown in the previous subsection is reminiscent of a long tail, and suggests that in-situ condensation in the southern branch could be the origin of the tail, and advection would not play a significant role. However, there are caveats with this interpretation. Both northern and southern branches of the cold pocket are associated with higher values of water ice and optical depth (Figures 6a and 6c). If the tail corresponded to the southern branch, we would expect another cloud coincident with the northern branch of the cold pocket that is not observed. In our interpretation of the model, this optically thin cloud corresponds to the observed hazes around the AMEC, which occasionally appeared forming almost symmetrical angles with respect to the tail (see Figure 1c).

Another possibility, as we proposed in Part 1 paper, is that condensation occurs mostly in the core (the head of the AMEC), where the cold pocket reaches its lowest temperatures. The core of the cold pocket coincides in location and extension with the observed head of the AMEC, and the narrow tail can be explained as the result of the advection of cloud particles that condense in this small region due to increased relative humidity.

We expect that cloud particles condense in high numbers in the head of the AMEC, due to the extreme saturation conditions found there. These particles would then be advected following the trajectory indicated schematically by the orange curve in Figure 7. In the model, condensed particles sublime as they leave the core of the cloud, and the model does not predict an important optical depth in the advection trajectory. The fact that the advection trajectory traverses the extended cold pocket, where temperatures are still low, could contribute to a slower sublimation, that would favor the AMEC tail.

The advection trajectory shown in Figure 7 reaches a length of around 600 km in 1.9 hr, which corresponds to a mean velocity of  $\sim 90$  m/s. In comparison, we reported in Part 1 paper a velocity of  $170 \pm 10$  m/s in MY34, and  $130 \pm 20$  m/s in other years. This large value of the expansion velocity repeated consistently from sol to sol in MY34 (see Figure 6 in Part 1 paper) and is not reproduced by the MM, probably a consequence of an underestimation of background velocities in the GCM (see Figure 3d). In addition, the GCM (Figure 3d) predicts sol-to-sol variations of around 20–30 m/s that were not observed in MY34 (there were not enough observations in previous years).

#### 4.3.3. Sensibility to Contact Parameter

Microphysics of the model do not reproduce the optical depth of the head or the advected tail of the AMEC. We tried to test microphysics by changing the contact parameter, which is a parameter related to the activation of condensation nuclei (see the nucleation theory described by Montmessin et al., 2002). This kind of test was also performed by Navarro et al. (2014).

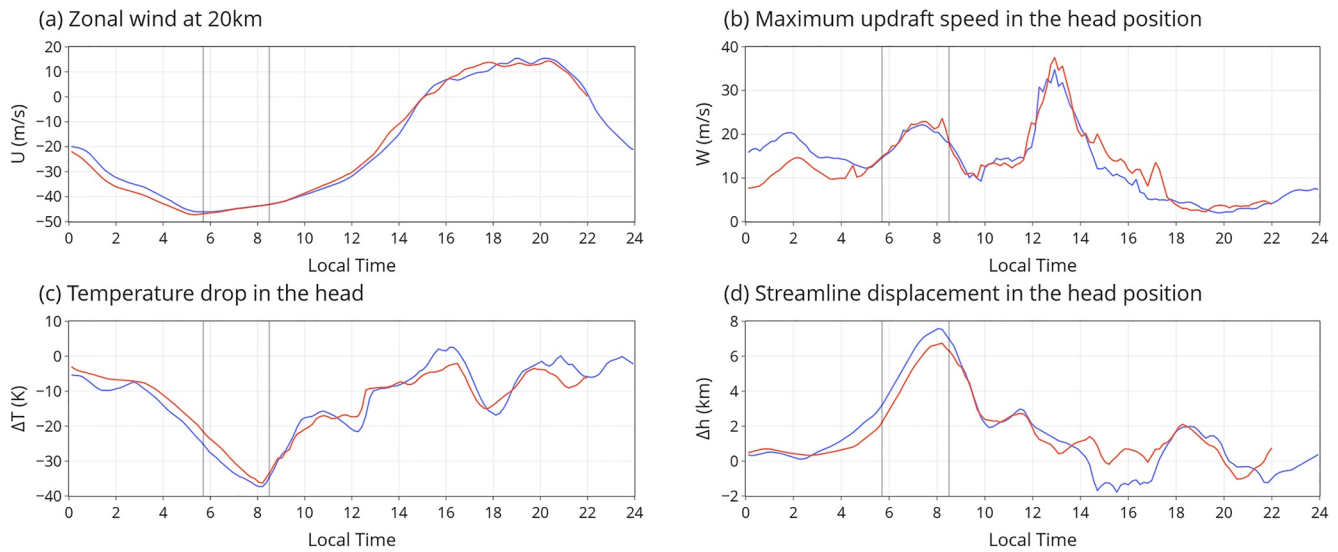


**Figure 8.** Local Time evolution of selected variables related to the strength of the head of the Arsia Mons Elongated Cloud. Blue curve corresponds to sol 2 in the mesoscale simulation, which is the sol displayed in figures in Section 4; red curve corresponds to sol 3. Vertical lines indicate the expected starting (5.7 LT) and end (8.5 LT) of the expansion phase according to observations. (a) Zonal winds at 20 km, easterly (negative) winds are strongest around sunrise. (b) Maximum vertical wind speed found in the column below the head. (c) Temperature drop in the head (at 45 km). (d) Maximum ascension of air parcels in the head (at 45 km), as estimated from the potential temperature field.

The default contact parameter in the reference simulation was 0.95, and in addition, we tested 0.85 and 0.99. Results are presented in Figure S2 in Supporting Information S1. The optical depth of the head does not change significantly, and the tail of the AMEC is still not reproduced in any case. Differences in the optical depth are present mostly in the branches of the cold pocket.

The result of this test indicates that variations in the contact parameter do not improve the reproduction of the AMEC in the model.

#### 4.3.4. Summary

In summary of this subsection. Extreme condensation conditions are present in the head of the AMEC as predicted by our simulation, however, it predicts low optical depth in the head compared to observations, and the tail of the AMEC is not reproduced. The model is not capturing with accuracy the microphysical processes involved in the AMEC, maybe because of a lack of condensation nuclei, and we propose that due to the extreme conditions in the head of the AMEC, a large number of small water ice particles could form there, and be advected by easterly winds, resisting sublimation both because they are small and because they traverse a cold area. Predicted winds do not match the observed expansion of the tail.

### 5. Diurnal Cycle in the MM

In Section 4, we discussed the physics of the AMEC at a fixed local time (7.6 LT), when the head of the cloud is fully developed. In this section, we explore the diurnal cycle of the AMEC as revealed by the MM, and compare it with observations. Videos S3 and S4 in Supporting Information S1 show the evolution with local time of Figures 4 and 5 respectively.

During the AMEC season, the onset, expansion and clearing of the cloud repeat daily in a regular way. In Part 1 paper we reported that the expansion phase of the AMEC starts with sunrise around 5.7 LT, and finishes around 8.5 LT, as deduced from observations in MY34. After 8.5 LT, the tail detached from Arsia Mons, probably because cloud formation ceased in the head while advection of the tail continued.

The head of the AMEC predicted by the MM is in good agreement with that diurnal cycle (see Video S3 in Supporting Information S1). In Figure 8 we illustrate the local-time evolution of different variables related to the strength of the head for the two sols of our reference simulation. As expected, the two sols evolve in a similar way.

Zonal winds at 20 km (Figure 8a, see also Figure 3a), which probably are the ultimate cause of the AMEC, reach their maximum intensity around sunrise. Vertical wind speed at the SVU (Figure 8b) reaches its maximum around 7.5 LT, however, as discussed in Section 4.1, the total ascent of air parcels and its consequent temperature drop depend also on the width of ascending cells and on the horizontal wind speed. Maximum drop in temperatures (Figure 8c) and maximum air parcel ascent in the head (Figure 8d) takes place around 8.2 LT.

As we can see in Video S3 in Supporting Information S1, the core cold pocket corresponding to the head collapses around 8.5 LT, in very good agreement with the observed end of the head of the AMEC. This might be a result of wave breaking when the amplitude of vertically propagating gravity waves exceeds a threshold.

The evolution of variables presented in panels b–d in Figure 8 is not symmetrical. Their slopes are higher at the end of the AMEC cycle. However, it is not straightforward to set thresholds in those variables that predict the life cycle of the head of the AMEC.

## 6. Sol-To-Sol and Interannual Variations From the GCM

Our previous analysis focused in the results of the MM for two consecutive sols in the AMEC season in MY34, the year when the behavior of the AMEC is best characterized. In this section we discuss the potential influence of sol-to-sol and interannual variations of the key physical parameters as shown in Section 3 from GCM outputs (Figure 3).

Water content suffers strong sol-to-sol variations (Figure 3g). This is likely linked through microphysics to some visual characteristics of the cloud (mostly its brightness), which have been observed to change from sol to sol.

In Figure 3d, we identify a potential threshold for the occurrence the AMEC season: Easterly winds at 20 km are larger than  $\sim 30$  m/s during that season. Day-to-day variations of environmental winds at 20 km could produce sol-to-sol variations, especially at the starting and end of the season, when wind speeds are close to that threshold. Even if the SVU happens, the tail might not expand. This is what we reported as “early anomalies” (see Part 1 paper), observed during the early sols of the AMEC in MY34. Since the head was there, the SVU was probably there too, just the tail did not expand because suitable microphysical conditions at 45 km were not met. Therefore, the starting of the AMEC season can be conditioned by the occurrence of the SVU or by microphysical conditions at 45 km.

We do not appreciate significant interannual variations during the AMEC season in Figure 3, with the exception of MY34, a year that was characterized by a Global Dust Storm (GDS) event (Sánchez-Lavega et al., 2019). Fast winds at 20 km were present earlier than usual, starting at Ls 207°. However, observations in Ls 223°–235° do not show the AMEC, which started in MY34 sometime between Ls 235° and Ls 242° (see Part 1 paper). We see in Figure 3e that GCM predicted for MY34 temperatures at 45 km 20 K higher than usual during the dust storm. The temperature slowly lowers until it reaches values comparable to those predicted by the GCM for other years at Ls 240°–245°. A higher temperature would prevent cloud formation, and this probably explains the appearance of the AMEC in MY34 after Ls 235°–243° and not before, even if zonal winds at 20 km were already fast.

## 7. Conclusions and Perspectives

We have used a mesoscale simulation to gain understanding into the physics behind the AMEC. We see that, due to the rise of the hygropause during the dusty season, the water pumping mechanism described by Michaels et al. (2006) for orographic clouds during the ACB is not the main driver of orographic clouds in this season. Instead, orographically generated gravity waves that reach and perturb the hygropause is the primary mechanism behind orographic clouds. The model predicts a dynamical process triggered by the interaction of winds with Arsia Mons. A downslope windstorm followed by a hydraulic-like jump forms on the western slope of Arsia Mons (the lee slope), which produces a SVU and leads to the formation of a cold pocket 30K colder than the environment temperature, due to the adiabatic expansion of air cells being transported upwards. The region with the highest drop of temperature ( $\Delta T = -20$  K) is compact, and spatially and temporally coincident with the observed head of the AMEC, at 45 km in altitude on the western slope of the volcano. The diurnal cycle of the AMEC is correctly reproduced by mesoscale modeling. Transiently fast winds on the summit of Arsia at the local time of the AMEC as part of the general circulation constrains the seasonal cycle.

Cold temperatures in the head imply a drop in saturation vapor pressure that produces cloud formation and extreme values of relative humidity. The model does not reproduce the observed optical depth of the head, but it predicts strong supersaturation. An enhanced availability of condensation nuclei in the model could induce more condensation, reduce the water vapor in excess of saturation and increase the predicted optical depth.

In the model, advected cloud particles sublimate, and the optical depth of the tail is not reproduced. Increased condensation at the head, together with the small size of condensates and the low temperatures in the area (caused by the interaction of the atmosphere with Arsia), which might slow sublimation, could lead to the observed expansion of the tail.

Easterly zonal winds at 45 km (Figure 3e) do not match observations well, and this might have important consequences. The advection trajectory predicted by the MM corresponds to an expansion velocity of  $\sim 90$  m/s, lower than the measured expansion velocity,  $170 \pm 10$  m/s in MY34, and  $130 \pm 20$  m/s in other years. This is an important discrepancy.

Our conclusions about the physical mechanism driving the AMEC are partially in agreement with those proposed by Clancy et al. (2021) for the Perihelion Cloud Trails. In their case, the proposed origin of the perturbation leading to the formation of cold pockets was insolation maxima in the afternoon. Since the AMEC happens in the early morning, that was not a possibility in this case. This work demonstrates that wind-surface interaction is another possible origin for this kind of feature.

Most previous works on clouds on Tharsis have focused on the ACB season (i.e.,  $L_s 0^\circ$ – $180^\circ$ ). In this work, we have run a MM on the region of Tharsis during the dusty season. We find that due to the different vertical distribution of water in the atmosphere and the higher altitude of the hygropause, the pumping of water by thermal slope winds found by Michaels et al. (2006) is not efficient during this season. Instead, vertically propagating gravity waves perturbing the hygropause is the predominant cloud formation mechanism. We show this result for the AMEC in the early morning, but it also applies to clouds on Tharsis at other LT (not shown).

Future observations that permit higher resolution cloud tracking of the tail are needed to confirm the very fast advection speeds. In addition, spectral observations of the head and the region where the tail extends, will allow the retrieval of parameters of interest for microphysics, such as temperature, water vapor and ice concentration, particle sizes, and condensation nuclei availability (dust). Future modeling efforts should focus on understanding the microphysics enabling the expansion of the AMEC, with the inputs of new observations. Jiang and Doyle (2006) examined two cases of “topographically generated cloud plumes” observed on Earth that visually resemble the AMEC, these plumes are a good terrestrial analog to the AMEC.

The AMEC is a natural laboratory to learn about the microphysics of the Martian atmosphere. The knowledge acquired in this work will be a valuable aid for the planning of new observations that will help improve our knowledge of the AMEC and other orographic clouds on Mars.

#### Acknowledgments

This work has been supported by the Spanish project PID2019-109467GB-I00 (MINECO/FEDER, UE) and Grupos Gobierno Vasco IT-1366-19. JHB was supported by ESA Contract No. 4000118461/16/ES/JD, Scientific Support for Mars Express Visual Monitoring Camera. The Aula EspaZio Gela is supported by a grant from the Diputación Foral de Bizkaia (BFA). The Applied Physics Department at UPV/EHU supported the stay of JHB in Paris. JHB acknowledges the welcoming hospitality by LMD colleagues during his stay. The estimated energy consumption associated with this work is 231 kWh, including a trip by train from Bilbao to Paris (110 kWh), simulations (110 kWh), and regular computing resources for data analysis and day a day working (11 kWh). 48 kWh were consumed in Spain and 183 kWh were consumed in France. The total amount of energy used in this work corresponds to 17.6 kg of  $CO_2$  and 5,200 mg of long lived radioactive waste.

#### Data Availability Statement

The GCM and mesoscale model and the configuration details are described in Section 2 and references therein. Netcdf files containing the data from the mesoscale model used in figures in this paper is available in: <https://doi.org/10.14768/75b44a04-fb39-4a5c-b097-00229d34e5c1>.

#### References

- Barnes, J. R., Haberle, R. M., Wilson, R. J., Lewis, S., Murphy, J. R., & Read, P. L. (2017). The global circulation. In *The atmosphere and climate of Mars* (pp. 229–294)
- Benson, J. L., Bonev, B. P., James, P. B., Shan, K. J., Cantor, B. A., & Caplinger, M. A. (2003). The seasonal behavior of water ice clouds in the Tharsis and Valles Marineris regions of Mars: Mars Orbiter Camera observations. *Icarus*, *165*(1), 34–52. [https://doi.org/10.1016/S0019-1035\(03\)00175-1](https://doi.org/10.1016/S0019-1035(03)00175-1)
- Benson, J. L., James, P. B., Cantor, B. A., & Remigio, R. (2006). Interannual variability of water ice clouds over major Martian volcanoes observed by MOC. *Icarus*, *184*(2), 365–371. <https://doi.org/10.1016/j.icarus.2006.03.014>
- Clancy, R. T., Grossman, A. W., Wolff, M. J., James, P. B., Rudy, D. J., Billawala, Y. N., et al. (1996). Water vapor saturation at low altitudes around Mars aphelion: A key to Mars climate? *Icarus*, *122*(1), 36–62. <https://doi.org/10.1006/icar.1996.0108>
- Clancy, R. T., Montmessin, F., Benson, J., Daerden, F., Colaprete, A., & Wolff, M. J. (2017). Mars clouds. In *The atmosphere and climate of Mars* (pp. 42–75).

- Clancy, R. T., Wolff, M. J., Cantor, B. A., Malin, M. C., & Michaels, T. I. (2009). Valles Marineris cloud trails. *Journal of Geophysical Research*, *114*(E11), E11002. <https://doi.org/10.1029/2008je003323>
- Clancy, R. T., Wolff, M. J., Heavens, N. G., James, P. B., Lee, S. W., Sandor, B. J., et al. (2021). Mars perihelion cloud trails as revealed by MARCI: Mesoscale topographically focused updrafts and gravity wave forcing of high altitude clouds. *Icarus*, *362*, 114411. <https://doi.org/10.1016/j.icarus.2021.114411>
- Durrán, D. R. (1990). Mountain waves and downslope winds. In *Atmospheric processes over complex terrain* (pp. 59–81). American Meteorological Society.
- Fedorova, A., Montmessin, F., Korabiev, O., Lefèvre, F., Trokhimovskiy, A., & Bertaux, J. L. (2021). Multi-annual monitoring of the water vapor vertical distribution on Mars by SPICAM on Mars Express. *Journal of Geophysical Research: Planets*, *126*(1), e2020JE006616. <https://doi.org/10.1029/2020je006616>
- Forget, F., Hourdin, F., Fournier, R., Hourdin, C., Talagrand, O., Collins, M., et al. (1999). Improved general circulation models of the Martian atmosphere from the surface to above 80 km. *Journal of Geophysical Research*, *104*(E10), 24155–24175. <https://doi.org/10.1029/1999je001025>
- Hernández-Bernal, J., Sánchez-Lavega, A., del Río-Gaztelurrutia, T., Ravanis, E., Cardesin-Moinelo, A., Connour, K., et al. (2021). An extremely Elongated Cloud over Arsia Mons volcano on Mars: I. Life cycle. *Journal of Geophysical Research: Planets*, *126*(3), e2020JE006517. <https://doi.org/10.1029/2020je006517>
- Jiang, Q., & Doyle, J. D. (2006). Topographically generated cloud plumes. *Monthly Weather Review*, *134*(8), 2108–2127. <https://doi.org/10.1175/mwr3177.1>
- Lott, F. (2016). A new theory for downslope windstorms and trapped mountain waves. *Journal of the Atmospheric Sciences*, *73*(9), 3585–3597. <https://doi.org/10.1175/jas-d-15-0342.1>
- Madeleine, J. B., Forget, F., Millour, E., Montabone, L., & Wolff, M. J. (2011). Revisiting the radiative impact of dust on Mars using the LMD Global Climate Model. *Journal of Geophysical Research*, *116*(E11), E11010. <https://doi.org/10.1029/2011je003855>
- Maltagliati, L., Montmessin, F., Fedorova, A., Korabiev, O., Forget, F., & Bertaux, J. L. (2011). Evidence of water vapor in excess of saturation in the atmosphere of Mars. *Science*, *333*(6051), 1868–1871. <https://doi.org/10.1126/science.1207957>
- Michaels, T. I., Colaprete, A., & Rafkin, S. C. R. (2006). Significant vertical water transport by mountain-induced circulations on Mars. *Geophysical Research Letters*, *33*(16), L16201. <https://doi.org/10.1029/2006gl026562>
- Montabone, L., Forget, F., Millour, E., Wilson, R. J., Lewis, S. R., Cantor, B., et al. (2015). Eight-year climatology of dust optical depth on Mars. *Icarus*, *251*, 65–95. <https://doi.org/10.1016/j.icarus.2014.12.034>
- Montabone, L., Spiga, A., Kass, D. M., Kleinböhl, A., Forget, F., & Millour, E. (2020). Martian year 34 column dust climatology from Mars climate sounder observations: Reconstructed maps and model simulations. *Journal of Geophysical Research: Planets*, *125*(8), e2019JE006111. <https://doi.org/10.1029/2019je006111>
- Montmessin, F., Forget, F., Rannou, P., Cabane, M., & Haberle, R. M. (2004). Origin and role of water ice clouds in the Martian water cycle as inferred from a general circulation model. *Journal of Geophysical Research*, *109*(E10), E10004. <https://doi.org/10.1029/2004je002284>
- Montmessin, F., Rannou, P., & Cabane, M. (2002). New insights into Martian dust distribution and water-ice cloud microphysics. *Journal of Geophysical Research*, *107*(E6), 4–1. <https://doi.org/10.1029/2001je001520>
- Navarro, T., Madeleine, J. B., Forget, F., Spiga, A., Millour, E., Montmessin, F., & Määttä, A. (2014). Global climate modeling of the Martian water cycle with improved microphysics and radiatively active water ice clouds. *Journal of Geophysical Research: Planets*, *119*(7), 1479–1495. <https://doi.org/10.1002/2013je004550>
- Peale, S. J. (1973). Water and the martian W cloud. *Icarus*, *18*(3), 497–501. [https://doi.org/10.1016/0019-1035\(73\)90159-0](https://doi.org/10.1016/0019-1035(73)90159-0)
- Rafkin, S. C., Haberle, R. M., & Michaels, T. I. (2001). The Mars regional atmospheric modeling system: Model description and selected simulations. *Icarus*, *151*(2), 228–256. <https://doi.org/10.1006/icar.2001.6605>
- Sagan, C., Veverka, J., & Gierasch, P. (1971). Observational consequences of Martian wind regimes. *Icarus*, *15*(2), 253–278. [https://doi.org/10.1016/0019-1035\(71\)90079-0](https://doi.org/10.1016/0019-1035(71)90079-0)
- Sánchez-Lavega, A., del Río-Gaztelurrutia, T., Hernández-Bernal, J., & Delcroix, M. (2019). The onset and growth of the 2018 Martian global dust storm. *Geophysical Research Letters*, *46*(11), 6101–6108. <https://doi.org/10.1029/2019gl083207>
- Skamarock, W. C., & Klemp, J. B. (2008). A time-split nonhydrostatic atmospheric model for weather research and forecasting applications. *Journal of Computational Physics*, *227*(7), 3465–3485. <https://doi.org/10.1016/j.jcp.2007.01.037>
- Slipher, E. C. (1927). Atmospheric and surface phenomena on Mars. *Publications of the Astronomical Society of the Pacific*, *39*(230), 209–216. <https://doi.org/10.1086/123714>
- Smith, D. E., Zuber, M. T., Frey, H. V., Garvin, J. B., Head, J. W., Muhleman, D. O., et al. (2001). Mars Orbiter Laser Altimeter: Experiment summary after the first year of global mapping of Mars. *Journal of Geophysical Research*, *106*(E10), 23689–23722. <https://doi.org/10.1029/2000je001364>
- Smith, R. B. (1980). Linear theory of stratified hydrostatic flow past an isolated mountain. *Tellus*, *32*(4), 348–364. <https://doi.org/10.1111/j.2153-3490.1980.tb00962.x>
- Smith, S. A., & Smith, B. A. (1972). Diurnal and seasonal behavior of discrete white clouds on Mars. *Icarus*, *16*(3), 509–521. [https://doi.org/10.1016/0019-1035\(72\)90097-8](https://doi.org/10.1016/0019-1035(72)90097-8)
- Spiga, A., & Forget, F. (2009). A new model to simulate the Martian mesoscale and microscale atmospheric circulation: Validation and first results. *Journal of Geophysical Research*, *114*(E2), E02009. <https://doi.org/10.1029/2008je003242>
- Spiga, A., Hinson, D. P., Madeleine, J. B., Navarro, T., Millour, E., Forget, F., & Montmessin, F. (2017). Snow precipitation on Mars driven by cloud-induced night-time convection. *Nature Geoscience*, *10*(9), 652–657. <https://doi.org/10.1038/ngeo3008>
- Wang, H., & Ingersoll, A. P. (2002). Martian clouds observed by Mars global surveyor Mars orbiter camera. *Journal of Geophysical Research*, *107*(E10), 8–1. <https://doi.org/10.1029/2001je001815>